INTERNAL BOILING TO FLAME FLICKERING: INSIGHTS INTO VARIOUS SPATIO-TEMPORAL DYNAMICS OF NANOFUEL DROPLET COMBUSTION

A Thesis submitted for the degree Of

Doctor of Philosophy

in the

Faculty of Engineering

by

Khushboo Pandey

INTERDISCIPLINARY CENTRE FOR ENERGY RESEARCH

INDIAN INSTITUTE OF SCIENCE

BANGALORE -560012, INDIA

January – 2020

To my parents

Mrs. Satya Bhama Pandey and Mr. Ajay Kumar Pandey

"My thesis is an embodiment of your hard-work"

Abstract

Addition of solid particles to liquid fuels is central to the idea of increasing the energy density of conventional fuels. Normally boron, aluminium, and carbon particles in the size range of ~ (5-200μm) are added to conventional fuels as "liquid-fuel extender". However, concerns regarding the long-term stability of such fuels inhibit their applicability in practical systems. Recent advances in nanotechnology have circumvented this problem by opening up avenues to synthesize energetic nanoparticles (NPs) with desirable traits, thereby intensifying their usage in application domains like automotive, pharmaceutical and microelectronics. Compared to their bulk form, increased surface area to volume ratio of NPs leads to enhanced catalytic properties, high reactivity, and significantly different thermo-physical properties. Nanofuels are prepared by uniformly suspending NPs (1-100 nm) of metals or metallic oxide particles in a liquid base. Extensive research studies pertaining to nanofuel combustion have unveiled a plethora of intriguing features. For example, nanofuels exhibit increased ignition probability, enhanced burning/evaporation rate, and reduced soot formation.

The first part of the thesis considers the multiscale combustion dynamics, shape oscillations, secondary atomization, and precipitate formation for both low and high vapour pressure nanofuel (n-dodecane seeded with alumina nanoparticles (NPs)) droplets in pendant mode. Dilute nanoparticle loading rates (0.1 - 1 %) have been considered. In case of nanofuels, intense heat release from the enveloping flame leads to the formation of micron-size aggregates (of alumina NPs) which serve as nucleation sites promoting heterogeneous boiling. The key mechanisms responsible for the growth, transport and rupture of the bubbles are deciphered. Bubble rupture causes ejections of liquid droplets termed as secondary atomization. Ejection of small bubbles (Mode 1) resembles classical vapour bubble collapse mechanism near a flat free surface. However large bubbles induce severe shape deformations as well as bulk oscillations. Rupture of large bubbles results in high speed liquid jet formation which goes under Rayleigh-Plateau tip break-up. Both modes contribute towards direct fuel transfer from droplet surface to flame envelope bypassing diffusion limitations. Combustion lifetime of nanofuel droplets consequently have two stages, stage I (where bubble dynamics are

dominant and stage II (formation of gelatinous mass due to continuous fuel depletion; NP agglomeration). In the present work, variation of flame dynamics and spatio-temporal heat release (HR) have been analysed using high speed OH* chemiluminescence imaging. Fluctuations in droplet shape and flame heat release are found to be well correlated. The coupling mechanisms among heat release, shape oscillations and secondary atomization that underline the combustion behaviour of such low and high vapour pressure nanofuels, is established.

The second part reports detailed analyses of evaporation and atomisation characteristics of nanofuel droplets in a contactless environment (acoustic levitation) under external radiative heating. Two base fuels, ethanol and n-dodecane with significant difference in respective vapour-pressures are considered. Nanoparticles (NPs) of Cerium oxides (CeO$_2$) are utilised as nano-additives at dilute particle loading rate (PLR) of 0-0.5 % by weight. Pure ethanol droplets vaporise at a faster rate than pure dodecane droplets and do not exhibit any secondary atomisation. However, pure dodecane droplets exhibit two modes of secondary break-up; Kelvin-Helmholtz instability induced stripping and catastrophic breakup beyond a certain threshold value of initial droplet size. Nanofuel droplets of ethanol neither exhibit any significant change in vaporisation rate nor secondary atomization. Contrarily, dodecane-based nanofuels show enhanced vaporisation due to heat absorption by nanoparticles and consequently different modes of secondary breakup. Interestingly, dodecane-based nanofuel droplets exhibit internal boiling induced atomization. A time scale analysis considering orthokinetic NP aggregation, evaporation lifetime and bubble growth rate is presented to elucidate the mechanism of such internal boiling. A theoretical non-dimensional time scale is coined to estimate the minimum value of droplet size necessary for exhibiting boiling. The analysis shows excellent agreement with the experimental observations. Furthermore, a unique three-dimensional regime map is proposed to correlate the breakup modes with droplet size, PLR, and heating rates.

For the third part of the thesis, the flame dynamics of free-falling contactless burning fuel droplets (pure and nanofuel) is investigated. A droplet under free fall undergoes acceleration resulting in progressive increase of its velocity (increase in Reynolds Number, Re) along the path. The consequent dynamic external relative

flow induced along the drop trajectory allows self-tuning of the flame through a series of transitions. At low Re, the droplet initially transitions from a fully enveloped buoyant diffusion flame to a premixed wake flame structure. It shown that this transition occurs due to flame extinction at the droplet forward stagnation point when critical strain rate is exceeded due to the external flow. Subsequently the wake flame topology undergoes significant variations with further increase in Reynolds Number. The flow conditions necessary for wake-flame stabilization is characterized. Using a round-jet analogy, a linear relationship between the flame height and Reynolds number is established. Droplet burning rate for all functional droplets exhibits minimal change due to reduced energy input from the wake flame. However, for nanofuel droplets, the global heat release is lowered due to the reduction in gasification rate brought about by the in-situ formation of porous structure by the agglomeration of nanoparticles. Furthermore, for particle laden droplets, absence of sufficient energy input from flame suppresses internal heterogeneous boiling as found in most pendant droplet experiments.

The last part of the work pivots around the acoustic-flame coupling for buoyant diffusion flame in droplets. The acoustic perturbations modulate the flame surface or heat release only at lower frequency bands by feeding energy into the natural vortical stability modes of a buoyant plume. Interestingly, it is unearthed that a flame is naturally unstable at all frequencies lower than $\sqrt{g/d}$, where d is the droplet diameter. Acoustic pumping at any such frequency $(<\sqrt{g/d})$ corresponds to a unique convective length scale h such that $f_{flame} = \sqrt{g/h}$. Subsequently, it is established that the shedding length scale of the droplet flame shortens by more than 25 % with increase in acoustic pressure. Further, it is also theoretically proved that using critical circulation argument, one can uniquely determine the shedding length scale at any acoustic loading. However, it is interesting to note that while the acoustic pressure amplitude is crucial for determining the convective length at which a flame rolls up, the frequency of excitation has no role to play. In other words, the velocity field introduced by the acoustic pressure is responsible for the shedding of the flame. The acoustic perturbations also lead to bulk oscillation of the flame surface near the forward

stagnation zone. This is attributed to the acoustic induced velocity that leads to transient shifting of the stoichiometric surface.

Acknowledgments

Publications from this thesis

A. Journal articles

1) **Khushboo Pandey**, Kamanio Chattopadhyay and Saptarshi Basu, Combustion dynamics of low vapour pressure nanofuel droplets. Phys. Fluids 29, 074102 (2017).

2) **Khushboo Pandey** and Saptarshi Basu, High vapor pressure nanofuel droplet combustion and heat transfer: insights into droplet burning time scale, secondary atomisation and coupling of droplet deformations and heat release, Combustion and Flame, 209, pp 167-179(2019).

3) **Khushboo Pandey** and Saptarshi Basu, How boiling happens in nanofuel droplets, Phys. Fluids 30, 107103 (2018) **(FEATURED ARTICLE)**

4) **Khushboo Pandey**, Saptarshi Basu, Bal Krishan, and Gautham V, Dynamic self-tuning, flickering and shedding in buoyant droplet diffusion flames under acoustic excitation. (Communicated to Proceedings of Combustion Institute, Accepted for Oral Presentation in the 38th International Symposium on Combustion, Adelaide, Australia, 24th -29th January 2021).

5) **Khushboo Pandey**, Saptarshi Basu, Gautham V, Aditya Potnis and Kamanio Chattopadhyay, Self-tuning and topological transitions in a free-falling nanofuel droplet flame. (Communicated to Combustion and Flame)

6) **Khushboo Pandey**, Deepu Prabhakaran, and Saptarshi Basu, Review of transport processes and particle self-assembly in acoustically levitated nanofluid droplets, *(INVITED FEATURED ARTICLE) Physics of Fluids, 31(11), 112102.*

B. Conference Articles

1) **Khushboo Pandey** and Saptarshi Basu, "Combustion dynamics of nanoparticle laden jet fuel", Proceedings of the International Conference on Sustainable Energy and Environmental Challenges (SEEC-2018), January 1-3, 2018, Bangalore, India

2) **Khushboo Pandey** and Saptarshi Basu, "Enhanced burning rate of jet fuel surrogate seeded with nanoparticles", ICLASS 2018, 14th Triennial International Conference on Liquid Atomization and Spray Systems, Chicago, IL, USA, July 22-26, 2018.

3) **Khushboo Pandey** and Saptarshi Basu, "Atomisation and combustion characteristics of high-vapour pressure nanofuel droplets", Asia-Pacific Conference on Combustion, 1-5 July 2019, Fukuoka, Japan.

4) **Khushboo Pandey** and Saptarshi Basu, "Boiling in nanofuel droplet", Poster Presentation, Droplets 2019, Durham, UK, September 16-18, 2019

5) **Khushboo Pandey** and Saptarshi Basu, "Boiling in acoustically levitated nanofuel droplets", Flash and poster presentations, 72nd Annual Meeting of the American Physical Society's Division of Fluid Dynamics (DFD), Seattle, Washington on November 23-26, 2019.

Publications (Not included in thesis)

A. Journal articles

1) Sandeep Hatte, Keshav Pandey, **Khushboo Pandey**, Suman Chakraborty and Saptarshi Basu, Universal evaporation dynamics of ordered arrays of sessile droplets, J. Fluid Mech. 886, pp 61-81(2019).

2) **Khushboo Pandey**, Sandeep Hatte, Keshav Pandey, Suman Chakraborty and Saptarshi Basu, Generalizing co-operative evaporation in two-dimensional droplet arrays, Phys. Rev. E 101, pp 043101 (2020).

3) Durbar Roy**, Khushboo Pandey**, Meneka Banik, Rabibrata Mukherjee, and Saptarshi Basu, Dynamics of droplet impingement on biomimetic surface: insights into spreading, anomalous stickiness and breakup, Proceedings of the Royal Society A, 475(2229), 20190260. ***(First and second authors are equal contributors).**

B. Conference Articles

1) Durbar Roy, **Khushboo Pandey**, Rabibrata Mukherjee, and Saptarshi Basu, "Droplet Impact on dry solid surfaces: Traditional vs Bio-mimetic", Poster presentations, Droplets 2019, Durham, UK, September 16-18, 2019.

2) Saptarshi Basu, Durbar Roy, **Khushboo Pandey**, and Rabibrata Mukherjee, "Droplet Impact on dry solid surfaces: Traditional vs Bio-mimetic", 72nd Annual Meeting of the American Physical Society's Division of Fluid Dynamics (DFD), Seattle, Washington on November 23-26, 2019.

Table of Contents

List of figures

List of tables

List of multimedia files

Multimedia files are available as Supporting Information along with the manuscript.

To access these files from OneDrive, please click on the link,

https://indianinstituteofscience-my.sharepoint.com/:f:/g/personal/kushboop_iisc_ac_in/Ekv7nRpk-V1Kh5WKIkDvKzcBCBIb6ubEIyvTOohtfacuRQ?e=1qNCaU

Video 2.1 Shadowgraphy of combusting nanofuel droplet.

Video 2.2 Bubble ejection event Mode 1.

Video 2.3 Bubble ejection event Mode 2.

Video 2.4 Surface accumulation of particles leading to the formation of gelatinous structure.

Video 2.5 Global flame fluctuations.

Video 2.6 Flame standoff fluctuations in flame zone II.

Video 3.1 Increased bubble counts in ceria laden ethanol-water droplets.

Video 3.2 Catastrophic break-up of Ethanol-Water droplet.

Video 3.3 Bubble tracking.

Video 3.4 Flame response to the ejection of daughter droplets.

Video 3.5 Simultaneous flame chemiluminescence and droplet shape imaging showing the variation with particle addition.

Video 4.1 Isolated bubble ejection (Type I) at the equator of an acoustically levitated droplet.

Video 4.2 Isolated bubble ejection at the pole (Type I) of an acoustically levitated

droplet.

Video 4.3 Droplet rupture with Type II bubble ejection.

Video 6.1 Wind effect of exhibited by the flame at the forward droplet stagnation point under the effect of external acoustic field.

Video 6.2 Tracking of bright spots which contribute to the transient flickering of the droplet diffusion flame.

Nomenclature

a_{agg}	size of the nanoparticle aggregate
A_b	area of the bounding rectangle for burning droplet
A_{DD}	dodecane droplet area exposed to the flame
A_f	line-of-site flame area
a_k	Mode temporal coefficient
a	vertical length scale of the levitated droplet
AR_d	droplet aspect-ratio
AR_{lig}	ligament aspect ratio
b	horizontal axis of the levitated droplet
B	heat transfer number
c_h	volumetric concentration of ceria NPs
c_{pg}	fuel vapor-phase specific heat capacity at $\overline{\text{T}}$
CM_{SL}	Control mass including the flame shear layer
d	instantaneous droplet diameter
d_0	initial droplet diameter
d_b	bubble diameter
d_{boil}	minimum droplet diameter exhibiting boiling
d_c	critical droplet diameter exhibiting catastrophic break-up
d_d	diameter of daughter droplets
d_f	flame stand-off diameter
d_p	diameter of nanoparticle

Do	Damköhler number.
$e\,(t)$	instantaneous ejection flux
$E_{residual}$	residual energy
$f_{excitation}$	frequency of the external acoustic perturbations
f_{flame}	frequency of the flame response
F_{imp}	impulse force
F_r	POD flame modes
F_{recoil}	recoil force of the vapor thrust
Fr	Froude Number
F_{st}	surface tension force
g	acceleration due to gravity
Gr	Grashof number
H_{ac}	flame shedding height under external acoustic field
H_{NC}	flame shedding height under natural convection
h_f	flame height
h_{fg}	Latent heat of vaporisation of the liquid
Δh_c	heat of combustion per unit mass
$I(i,j)$	flame intensity for pixel (i, j)
$\overline{I_f}$	average OH* intensity
I_{laser}	laser heating rate
$Intden$	Integrated density of the flame intensity
J	Solvent mass flux through porous media
k	permeability
k_g	vapor-phase thermal conductivity of fuel and air $\overline{\mathrm{T}}$
k_r	wavenumber in the radial direction
k_z	wavenumber in the axial direction
KE_{lig}	kinetic energy of ligament
L_{lig}	ligament length
Ma	acoustic Mach number
m_{bubble}	vapour bubble mass
m_{lig}	ligament mass

$\dot{m}\|_{conv}$	droplet burning rate in convective environment
$\dot{m}\|_{porous}$	evaporation rate through porous media
$\dot{m}\|_{NPs}^{*}$	mass burning rate for NP laden droplet
$\dot{m}\|_{EW}^{*}$	mass burning rate for ethanol-water droplet
N_t	Total number of ejection events
Nu	Nusselt number
Δp	pressure difference between droplet pole and equator
ΔP	pressure difference
ΔP_{cap}	capillary pressure difference
$P_{equator}$	pressure at droplet equator
P_{pole}	pressure at droplet pole
P_{rms}'	root mean square pressure amplitude of the acoustic perturbation
Q	flame heat release
$|Q_{acoustics}|$	flame spectral energy of low-frequency-band under acoustic perturbations
$\dot{Q}_{laser}$	laser power absorbed by the droplet
$|Q_{NC}|$	naturally buoyant flame spectral energy of low-frequency-band
r	instantaneous droplet radius
r_0	initial droplet radius
r_b	bubble radius
r_c	critical bubble radius
R_c	droplet equatorial radius of curvature
Re	Reynolds number
Ri	Richardson number
$Re_{f,cold}$	Reynolds number for cold-flow
R_f	flame stand-off distance
r_{lig}	ligament radius
r_{local}	locally perturbed region
S_r	POD droplet shape modes
St	Strouhal Number
t	time
t_{ac}	characteristic timescale of external acoustic field

t_{break}	ligament break-up timescale
t_{bubble}	bubble growth timescale
$t_{diffusion}$	diffusive timescale
$t_{flicker}$	time period of flame flicker
t_{total}	total droplet combustion/evaporation time
$t_{total}|_{NPs}$	total combustion time for ethanol-water droplet
$t_{total}|_{NPs}$	total combustion time for particle laden droplet
$t^*|_{EW}$	theoretical burning time for ethanol-water droplet
$t^*|_{NPs}$	theoretical burning time for particle laden droplet
T_b	boiling temperature of the droplet
T_f	flame temperature
T_i	initial temperature of the droplet
T_s	droplet surface temperature
$T_{wet-bulb}$	wet-bulb temperature of droplet liquid
T_∞	ambient temperature
$\bar{T}$	arithmetic mean of T_s and T_f
U'_a	root mean square velocity amplitude of the acoustic perturbation
u_0	sound velocity in the air
$u_{internal}$	droplet internal velocity
u_r	radial velocity component of the fkow
U_j	ligament jet velocity
u_{max}	speed of sound in the gaseous phase
u_θ	tangential velocity component of the flow
V_∞	Convective free-stream (air) velocity
V_b	bubble velocity
V_{dd}	daughter droplet velocity
V_f	characteristic flame velocity scale due to natural convection
ΔV_{crater}	volume of crater
v_{lig}	Experimental ligament velocity
$v_{lig}|_{th}$	theoretical ligament velocity
w	particle loading rate

w_f	flame width
w_{jet}	inlet jet radius
We	Weber number
W_{lig}	ligament width
We_{local}	local Weber number
y_{vo}	virtual origin position
z_{cg}	pressure node position

List of symbols

α	thermal diffusivity of liquid
α_{local}	local ejection parameter
ϵ_s	spread fraction
α_{local}	flame tangential strain
υ	stoichiometric air-fuel (mass) ratio
υ_∞	kinematic viscosity of air free stream
β	coefficient of thermal expansion
δ_{flame}	flame stand-off distance at the forward stagnation zone
δ_{mean}	mean flame stand-off distance
ρ_∞	density of free stream around the droplet
ρ_{air}	density of air/oxidiser
ρ_{flame}	density of the flame
ρ_v	vapor-phase density of ethanol
ρ_l	liquid -phase density of ethanol
μ_∞	dynamic viscosity of free stream around the droplet
μ_{eff}	effective fuel viscosity
μ_i	initial fuel viscosity
η	local mass evaporation rate
σ	liquid surface tension
$\dot{\gamma}$	shear rate
τ_{crust}	crust thickness

φ_{crust}	particle packing fraction of the crust
φ_k	orthogonal spatial modes
λ_k	kth eigenvalue
v_k	kth eigenvector
x_e	modal energy fraction
Γ	circulation
$\Gamma_{critical}$	critical circulation
$\Gamma_{initial}$	initial circulation
$\Gamma_{citical}\|_{NC}$	critical circulation of naturally buoyant flame
$\Gamma_{citical}\|_{ac}$	critical circulation of acoustically perturbed droplet diffusion flame
τ^*	theoretical non-dimensional time-scale
τ^{**}	experimental non-dimensional time-scale
τ_{agg}	nanoparticle aggregation time scale
τ_{boil}	boiling time scale
$\tau_{burning}$	final residue leftover burning time
$\tau_{recovery}$	shape recovery time scale
ξ	vorticity
ω	angular frequency

List of abbreviations

1. 2D   Two dimensional
2. 3D   Three dimensional
3. BVK   Bernard Von-Karman
4. CB   Catastrophic break-up
5. CWT   Continuous wavelet transform
6. DEHS   Diethyl hexa sebacate
7. DD   Dodecane
8. DL   Darrieus–Landau
9. EW   Ethanol-Water
10. fps   frames per second

11.	FFT	Fast Fourier Transform
12.	HLB	Hydrophilic-lipophilic balance
13.	HR	Heat Release
14.	IB	Internal boiling
15.	IRO	Intense Relay Optics
16.	Nd:YAG	Neodymium-doped Yttrium Aluminium Garnet
17.	NP	Nanoparticle
18.	SA	Secondary Atomisation
19.	SEM	Scanning Electron Microscope
20.	PE	Pure evaporation
21.	PIV	Particle Image Velocimetry
22.	PLR	Particle loading rate
23.	POD	Proper Orthogonal Decomposition
24.	PTU	Programmable Terminal Unit
25.	r.m.s.	root mean square
26.	TIFF	Tagged Image File Format
27.	RZ	Recirculation zone
28.	UV	Ultraviolet

Chapter 1

Introduction and Motivation

The continuing requirement of compact and efficient heat transfer or power generation systems stipulate search of fluids (fuel or heat transfer medium) with high thermal conductivity and enhanced heat capacity. Choi [1] formulated conventional heat transfer fluids loaded with dispersed metallic nanoparticles (NPs). Metals exhibit higher thermal conductivity than conventional fluids thereby augmenting the thermal performance. Similarly, dispersing micron-sized solids was opted as a measure for combustion enhancement of liquid fuels. However, problems such as clogging, agglomeration, differential settling of dispersed particles have stymied the applications of such fuels at large scale. In the past couple of decades, research focusing on nanofluids has drawn great attention. Nanoparticles with physical dimension ranging from 1 to 100 nm offer high surface area to volume ratio enabling better dispersion in base liquid, without clogging or agglomeration. Lee et al. [2] reported linear increment in thermal conductivities with volume concentration of NPs in dilute Water-Al_2O_3 nanofluids. NPs manifest different optical, chemical, magnetic properties as compared to their respective bulk mediums resulting in custom engineered dispersions. Research studies of NPs have stridden all the way from DNA probing [3], biomedical applications [4], [5] to fuel atomization and combustion applications.

Addition of solid particles to liquid fuels is central to the idea of increasing the energy density of conventional fuels. Normally boron, aluminium, and carbon particles in the size range of ~ (5-200μm) are added to conventional fuels as "liquid-fuel extender" [6]. However, concerns regarding the long-term stability of such fuels inhibit their applicability in practical systems. Recent advances in nanotechnology have circumvented this problem by opening up avenues to synthesize energetic nanoparticles (NPs) with desirable traits, thereby intensifying their usage in application domains like automotive, pharmaceutical and microelectronics. Compared to their bulk form, increased surface area to volume ratio of NPs leads to enhanced catalytic properties, high reactivity, and significantly different thermo-physical properties. Nanofluids with base fluid as conventional fuels are designated as nanofuels. The studies of these

nanofuels where NPs of energetic metals like aluminium, iron, boron as well as metal oxides such as aluminium oxide, cerium oxide, are employed have shown significantly different combustion characteristics. Nanofuels are prepared by uniformly suspending NPs of metals or metallic oxide particles in a liquid base. Extensive research studies pertaining to nanofuel combustion have unveiled a plethora of intriguing features. In the seminal work, Tyagi et. al. [7] reported higher ignition probability of diesel blended with aluminium and aluminium oxide as compared to pure diesel in a hot-plate experiment. Sabourin et. al. [8] explored the effect of nanostructured particles of inert oxides of aluminium and silicon on combustion of liquid nitromethane, a monopropellant, under high pressure. The addition of inert particles increased burning rate coefficient (up to 50%) by increasing the absorptivity of the propellant. In a shock tube experiment employed for the study of n-dodecane blended with aluminium NPs, Jackson et al. [9] reported reduced ignition delay for temperature above 1157 K. Reduction in ignition delays of ethanol and JP-8 with addition of aluminium NPs by 32% and 50% respectively was reported by Allen et al. [10]. Rotavera et al. [11] found reduced soot formation in toluene combustion in the presence of nano-ceria (CeO_2). Lenin et al. [12] have reported decreased level of pollutants in diesel engine exhaust using nano-additives of manganese oxide (MnO) and copper oxide (CuO). Shaafi et al. [13] have provided a comprehensive review on performance and exhaust of CI engine fuelled with nano-additive enhanced biodiesel. Sajith et al. [14] have reported an appreciable improvement in brake thermal efficiency of a single cylinder CI engine fuelled with biodiesel laden with Ceria NPs. Mehta et al. [15] have shown reduced CO (25-40 vol %) and hydrocarbon emission with aluminium and iron NP in a CI engine. NPs like cerium oxide (CeO_2) work as oxygen carriers, thereby aiding in oxidation of soot particles and reduction in NOx emissions [16]. Additionally, these particles serve as heterogenous nucleation sites for vaporization thereby increasing the effective area of propellant.

1.1 Nanofuel droplet combustion

Active research on nanoparticle laden fuel droplet combustion is turning out to be a novel encrypt of modern interdisciplinary technology evolution where combustion represents one part of the problem while NP-design and synthesis being the other.

Usages of nanofuels in such combustors require analyses related to altered droplet atomization and burning so that newer designs can be evolved. Spray combustion is ubiquitous in most practical combustors across a multitude of application domains ranging from power generation to aero propulsion. Combustion of liquid-fuel droplets has been one of the building blocks of combustion research striding all the way from fundamental understanding of flame dynamics, atomization and vaporization to the design of next generation fuel injectors. Unravelling the mass and heat transfer mechanisms at the droplet sub-grid level controls global phenomena such as mixing, combustion instability and pollutant formation in any system [6], [17]–[19] . Hence, exploration of droplet combustion dynamics has been the cornerstone of fundamental combustion research.

Investigations pertaining to nanofuel droplet combustion can be carried out in; **(a)** Pendant mode, where droplet is suspended on a fibre or cross-wire arrangement. This mode of experiment offers the easiness of droplet shape and flame imaging. However, the suspended droplet sizes are limited to order of millimetres can be suspended with shape distortion due to the wire. Furthermore, previous studies [17] have established that the wire effects (heat transfer) can be neglected if the wire dimension is $< 100 \mu m$ **(b)** Free-falling/contactless mode; here the burning characteristics can be studied for smaller droplets in free-fall without wire effects although experimental imaging is arduous due to droplet motion as compared to the pendant mode.

1.1.1 Pendant mode nanofuel droplet combustion

Recent studies of combustion characteristics of nanofuel droplets in pendant mode have shown their dependence on material, structure, and size of suspended particles along with particle loading rates (PLRs). Gan and Qiao [18] experimentally established different stages of combustion for n-decane/nano-Al and n-decane/micron-Al droplets on Si-C (Silicon carbide) fibre. During their combustion lifetime, droplets seeded with nano-aluminium (<100 nm) exhibit five distinct stages: preheating, classical droplet combustion, micro-explosion, surfactant flame, and aluminium droplet flame. Contrarily, droplets laden with micro-aluminium (1–200μm), exhibit three stages; preheating, classical droplet combustion, and micro-explosion. Proceeding with the

similar particle loading rate and surfactant concentration, they report variation in micro-explosion occurrences; in micro-suspension micro-explosion is found to be delayed as compared to the nanosuspension, leading to catastrophic parent droplet fragmentation. Further, dependence on the base fluid variation is also shown; ethanol vs n-decane. Ethanol being more viscous forms skeletal network around the suspended particle ensuring better suspension stability. Owing to the large difference between the boiling points of ethanol and surfactant, the mother droplet undergoes continuous fragmentation generating satellite droplets. They also laid out a theoretical approach to understand the effect of particle size on collision mechanism and aggregation rate in such combusting droplets. In the following work, Gan et al. [6] also investigated the dependence of combustion behaviour on particle type and loading rates (dilute and dense). They investigated the effects of high-energy density NPs; boron and iron, on the combustion behaviour of n-decane and ethanol nanofuel droplets. For densely loaded droplets, NPs burn as a bigger aggregate near the completion of liquid combustion. On the other hand, for dilute loading continuous fragmentation of the primary droplet ensures simultaneous combustion of energetic NPs and fuel droplet.

Next, experimental investigation of Javed et al [20] pertaining to the autoignition of heptane droplets seeded with nano-aluminium, reported exponential reduction of ignition delay with ambient temperature. At temperature range (600–700°C) for dilute loading (<0.5w%) ignition delay is reduced, however at higher loadings 2.5w% and 5w% increase in the ignition delay is observed. They also report, continuous ejection events for NP laden droplets which become more intense with temperature increment. In a similar study, Javed et al. [21] reported the autoignition and combustion characteristics of nano-aluminium seeded kerosene droplets at dilute loading rates (0.1w%-1w%). As per the Arrhenius equation, both pure and nanofuel droplets of kerosene exhibit exponential decline of ignition delay with increase in the working temperature. Additionally, incessant nanofuel droplet fragmentation enhances the droplet burning rate, leaving no residue at the supporting fibre at the combustion completion.

Bello et al. [22] reported for the first time, the inclusion of magnesium oxide (MgO) NPs as a nanoadditive for rocket propellant, RP-2. Pure RP-2 droplets exhibit two

stages of combustion process; droplet heat-up followed by classical combustion regime. Whereas MgO NP (coated with surfactant, Oleic acid) laden droplets demonstrate three distinct stages; 1. droplet heat-up period, 2. liquid combustion, and 3. stabilizer combustion. MgO NPs enhances the gasification rate of liquid propellant RP-2 by nearly two orders for 0.5w% loading. They further emphasized that an optimum concentration (0.5w%) of MgO NPs is necessary for the reported enhancement as for less particle loading Stage 3 is hindered, and formation of particle aggregate is dominant at loadings >0.5w%.

Next, Miglani et al. [23] provided the detailed analyses of the instabilities initiating inside a burning bi-component (Ethanol-water) droplets with and without nanoparticles in a pendant mode. They isolated the sputtering effects arising with localised fragmentation of the mother droplet due to continuous bubble ejection events with characteristic timescale and velocity of O(2ms) and 5 m/s, respectively. In order to quantify the extent of ejections events, they introduced an *ejection impact parameter;* defined as the ratio of the bubble volume pre-ejection and instantaneous droplet volume [23]–[26]. Depending upon this parameter, they isolated several modes of droplet secondary atomisation. Furthermore, they reported a transient evaporative instability at the droplet-bubble interface, Darrieus–Landau (DL) instability, which is famously reported for laminar flames. They described two-part growth of a pre-ejection bubble. The first part growth is characterised by rapid bubble growth (evaporation front speed ~8–9 mm/s), whereas the second part marks the decay of this growth rate. During the first part growth, the instability waves on the bubble surface is found to be instantaneously transferred to the droplet surface suggesting their coupled oscillator behaviour with dominant frequency of around 30 Hz.

In the seminal work, Miglani et al. [24] reported a novel concept of suppressing the internal ebullition instabilities (droplet volumetric shape oscillations/atomization) using preferential acoustic excitation. Ethanol-water based pure and nanofluid fuel droplets exhibit non-periodic swell-contract deformation cycle with varying ejection impact parameters at multiple spatio-temporal length scales. It is shown that for the external stimuli of band-width between 80 Hz-120Hz, DL instability can be suppressed. They

further corroborated with reduced magnitude of ejection impact parameter. External perturbation also results in the homogeneous combustion residue with low porosity.

The first two chapters of the thesis will probe the intricacies of nanofuel droplet combustion for base fuels with large volatility differential. Using simultaneous droplet shadowgraphy and flame chemiluminescence imaging, the previously established qualitative droplet-flame causality [23]–[26] is attempted to be quantified.

1.1.2 Contactless mode nanofuel droplet combustion

The preceding literature pertaining to nanofuel droplet combustion in a pendant mode demonstrates the interdependence of combustion dynamics on the fuel-type, particle loading rate, and type of NPs added. However, the above studies report the existence of internal heterogeneous boiling on a relative term i.e. increases in the bubble count as compared to the pure droplet. Furthermore, the nucleation sites offered by the fibre support along with their role in particle aggregation is not considered above. Research studies [6], [18] have shown that for the size-range 0.5-2.5 mm of droplets, particle aggregation is a dominant factor which affects their combustion process. Hence, studies of smaller droplets without wire effects are necessary.

Huang et al. [27] theoretically investigated the burning behaviour of a liquid droplet exposed to an external convective flow (an arrangement which mimics the falling droplet). They have studied the effects of two specific parameters, free stream velocity and the droplet diameter. Flame structure is reported to vary between full envelope to wake flame with variation in the bulk velocity. For low-velocity regimes, the pure diffusion droplet flame is retained. While continuous increase in the flow velocity the envelope retreats to droplet downstream forming a wake flame.

Recently, Tanvir et al. [28] studied the combustion of nanofuel droplet stream (ethanol seeded with and without aluminium NPs). They report enhanced droplet gasification rates for dilute loading 1w%-5w%. NP laden droplets combust in two stages; initial pure liquid combustion followed by cumulative combustion of ethanol, and nano-aluminium. They also provide a theoretical prediction which includes radiation absorption by the suspended NPs from the flame. This mechanism mainly contributes to

the enhanced evaporation of larger droplets (400 μm). Whereas for smaller droplets (176 μm), they hypothesize that alter parameters with particle addition such as, higher flame temperature, enhanced surface area for evaporation due to particle wetting, increased thermal diffusivity of the liquid fuel, and reduction of surface tension and surface energy, all as a result of particle addition, may also contribute to droplet-burning rate enhancement. Next, Tanvir et al. [29] examined the radiation absorption by ethanol droplets seeded with nano-graphite NPs of two sizes, 50 nm and 100 nm. Similar to the previous study, nanofuel droplet gasification rate is found to be enhanced with maximum enhancement of 62% for 3 wt.% 50 nm graphite NPs. Further, with Monte Carlo simulation they established that penetration depth of photon decreases with increase in NP loading rates. Consequently, radiation absorption is maximum at the droplet surface leading to localised boiling and enhanced vaporisation rate.

While investigating the phenomenology of atomization in acoustically levitated (contactless) particle laden droplet under external radiative heating, Pathak et al. [30] demarcated several atomisation regimes. They emphasised that droplet secondary atomisation can be tuned by externally varying the laser power. A heat utilization parameter (α_h) is defined, given as the ratio of the cumulative heat utilised to evaporate the droplet and the incident laser power. For $\alpha_h \geq 0.2$ and Weber number (We) >1, droplets undergo capillary stripping and disintegration. At high laser power, the droplet is susceptible to secondary breakup due to surface tension (resistive force) reduction. For $\alpha_h < 0.2$ (for any We), droplets exhibit only primary atomisation due to Kelvin Helmholtz (KH) instability (from acoustic streaming) at the droplet equator.

Utilizing for the first time a novel aluminium based molecular additive ([AlBrNEt$_3$]$_4$), Guerieri et al. [31] investigated the variation of a single droplet burning rate in a drop-tower arrangement. Toluene-diethyl ether fuel droplets with [AlBrNEt$_3$]$_4$ additive (along with 39 mM of active aluminium additive ~ 0.16 wt. %) manifest increased burning rate constant by 20% in a room temperature. Internal phase change of the liquid fluid droplet is pointed as the primary mechanism for the rate augmentation. However, experiments with nano-aluminium without [AlBrNEt$_3$]$_4$ additive exhibit no discernible enhancement. This study marks a novel mechanism to enhance burning rate constant of conventional hydrocarbon fuels by imaprting more reactivity relative to nano-aluminium.

The next part, **Chapter 4** and **5** of the thesis is focused on understanding the nanofuel droplet behaviour in a contactless environment; using acoustic levitation as well as the free-fall mode.

1.2   Droplet flame transitions and instabilities

In parallel to the droplet internal dynamics, it is also necessary to understand the flame instabilities transpiring from the surround flow conditions and perturbations. As previously mentioned in the theoretical work of Huang et al. [27] , flame structure and transitions are interlinked with the droplet motion relative to its surrounding. In a similar work, Chen et al. [32] theoretically delineated the parameters associated with flame stabilisation and blow-off over a porous cylinder by varying the Damkohler number (Do) and fuel injection rate. The fuel is injected through the porous cylinder into an incoming air stream. They report three distinct flame structures; envelope, side and wake flame. For Do >13.64, envelope diffusion flame surrounds the cylinder. Gradual decrease in Do results in a side flame and eventually transfers to the wake which is partially premixed. Below a critical value, the flame blow-off occurs. Similar observations are also reported for the fuel injection rate variations. Below a critical value of fuel injection rate, the flame retreats to the droplet downstream stagnation point. The wake-flame stabilization is possible due to the presence of a recirculating flow at the droplet downstream.

In a similar study, Parag et al. [33] investigated the flame dynamics for ethanol and ethanol blends with water and diesel, in a porous sphere (8.0 mm to 13.6 mm) configuration subjected to external convective flow, V_∞ ~ (0.44 m/s to 1.12 m/s). Pure ethanol flame transition from envelope to wake flame (as mentioned in previous studies) is observed at a unique Froude number of 3.25 when the Damköhler number reaches a critical value of 504. Addition of water, diesel, and gasoline alter the burning characteristics such as rate of combustion, flame stand-off distance, and flame intensity, along with the critical velocity necessary to exhibit flame transition from envelope to wake structure. A theoretical formulation is presented for the burning rate with variation in Reynolds number, Damköhler number, and Froude number.

The drop-tower experiments presented in the later part of the work mainly focuses on the flame topology (width and height) and transitions with surrounding flow conditions.

Diffusion flames form the fundamental plinth for both fundamental research and commercial applications such as fire research, household cooking stove, to name a few. Naturally buoyant flames are famously known for their flicker and flare, which has fascinated myriads [34]–[37] of research investigation since several decades now. Natural flickering/puffing of the diffusion flames is an outcome of buoyancy induced instabilities. The associated frequencies fall in the range of 10-20 Hz [34]. Buckmaster et al. [38] theorized that these flame perturbations are the outcome of convective instability (modified KH instability) of the buoyancy driven flow of hotgases. Subsequently, Cetegen et al. [36] through experimental investigation asserted that the global flame flicker arises from the locally unstable region near the fuel exit. Chen et al. [34] through experimental visualization of laminar jet diffusion flames, indicated the presence of local vortices of different sizes; small vortices inside the flame luminous zone and large vortices outside the flame. The inner vortices are the outcome of the jet instability, whereas the large vortices are developed due to the buoyancy induced KH instability. They further asserted that merging /pairing of these vortices impart flame puffing and pinch-off.

Cetegen et al. [37] using Bernoulli equation derived the expression for flickering frequency as a function of Richardson number (*Ri*) and dimension of the fuel entry point. As stated by Xia et al. [39], one of major lacunae of studies germane to flickering diffusion flames lie in establishing the correlation between flame vortex-sheet dynamics and flickering frequency scaling. They theoretically revisited the problem by evaluating the initial vortex growth rate and further accumulation of circulation up to a critical value beyond which detachment of the toroidal vortex occurs.

The last section, **Chapter 6**, of the work reports the flickering of the droplet diffusion flame with and without external acoustic perturbations. It especially construes the effect of transient droplet diameter (due to regression) on the flame flickering frequencies.

1.3   Outline of the thesis

Dynamics of secondary atomisation and flame heat release fluctuations are studied for low vapour pressure (n-dodecane) nanofuel droplets in pendant mode using simultaneous high-speed shape and flame (chemiluminescence) imaging. The possible mechanisms responsible for internal boiling characteristics and its effect on volumetric oscillations and shape deformations of droplets, perikinetic aggregation of NPs and their definitive effect on average HR. is articulated in **Chapter 2**. **Chapter 3** encompasses the combustion characteristics of high-vapour pressure nanofuel droplets: ethanol-water (EW) droplets laden with ceria nanoparticles. This chapter focuses on three facets of EW droplet combustion; (i) burning time scale of droplets with and without NPs, (ii) pathways of secondary atomisation due to interface deformations and (iii) coupling of droplet shape deformations and flame heat release. In **Chapter 4**, detailed analyses of evaporation and atomisation characteristics of nanofuel droplets in a contactless environment (acoustic levitation) under external radiative heating is carried out. Two base fuels, ethanol and n-dodecane with significant difference in respective vapour-pressures are considered. Nanoparticles (NPs) of Cerium oxides (CeO_2) are utilised as nano-additives at dilute particle loading rate (PLR) of 0-0.5 % by weight. A time scale analysis considering orthokinetic NP aggregation, evaporation lifetime and bubble growth rate is presented to elucidate the mechanism of such internal boiling. In **Chapter 5,** combustion dynamics of free-falling droplets with and without nanoparticles is reported. A droplet under free fall undergoes acceleration resulting in progressive increase of its velocity (increase in Reynolds Number, Re) along the path. The consequent dynamic external relative flow induced along the drop trajectory allows self-tuning of the flame through a series of transitions. At low Re, the droplet initially transitions from a fully enveloped buoyant diffusion flame to a premixed wake flame structure. The flow conditions necessary for wake-flame stabilization is characterized. Further, it is shown that topological transitions are predominantly hydrodynamic in nature. The mechanism of acoustic-flame coupling for buoyant diffusion flame in droplets is established in **Chapter 6**. The flame under acoustic excitation exhibits differential varicose and sinuous modes including partial extinction and pinch offs at certain shedding heights. Further, it is also shown that a droplet exhibits multi frequency response with advent of new oscillations modes at different points of the burning

lifetime. The thesis is concluded in **Chapter 7** and a brief discussion on the future scope of the current work is also provided.

Chapter 2

Combustion dynamics of low vapour pressure nanofuel droplets

Our previous studies were mainly concentrated on ethanol-water droplets with added NPs [23]–[26]. In all the studies, the droplet was stabilized in a pendant mode. Low boiling point fuels (like ethanol) have been studied earlier by some groups. Ethanol (C_2H_5OH) has high vapour pressure at room temperature (5.95 kPa) resulting in rapid burning. Combustion characteristics of nano-additives such as nanoceria, alumina NPs and titania NPs at both dilute ($< 1\%$) and dense PLRs ($> 1\%$ up to 7.5%) have been studied. The works brought out some key physical insights. Preferential entrapment of high volatile species (ethanol) lead to boiling, as observed in these studies. Addition of NPs and variation of PLR initiated enhanced (~ 1 bubble/ms) internal ebullition activity in nanofuel droplets as compared to neat ethanol-water blend. Bubble-droplet system acted as a self-excited coupled oscillator [23]. Severe volumetric shape oscillations were produced due to bubble incipience and growth. Rupture and expulsion of these bubbles lead to high intensity ejection events, which distort the flame envelope. Various modes of atomization were quantified using local *ejection parameter* α_{local}. The results of these studies also suggest that that the droplets towards the later stages of burning form a gelatinous cocoon with trapped bubbles. In these studies, the nature of dynamic of coupling among bubbles, droplet shape oscillations and ejection events have been established. All of these events eventually lead to flame shape oscillations and possible fluctuations in heat release. However, the connection between aforementioned dynamics was not quantified in a holistic manner. For example, the flame analysis in these works was restricted. Although flame parameters like area and stand-off distance, were studied for global analysis, fluctuations in heat release were never quantified. In addition, the key linkages among the droplet shape oscillations, ejections and heat release signature were never rigorously established. For the present work, the focus is on n-dodecane, a long chain hydrocarbon fuel of practical applicability with typically

low vapour pressure ($\sim$17.65 Pa at room temperature). Jet fuels are multi-component blend of long chain aliphatic and aromatic hydrocarbons with additives that makes the analysis of their combustion characteristics and kinetics arduous. To overcome such difficulties, surrogates with less complex chemistry and structure are identified. For jet fuels, n-dodecane is one of the widely accepted surrogates [40] and is shown to be useful for shock-tube experiments and ignition delay analysis [41], [42]. Therefore, in the present paper, n-dodecane being principle surrogate of Jet A is chosen as the base-fuel. Alumina is a passive component which does not participate in reactions. For this reason, to understand atomization and heat release changes due to NP addition without affecting chemical kinetics, Alumina NPs are utilised. Alumina NPs are added to the base fuel at dilute PLRs $(0.1 - 1\%)$. The main idea of this work is to understand combustion characteristics of *low vapour pressure* fuel containing NPs. For this experimental study, simultaneous high-speed imaging of droplet shape and flame heat release (HR) has been conducted for the better understanding of the interlinked processes. The current chapter encompasses the **(i)** global oscillatory behaviour of droplet shape, **(ii)** internal ebullition mechanism which induces secondary droplet atomization through two ejection modes and Rayleigh-Plateau ligament break-up, **(iii)** spatial HR fluctuations, and **(iv)** combustion residue analysis (for nanofuels). Here the possible mechanisms responsible for internal boiling characteristics and its effect on volumetric oscillations and shape deformations of droplets, perikinetic aggregation of NPs and their definitive effect on average HR, are articulated. Physical mechanisms related to the aforementioned phenomena are put together under one umbrella for holistic analysis of low vapour pressure nanofuel droplet combustion.

2.1 Experimental Procedure

2.1.1 Nanofuel preparation

The nanofuels are prepared with n-dodecane as the base fluid and aluminium oxide (Alumina, Al_2O_3) NPs as the additive for the present experimental study. Their respective physical properties are compiled in Table 1. Alumina NPs (procured from Reinste Nano Ventures) usually have spherical shape with average size of 40 nm. Transmission Electron Microscopy (TEM) micrographs (**Figure 2.1**) of Alumina NPs (FEI Tecnai F30) confirms the spherical and smooth morphology.

	Molecular Weight (g/mol)	Density (kg/m^3)	Vapour Pressure (Pa)	Surface Tension (N/m)
n-dodecane [43]	170.33	749.5	17.65 (at 25^{0}C)	0.025 (at 25^{0}C)
Alumina (Al$_2$O$_3$) [44]	101.96	3970	0	_

Table 2.1 Physical Properties of n-dodecane and Alumina
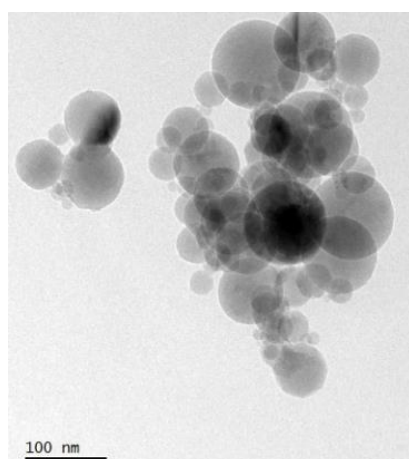
Figure 2.1. TEM image of Alumina NPs

Stability of the nanofuel is ensured by adding a non-ionic surfactant (Tween 85; Polyoxyethylene sorbitan trioleate) with HLB value of 11. Five different functional droplet cases are considered i) Pure dodecane ii) Dodecane with 0.1w% (0.019 vol. %) Alumina iii) Dodecane with 0.25w% (0.045 vol. %) Alumina iv) Dodecane with 0.5w% (0.096 vol. %) Alumina v) Dodecane with 1w% (0.191 vol. %) Alumina. These suspensions (base fluid and nanoparticles) were sonicated for nearly 30 minutes using ultrasonic disruptor (Trans o sonic D120/P model) with 15 seconds alternate ON/OFF cycles (inherent settings of the sonicator). Obtained suspensions were sufficiently stable for long periods of time. Sonication induces series of compression and rarefaction waves through the suspension. During rarefaction cycle microbubbles (cavitation) are formed, which collapse violently in compression cycle producing localised high temperature and pressure. In nanofluids, collapsing of microbubbles near solid

boundary enhances mass transport due to turbulent mixing and acoustic streaming [45] resulting in homogeneous stable suspension.

2.1.2 Experimental set-up
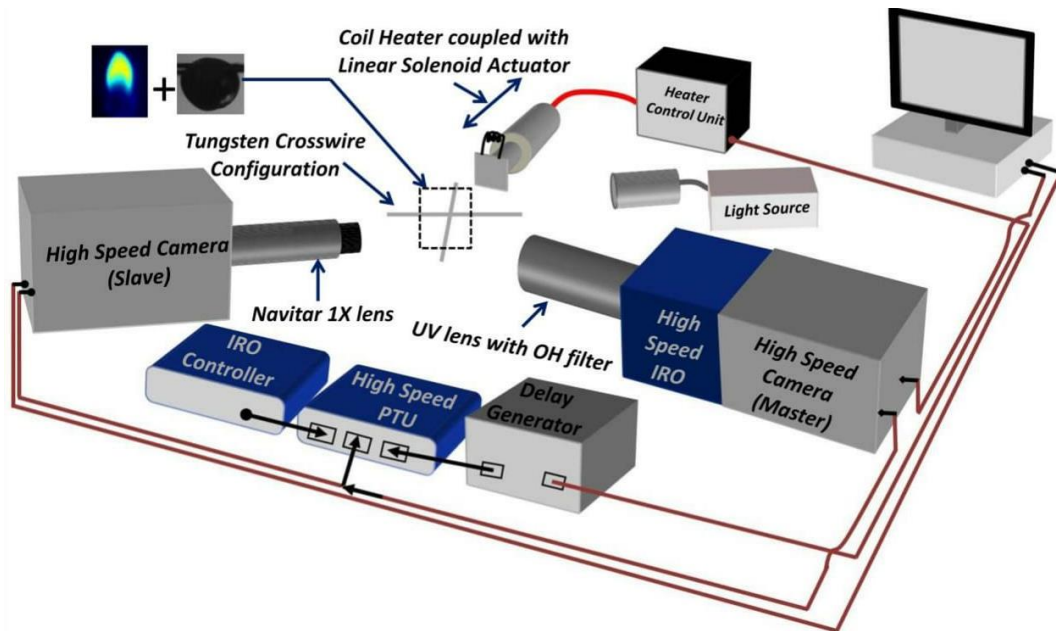
Figure 2.2 Schematic of the experimental set-up comprising of high-speed camera and chemiluminescence imaging systems for simultaneous capture of droplet shape and flame. Both imaging systems are synced with droplet ignition apparatus. Inset figure shows tungsten cross-wire arrangement for suspending functional droplets.

Figure 2.2 shows the schematics of the experimental set-up. Droplets (~750-850μm) are suspended at the junction of a 100μm diameter tungsten crosswire arrangement in a pendant configuration. Heat loss effects are usually neglected for wires of diameter less than 100μm [17]. It is to be noted that the suspender's conductivity effect (if any) is present across all the experimental cases (pure and NP laden droplets). In addition, conductivity of the suspender may actually be beneficial since it might aid in prevention of hotspots along the wire surface thereby curtailing formation of bubbles due to wire only. Therefore, on a relative basis, the physical arguments, combustion behaviour, nucleation and bubble mechanisms along with key conclusions should remain largely unaltered. A coil heater coupled with a linear solenoid actuator (synced with imaging system through a delay generator) is incorporated to achieve fuel ignition under atmospheric pressure. Coil heater is triggered using an electronic TTL signal (of 200 ms

period). The heater heats up the droplet during this period thereby igniting it. Subsequent to ignition, the heater is retracted away from the initial position.

2.1.3 High speed Imaging

(a) Simultaneous imaging of droplet shape and heat release

Simultaneous imaging of droplet shape and flame heat release (HR) is accomplished. Two high speed cameras (Photron SA5) are synchronised and placed orthogonal to each other for this purpose (**Figure 2.2**). A LED light source (Schott LLS) is used for backlighting the pendant droplets. One high speed camera is coupled to a 1X Navitar lens to acquire shadowgraphs of droplet shape variations, breakup and regression at 5000 fps with a pixel resolution of 1024 X 1024 (temporal resolution and spatial resolution of 0.2ms and ~6.67µm/pixel respectively).The other high speed camera is coupled to *high speed intensified relay optics (HS-IRO) (LaVision; IV Generation)* with UV lens (Nikon Rayfact PF10445MF-UV lens) and OH* bandpass filter (308 ± 10 nm) for the visualisation of flame shape and HR fluctuations throughout the droplet lifecycle. High speed OH* chemiluminescence images are acquired at 5000 fps with pixel resolution of 1024 X 1024 (temporal resolution and spatial resolution of 0.2ms and ~0.089 mm/pixel respectively).

(b) High speed imaging of the droplet interior

A different set of experiments are performed for capturing bubble incipience, growth, merging and ejection events inside the burning droplet. The same high-speed camera is mounted with a 5 X Navitar microscopic lens resulting in a pixel resolution of 1024 X 1024 (temporal resolution and spatial resolution of .2ms and ~ 2 µm/pixel respectively). The images are acquired at 5000 fps. Volumetric illumination of droplets using LED light source (Schott LLS) is accomplished for better visualisation of bubbles.

(c) Image processing and data analysis

Acquired droplet images are converted from gray scale to binary using Otsu thresholding technique [46] for calculating instantaneous projected area of the droplet. Equating the projected area to equivalent circle, instantaneous diameters are calculated

throughout the droplet lifetime within an error of $\pm$ 3.5 % over three experimental runs for each class of nanofuels.

Similar image processing is performed for flame analysis based on cut-off intensity (I). Pixels (i, j) with local intensity counts ($I_{i,j}$) $\geq I$ are assigned a binary value of 1 and those with intensity $< I$ are taken as 0. This binary region is used to calculate the instantaneous flame area (A_f) and spatial HR (explained in **section 2.7**).

Ejection events ($n_{ejection}$) are instantaneous ligament counts protruding from the droplet surface. Photron Fastcam Viewer (PFV) Ver.361 software is used to measure these ligament counts at a temporal resolution of 0.2 ms. Diameter of bubbles (d_b) inside the droplet is calculated using similar thresholding technique (as with droplet diameter). In addition, assuming that the droplet surface behaves as a convex spherical interface, magnification factor for pure dodecane turns out to be 1.42 based on refractive index calculation. For pure dodecane droplets, no change in refractive index (1.4192 for pure dodecane) occurs throughout the burning process (as initial and final compositions are ~100% dodecane). This magnification factor has been incorporated in calculating the bubble sizes.

Addition of Alumina NPs does not appreciably change (~ 1%) the refractive index of the resultant suspension [47] mainly due to the low PLR. Therefore, aforementioned magnification factor of dodecane has been utilised for bubble diameter calculations across all experimental runs. Reported statistics of $n_{ejection}$ and d_b are averaged over three experimental runs.

2.2 Global Observations
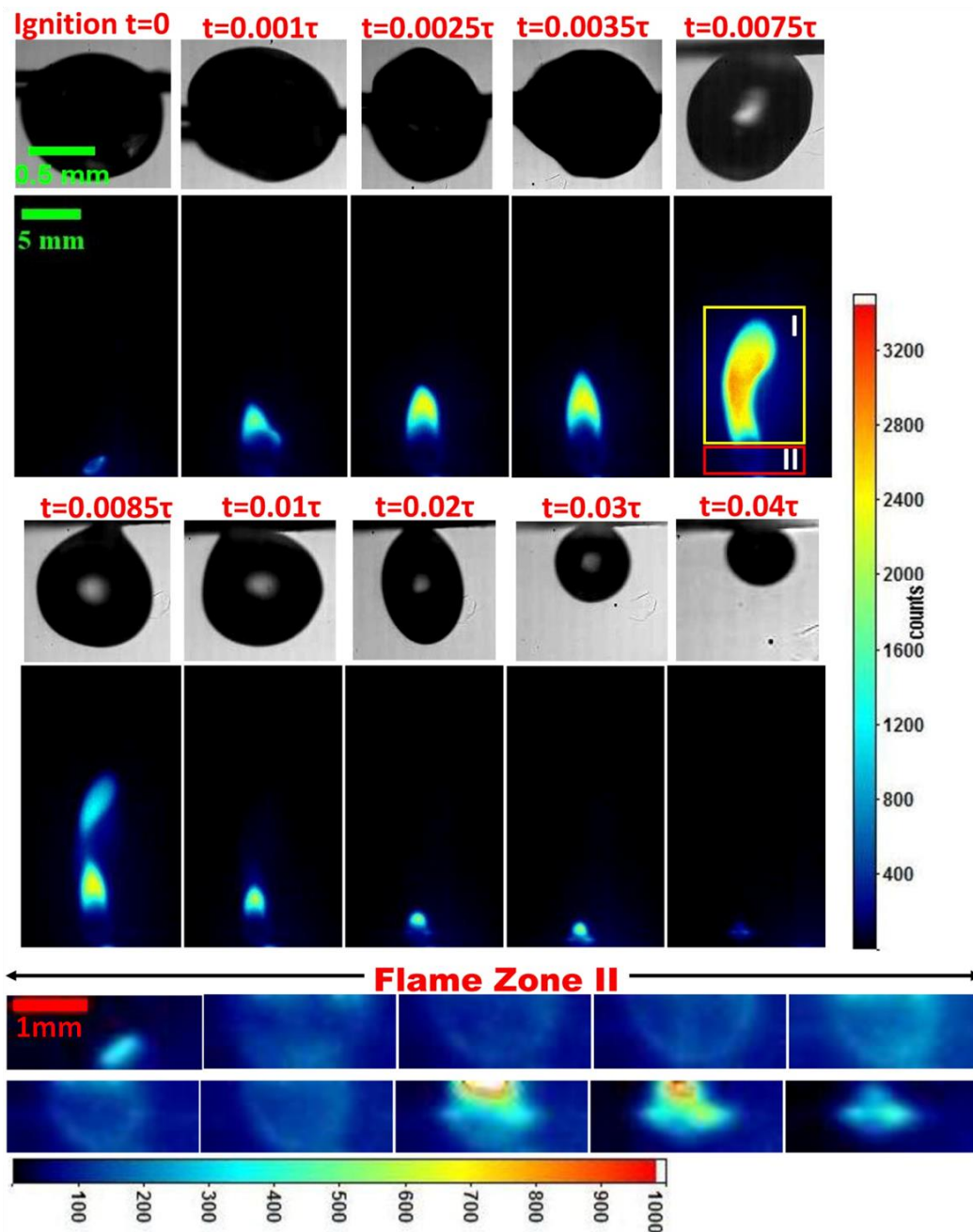
Figure 2.3. Simultaneous high speed imaging of surface oscillations and flame heat release for pure dodecane droplets at various time instants, where $\tau = (d_0^2/\alpha)$ is thermal diffusive time-scale, d_0 is initial droplet diameter and $\alpha = (\rho_l/C_{pl}k)$ is dodecane thermal diffusivity, ρ_l is density, C_{pl} is specific heat capacity and k is thermal conductivity of dodecane (at $T_{wet-bulb}$). Two flame zones are distinctly marked i.e. Flame Zone I(sooty tail) and Flame Zone II(region near droplet). Scale bar for Flame Zone II represents 1mm.

Dodecane is a low-vapour pressure fuel (~17.65 Pa at room temperature). Consequently, pure dodecane droplet burns at a very slow rate exhibiting a long plume shaped diffusion flame (**Figure 2.3**). Pure fuel droplets also exhibit minimal shape oscillations (**Figure 2.3**). However, droplets loaded with alumina nanoparticles showcase severe volumetric oscillations and surface undulations (**Figure 2.4** and **Figure 2.5**). **Figure 2.4** and **Figure 2.5** depict the global picture of droplet shape transitions and flame dynamics for two different particle loadings (0.1w% and 1 wt %). The shape oscillations in nanofuel droplets are mainly attributed to surface tension variations due to heating and formation, growth and ejection of bubbles due to heterogeneous boiling. Both of these phenomena are explained in great details in subsequent sections. Agglomeration of alumina NPs forms a gelatinous skeletal structure entrapping fuel and bubbles towards the later parts of the droplet lifecycle. Gelation is evident with increase in PLR beyond 0.1%. Two flame zones (Flame Zone I and Flame Zone II) are marked for pure dodecane as well as for nanofuels. Flame zone I is distinguished with yellow luminosity because of soot radiations. Flame zone II is blue which is generally termed as primary reaction zone. Flame height shows a sharp temporal increase for pure dodecane. After a burning time $\sim 100\ ms$, flame height subsidises and shows nearly linear regression till the end. Similar observations can be made for spatial heat release i.e. initial sharp increase followed by linear decay. Flame characteristics of nanoparticle laden droplets exhibit different behaviours like flame height and width (~ 2 times to that of pure dodecane **Figure 2.23a** and **b**). The increased flame height leads to low frequency flickering (explained in **Section 2.7**) in nanofuel flames. In addition, dynamics like bubble formation and rupture leads to continuous liquid ejections throughout the droplet lifetime. Such ejection events act as carriers of daughter droplets from droplet surface to the flame front. These ejection events are also responsible for mulitmodal flame distortion and heat release fluctuations (Flame zone II in **Figure 2.4-2.5**). For explaining the droplet break-up dynamics, different ejection modes based on size of rupturing bubbles are advocated; (i) Mode 1 $(d_b \sim O(.1d_0 - .2d_0))$ and (ii) Mode 2 $(d_b \sim (0.6d_0 - 0.83d_0))$, where d_b is the bubble diameter. The modes are further quantified using local ejection parameter (α_{local}) and are described in detail in the following sections.
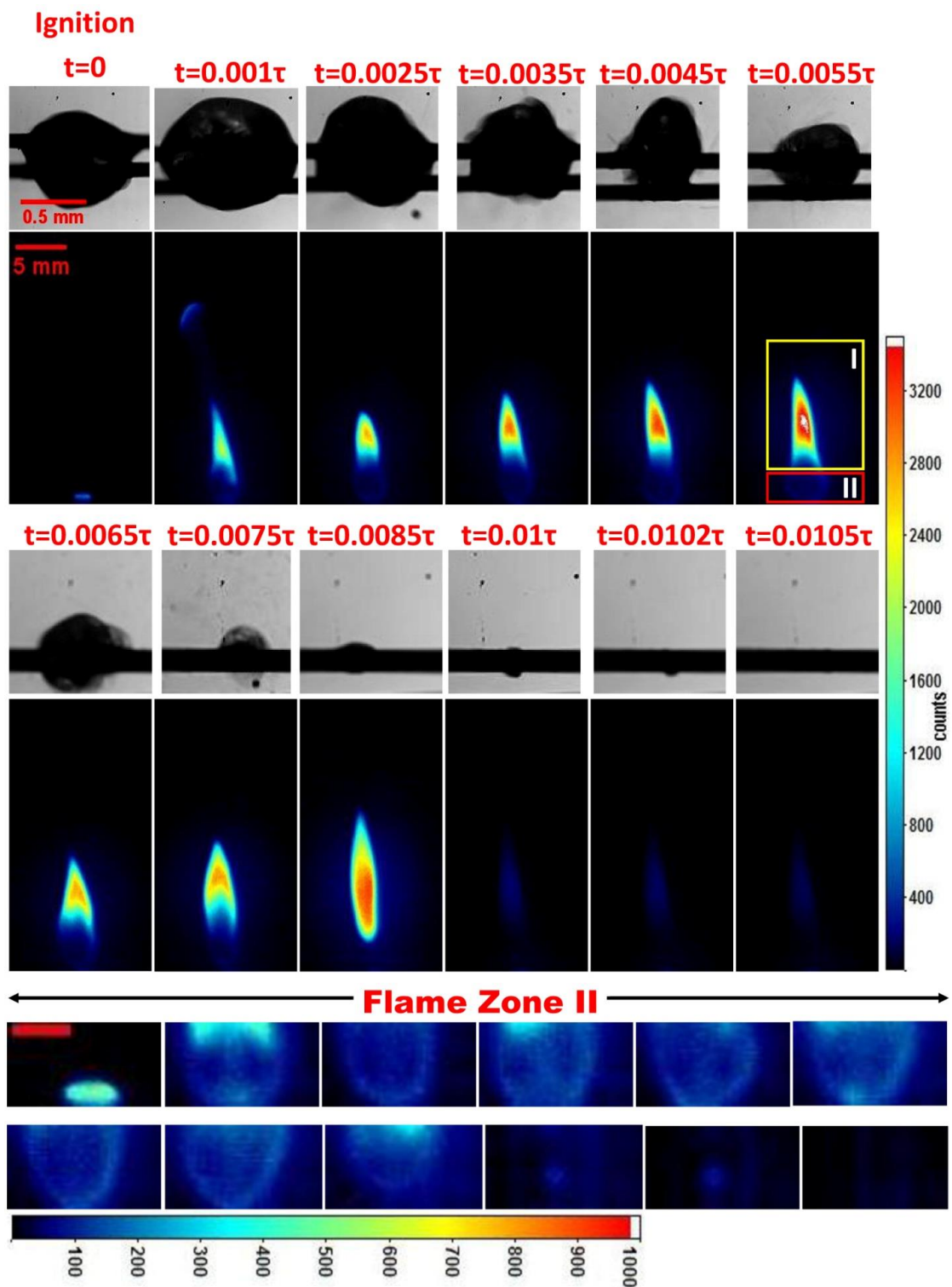
Figure 2.4. Simulatneous high speed imaging of shape oscillations and flame HR for PLR 0.1%. Flame Zone I and II are demarcated. Gelatinous mass is nearly non-existent here. Scale bar represents 2mm.
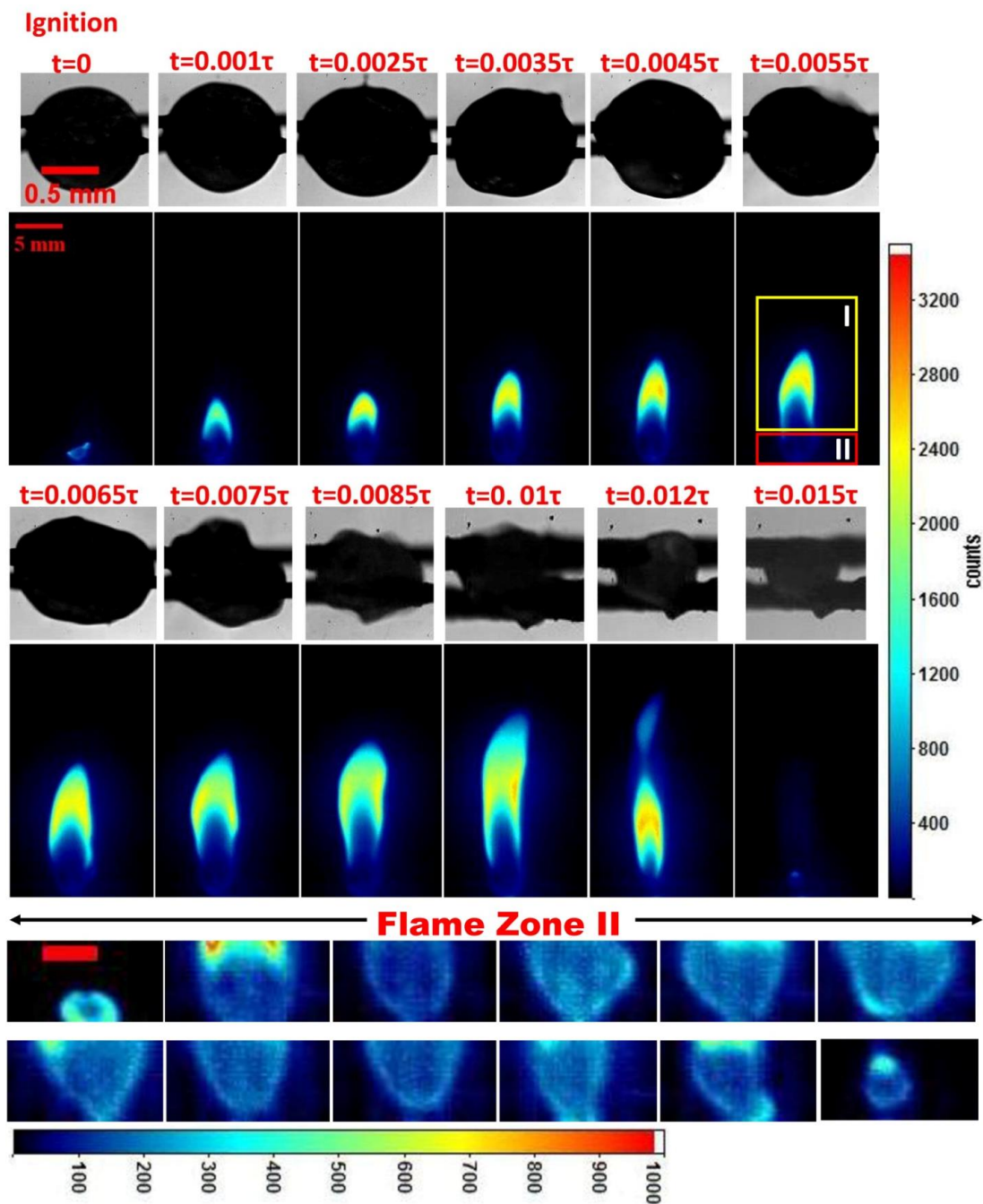
Figure 2.5. Simulatneous high speed imaging of shape oscillations and flame HR for PLR 1%. Flame Zone II shows intense and localised fluctuations of flame envelope due to ejection events. At the end stages gelatinous mass is evidently present. Scale bar represents 2mm.

2.3 Combustion characteristics of pure fuel droplet

Combustion of pure dodecane droplets can be categorized into two different stages. Stage I is characterized by the presence of surface undulations after ignition for a period $\sim 0.1 t_{total}$ (t_{total} is the total droplet lifetime) . This stage can be designated as droplet heat-up period; the time span (around 5 to 10 % of droplet lifetime) required for increasing the droplet temperature to the final wet bulb limit. Presence of surface undulations (**Fig. 2.6**) is attributed to the gradual change (~ 34 %) in surface tension of dodecane from 0.025 N/m (at room temperature, 298K) to 0.017 N/m (at wet bulb temperature of dodecane, 393K). Furthermore, Marangoni convection and small undetected bubbles can also lead to such surface undulations. This period is followed by Stage II of quiescent droplet combustion process (**Figure 2.6**). Interestingly, bubble count due to boiling in pure dodecane is found to be minimal throughout the droplet lifetime. Therefore, one can neglect the wire effect acting as heterogeneous nucleation source in our current experimental study. Absence of vapour bubble formation in pure dodecane can be rationalized considering two physical aspects (i) nucleation and (ii) superheating. Boiling can be initiated in pure dodecane either by homogeneous or heterogeneous nucleation. Homogeneous nucleation requires large amount of superheat as compared to heterogeneous boiling. Under the current scenario, it is impossible to supply such superheat for pure dodacene droplet (without any volatile component like ethanol). The suspension wire surface on the other hand usually contains crevices that assist in the formation of vapour bubble embryos leading to heterogeneous boiling. However, a limiting value of superheat ($\Delta T = T_{sup} - T_{boil}$) is required for the vapour bubbles to attain the critical bubble radius R_c given as [48]

$$R_c = \frac{2\sigma T_{sat}}{h_{fg}\rho_v \, \Delta T} \tag{2.1}$$

σ is surface tension, T_{sat} is saturation temperature, ρ_v is vapour-phase density, h_{fg} is latent heat of vaporisation at saturation temperature. Vapour bubbles with radius greater than critical value will grow while the rest will collapse. In the current experiment, the wire does not seem to promote heterogeneous boiling for pure dodecane. It is entirely possible that either the wire is not able to supply the superheat required for bubble nucleation or the vapour embryos formed on the wire do not attain the critical size as

mandated by equation 2.1. For examining droplet oscillations, fluctuations of instantaneous diameter from the mean value are considered. This mean value (d_{mean}) is obtained by fitting a polynomial through the time series data of diameter regression for each case. Fast Fourier transform (FFT) of $(d - d_{mean})^2$ shows a dominant frequency $\sim 4 Hz$ for pure dodecane (**Figure 2.7**). In the absence of unbalanced aerodynamic shear forces near droplet surface (combustion in quiescent and atmospheric conditions) and negligible bubble counts (thus negligible ejection flux), secondary atomization in pure dodecane droplets is not feasible.

2.4   Nanofuel droplet combustion
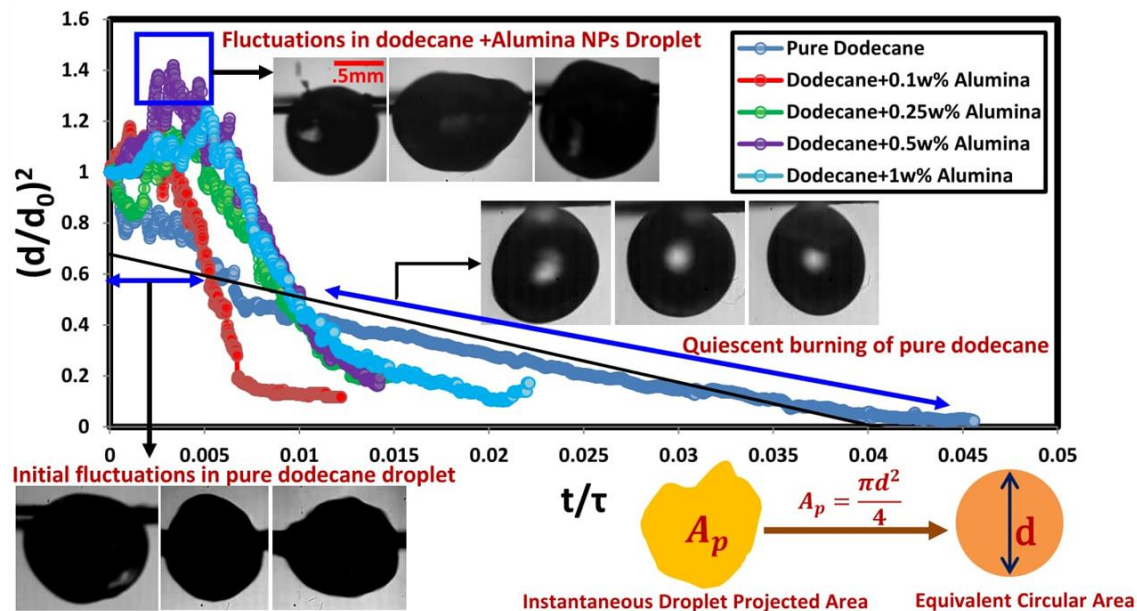
Figure 2.6. Temporal variation of normalised droplet diameter showing linear regression for pure dodecane and heightened fluctuations for nanofuel droplets. For PLRs > 0.1%, surface regression is nearly similar. Droplet lifetime is normalised by thermal diffusive time-scale τ. (**Video 2.1**)

For PLR 0.1 %, diameter regression time reduces drastically (lateral shift in **Figure 2.6**). Droplet life time is normalised by thermal diffusive time- scale $\tau = (d_0{}^2/\alpha)$, where d_0 is initial droplet diameter and $\alpha = (\rho_l/C_{pl}k_l)$ is dodecane thermal diffusivity, ρ_l is density, C_{pl} is specific heat capacity and k_l is thermal conductivity of dodecane (at $T_{wet-bulb}$). With increase in PLR (> 0.1 wt %), the temporal trend rather than following the same path corresponding to PLR 0.1 %, shows a slight increase in diameter reduction time (still much

lower than pure dodacene). In **Figure 2.4** it is evident that for PLR 0.1% gelatinous mass (explained in **Figure 2.19**) due to agglomeration of NPs is minimal near the droplet surface as compared to PLR=1w% (**Figure 2.5**). Formation of gelatinous mass inhibits rapid regression of droplet diameter even though the evaporation rate maybe significantly high. For high PLRs, diameter reduction is therefore not a true indicator of the evaporation rate.

Combustion of nanofuel droplets is accompanied with increase in bubble density (number of bubbles per unit droplet volume), bubble coalescence, bubble expansion and expulsion resulting in droplet swelling and severe volumetric oscillations (**Figure 2.6**). Ebullition phenomenon in nanofuel droplets is distinctly evident unlike pure fuel droplet. This incongruity in physical behaviour is because of different modes of boiling. In the absence of wire effects, homogeneous boiling mode which requires relatively large superheat is the only way for bubble incipience in pure fuel droplets. However, presence of agglomerated NPs opens up the heterogeneous boiling mode for nanofuel. The agglomerates act as nucleation sites at multiple length scales.

Increased bubble density for nanofuel droplets induces a cascading effect of increased ejection flux (number of ejections per unit surface area). Internal boiling triggers bubble formation of various sizes which are further ejected from droplet surface as continuous localised and major ejections. These ejections cause spatio-temporal fluctuations of droplet shapes (**Figure 2.3-2.6**). **Figure 2.7** illustrates augmentation in droplet oscillations for both lower frequency ($< 25Hz$) as well as higher frequency ($> 25Hz$) bands with increasing PLR. Maximum oscillations occur for PLR 1% which exhibits two principal frequency bands ($\sim 8Hz$ and $\sim 70Hz$). Time evolution of droplet oscillation frequencies is further investigated by continuous wavelet transform (CWT) of $(d - d_{mean})^2$ for all cases. To illustrate the correlation between wavelet and droplet shape, reference high speed images are provided in **Figure 2.8** and **Figure 2.9.** For the case of pure dodecane as explained earlier, two different combustion stages are evident i.e. initial heat-up period followed by quiscent droplet combustion. CWT spectrum of $(d - d_{mean})^2$ for pure dodecane(**Figure 2.8**) likewise shows the presence of oscillation frequencies during initial heat-up period ($\sim .1t_{total}$) with no other distinct frequencies for the rest of droplet lifetime. In nanoparticle laden droplets from ignition ($t = 0$) to flame extinction ($t = t_{total}$), two stages (will be described in detail later) can be

distinctly demarcated; Stage I time-period of dominant bubble dynamics, Stage II time-period when peri-kinetic aggregation leading to gelation of NPs into large structures. During Stage I formation of particle clusters initiates vapour bubble nucleation. These clusters collide and form bigger aggregates throughout the burning process. Stage II is identified as the time-period when restricted bubble dynamics and ejection events are observed due to the formation of gelatinous sheath. **Figure 2.8 (b)** and **Figure 2.9** represent CWT spectra of nanofuels with different PLRs. Droplet oscillating frequencies are present mostly during Stage I when deviation of droplet diameter from its mean value is prominent ($\sim 13\%$ to 16%). Normalised $(d/d_0)^2$ profiles show $\sim 18\%$ to 24% increase. These variations are the outcome of bubble dynamics (growth and transport) and modes of secondary atomization (Modes 1 and 2 explained in **section 2.6**) due to bubble rupture.
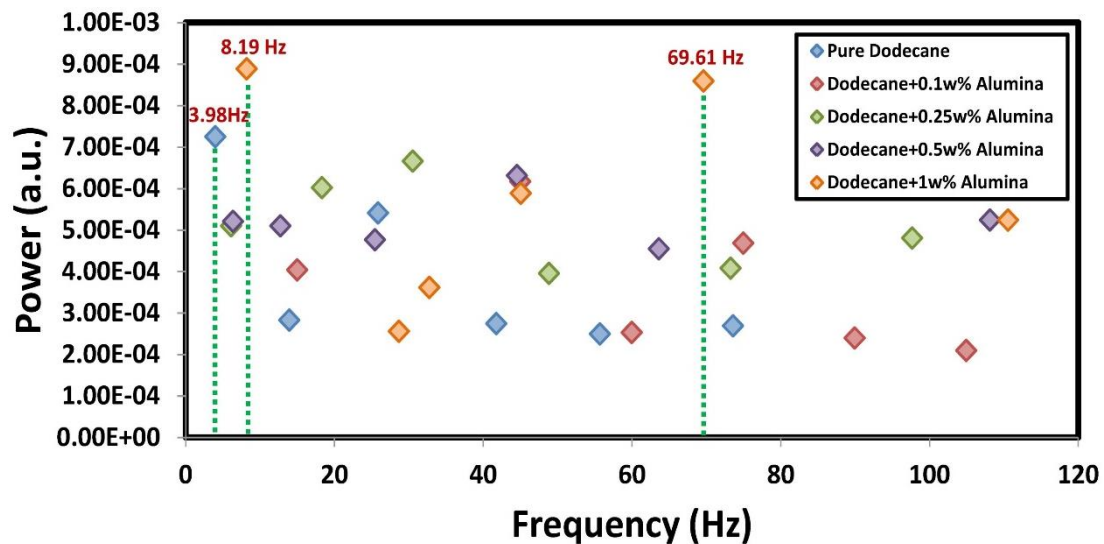
Figure 2.7. Dominant frequencies present in FFT spectra of $(d - d_{mean})^2$ for nanofuel droplets. PLR ranges from 0-1 wt %. Full FFT spectra not shown.
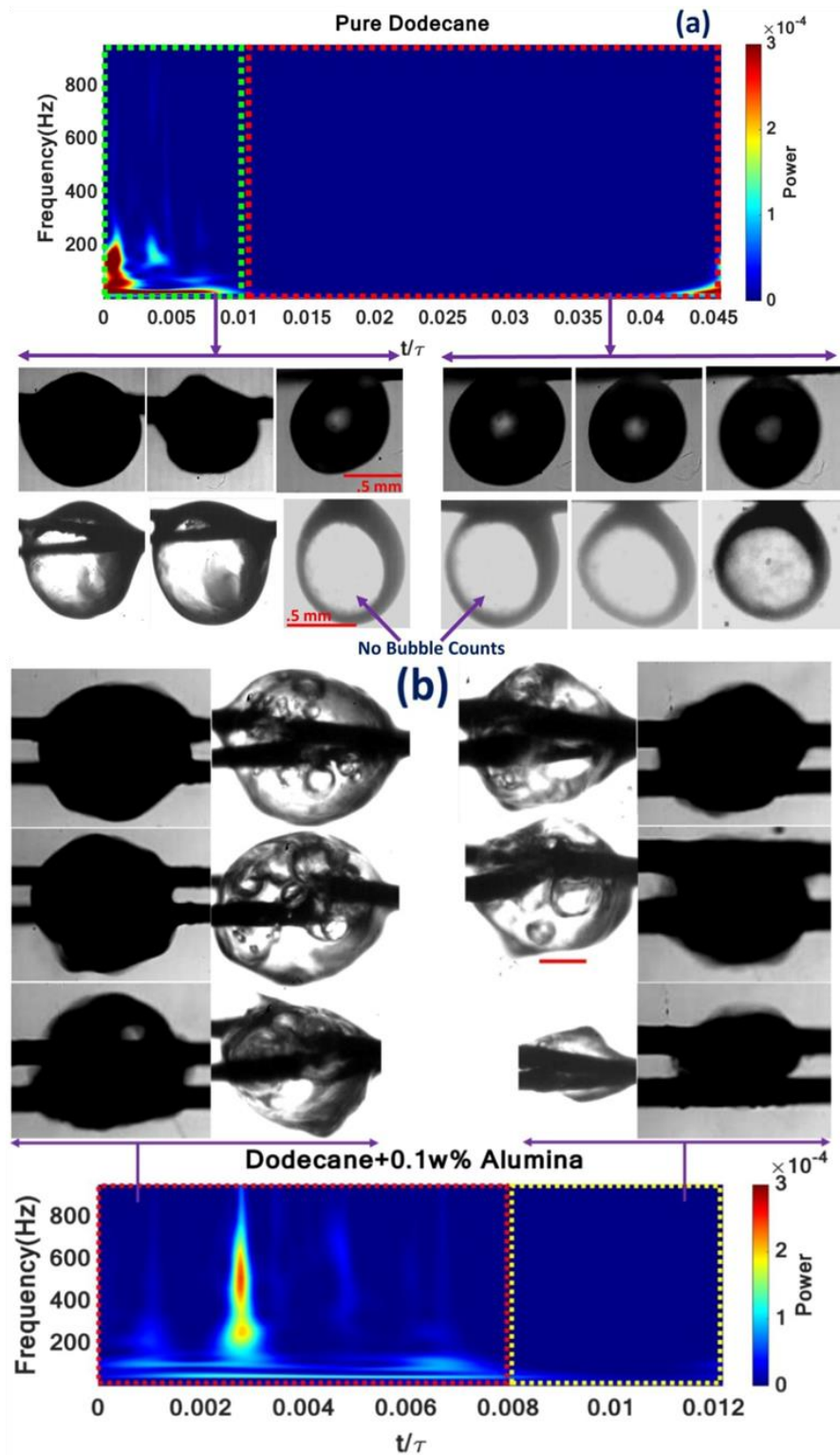
Figure 2.8. (a) Continuous Wavelet Spectra of $(d - d_{mean})^2$ for pure dodecane. Low frequency oscillations are visible during the initial heat-up period $\sim 0.1 t_{total}$. No distinguishable fluctuations are present for rest of the droplet lifetime due to negligible bubble count (b) CWT spectra for PLR 0.1w%. Frequency fluctuations are present mostly during $\sim 0.6 t_{total}$ when bubble dynamics and corresponding ejection events are dominant. Scale bar represents 0.2mm.
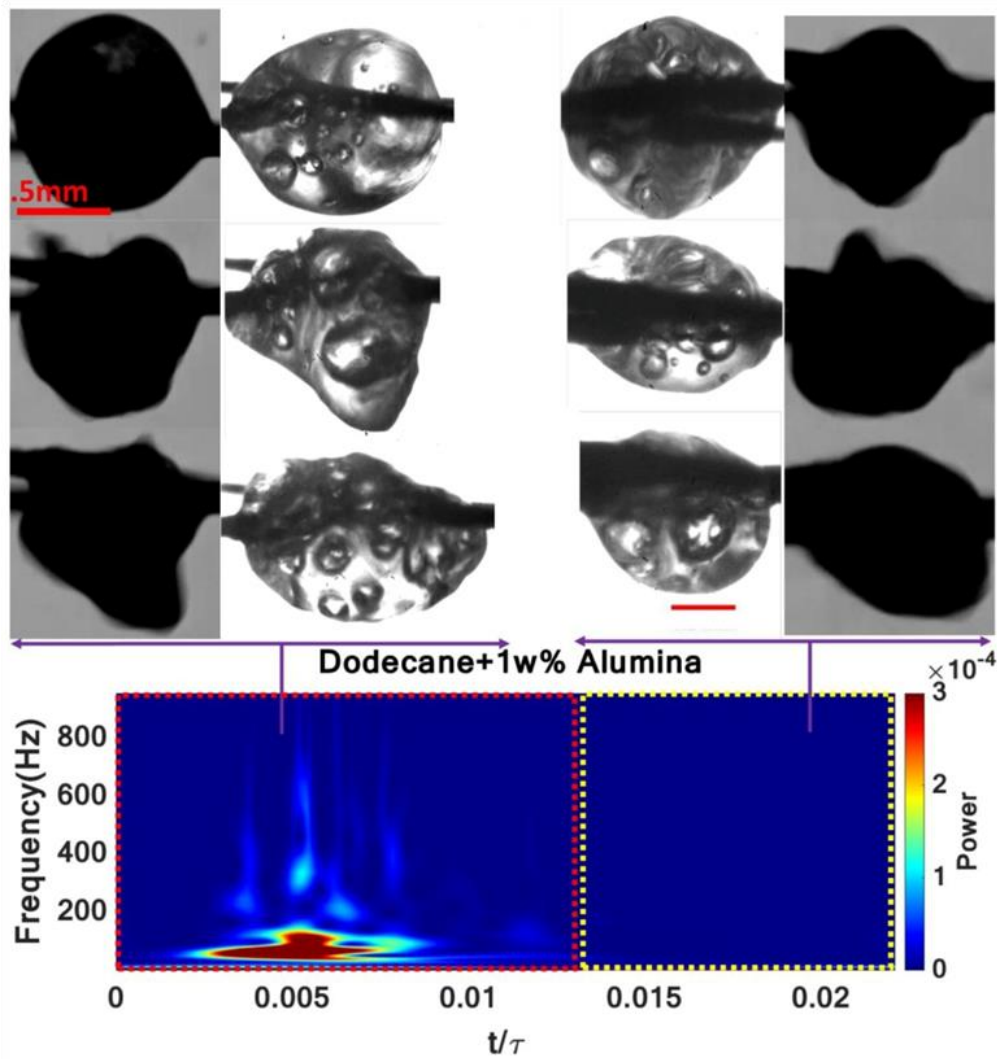
Figure 2.9. CWT spectra for PLR 1w%. It illustrates presence of shape oscillation frequencies for Stage I~0.6t$_{total}$ as a result of increased bubble population and ejection events. For rest of the period ~0.4t$_{total}$ minimal fluctuations are observed due to the formation of gelatinous mass. Scale bar represents 0.2mm.

Fluctuations in $(d - d_{mean})^2$ for pure and NP laden droplets only account for projected area variations. Thus, to elucidate changes in bulk movement of droplet, temporally varying instantaneous droplet centroid has been projected in **Figure 2.10.** Centroid motion of pure dodecane droplet is nearly stagnant close to the vertical axis (y*) for most of its lifetime. Centroid motion of nanofuel droplet shows extremely sporadic behaviour. With increase in particle loading, movement of droplet centroid is observed in both horizontal and vertical directions. For quantification of the extent of droplet centroid span, spread fraction (ϵ_s) is defined as follows

$$\epsilon_s = \frac{A_b}{\pi r_0{}^2} \qquad 0 < \epsilon_s < 1 \qquad (2.2)$$

where A_b is area of minimum bounding rectangle encompassing the droplet centroids and $\pi r_0{}^2$ is the initial droplet projected area. Concept of minimum bounding rectangle is generally applied to measure the maximum extent of two-dimensional objects. In our case, minimum bounding rectangle is used to measure the extent of centroid fluctuation throughout the droplet lifetime. As particle loading increases, values of ϵ_s also show increasing trend; from $\sim$.115 for pure dodecane to $\sim$.335 for PLR= $1w$%. For PLR> 0.1% , value of ϵ_s increases by nearly 3 times. This phenomenon is a result of bubble size variation along with random bubble motion and recoil actions due to major ejection events.
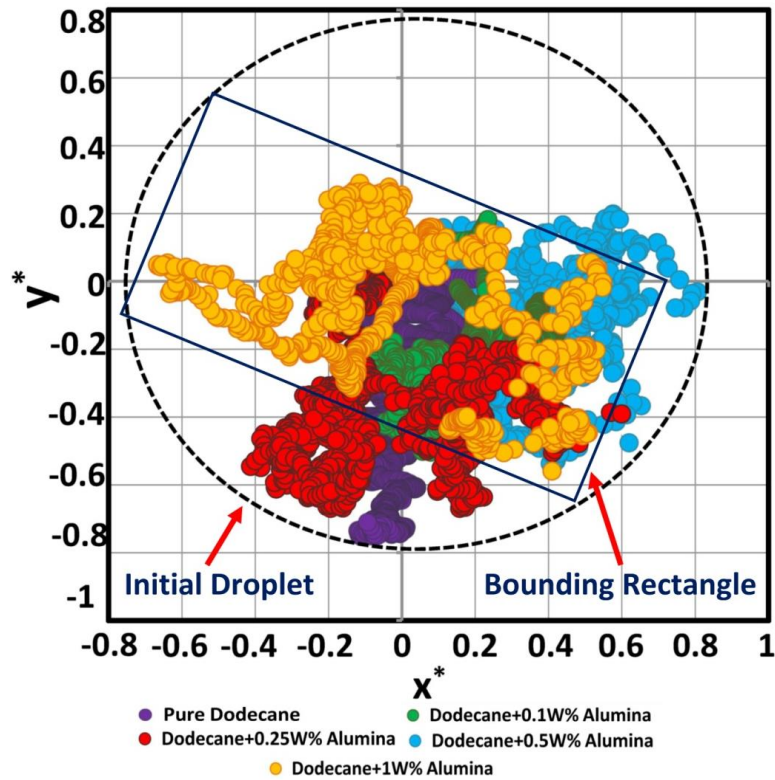
Figure 2.10. Spatial shift of instantaneous droplet centroid (x^*, y^*) for different PLRs, where (x^*, y^*) are normalised horizontal and vertical centroid displacement given as; $x^* = \frac{(x - x_0)}{r_0}$ and $y^* = \frac{(y - y_0)}{r_0}$. (x_0, y_0) is the initial position of droplet centroid. Bounding rectangle is represented here to depict the spread of droplet centroid throughout the lifetime.

2.5   Bubble dynamics in nanofuel droplets

Holistic dynamics of droplet such as projected area variation and volumetric oscillations are determined by vapour bubble inception, growth and expulsion. Thus, understanding elementary concepts of bubble incipience and growth is crucial for our experimental studies. Enhancement of bubble counts for droplets with PLRs $(0.1 - 1)w\%$ is found to be $\sim 1 - 2$ bubbles/ms relative to pure dodecane. Since these bubbles stem from heterogeneous nucleation, kinetics of aggregate formation and initial nanoparticle size in nanofuels is pivotal for understanding their dynamics. Three transport mechanisms which are responsible for aggregation are (i) Brownian diffusion leading to perikinetic aggregation, (ii) fluid motion resulting in orthokinetic aggregation and (iii) differential settling [49]. Currently, perikinetic aggregation is mainly considered due to the strong dominance of Brownian motion in nanosuspension as theoretically explained by Gan and Qiao [18]. In one of our previous studies [50] using an agglomeration model based on population balance, it is shown that single nanoparticles form multi-fold (multiple particles forming a single cluster) aggregates with progression in time. Large number of small aggregates tends to form initially but number density of large aggregates shows an increasing trend (higher order folds) towards the later part of droplet lifetime. As the base fuel depletes, alumina NPs collide and form aggregates via perikinetic collision. Time scale for particles to reduce to half of its initial concentration due to formation of higher order folds is given as [49]

$$\tau_{agg} = \frac{1}{k_a n_0} \tag{2.3}$$

where k_a is the rate constant of perikinetic collisions. For identical particle collision it takes the form $8k_b T_s / 3\mu$, where μ is the fluid viscosity, k_b is the Boltzmann constant, T_s is the droplet surface temperature (393K, wet-bulb limit of n-dodecane) and n_0 is initial volumetric concentration of particles. Time scale of aggregation (τ_{agg}) comes out to be $\sim O(10^{-3} - 10^{-4})\, s$ for PLRs $(0.1 - 1.0)\%$ which is much smaller than droplet lifetime $t_{total} \sim O(10^{-1})s$. Hence substantial agglomeration of alumina NPs will occur during nanofuel droplet combustion forming aggregate cluster network inside the droplet.
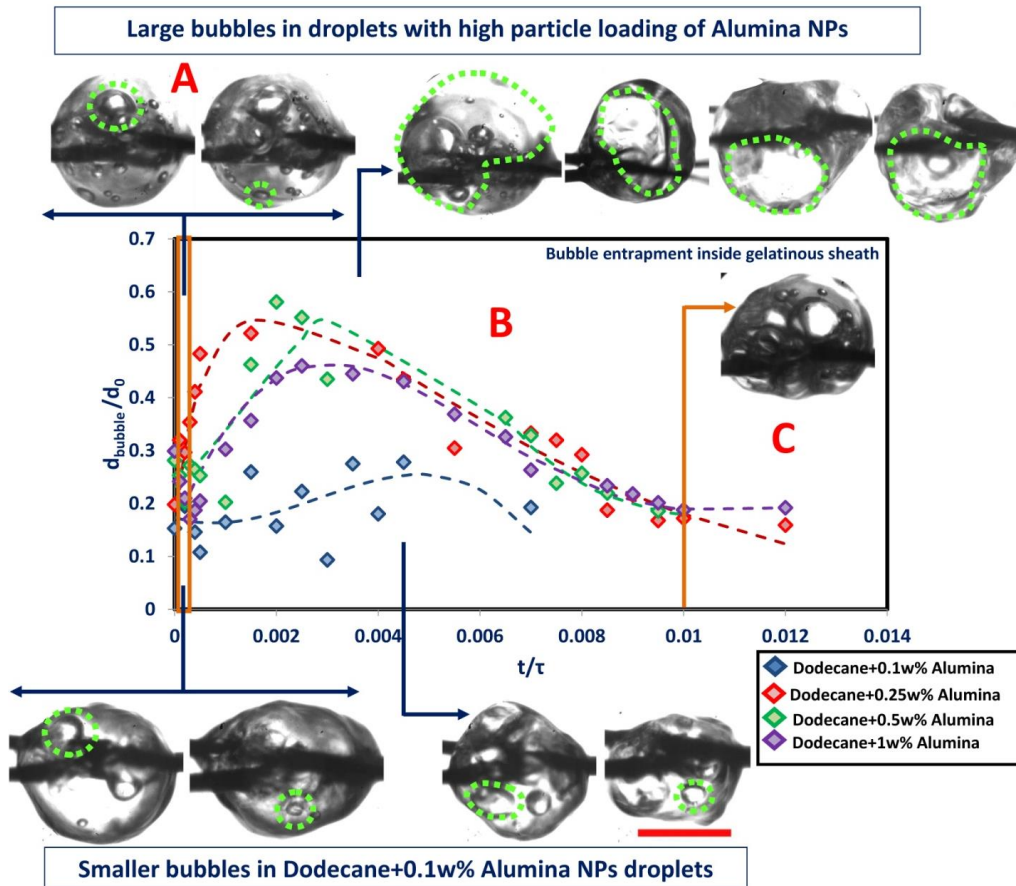
Figure 2.11. Temporal variation of instantaneous spatially averaged bubble diameter. Depending on scale variation and residence time, three main regimes are illustrated here A, B and C. Large bubbles are observed for PLRs > 0.1%. Scale bar represents 0.5mm. Refractive index change has been incorporated in bubble size calculation assuming single curvature interface.

Instantaneous spatially averaged diameter of bubbles (detectable through imaging) has been represented using Sauter Mean diameter (SMD) (d_b)

$$d_b = \frac{\sum_{i=1}^{N} d_i^{\,3}}{\sum_{i=1}^{N} d_i^{\,2}} \tag{2.4}$$

where N is instantaneous bubble population and d_i is diameter of ith bubble. Three main regimes of bubble scale variation based on d_b have been identified, (A) Rapid nucleation of vapour bubbles for $\sim 5ms$ where d_b varies $\sim(0.1d_0 - 0.4d_0)$ (B) Period of $O(\sim 90 - 100\ ms)$ where the bubbles grow in size $\sim(0.4d_0 - 0.83d_0)$ (C) Reduction in bubble size and entrapment of bubbles under gelatinous sheath (**Figure 2.11**). For Regime B, when the bubble becomes comparable to droplet size, it is understood that it

cannot be greater than the droplet diameter. Errors in bubble sizes pertaining to this regime cannot be greater than the error in calculation of the droplet diameter ($\pm$ 3.5%). A limiting PLR (0.1%) exists beyond which no appreciable change in average bubble diameter is observed. However large sporadic instantaneous deviations from the average bubble size ($\sim 21 - 71\%$) has been observed for all the PLRs at all time instants.

Solid body rotation of nanofuel droplet in the imaging plane is observed predominantly for PLRs> 0.1% during regime B of bubble size variation. Two observed phenomena namely (i) random motion of large bubbles inside the droplet and (ii) spatially non-uniform ejection events (and subsequent recoils), are macroscopically responsible for droplet centroid spreading (**Figure 2.10**).
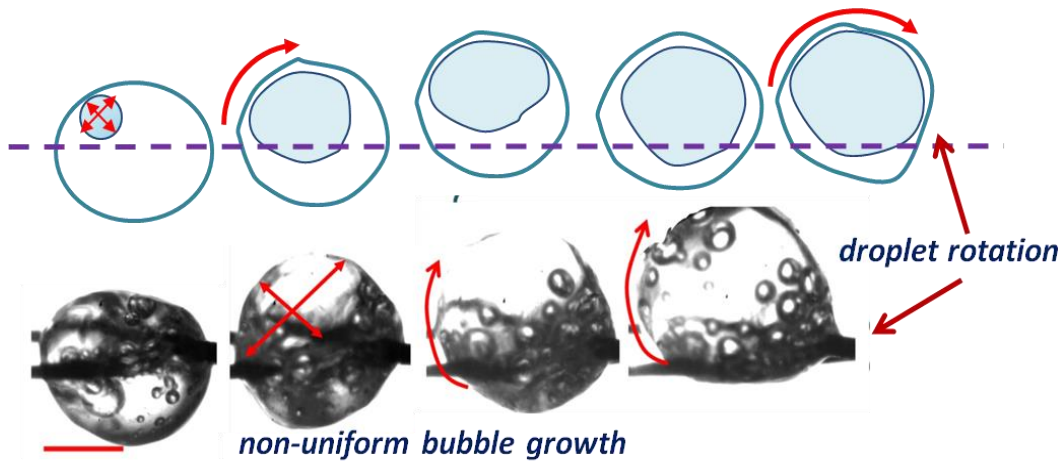
Figure 2.12. Schematic representation of random motion of nanofuel droplet due to bubble movement. High speed images show the non-uniform growth of bubble and droplet rotation. Scale bar represents 0.5mm.

During regime B, large bubble $\sim(0.4d_0 - 0.83d_0)$ and droplet act as a coupled system. These large bubbles show directional expansion and random motion. As these bubbles grow, the droplet also exhibits uneven expansion (solvent is virtually incompressible). Uneven expansion and random motion of bubble-droplet system lead to droplet centroid spreading (**Figure 2.10** and **Figure 2.12**). Subsequent to ejection (Mode 2, **Figure 2.16**) of large bubbles, droplet undergoes a recoil motion leading to vigorous and random trajectory of droplet centroid, an observation that is consistent with our previous droplet instability study [23] for ethanol based nanofuel. Thus, absence of large bubbles for

PLR <0.1% droplets diminishes the sporadic spreading of its centroid (as shown in **Figure 2.10**). Presence of suspension wire aids in observed solid body rotation of droplet. However, inside real combustors presence of highly turbulent swirl (rotational) flows can lead to such droplet motion.

2.6 Break-up dynamics of nanofuel droplets

Disintegration of parent droplet into daughter droplets is a secondary pathway of fuel transfer from droplet surface to flame front. Vapour bubbles inside nanofuel droplets cause local deformations as well as global perturbations which have been described previously. Vapour bubbles inside the droplet finally burst near the droplet surface after a series of sequential events like growth and merger. Phenomenon of vapour bubble bursting near free surface have been extensively investigated, numerically as well as experimentally [51]–[55]. In this section, the mechanism of vapour bubble collapse at free droplet surface using the model explained by Aybers et al. [51] is elucidated. When a bubble reaches the free surface of droplet either by buoyancy or by expansion, a liquid film (δ_{film}) forms between the vapour and free liquid (as shown in **Figure 2.13**). At this point, bubble segment protruding (assuming hemispherical) to the right side behave like a soap bubble film i.e. both sides subjected to interfacial tension. Force balance shows pressure difference ($P_i - P_0$) across such film is given by [56]
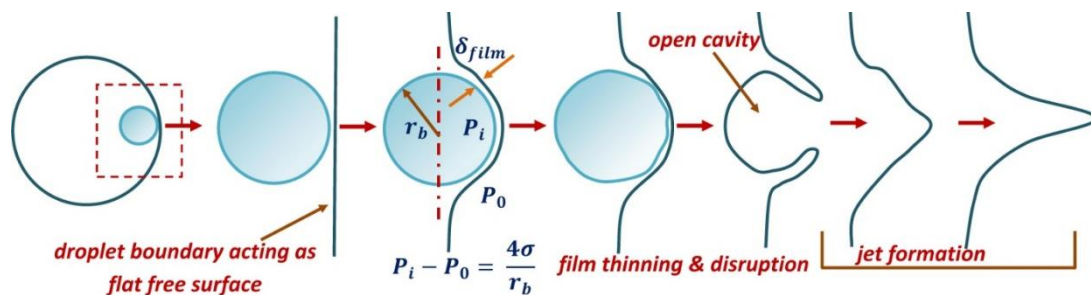
Figure 2.13. Schematic representation of vapour bubble collapse mechanism at a free surface (due to shear thinning of film) resulting in bubble expulsion, open-cavity formation and final liquid jet formation (Wärme - und Stoffübertragung, The mechanism of drop formation from gas or vapour bubbles, 1, 1968, 80, N.M. Aybers, A.K. Dagsöz, "With permission of Springer" [51])

$$\Delta p = 4\sigma/r_b \tag{2.5}$$

where P_i and P_0 are the pressures inside and outside of the bubble respectively, σ is the surface tension and r_b is the bubble radius. As only half of the bubble is subjected to free surface, half of the calculated force is balanced and rest of it is transferred to exterior of bubble. This results in squeezing and rapid-thinning of liquid film (δ_{film}) which disrupts the bubble boundary thus forming an open cavity [51]. The cavity formation triggers rapid movement of adjoining fluid to fill the void. Consequently, a liquid-jet is formed due to the momentum of in-flowing fluid. Unbalanced force F_{unb} resulting in bubble rupture is given by [51]

$$F_{unb} = (\pi r_b{}^2) * \frac{\Delta p}{2} = 2\sigma\pi r_b \qquad (2.6)$$

For bubble sizes between $\sim O(.1d_0 - .2d_0)$, instantaneous radius ratio (r/r_b) varies between $\sim(5.3 - 11.25)$. Hence, the free droplet surface can be assumed to act as a flat free surface with respect to these small bubbles. F_{unb} is found $\sim O(10^{-5})$ N for the aforementioned bubble sizes. F_{unb} is an impulsive force acting on the liquid film for a very short amount of time (t_{imp} taken as $3X10^{-5}$ seconds [52]). From high speed images, ejection velocity of liquid emerging after small bubble rupture is found $\sim(0.25 - 0.5)$ m/s. For validating this conjecture, the predefined jet velocity as given by Aybers et. al. is considered [51],

$$U_{jet} = \frac{F_{unb}}{2} * \frac{t_{imp}}{M} \qquad (2.7)$$

where M is the entraining mass of liquid to fill the open cavity given as $2\pi\rho_l r_b{}^3/3$. The calculated theoretical jet velocity comes out $\sim(0.17 - 0.682)$ m/s. Thus, experimental as well as theoretical results are of same order. This comparison establishes that collapse mechanism of small vapour bubbles. However, results pertaining to rupture of large bubbles deviate from values obtained from the above model. In Regime B droplet and bubble radius are comparable. Hence for large bubble, droplet surface cannot be considered to be a flat free surface. Break-up time scale (t_{break}) of ligaments (L_{lig}) generated from small vapour bubble collapse is theoretically estimated considering mean jet velocity($U_{jet}/2$), given as [51]

$$t_{break} = \frac{L_{lig}}{(U_{jet}/2)} \qquad (2.8)$$

Calculated values of t_{break} are found $\sim(0.2 - 0.8)ms$. This range nearly corroborates our experimental findings ($\sim(0.2 - 0.4)ms$) as shown in **Figure 2.15.**

To distinguish between different ejection modes, a local ejection parameter (α_{local}) [23] is determined which is given as the ratio of pre-ejection bubble and instantaneous droplet volume

$$\alpha_{local}(t) = d_b{}^3/d^3 \qquad (2.9)$$

d_b denotes pre-ejection bubble diameter and d is the instantaneous projected area diameter of the droplet. Detached daughter droplets of diameter $\sim(15 - 90)$ μm are ejected at velocity $\sim O(10^{-2} - 10^{-1})$ m/s. Based on collective observations of bubble dynamics and secondary atomization, nanofuel droplet lifetime is differentiated in two distinct stages (**Figure 2.14**).
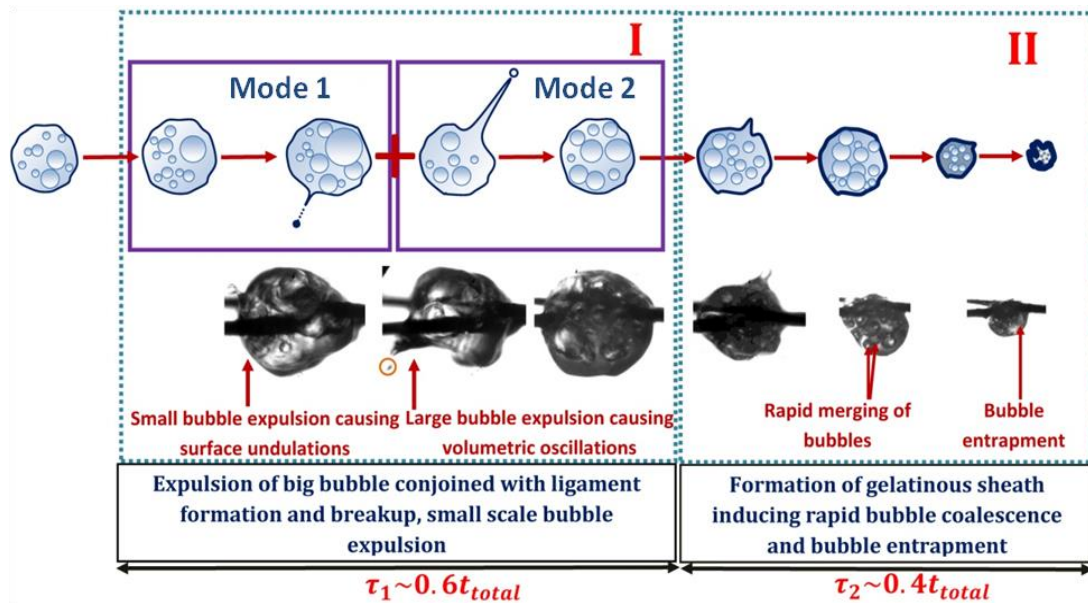
Figure 2.14. Schematic illustration of two different stages of droplet combustion Stage I: residence time $\tau_1 \sim 0.6t_{total}$ characterised by the presence of two modes of ejection (1 and 2) and Stage II: $\tau_2 \sim 0.4t_{total}$ mostly with I(a) ejection mode and bubble entrapment due to formation of gelatinous sheath.

(I) Stage-I constitutes ~60% of total droplet lifetime and accounts for ~75% of total droplet volume reduction. It further incorporates first two regimes of bubble size variation; Regime A $\{d_b \sim (0.1d_0 - 0.4d_0)\}$ and Regime B $\{d_b \sim (0.4d_0 - 0.83d_0)\}$ including major $(0.5 < \alpha_{local} \sim 0.6)$ as well as minor $(\alpha_{local} \sim O(10^{-3} - 10^{-2})$ ejection events. **(II) Stage-II** comprises the rest ~40% of total droplet lifetime. In this period of burning, droplet surface regresses at a slower rate because of the formation of gelatinous sheath around. There is minimal deviation of droplet diameter from mean value as seen in Figure 2.8 and Figure 2.9 (no dominant frequencies are present in this period of time). Bubble population as well as bubble dimensions are relatively higher during **Stage I** thus making it susceptible to ejection events with varying levels of severities quantified by α_{local} . Figure 2.15 and Figure 2.16 illustrate two modes of ejection events, **Mode 1** $(\alpha_{local} \sim O(10^{-3} - 10^{-2})$ conjoined with **Mode 2** $(0.5 < \alpha_{local} < 0.6)$ which form a part of **Stage I**. Both modes are cognate in their driving mechanism of bubble collapse near a free surface as described earlier. However, disparity in their respective effects i.e. surface oscillations for Mode 1 and volumetric oscillations for Mode 2 is because of varying bubble dimensions. Small scale deformations are mainly due to Mode 1 ejections (high frequency) while bulk oscillations can be attributed to Mode 2 (low frequencies) ejections. These ejection modes are primarily responsible for the principal frequencies shown in Figure 2.7.

Small bubbles $\sim O(.1d_0 - .2d_0)$ due to buoyancy effects rise to free droplet surface where they rupture and result in **Mode 1** ejection events. These occurrences are fast $\Delta t_{ejection} \sim O(0.2 - 0.4ms)$ and resultant recoil is restricted only to surface undulations. Minor ejection events (Mode 1) (Figure 2.15) result in needle-shaped ligaments of dimension $\sim 50 - 100\mu m$ and daughter droplets $\sim (15 - 30\mu m)$. Irrespective of particle loading, Mode 1 ejection events are existent for all cases of nanofuel droplets whereas Mode 2 is present for PLRs > 0.1%.

Mode 2 ejection events are concomitant of rupture of bubbles with dimension $d_b \sim (0.6d_0 - 0.83d_0)$ and residence time $(\tau_{residence})$ of $\sim O(60 - 100ms)$. Here $\tau_{residence}$ is the time duration between bubble inception, growth, merging and further expansion before expulsion takes place. An intrinsic explanation of small bubble rupture is its movement up to free surface due to buoyancy effects but for big bubbles it is the expansion of evaporating front. The instant this evaporative front merges with free droplet surface, bubbles collapse followed by fluid movement into the toroidal void

so created. Entrainment of fluid thus results formation of high-speed $\sim O(1-2\,m/s)$ liquid jet protruding from droplet surface as a ligament (Figure 2.16) which further undergoes break-up at the tip. Post-ejection droplet undergoes a vigorous bulk movement following random centroid trajectories. It takes $\tau_{relax} \sim O(4-6ms)$ to regain its shape. In order to determine the characteristic of jet tip break-up, aspect-ratio of ligament is calculated by

$$AR_{lig} = (L_{lig}/W_{lig}) \qquad (2.10)$$

where L_{lig} is total ligament length and W_{lig} is its width at centre (**Figure 2.16**). Calculations are done for four experimental trials for each case of nanofuel droplets with PLRs $> 0.1\%$. Value of AR_{lig} is found to be $> \pi$ thus establishing it to be a Rayleigh-Plateau break-up mechanism. As previously stated, and illustrated in **Figure 2.11**, bubbles for PLRs $> 0.1\%$ are nearly half in size to that of $w > 0.1\%$. Thus, ejections corresponding to Mode 2 are not present for $w = 0.1\%$.

Flame response in case of pure dodecane droplet is given by its characteristic diffusive time-scale $t_{diff} = (r_f{}^2/D) \sim O(150ms)$ where R_f is the flame stand-off distance $\sim 1.4\,mm$ measured from droplet centroid in vertical direction and D is vapour-diffusivity of doedecane. This diffusion time scale creates a time-lag between mass evaporated at droplet surface and its advent at the flame. For pure dodecane droplet, effective mass burning rate $(\dot{m}_{effective})_d$ is found $\sim O(10^{-6})kg/s$. Interestingly inclusion of nanoparticles results in a lateral shift of $(d/d_0)^2$ in temporal space (**Figure 2.6**) with reduced droplet burning time $\sim$ half of pure dodecane. For better understanding of burning time reduction for nanofuels, burning time (t_{total}) is determined using classical $d^2 - $ law for droplet combustion given as

$$d^2 = d_0{}^2 - Kt \qquad (2.11)$$

where d and d_0 are instantaneous and initial droplet diameters, and t is time. Note that the classical $d^2 - $ law have been only used to evaluate droplet burning time in the diffusion limit.
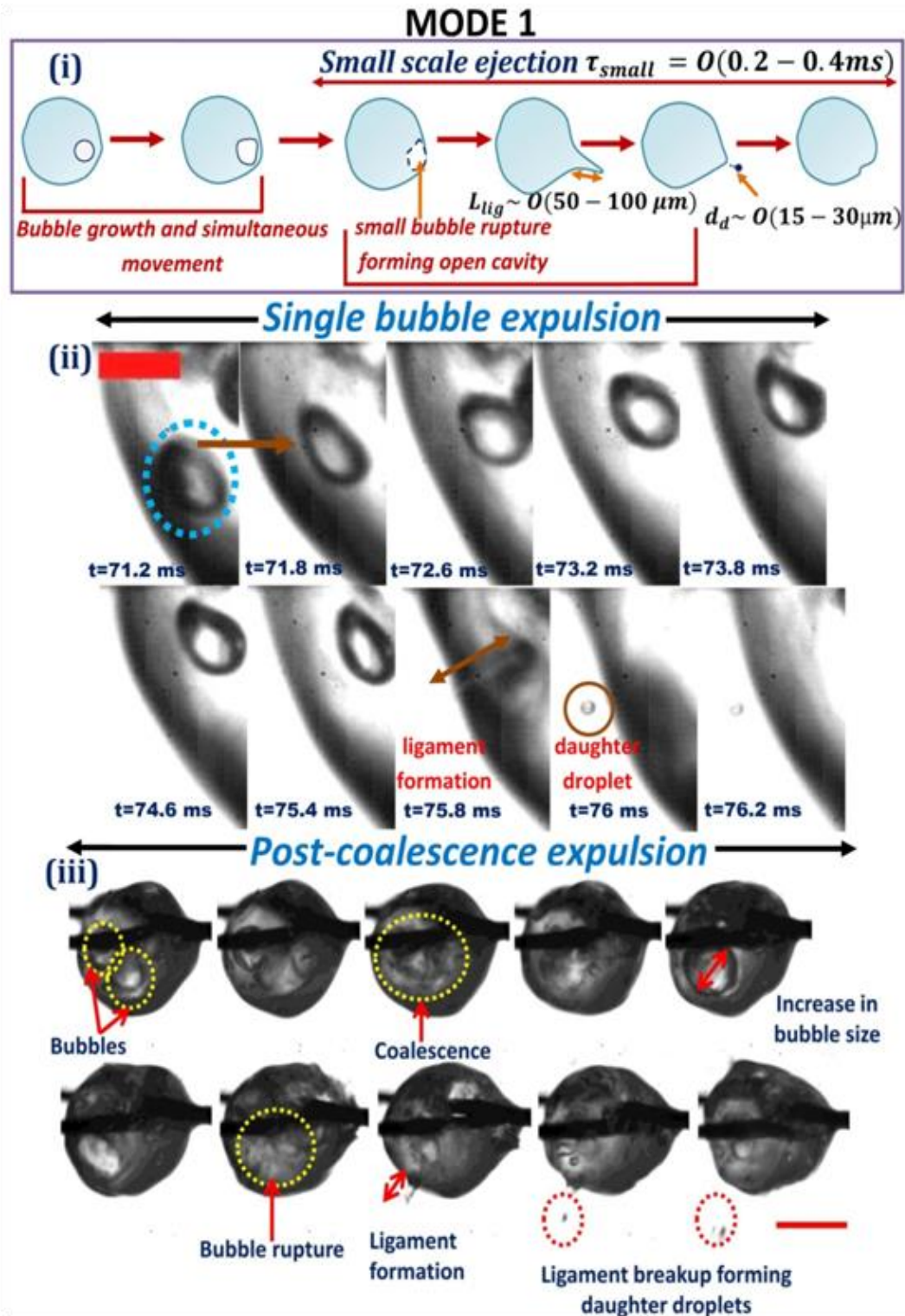
*Figure 2.15. (i) Schematic of I(a) ejection event occurence i.e.mode 1 causing local disturbances (ii) high speed images of localised single bubble expulsion from droplet surafce with $\alpha_{local} \sim O(10^{-3})$ resulting in needle-shaped ligament (L_{lig}). Scale bar represents 0.1mm (iii) Time-series snapshots of bubble expulsion after coalescence with $\alpha_{local} \sim O(10^{-2})$. Scale bar represents 0.5mm. (**Video 2.2**)*
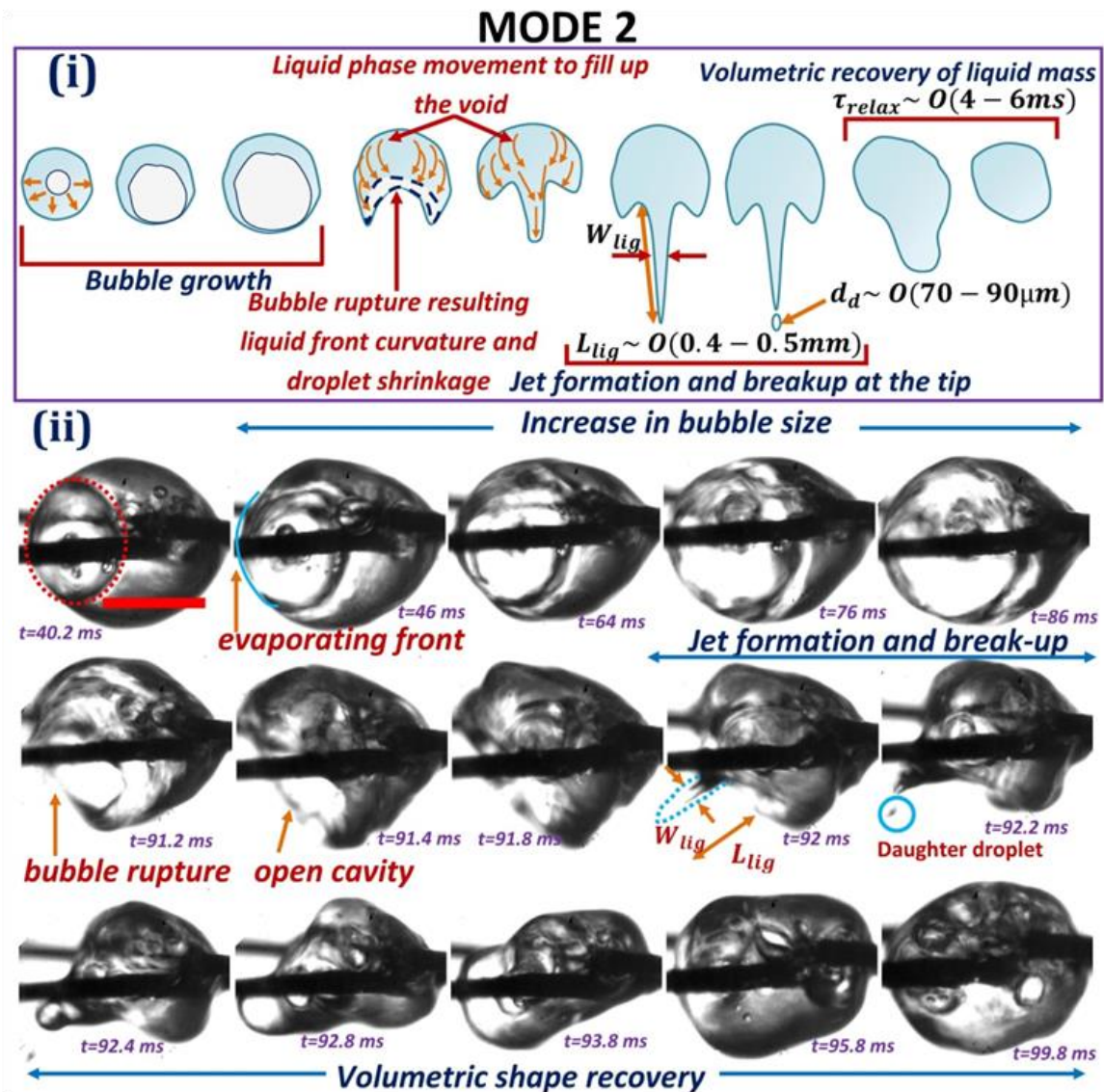
Figure 2.16. (i) Illustrative representation of mode 2 ejection event which exist mostly for PLRs $> 0.1\%$ depicting bubble growth, bubble rupture, formation of an open cavity followed by jet formation and Rayleigh-Plateau ligament tip break-up $(L_{lig}/W_{lig}) > \pi$ forming daughter droplets (d_d) and final volumetric recovery (ii) High Speed time series images of Mode 2 ejection resulting in volumetric deformation. Scale bar represents 0.5mm. (**Video 2.3**)
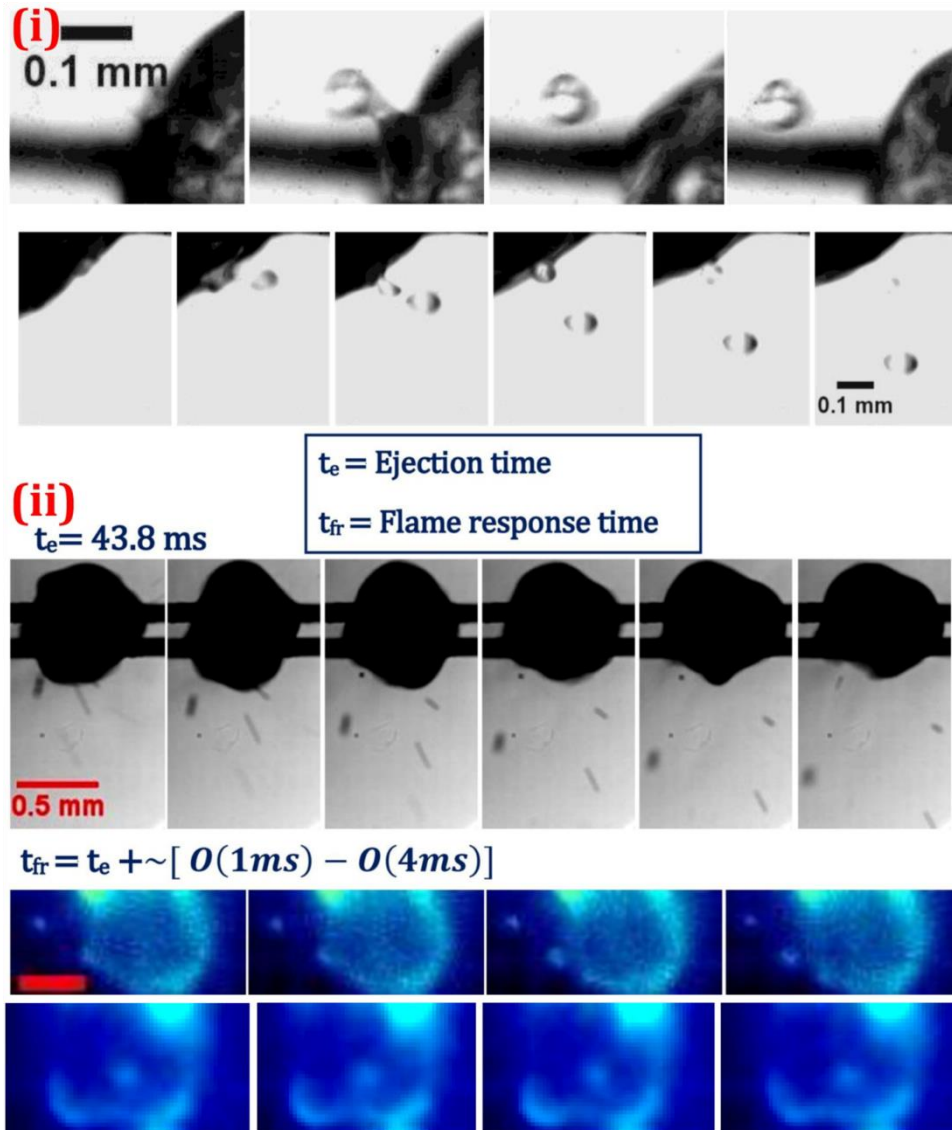
Figure 2.17 (i) Isolated high speed images (0.2 ms temporal resolution) of continuous ejection events working as a secondary pathway of fuel transfer from droplet surface to flame front (ii) High speed and high resolution (1024X1024) *droplet shape and flame images representing time-lag* (Δt_{lag}) *between an ejection event* (t_e) *and the corresponding flame response* (t_{fr}). *Scale bar represents 1mm.*

Burning rate constant (K) is given as

$$K = \frac{8k_g}{\rho_l C_{pg}} \ln (1 + B) \qquad (2.12)$$

$$B = \frac{(\Delta h_c / v) + C_{pg}(T_\infty - T_s)}{h_{fg}} \qquad (2.13)$$

where k_g and C_{pg} are gas-phase thermal conductivity and specific heat of fuel respectively, ρ_l is liquid-phase density, Δh_c is the heat of combustion per unit mass, v is the stoichiometric air-fuel (mass) ratio, h_{fg} is the latent heat of vaporisation, T_∞ and T_s are ambient and droplet surface temperature respectively and B is the heat transfer number. Theoretical estimate of t_{total} for pure dodecane using classical d^2-law yields a value $\sim 32.5\%$ higher than experimental finding. As pure dodecane manifests mostly quiescent burning (without bubbles or ejections), this discrepancy can be attributed to natural convection and buoyancy effects. Whereas, theoretical burning time of NP laden droplets calculated using classical model is found $\sim 381 - 430\%$ higher than experimental values. Therefore, classical $d^2 - law$ of droplet combustion is not valid for NP laden droplets. The theoretical burning time using classical d^2- law for various functional droplets is reported to show the wide disparity of the same with experimental findings. Reduction in burning time and enhanced burning rate can be a cumulative outcome of a) secondary atomization: continuous bubble rupture and ejection events rapidly transport fuel to the flame front, b) enhanced surface area: continuous swelling of the droplet due to bubble growth increases its exposure to flame, c) internal flow inside the liquid phase: severe droplet churning, bubble motion and volumetric/surface oscillations lead to vigorous internal recirculation in the liquid phase. As explained in [57], this internal flow field increases droplet vaporization rate. One other reason for enhanced burning rate can be through enhanced absorption of heat from flame by the alumina NPs. In one of our experimental studies [30], it is established that addition of alumina NPs increases heat absorption rate for nanofuel droplets (with dodecane as base fuel). Absorption of radiative energy emitted from the flame, has been explored in previous studies of Tanvir and Qiao [28]. Thus, enhanced mass evaporation rate $(\dot{m}_{NPs})$ due to enhanced heat absorption long with secondary atomization (formation of daughter droplets) is due to addition of alumina NPs. Taking into account enhanced evaporation rate for nanofuel droplets, expulsion of accumulated vapour and detached daughter droplets, effective mass burning rate for nanofuels $(\dot{m}_{effective})_{NPs}$ can be given as

$$(\dot{m}_{effective})_{NPs} = \dot{m}_{NPs} + \frac{\sum_{i=0}^{N_{1total}} \frac{\rho_v \pi d_b{}^3}{6} + \sum_{i=0}^{N_{2total}} \frac{\rho_l \pi d_d{}^3}{6}}{t_{total}} \qquad (2.14)$$

where ρ_v and ρ_l are vapour and liquid phase density respectively, d_b and d_d are pre-ejection bubble diameter and diameter of daughter droplet respectively, N_{1total} and N_{2total} are total number of bubble disruptions and detached daughter droplets throughout droplet lifetime respectively. Second term denotes mass of accumulated vapour discharged when disruption of bubble takes place and the third term represents the corresponding mass of total daughter droplets formed after the disintegration of parent droplet. Therefore, cumulatively $(\dot{m}_{effective})_{NPs}$ comes out $\sim(2-3)$ times $(\dot{m}_{effective})_d$.
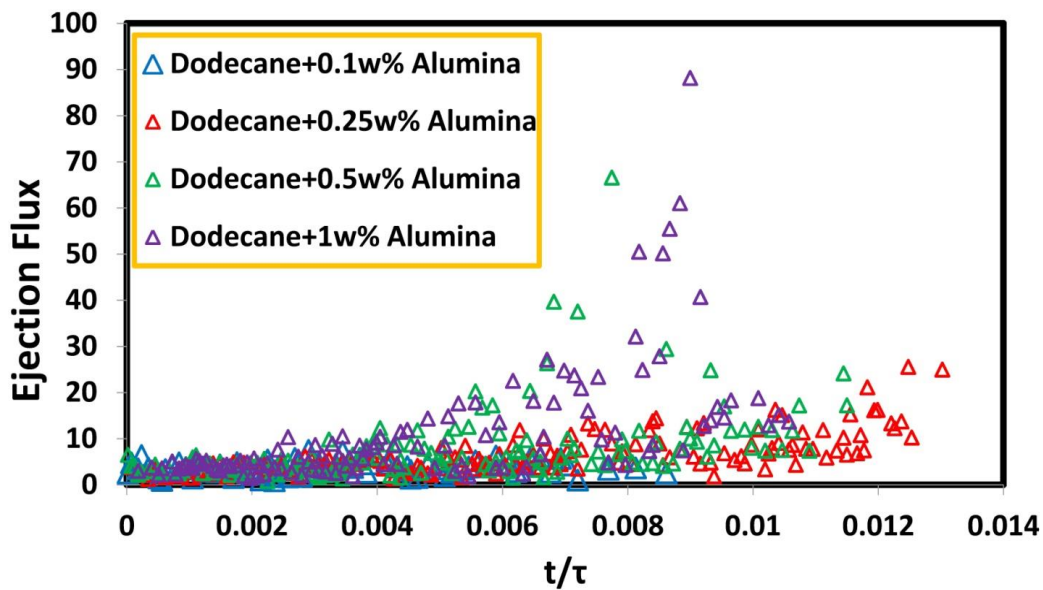
Figure 2.18. Temporal variation of ejection flux for different PLRs

For nanofuel droplets a time-lag given as $\Delta t_{lag} = (t_{fr} - t_e) \sim O(1-4\ ms)$ is observed between occurrence of an ejection event and its corresponding effect on flame, where t_e is the time instant when an ejection event transpires and t_{fr} is the time after which the flame envelope shows the corresponding response through a variation in flame stand-off distance (**Figure 2.17**). Variation of instantaneous ejection flux $e\ (t)$ given as the ratio of total instantaneous ejecting ligaments $(\sum n_{ejection})$ to instantaneous droplet area (πr^2)

$$e(t) = \frac{\sum n_{ejection}}{\pi r^2} \tag{2.15}$$

is illustrated in **Figure 2.18** for total droplet lifecycle. With increase in PLRs, ejection flux also shows the same trend. Instantaneous ejection flux $e(t)$ for PLR 0.1% remains $\sim 8 - 9$ times less than $e(t)$ of PLRs 1% and 0.5% due to lower ejection frequency.

An approachable analogy with sol-gel process is drawn here for understanding the formation of gelatinous sheath. Stage I ($\tau_1 \sim .6t_{total}$) of nanofuel droplet combustion is similar to the constant evaporation period of gel drying [58]where aggregates form. At later period of time the aggregates behave like a skeletal network referred as gelatinous sheath (**Figure 2.19**) filled with dodacene. As this stage approaches its close, ejection events corresponding to Mode 2 also cease to appear although Mode 1 ejections persist. For subsequent Stage II ($\tau_2 \sim .4t_{total}$) enhanced particle loading of NPs enters the scenario. During this period reduction in fuel content and capillary pressure within the structure leads to bubble and liquid entrapment under gelatinous sheath [58] (**Figure 2.11** and **Figure 2.14**).
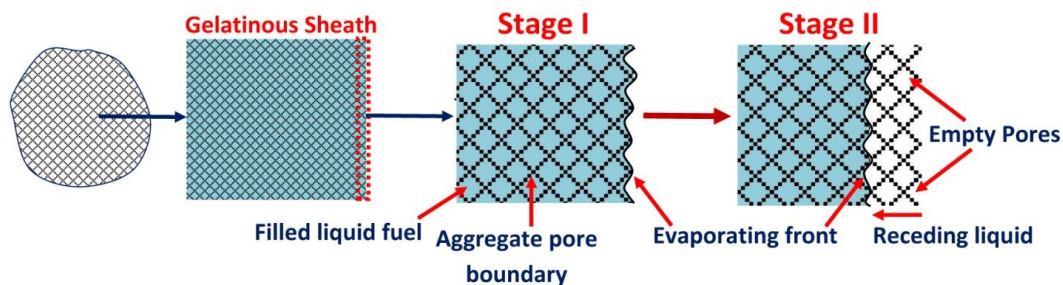
Figure 2.19. Pictorial illustration of fuel evaporation though gelatinous sheath (formed from interconnected aggregate chains). During Stage I, pores of this skeletal structure are filled with base fuel, providing enough surface area for evaporation. Fuel recedes inside the gel-structure causing its entrapment during Stage II. (Video 2.4)

2.7 Flame dynamics of nanofuel droplets

In order to understand the influence of alumina NPs addition on flame dynamics and average heat release, OH^* emission signature is captured through high speed chemiluminescence imaging. From the standpoint of combustion studies,

chemiluminescence is emission of light from excited radical species like OH^*, CH^* etc formed during combustion processes. Substantial amount of work has been done in the past where emissions from aforementioned radical species have been considered as a measure of heat release for premixed as well as non-premixed hydrocarbon flames for both turbulent and laminar conditions [59]–[63]. Global instantaneous line-of-sight flame area (A_f) and mean OH^*chemiluminescence signal ($\overline{I_{OH^*}}$) per unit area contribute to HR. Therefore, in this present work, instantaneous integrated intensity given as $Intden = (A_f * \overline{I_{OH^*}})$ is determined and averaged over three experimental runs for all cases. Natural convection gives a plume structure to dodecane flame (**Figure 2.3-2.5**). Dominance of buoyant force is determined by the ratio of gravitational and viscous forces i.e. Grashof Number (Gr) given as

$$Gr = \frac{\rho_a{}^2 g\beta\Delta T h_f{}^3}{\mu^2} \tag{2.16}$$

where ρ_a is surrounding air density, g is acceleration due to gravity , β is the thermal expansion coefficient, $\Delta T = T_f - T_0$ difference between flame and ambient temperatures, h_f is characteristic flame length and μ is viscosity of surrounding air. Considering maximum flame height Gr varies from $\sim O(10^3)$ for pure dodecane flame to $\sim O(10^3 - 10^4)$ for nanofuels. In this section, the presence of flame oscillation and its coupling with droplet shape oscillations (discussed previously **Figure 2.7**) based on temporal variation of instantaneous heat release $Q_t = Intden = (A_f * \overline{I_{OH^*}})$ is discussed. OH^*chemiluminescence signal fluctuations are given as

$$Q_t{}' = (Q_t - \bar{Q})^2 \tag{2.17}$$

Time series data is converted to frequency domain by Fast Fourier Transform (FFT). Calculations have been presented for complete structure of flame i.e. considering total height and width of flame. Pure dodecane droplet flame shows dominance of an inherent frequency $\sim 4Hz$ which is exactly the same value obtained for dodecane droplet oscillations. The dominant oscillation frequency of 4 Hz hence can be solely attributed to the natural flickering of a buoyant flame. The flickering modulates the flame heat release leading to fluctuations in heat transferred to the droplet. Buoyancy driven

instabilities are responsible for low frequency flame oscillations also referred as flame flicker and flare which are generally observed between $(10 - 20)\ Hz$ for non-premixed and partially premixed flame [34]. With increase in PLR beyond 0.1%, dominant frequency values corresponding to buoyant flame flickering $\sim(8 - 20\ Hz)$ are observed (**Figure 2.20**).
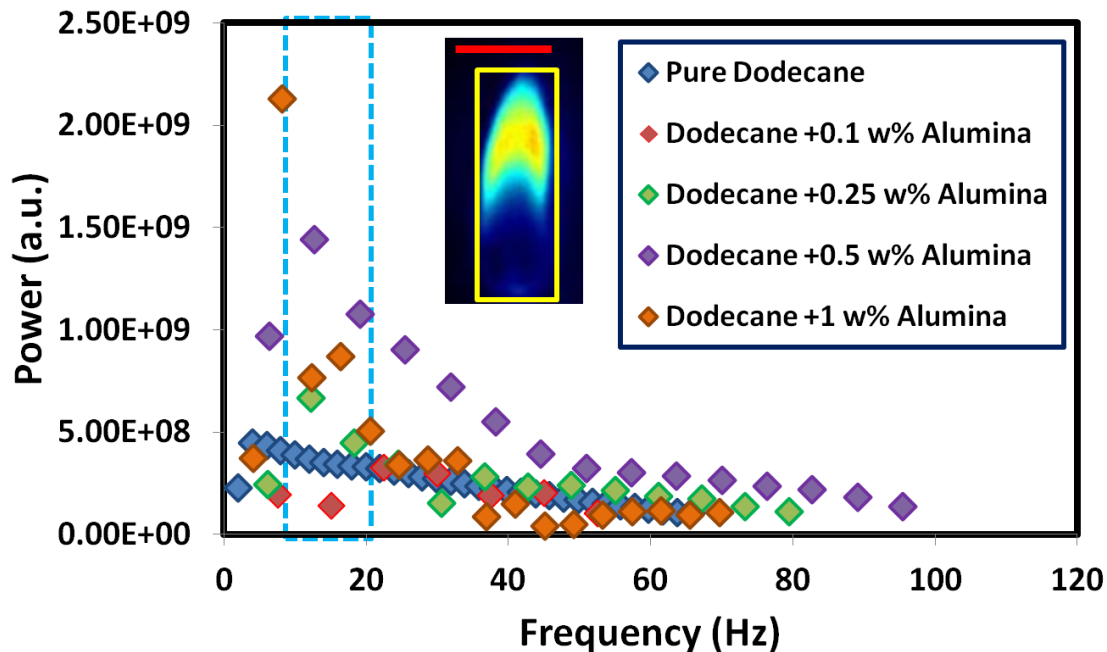
*Figure 2.20. Dominant frequency spectra of fluctuations in OH^* chemiluminescence signal calculated using equation (2.17) considering global flame shape. Intensity counts are shown in inset figure; scale bar represents 5mm. Region bound by dashed blue rectangle is the flickering frequency range$\sim(8 - 20\ Hz)$. (**Video 2.5**)*

For reassuring the presence of these frequencies throughout droplet lifecycle the CWT of $Q_t{}'$ is analysed. **Figure 2.21a** shows the CWT spectra for pure dodecane heat release data. Coherence between droplet and flame can be established as heat release shows similar instantaneous fluctuations during initial heat-up period like the droplet shape. A constant low frequency band $(\sim3 - 4Hz)$ is present throughout the droplet lifetime. Similar approach was employed for nanofuel droplets as well and a constant frequency band $\sim8 - 20\ Hz$ is discernibly present throughout the droplet lifetime. Self-excited flame frequencies have been studied in details and possible mechanisms have been

postulated such as laminar jet instability [64]and Tollmien-Schlichting disturbance wave theory [65] (responsible for laminar to turbulence transition).

Flame height (h_f) and width (w_f, measured from droplet equatorial axis) for nanofuels show ~ 2 times increase with respect to pure dodecane (**Figure 2.23**). Flame height (h_f) considers global flame shape therefore to understand the coupling of droplet shape and flame oscillations. Buoyancy effects lead to asymmetric HR and droplet heating which is also responsible for soot formation in flame zone I. Truncated flame zone (flame zone II) with ROI of (10 mm X 5mm) (shown in **Figures 2.3-2.5** and **Figure 2.22**) is considered for time-frequency data calculations. Two reasons ensure flame zone II to be a better ROI; (i) it discards the flame region with a tendency of soot accumulation (ii) truncated flame structure is in direct vicinity of droplet. Flame zone II shows intense oscillations at frequencies different from the flickering band (flame zone II **Figure 2.7**). These auxiliary frequencies are evident in **Figure 2.22,** for different PLRs. The source of the additional oscillation bands can be correlated to the droplet shape deformation frequencies (**Figure 2.7**). Droplet shape oscillations and truncated flame fluctuations indicate a preferential frequency coupling for PLR=1 wt %. Even for the rest of the PLRs, weak coupling exists between shape and flame oscillations. As discussed previously, ejection modes 1 and 2 contribute to droplet shape oscillations. The ejections transport parcels of high momentum fuel laden with NPs to the flame front. The flame heat release (and structure) subsequently responds (increased local burning) to such high momentum projectiles. Flame distortion as a result of Mode 1 is not severe due to its low intensity as compared to Mode2. Possible reason for weak coupling in PLR $< 1\%$ may be reduction of secondary atomization rate. In addition, ejected daughter droplets may experience a momentum loss (dominance of mode 1 over mode 2) within the established flame distance.

Fluctuations in shape and flame for other PLRs however show similar frequencies but they manifest lower maximum values (**Figure 2.7** and **Figure 2.22**).
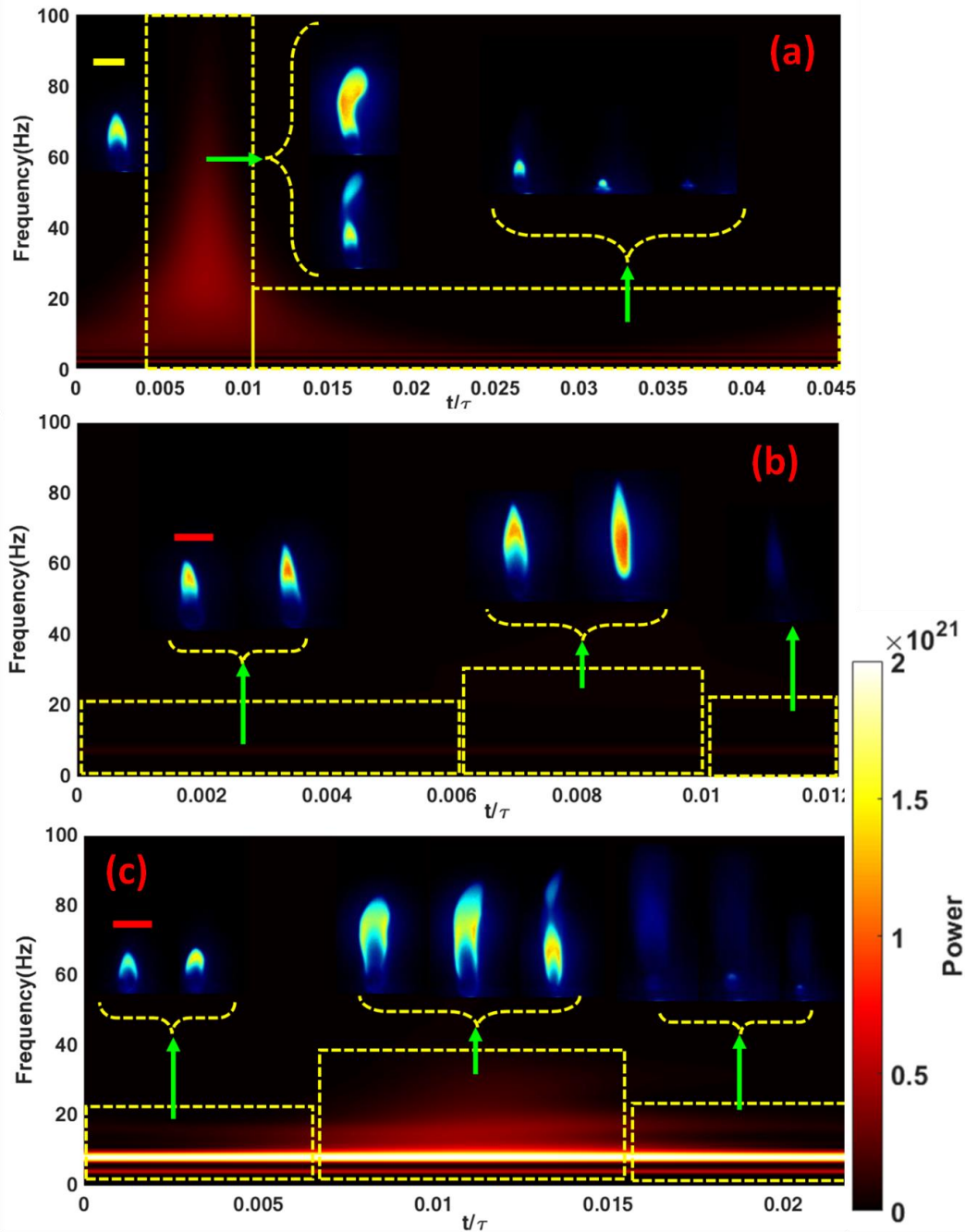
Figure 2.21   CWT spectra of $(Q_t - \bar{Q})^2$ for (a) Pure Dodecane, flame images showing maximum fluctuation during initial heat-up period with inherent frequency $\sim 4Hz$ (b) Dodecane +0.1w% Alumina NPs, an inherent frequency $\sim 8Hz$ is visible throughout (c) Dodecane + 1w% Alumina NPs, an inherent frequency $\sim 8Hz$ similar to previous case is evident throughout but with $\sim O(10^2)$ magnification in power along with auxiliary instantaneous frequencies. All scale bars represent 5mm.
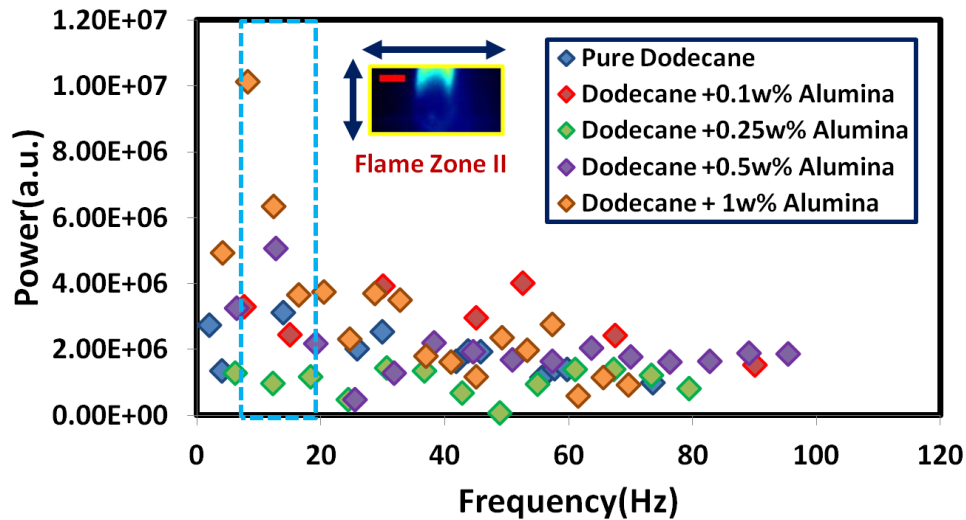
*Figure 2.22. Dominant frequency spectra of fluctuations in OH^* chemiluminescence signal considering flame zone II (inset figure), scale bar equals 2mm. Flame flickering frequency $\sim(8-20\ Hz)$ is denoted by region bounded by dashed blue rectangle. (**Video 2.6**)*
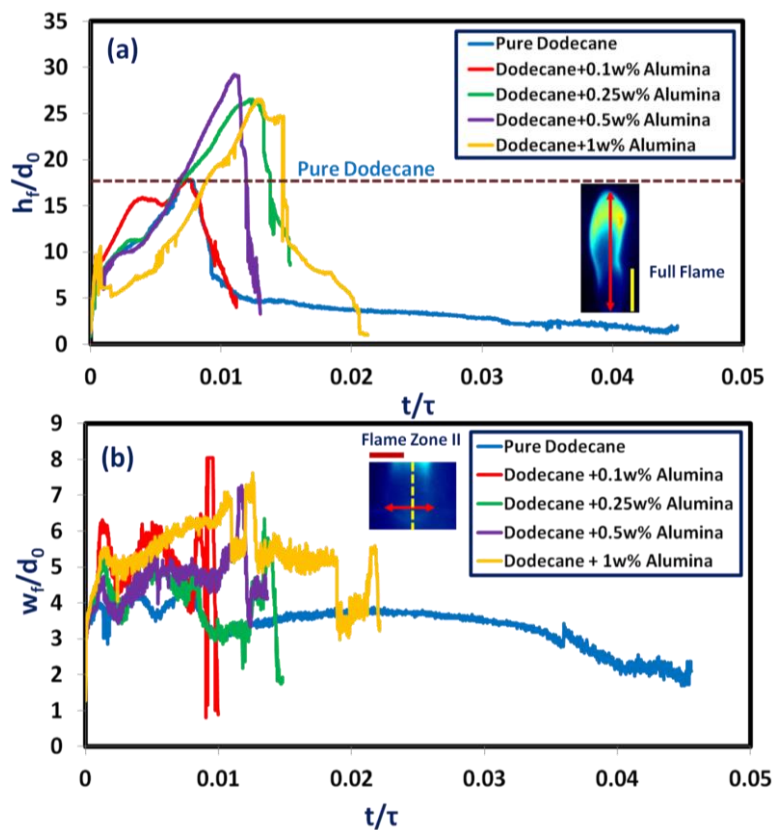
Figure 2.23. (a) Variation of normalised flame height with time for pure as well as nanoparticle laden dodecane droplets. Horizontal dashed line at $(h_f/d_0)\sim 18$ is the maximum vertical normalised flame length for pure dodecane. Inset figure shows the dimension taken into consideration. Scale bar is 5mm (b) temporal variation of normalised flame width measured from droplet equatorial axis in the horizontal direction (inset figure). Scale bar represents 2mm.

Instantaneous fluctuation in local HR (**Figure 2.24a**) is the result of local flame perturbations arising from vigorous droplet shape deformation due to Mode 2 ejections. Whereas variation in average HR indicates global variation in burning rate due to NP induced droplet heat absorption rate enhancement. Furthermore, secondary atomization (through Modes 1 and 2) leads to enhanced transfer of fuel daughter droplets to the flame front. Therefore, it increases the global fuel burning rate.
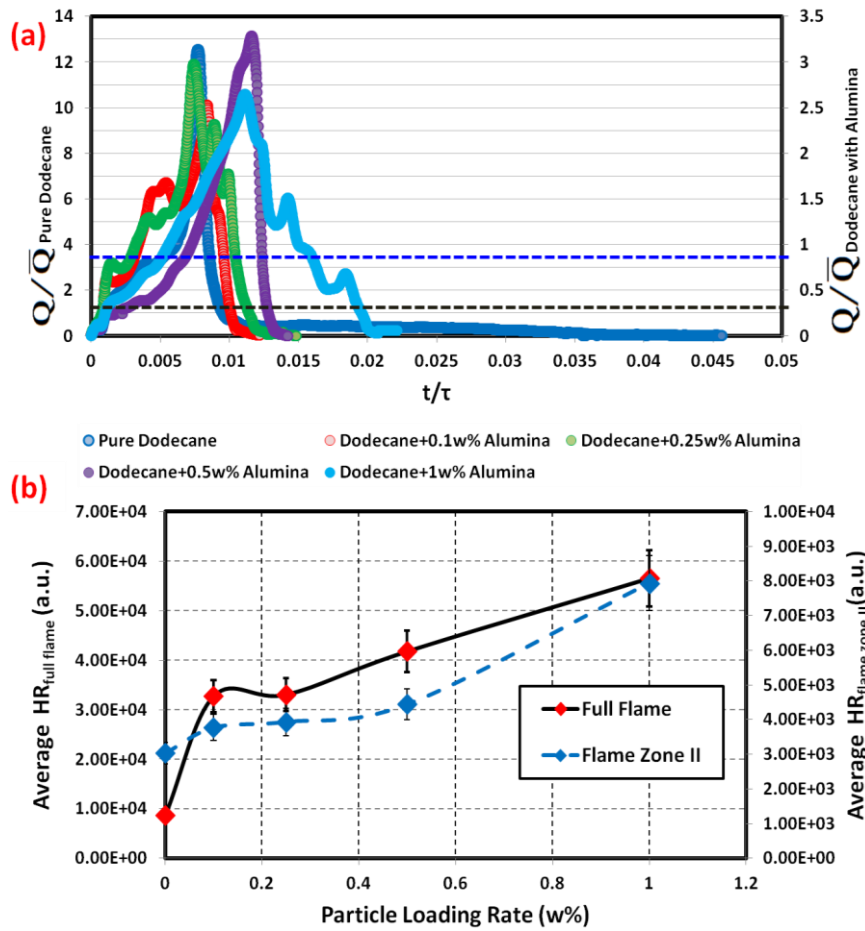
Figure 2.24. (a) Temporal history of normalised instantaneous heat release for all cases. (b) Average heat release (considering full and flame zone II) variation with PLR.

Average HR ($\bar{Q}$) is calculated as

$$\bar{Q} = \frac{\int_0^t Q_t \, dt}{\int_0^t dt} \tag{2.18}$$

Q shows an increasing trend with increase in particle loading (**Figure 2.24**). The increase in heat release with PLR is also true for flame zone II as well (discarding the

sooty tail). In short, enhancement of burning rate reduced burning time and increased heat absorption (**Figure 2.23**) culminates into an increase in average HR with PLR.

2.8   Combustion residue characterization and analysis

Precipitate left after flame extinction is characterised with scanning electron microscopy (SEM) technique under high vacuum (HV) mode of FEI ESEM Quanta 200 for comprehensive analyses of precipitates.
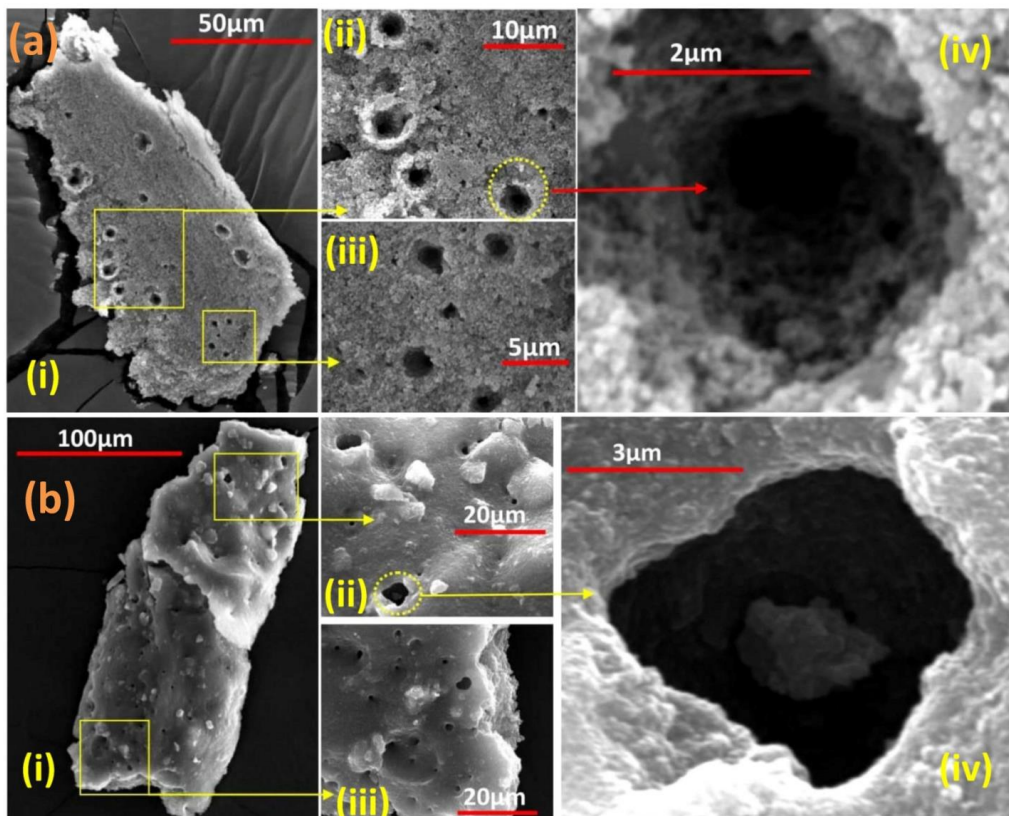
Figure 2.25. (a) SEM images of final combustion residue of PLR 0.1w% (i) Overall residue at 0.7KX magnification (ii) and (iii) show sporadic blow-holes at 4.6KX and 6.7 KX magnifications respectively (iv) Image of a single isolated blowhole at 30 KX magnification (b) SEM images of final combustion residue of PLR 1w% (i) Overall residue at 0.57KX magnification (ii) and (iii) show uniform blow-holes at 2.8 KX and 2.6 KX magnification respectively (iv) Image of a single isolated blowhole at 19 KX magnification.

In this section the arguments responsible for combustion residue formation and their respective structure is presented. **Figure 2.25** shows SEM micrographs of combustion residue for different PLRs with suffused porosity and localised blowholes for different

nanofuel cases. Possible cause for these open cavities is localised escape of entrapped dodecane vapour though chrysalis gelatinous structure formed at the end of Stage II. These blowholes are of sizes $\sim O(< 1 \, to \, 7\mu m)$. With increase in PLR aggravation in both size and numbers of these cavities is observed (**Figure 2.26**). These combustion residues manifest three different distinguishable characteristics namely (i) superficially discernible porous morphology, (ii) Surface and sub-surface blowholes and (iii) Sub-surface bubble entrapped cavity. As explained before, major portion of the base fuel gets depleted throughout Stage I. Consequently, bubble growth ceases during Stage II. With reduction in size of droplet, entrapped bubbles are subjected to compressive forces. This leads to their localised rupture. Absence of liquid mass and high viscosity inhibits instant filling of these cavities resulting in longer shape recovery time scales ($\tau_{recovery}$) compared to the leftover burning time($\tau_{burning}$). The formation mechanism is pictorially represented in (**Figure 2.27a**). **Figure 2.27b** shows bubble cavity present in sub-surface of residue. Entrapment of a bubble under gelatinous sheath impedes its growth and movement towards free surface. In this case the bubble growth time scale exceeds the leftover burning time.
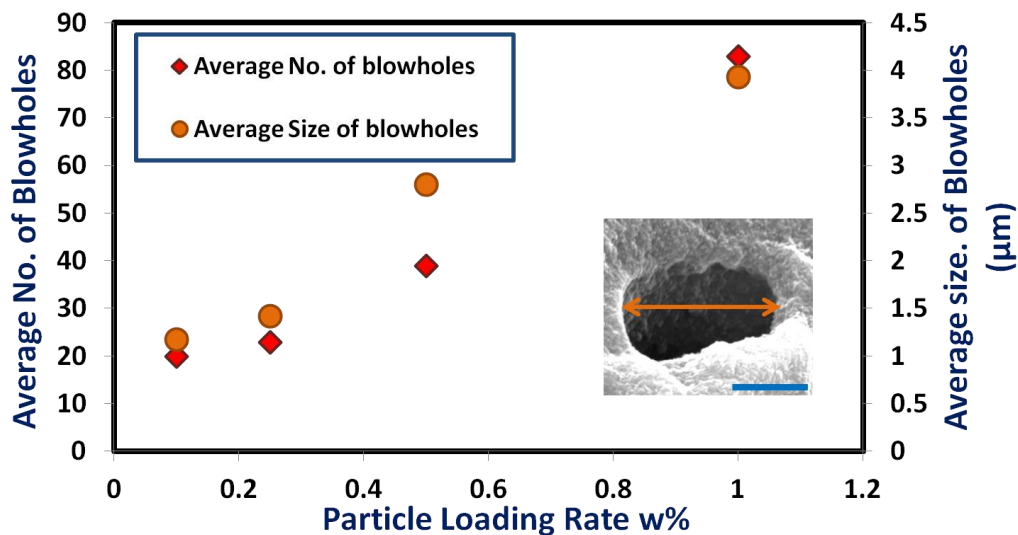
Figure 2.26. Variation of average number of blowholes on combustion residue and variation in their average size (μm) with PLR. Inset figure shows the dimension (feret's diameter) considered for blowholes. Scale bar equals 3 μm.
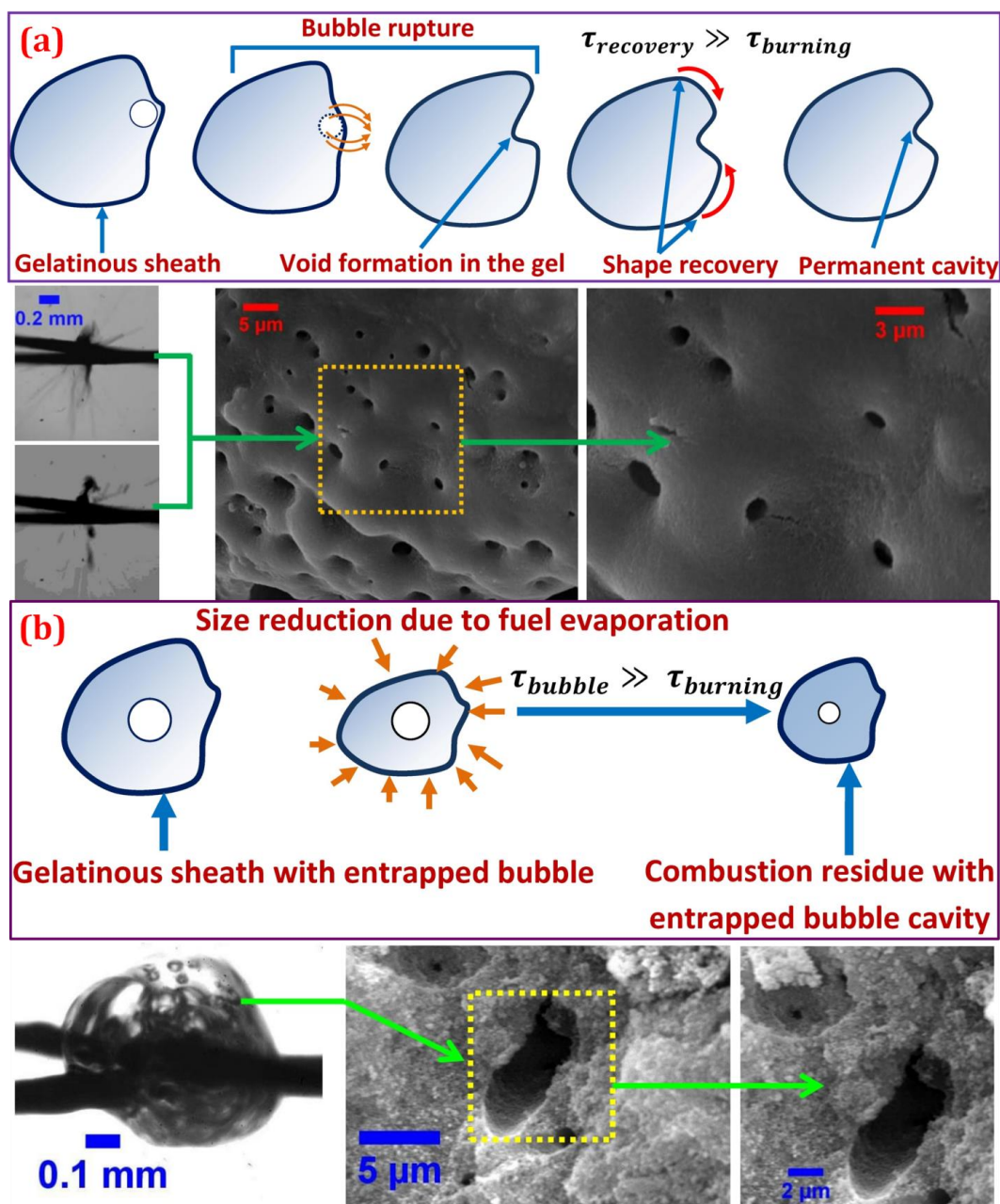
Figure 2.27. (a) SEM micrographs of combustion precipitate showing blowholes (at 1.4 KX and 2.9 KX magnification) and physical mechanism of their formation, (b) Bubble entrapment inside the gelatinous agglomerate forming cavity in sub-surface of combustion residue as shown in corresponding SEM image (at 3.5 KX and 6.65 KX magnification).

2.9   Conclusion

In this experimental work, a detailed study of the combustion dynamics of low vapour pressure fuel; pure dodecane and dodecane seeded with alumina NPs at dilute PLRs (0.1-1 w %) is presented. The respective analyses in delineated in four segments; (i)

shape oscillations (ii) internal ebullition dynamics (iii) spatial HR and (iv) combustion residue characterisation. In contrast to our ethanol-water based previous works, where diffusional entrapment of ethanol causes boiling, pure dodecane exhibits negligible bubble counts, thus minimal shape oscillations. However, variation of surface tension during initial heat-up period $\sim 0.1 t_{total}$ leads to transient shape fluctuations. Subsequently for rest of the droplet lifetime pure dodecane droplets closely follow the classical d^2 –law of droplet combustion. Addition of alumina NPs induces heterogeneous mode of boiling in the droplets. Formation of vapour bubbles followed by their growth, coalescence and expulsion, opens a pathway of secondary atomization in NP laden droplets. Different regimes of bubble growth (A, B and C) and different modes of ejections (Mode 1 ($\alpha_{local} \sim O(10^{-3} - 10^{-2})$) and Mode 2 ($0.5 < \alpha_{local} <$ 0.6) have been deciphered. Mechanism corresponding to collapse of small bubbles$\sim O(.1d_0 - .2d_0)$ is found to be similar to that of bubbles collapsing near flat free surface. Rupture of large bubbles $d_b \sim (0.6d_0 - 0.83d_0)$ results in high speed liquid jet formation which undergoes Rayleigh-Plateau tip break-up. Non-uniform expansion and random motion of large bubbles result in sporadic spreading of droplets with PLR > 0.1 %. Flames corresponding to nanofuel droplets show ~ 2 times enhancement in heat release with respect to pure dodecane. Flames of NP laden fuel droplets exhibit a dominant frequency band $\sim(8 - 20 \text{ Hz})$ corresponding to buoyant flickering. In addition to flame flicker, auxiliary oscillation modes are present. These modes correlate well with the droplet shape oscillations. These auxiliary oscillations arise due to interactions of the daughter droplets (via secondary ejections) with the flame envelope. Burning time of NP laden droplets is found to be nearly half of pure fuel droplet. The possible reasons for this reduction are also reported; (i) heat absorption rate enhancement, (ii) absorption of radiative energy by NPs from flame and (iii) rapid transfer of fuel from droplet surface to flame front through secondary ejections (Modes 1 and 2). These aforementioned enhancements increase the average HR of nanofuel droplets. Combustion residues for different PLRs show porous morphologies with localised blowholes (open cavities). With increase in PLR, population and size of these blowholes show an increasing trend. Possible mechanisms involving times scales; $\tau_{recovery}, \tau_{bubble}$ and $\tau_{burning}$, have been described to explain the formation of these

blowholes and sub-surface bubble cavities. **Figure 2.28** shows a pictorial representation of the nanofuel combustion behaviour.
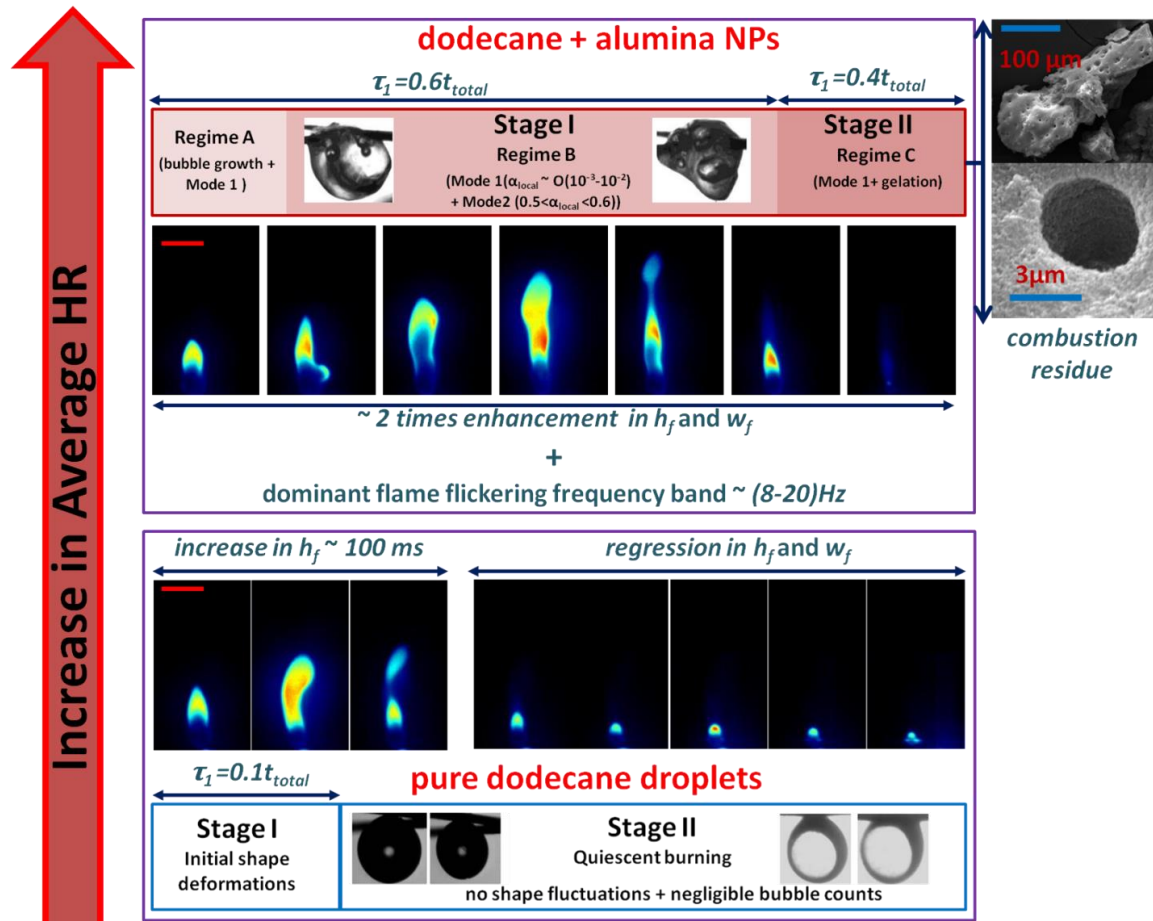
Figure 2.28. Pictorial representation of droplet life-time summary for pure dodecane droplets and dodecane laden with alumina NPs. Scale bar for flame pictures represents 5 mm.

Chapter 3

High vapour pressure nanofuel droplet combustion and heat transfer: insights into droplet burning time scale, secondary atomisation and coupling of droplet deformations and heat release

Phenomenology of internal ebullition with NP addition is well explained in our previous works [23], [25], [26], [44]. Darrieus-Landau (DL) instability is one of the key findings which suggested the coupling between internal ebullition and volumetric shape oscillations of the nanofuel droplets. Further, it has also been qualitatively established that bubble rupture and local ejection of daughter droplets lead to flame fluctuations. These findings also led to the conclusion that during droplet combustion, surface events are well correlated with spatial heat release (HR). In **Chapter 2**, causality between these events through simultaneous imaging of droplet shape and flame heat release (HR). Fast Fourier Transform (FFT) and Continuous Wavelet Transform (CWT) analyses suggest that the spectral signature of droplet shape and flame oscillations are similar indicating coupling albeit with a time delay. Furthermore, addition of NPs also changes the evaporation/burning rate of fuel [25], [28]. Plausible explanations for changes in burning rate include increase in surface area due to droplet swelling and rupturing, enhanced heat absorption by NPs, and secondary atomisation due to bubble ejections. Most importantly, these findings indicate altered fuel evaporation mechanism due to nanoadditives. Interestingly, a timescale incorporating all the essential physics of NP laden droplet combustion has not been reported in the literature. Furthermore, instantaneous area equivalent diameter (d) for droplet shape oscillations, as used in literature, is rather inappropriate since it reduces a multi degree of freedom system to single degree. As an example, asymmetric and multi length scale variation of droplet shape is converted to an axisymmetric radial variation problem. Hence, previously mentioned algorithms tend to display global fluctuations of a reduced system without offering significant insights. Considering these deficiencies in the research literature, a series of insightful analyses of high vapor pressure nanofuel combustion in the current work is presented. The aforementioned studies either being numerical or experimental

are mostly concentrated on one aspect of particle laden droplet combustion and do not provide end-to-end relation of droplet regression rate, secondary break-up and final heat release. The current work encompasses all the three aspects; droplet combustion timescales, secondary atomization, and the coupling of droplet deformations and heat release, under one umbrella

Section 3.2 encompasses the global experimental observations. The detailed analyses pertaining to the global observations are structured in the following fashion. First, a semi-analytical time scale (t^*) is proposed to provide a universal representation of the droplet burning rate. This analysis considers different mass depletion mechanisms corresponding to natural convection, ejection of daughter droplets, and fuel percolation through a porous media (Darcy's law) (**Section 3.3**). Secondly, secondary break-up mechanisms for the functional droplets with and without ceria NPs are elucidated. A comprehensive understanding of the surface deformations of the fuel droplets as a function of nanoparticle loading is provided. Rapid vaporisation of EW droplet exerts a thrust on the air-fuel interface leading to the formation of surface craters. These dynamics are described using a modified local weber number (We_{local}) (**Section 3.4**). However, for nanofuel droplets, crater formation on the droplet surface is an outcome of vapor bubble rupture. Inflow of liquid mass into surface crater for both types of fuel (EW and EW+NPs) forms a high-speed ligament which stretches and undergoes Rayleigh-Plateau tip break-up. The velocity scaling for such ligaments is also provided. Thirdly, the droplet effect of droplet vaporising and break-up (as described in previous sections) on flame heat release is discussed. Droplet shape and spatial HR are conjectured to be a coupled system. In **Section 3.5**, proper orthogonal decomposition (POD) technique is utilised to investigate the stated coupling across various energy containing modes. Finally, all the results and their respective discussions are summarised in the conclusion.

3.1 Experimental Methodology

(a) **Nanofuel preparation: Base fluid**: ethanol-water (EW) blend (81.82 vol% ethanol and water 18.18 vol %), **Nanoadditive:** Cerium Oxide, CeO_2 nanoparticles, aqueous suspension of 5 wt.% ceria procured from Reinste Nano Ventures with average particle

size of 4nm. Ethanol being a polar and hydrophilic liquid [28] provides better stability without the necessity of surfactant addition. Aqueous suspension of 5 wt.% ceria is diluted by adding ethanol for the required NP loading. Mixture of base fluid and nanoparticles are subjected to ultrasound sonication (Trans o sonic D120/P model, 30 ± 3 kHz with 15 seconds alternate ON/OFF cycles) for nearly 30 minutes. Functional droplets with NP PLRs (particle loading rates) of weight percentage 0 w%, 0.5 w% (0.095 vol%), 1.0 w% (0.191 vol. %), and 1.5w% (0.2865 vol. %) are considered. Ethanol to water ratio by volume is maintained constant for all cases.

Combustion dynamics of base fuel as well as NP laden droplets in pendant mode are observed. Droplets are deployed on a tungsten cross-wire arrangement (100 μm) using a syringe needle with inner diameter of 0.25mm. Droplets of sizes between ~ (1.1± 0.05) mm are considered for the present study. Droplets are ignited at atmospheric condition by a coil heater coupled with a linear solenoid actuator. The experimental set-up is as described in **Figure 2.2** (**Chapter 2**). Even though, wire/fibre effects are present, the same can be neglected if their dimensions are below 100 μm [17]**.** It is to be noted that the suspender's effect (if any) is present across all the experimental cases (pure and NP laden). Therefore, on a relative basis, the physical arguments, combustion behaviour, nucleation and bubble mechanisms and key conclusions should remain largely unaltered. Furthermore, it should also be noted that the droplet dimensions are larger than the commonly encountered sizes for fuel combustors. However, this is a canonical study which attempts to quantitively explain the interlinking mechanism of droplet evaporation, shape deformations and flame dynamics. There exists evidence that even in much smaller droplets [30], the physics remains phenomenologically similar.

(b) High speed imaging of pendant droplets (Figure 2.2): Simultaneous high-speed shadowgraphy of droplet shape, and flame imaging is done at 10,000 fps (temporal resolution of 0.1ms and pixel resolution of 704X696). Droplet shadowgraphy images are acquired at a spatial resolution of ~3.8 μm/pixel. High speed camera at spatial resolution ~89 μm/pixel coupled with *high speed intensified relay optics (HS-IRO) (LaVision; IV Generation)*, UV lens (Nikon Rayfact PF10445MF-UV lens) and OH* bandpass filter (308 ± 10 nm) is utilised for visualisation of the flame. Droplet internal ebullition and bubble dynamics are recorded (with volumetric illumination of droplets)

at 7500 fps with pixel resolution of 1024X1024 (temporal resolution and spatial resolution of ~0.133 ms and ~2.0 µm/pixel respectively).

(c) Data Processing:

Recorded droplet images are converted from gray-scale to binary using Otsu thresholding technique using an in-house MATLAB code for extracting the temporal history of projected droplet area. Reported normalised squared droplet diameter $(d/d_0)^2$ is an ensemble average of five experimental runs with an uncertainty of ±4.5%. Instantaneous ejection events (N_t) are obtained through ligament counts at a temporal resolution of 0.2 ms using Photron Fastcam Viewer (PFV) software. Vapor bubble diameter (d_b) (with an error of ±5%), velocity of ejected droplets (V_{dd}), and bubble velocity (V_b) are obtained using particle tracking technique of Mosaicsuite plugin of Imagej Software. Similar thresholding is used to isolate ligaments and daughter droplets and their dimensions. These calculations are made over five experimental runs with an uncertainty of ±5%. Flame dynamics and HR variations of burning droplets are captured using high-speed chemiluminescence imaging of OH* emission. Flame contours and global areas are calculated from flame images using similar thresholding technique as used for droplet diameter calculation. Extensive combustion studies have suggested that OH* emission is a measure of flame HR (Q). Hence, $Q \propto ID_f$ [44] where ID_f is integrated density of flame given as, $A_f \times \overline{I_f}$ (A_f is the instantaneous line-of-sight area of flame and $\overline{I_f}$ represents average OH* intensity over A_f). Instantaneous flame HR (Q) is calculated with an error of ±14.5% by averaging over five experimental runs.

3.2 Global observations

Figure 3.1 presents a global overview of shape oscillations and flame response for NP PLRs of 0 and 1.5 w%. the droplet undergoes uniform surface regression during the initial heat-up period $\sim\Delta t = .05 t_{total}$ $(t_{total} \sim 350 \text{ ms})$. However, bi-component EW droplets subsequently undergo instantaneous deformations which initiate the formation of surface craters. High-speed ligaments emerge from the chaotic surface undulations and are further subjected to Rayleigh-Plateau break-up at the tip thus forming daughter

droplets. These ejected daughter droplets serve as fuel carriers from the droplet surface to the flame envelope. Continuous ejection events are manifested as instantaneous hotspots in the flame contours (**Figure 3.1**) before being convected through the flame tail.
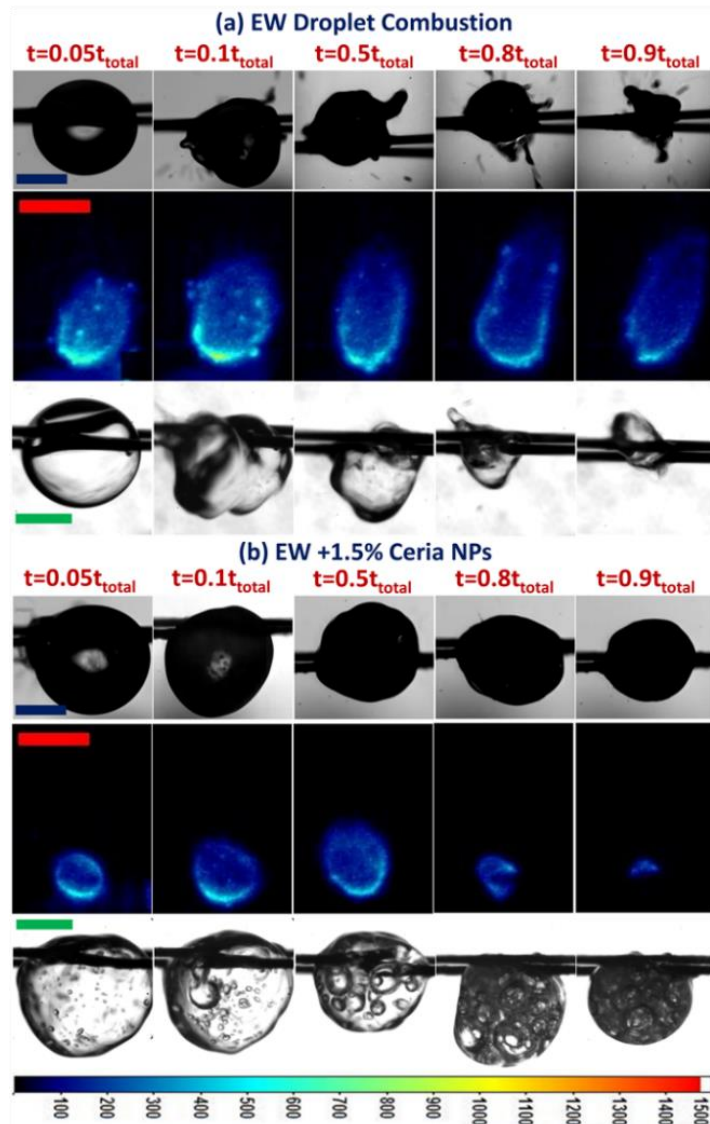
*Figure 3.1. (a) Simultaneous high-speed images (10,000 fps) of droplet shape (top, scale represents 0.5mm), flame (middle, scale represents 5mm) and internal (bottom, scale represents 0.5mm) at different instants for Ethanol-water (EW) droplet. (b) Simultaneous droplet shape (top, scale represents 0.5mm), flame (middle, scale represents 5mm) and internal (bottom, scale represents 0.5mm) images for EW droplet laden with 1.5 w% Ceria NPs Scale. Colour map represents flame intensity counts. Nanofuel droplets manifest increased bubble counts. (**Video 3.1**)*

Initial heat-up period of nanofuel droplets is characterised by pure evaporation conjoined with vapor bubble incipience. Inclusion of ceria NPs initiates the heterogeneous boiling mode. Bubble population shows $\sim (2-4)$ times increase for PLRs of $w = (0.5\% - 1.5\%)$ as compared to EW droplets. A gelatinous crust starts to appear at droplet surface after $\Delta t \sim 0.1 t_{total}$. Consequently, droplets display dormant regression and increased combustion lifetime with increase in PLRs i.e. $t_{total}|_{NPs} \sim (2-2.5) t_{total}|_{EW}$ for $w = (0.5\% - 1.5\%)$, where $t_{total}|_{NPs}$ and $t_{total}|_{EW}$ are total burning time of droplets with and without NPs. Perikinetic aggregation of ceria NPs leads to the formation of a gelatinous structure entrapping the base fuel thus reducing the burning rate. It also prevents catastrophic break-up of primary droplet as in the case of pure EW droplets. Although increase in bubble population is evident with particle loading, ejection events are found to be subdued. Droplet flame also exhibits a passive behaviour as the droplet shape. Flame height and width show a reduction of $\sim 27\%$ and $\sim 12\ \%$ respectively with increase in PLR. Furthermore, decreased ejection events, reduced mass burning rate and increased burning time collectively contribute towards reduction of average HR with increase in PLR. It should be noted that though the combustion rate is reduced, the energy content of the system is not. Ceria NPs are non-energetic species which do not add to the heat of combustion; therefore, there is no enhancement in energy content either.

3.3 Droplet burning timescales

As stated earlier, the NP laden droplets exhibit increased burning time. Therefore, the objective of the current section is to understand the influence of NP addition, and particle agglomeration on the mechanism of droplet vaporisation and consequently, on the burning timescale. Therefore, a semi-analytical approach to obtain an appropriate time scale is adopted. Natural convective effects are invariably present in the current experiments due to atmospheric conditions. Expression for the droplet burning rate considering classical $d^2 - law$ with convective effects [66] and assuming constant droplet surface temperature, is given as

$$\dot{m}|_{conv} = \frac{2\pi k_g r_0\ Nu}{c_{pg}} \ln{(1 + B)} \tag{3.1}$$

where k_g and c_{pg} are the thermal conductivity of the air-fuel gaseous mixture and specific heat capacity of the fuel vapor, respectively, calculated at an average value of flame and droplet surface temperatures, $\bar{T} = (T_s + T_f)/2$ [19], B is the given as [66]

$$B = \frac{(\Delta h_c / v) + c_{pg}(T_\infty - T_s)}{h_{fg}} \tag{3.3}$$

T_∞ is taken as $303\ K$ and $T_s \sim 331K$ (wet-bulb temperature of ethanol). Nu for natural convection [17] is given as

$$Nu = 2\left(1 + 0.51\ Gr^{1/2}\right), Gr < O(1) \tag{3.3}$$

where

$$Grashof\ Number\ (Gr) = \frac{\rho_\infty{}^2 g\beta\Delta T d_0{}^3}{\mu_\infty{}^2} \tag{3.4}$$

$\Delta T = T_f - T_s$, in the current study Gr is found to be $< O(1)$. Mass burning rate of pure EW droplets evaluated from equation (3.1) overestimates the total burning time by $\sim 375\%$ when compared to experimental data. This disparity is attributed to the continuous ejection of daughter droplets (**Figure 3.2 (a)**), which serves as additional fuel carriers to the flame front. Therefore, these events are accounted in the modified burning rate ($\dot{m}|_{EW}^*$) as

$$\dot{m}|_{EW}^* = (\dot{m}|_{conv}) + \frac{\sum_{t=0}^{t=t_{total}} \frac{\pi}{6} \rho_l d_d{}^3 N_t}{t_{total}} \tag{3.5}$$

N_t, a dimensionless quantity representing the number of instantaneous ejection events generating daughter droplets $\sim O(10^1)$, $d_d \sim (30 - 200)\mu m$. This is a theoretical expression. However, the values of daughter droplet diameter, d_d and instantaneous ejection events, N_t are plugged in from the experimental observations.
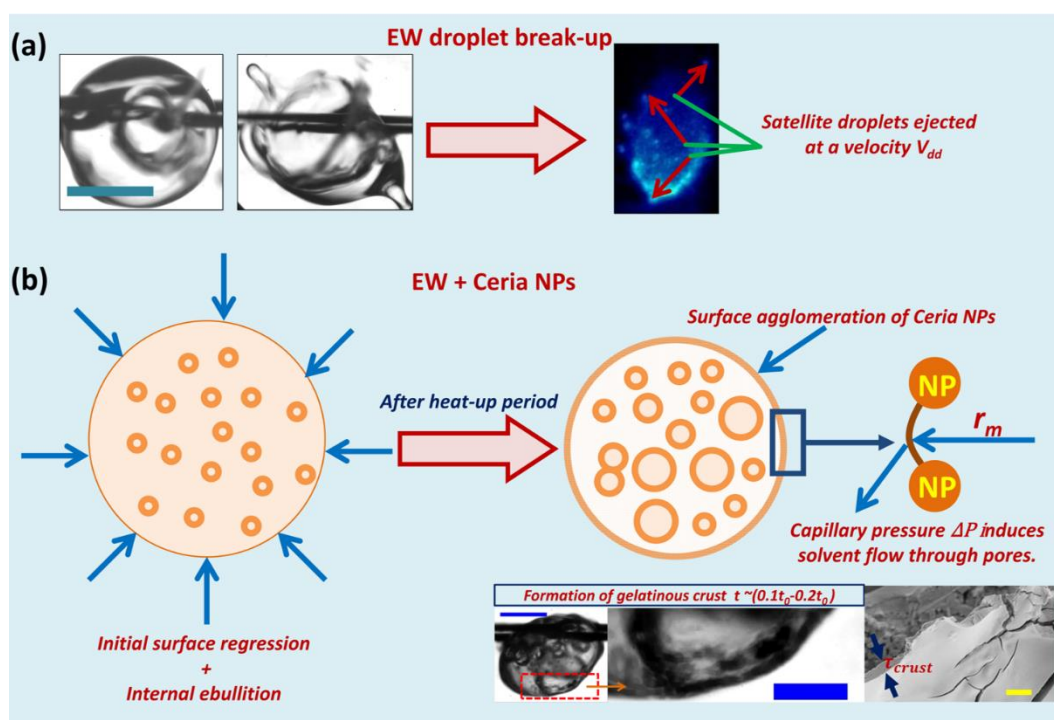
Figure 3.2. (a) Severe disintegration of EW droplet results in satellite droplets ejecting at a velocity $\boldsymbol{V_{dd}}$. Scale represents 0.5mm. (b) Illustration of nanofuel droplet combustion. Post initial heat-up period $\sim \Delta t = \boldsymbol{0.1\, t_{total}}$, agglomeration of ceria NPs leads to formation of gelatinous crust on droplet surface. Capillary action induces flow of solvent through the pores of skeletal network. Scale represents 0.5mm and 0.1 mm. Scale for SEM image represents 3μm.

For nanofuel droplets, two distinct burning stages are present; (i) Stage I- span of pure evaporation of base fuel combined with vapor bubble nucleation and (ii) Stage II- vaporisation of base fuel through gelatinous sheath formed on the droplet surface. Inside this crust, a wet central core is formed. These observations are similar to metal-slurry droplet combustion as described by [57], [67]–[71]. From SEM images (**Figure 3.2 (b)**), the thickness of this crust (τ_{crust}) is found to be $\sim 1 - 1.5\ \mu m$ for PLRs of $0.5 - 1.5\ w\%$. Base fuel percolating through skeletal network of NP aggregates is analogous to flow through a porous medium (**Figure 3.2 (b)**). Thus, Darcy's Law can be utilised for approximating the evaporation dynamics of nanofuels during Stage II. Capillary pressure is given as $\Delta P_{cap} = -2\sigma/r_m\ (\sim -10\ MPa)$ where, σ is the base fuel surface tension $\sim 0.02\ N/m$, r_m is the meniscus radius ($\sim 4nm$, order of NP particle size). ΔP_{cap} ensures the flow of solvent through the porous network. Solvent mass flux through porous media [72] is given as

$$J = -\frac{k\Delta P_{cap}}{\mu_{eff}\tau_{crust}} \tag{3.6}$$

k is the shell permeability given by Carmen-Kozeny relation i.e. $k = \left(\frac{1}{180}\right)\frac{(1-\varphi_{crust})^3}{\varphi_{crust}^2}d_p^2$ (d_p is the NP size and φ_{crust} is the particle packing fraction ~ 0.52 [57]) and μ_{eff} is the effective fuel viscosity. Effective fuel viscosity due to increase in PLR is estimated using the relation $\mu_{eff} = \mu_i (1 + 2.5\, c_h + 6.5c_h^2)$ [73], where μ_i is the initial viscosity and c_h is the volumetric concentration of ceria NPs. From equation (3.6), J scales as $\sim(10^{-4} - 10^{-5})m/s$ for PLRs of $0.5 - 1.5\, w\%$. Mass evaporation rate for the abovementioned values of J is given as

$$\dot{m}|_{porous} = 4\pi\rho_l r^2 J \tag{3.7}$$

The mass flux thus calculated varies $\sim(10^{-6} - 10^{-7})kg/s$.

Formation of a gelatinous crust is visibly evident after the initial period (**Figure 3.2b**) of $\Delta t \sim 0.1 t_{total}$. Continuous ejections of daughter droplets on the other hand are highly suppressed for nanofuel droplets. Therefore, burning rate corresponding to the initial period is same as in a convective environment. Subsequently, an integrated mechanism of droplet evaporation is evidenced. Therefore, mass burning rate of nanofuel droplets (considering previously mentioned stages) is given as

$$\dot{m}|_{NPs} = \begin{cases} \dot{m}|_{conv} & t < 0.1t_{total} \\ combination\ of\ \dot{m}|_{porous} and\ \dot{m}|_{conv} & t \geq 0.1t_{total} \end{cases} \tag{3.8}$$

For nanofuel droplets, mass burning rate from equation (3.1) overestimates experimental combustion time by $(200)\%$ whereas sole consideration of Darcy's Law underestimates the same by $\sim 10\%$. Therefore, an average mass burning rate ($\dot{m}_{th}|_{NPs}^*$) needs to be formulated for estimating the total life span. Considering mass conservation

$$\dot{m}|_{NPs}^* \times t_{total} = (\dot{m}|_{conv} \times \Delta t_{conv}) + \tag{3.9}$$

$$\left(\dot{m}|_{conv} \times \chi + \dot{m}|_{porous} \times (1-\chi)\right) \times \Delta t_{comb} + \sum_{t=0}^{t=t_{total}} \frac{\pi}{6}\rho_l d_a^3 N_t$$

To account for the integrated evaporation mechanism in the post heat-up period for nanofuels, a weighting factor (χ) is utilised. Δt_{conv} represents the time span of combustion in natural convection mode and Δt_{comb} represents the time segment for combination of $\dot{m}|_{porous}$ and $\dot{m}|_{conv}$. Hence equation (3.9) for nanofuels can be written as

$$\dot{m}|^*_{NPs} = \left\{ \left(\dot{m}|_{conv} \times \frac{\Delta t_{0.1}}{t_{total}} \right) + \left(\dot{m}|_{conv} \times \chi + \dot{m}|_{porous} \times (1-\chi) \right) \times \frac{\Delta t_{0.9}}{t_{total}} \right\} \quad (3.10a)$$
$$+ \frac{\sum_{t=0}^{t=t_{total}} \frac{\pi}{6} \rho_l d_d^3 l}{t_{total}}$$

A weighted average of $\dot{m}|_{conv}(\sim 10\%)$ and combination of $\dot{m}|_{porous}$ and $\dot{m}|_{conv}$ $(\sim 90\%)$ is utilised for nanofuel droplets. Note that there can be a gradual change in the evaporation mechanism during combustion period i.e. from pure liquid evaporation to evaporation through porous media. However, for present scaling analysis, such variations are neglected. Equation 3.10b can be cast as follows,

$$\dot{m}|^*_{NPs} = \left\{ \left(\dot{m}|_{conv} \times \frac{\Delta t_{0.1}}{t_{total}} \right) + \left(\dot{m}|_{porous} \right) \times \frac{\Delta t_{0.9}}{t_{total}} \right\} + \frac{\sum_{t=0}^{t=t_{total}} \frac{\pi}{6} \rho_l d_d^3 l}{t_{total}} \quad (3.10b)$$
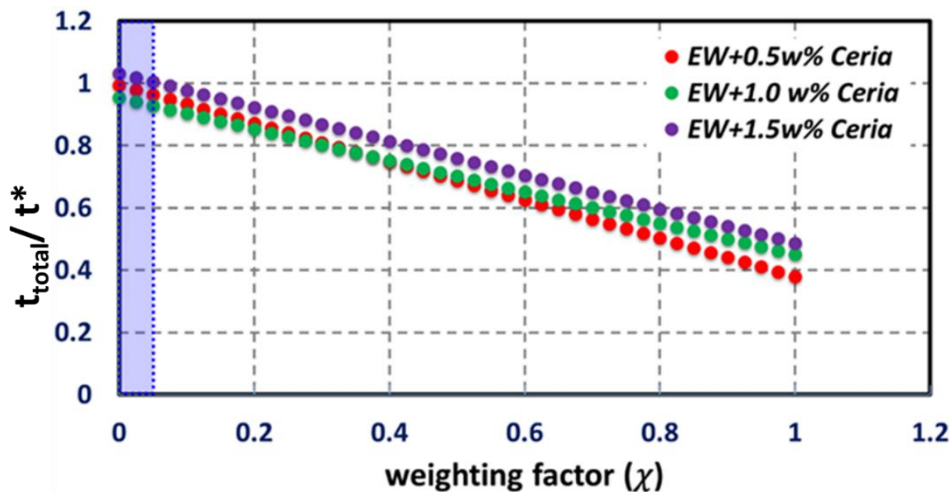
Figure 3.3. Variation of the ratio of experimental time scale and t^* with weighting factor. Data within the box represents spectrum of χ for the current work. An average value of χ over this range is utilised for calculating t^*.

Parameter χ assumes values of $0.0, 0.0,$ and 0.05 corresponding to PLRs of $0.5\,\%, 1.0\,\%,$ and $1.5\,\%$ respectively (**Figure 3.3**). The maximum variation in χ is $\sim5\%$ for all PLRs. This minimal value of χ suggests suppression of convective mode of fuel evaporation during Stage II for dilute PLRs. Thus, neglecting χ does not affect the timescale calculations. This outcome provides a universal feature of the presented semi-analytical model irrespective of initial PLRs (dilute). Therefore, the semi-analytical timescales are calculated without incorporating χ (Equation 3.10 (b)).

A semi-analytical time scale (t^*) is hence defined as the ratio of initial droplet mass and theoretical burning rate. For EW droplets

$$t^*|_{EW} = \left(\frac{4\pi r_0{}^3 \rho_l}{3}\right) / \dot{m}|_{EW} \tag{3.11}$$

whereas for nanofuel droplets

$$t^*|_{NPs} = \left(\frac{4\pi r_0{}^3 \rho_l}{3}\right) / \dot{m}|^*_{NPs} \tag{3.12}$$

This analysis provides a window into the different possible interplays of evaporation mechanisms due to NP addition. It also sheds light on the fact that for NP laden droplets, sole consideration of classical $d^2 - law$ does not provide a complete picture of combustion process. Intra-particle interactions of NPs as well as rheology are important aspects that should be addressed. Nevertheless, for the present study, normalising all temporal data with an effective timescale helps in providing insights into droplet diameter regression and HR rate. Temporal variation of normalised droplet diameter and instantaneous HR is represented in **Figure 3.4**. For EW droplets, t^* provides a good approximation with $\sim3.0\%$ uncertainty as compared to its experimental counterpart. Values of $t^*|_{NPs}$ agree with $t_{total}|_{NPs}$ within $\pm2\%$ error across all experimental conditions. This time scale for nanofuel droplets is valid for all the scenarios of droplet combustion with cumulative effects of convection, flow through porous media and secondary atomisation. The heat-up period attributed till $t/t^*\sim0.1$ exhibits increase in the values of $(d/d_0)^2$. During this initial droplet heat-up period most of the energy input is conducted to the droplet interior to increase the droplet

temperature. This reduces the availability of heat for surface gasification. As a result, with reduction in liquid density with initial increase in droplet temperature causes liquid thermal expansion leading to $\sim 1.4\%$ increase in the droplet diameter. Flame extinction for EW droplets is correlated with droplet diameter regression. However, for nanofuel droplets, flame extinction occurs at $(d/d_0)^2 \sim 0.2$ (as shown in **Figure 3.4**). Post-flame extinction, a solid mass of NP agglomerates is left behind as combustion residue. Interestingly, the data suggests that rates of diameter regression and spatial HR for all functional droplets, can be represented by a universal function using the suggested time scaling. From this observation, it can be safely concluded that addition of ceria NPs changes the physical mechanism of evaporation which is further responsible for increased burning time and reduced HR.
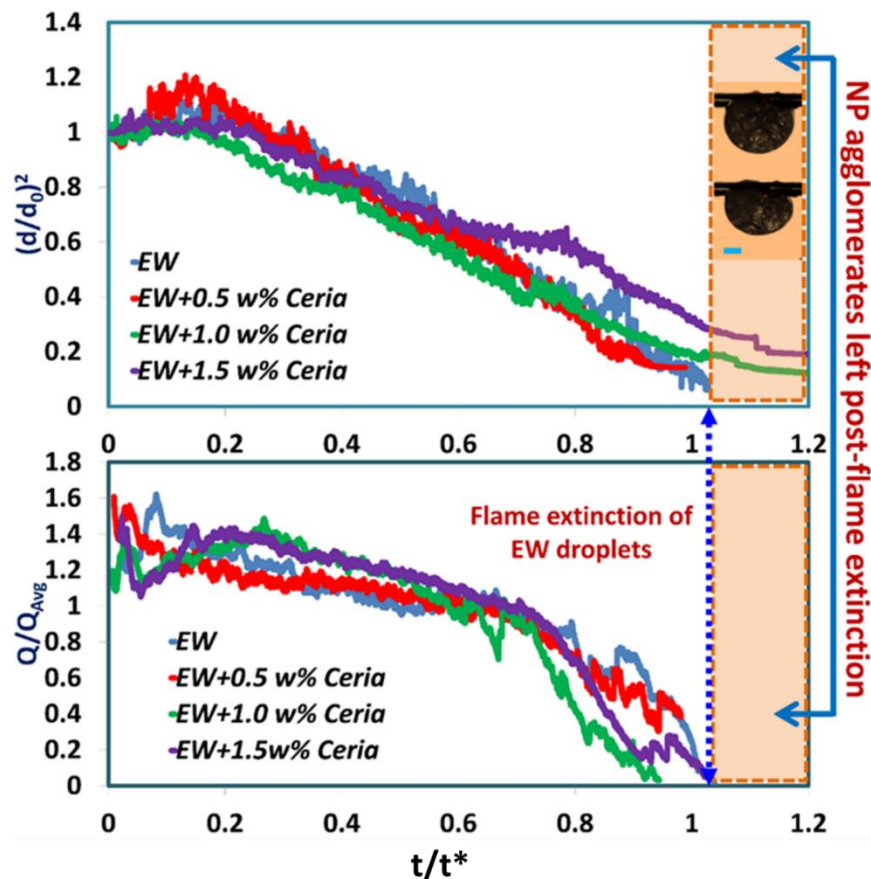
Figure 3.4. Transient variation of normalised droplet diameter and normalised instantaneous spatial heat release (HR) with PLR. Time scale is normalised using t^*. Droplet diameter and Flame extinction is simultaneous for EW droplets. For nanofuels flame is not present after $(d/d_0)^2 \sim 0.2$ due to formation of solid agglomerate of ceria NPs.

3.4 Mechanisms of droplet secondary atomisation
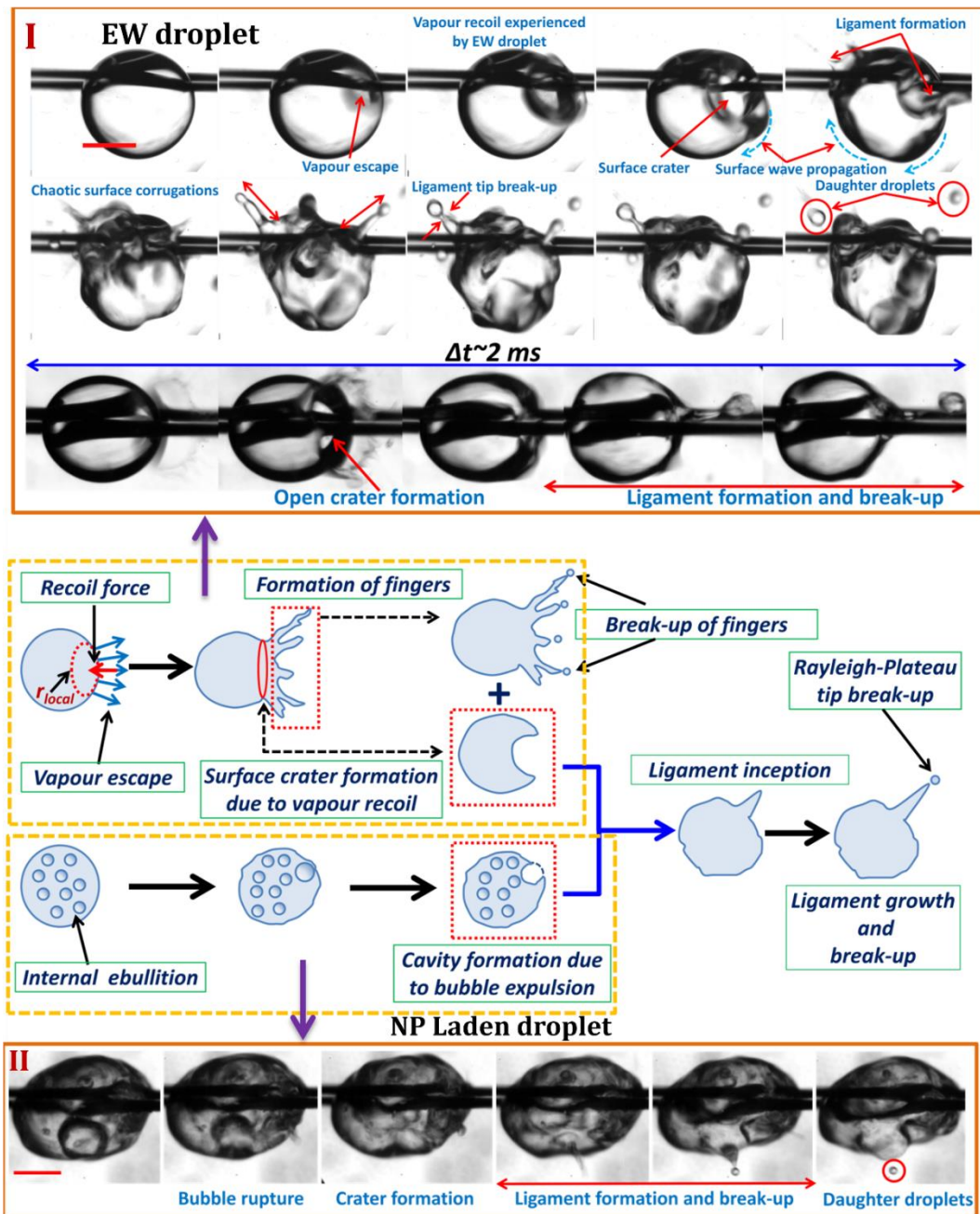
Figure 3.5. A pictorial representation of mechanisms leading to droplet (with and without ceria NPs) break-up. I. Isolated high speed (7500 fps) images of EW droplet undergoing severe initial disintegration. Scale represents 0.5 mm II. High speed (7500 fps) images of bubble rupture in droplets laden with nanoceria. For nanofuels, vapor expulsion is the mechanism for surface crater formation. Scale represents 0.5 mm.

The previous section addressed the variation in the evaporation mechanism with nano-ceria inclusion in the base fuel. The auxiliary mass loss (as shown in the eq. 3.6 and eq. 3.11), other than the droplet vaporisation is attributed to the ejected daughter droplets. Hereinafter, detailed discussions pertaining to EW and nanofuel droplet break-up mechanisms are provided. The instigating factors of the droplet surface rupture are looked into. Subsequently, also the phenomena of ligament inception and break-up post droplet surface break-up is analysed though energetics and scaling. EW droplets undergo instantaneous shattering after an initial period of quiescent surface regression for $\Delta t \sim .05 t_{total}$. This occurrence is globally similar to microexplosion phenomenon reported in the literature [70], [74]. However, unlike microexplosion, plausible cause for this shattering is not explosive boiling, as no bubbles are observed inside the liquid phase. EW droplets do not manifest either volumetric swelling or surface fluctuations before the catastrophic rupture. On the other hand, nanofuel droplets exhibit increased internal ebullition activity. Therefore, secondary atomisation of EW and nanofuel droplets happens due to separate reasons. Instantaneous ejection events are found to be highly suppressed (~ 4 times) in nanofuels as compared to EW droplets.

(a) Formation of surface openings

During transient heat-up of EW droplets, ethanol, being more volatile (compared to water) is preferentially vaporised. EW droplets experience vapor recoil due to rapid evaporation of ethanol. Theory of vapor recoil have been extensively studied and reported as part of boiling investigations [75]. It is analogous to the thrust experienced by a rocket due to exhaust gases. Once vapor recoil hits the droplet surface, a severe perturbation is set in motion. This results in the formation of a surface crater surrounded by a crown of liquid fingers which are subjected to thinning and break-up (**Figure 3.5**, **Video 3.2**). Further, a high-speed ligament emerges from the collapse of this surface crater and undergoes tip break-up generating daughter droplets. This cycle is repeated throughout the droplet lifespan.

Local instabilities exhibited by droplets of ethanol as well as ethanol-hydrocarbon blends have been reported in many studies [6], [76]. Explanations such as rapid vaporisation and internal boiling of ethanol are suggested for the catastrophic droplet rupture. However, a quantitative analysis of such instability is not presented in these past investigations. Therefore, a first order analysis of forces responsible for initial droplet break-up is presented. To quantify confined instabilities, a modified local weber number (We_{local}) is defined as

$$We_{local} = F_{recoil}/F_{st} \tag{3.13}$$

where F_{recoil} is the vapor recoil force exerted on droplet surface given as,

$$F_{recoil} = P_{recoil}4\pi r_{local}{}^2 \tag{3.14}$$

$$P_{recoil} = \eta^2 \left[\frac{1}{\rho_v} - \frac{1}{\rho_l}\right] \tag{3.15}$$

where P_{recoil} is the vapor recoil force per unit area [75], η is the local mass evaporation rate [75] (per unit time and interface area). Mass evaporation rate (η) is calculated for locally perturbed region (for which the estimated time scale is $\sim O(10^{-4}\ seconds)$). This approach of quantifying local forces through local weber number has been employed to understand hydrodynamic stability and interface shape of liquid sheets [77], [78].

Local resistive force i.e. surface tension force F_{st} is given as

$$F_{st} = 2\pi\sigma r_{local} \tag{3.16}$$

In equations (3.14) and (3.16), $r_{local} \sim O(10^{-1}\ mm)$ (found through image segmentation technique) represents local perturbation length scale **Figure 3.5I**). For EW droplets, We_{local} is found to be $\sim O(10^1 - 10^3) \gg 1$. Therefore, superficial

instabilities are generated in the form of surface craters on EW droplets (as shown in **Figure 3.5I**)

On the other hand, droplets with nanoceria exhibit formation of vapor bubble mushrooms (Fig. 3.4II). Experimental observations reveal that either these nucleates grow and traverse to the free surface, or multiple bubbles coalesce to form a bigger bubble before ejecting. Using particle tracking technique of Mosaicsuite of Imagej software [79], bubble velocity (V_b) is found $\sim O(10^{-2} - 10^{-1} \, m/s)$ (**Video 3.3**). Two possible mechanisms lead to droplet surface rupture; (i) surface shearing of smaller bubbles $(d_b \sim O(0.1d_0 - 0.2d_0))$ as it advances to liquid-air interface and (ii) growth rate $\sim O(10^{-2} \, m/s)$ of large bubbles $(d_b \sim O(0.4d_0 - 0.6d_0))$. In either case, thinning of bubble-liquid boundary punctures the droplet surface (explained in detail by [44]). Puncturing leads to the formation of a hollow cavity. This cavity serves as the triggering mechanism for liquid jet formation as discussed in the next section.

(b) Ligament inception, growth and tip-break-up

Previously, it has been established that imbalance between surface tension and vapor thrust results in surface undulations on EW droplets. A pressure difference $(\Delta P = \sigma/r_{local})$ arises due to interfacial curvature of formed crater (**Figure 3.5**) [80]. Vicinal liquid surges into this low-pressure crater forming a high-speed ligament. Note that as shown in **Figure 3.5**, formation of a single crater is not an isolated phenomenon. Thus, the formation mechanism of this ligament is volume stretching under pressure forces. Energy balance suggests that work done for stretching should scale to the acquired kinetic energy (KE_{lig}) of the ligament. Hence, for a single jet formation, it is reasonable to evaluate a theoretical ligament velocity $\left(v_{lig}\big|_{th}\right)$ by considering residual energy $(E_{residual})$ required for ligament growth.

$$E_{residual} \sim \Delta P * \Delta V_{crater} \tag{3.17}$$

$$KE_{lig} = 0.5 m_{lig} \left(v_{lig}\big|_{th}\right)^2 \tag{3.18}$$

Equation (3.17) represents energy available due to the collapse of local crater $(\Delta V_{crater} = 2\pi r_{local}{}^3/3$, considering hemispherical geometry of the crater) for

ligament elongation [51], [53]–[55], [80], [81]. Equation (3.18) represents the kinetic energy acquired by the ligament. Mass of ligament is given by $m_{lig} = \pi \rho_l L_{lig} r_{lig}{}^2$, r_{lig} is the radius of ligament $= (W_{lig}/2)$. Considering energy balance

$$0.5 m_{lig} \left(v_{lig}\big|_{th} \right)^2 \sim \Delta P * \Delta V_{crater} \tag{3.19}$$

$$v_{lig}\big|_{th} \sim \sqrt{\frac{4\sigma r_{local}{}^2}{3\rho_l L_{lig} r_{lig}{}^2}} \tag{3.20}$$

The above approach is similar to multiple studies encompassing break-up dynamics of levitated droplets [82] as well as phenomenology of droplet breakup on vibrating substrate [80]. For a statistical estimate of ligament velocities, a normalised velocity variation i.e. $v_{lig}/v_{lig}\big|_{th}$ is presented in **Figure 3.6(a)**. For $W_{lig} \sim (20-100)\mu m$ and $L_{lig} \sim (100-600\ \mu m)$, theoretical and experimental velocities for most cases turn out to be of the same order. Hence, the theoretical ligament velocity closely imitates experimental value. This resemblance suggests that interfacial pressure perturbations on droplet surface induce ligament inception. The ligament aspect ratio $AR_{lig} = L_{lig}/W_{lig}$ at pinch-off point is found $> \pi$ which suggests Rayleigh-Plateau jet breakup mechanism.

Mechanism of surface crater formation further leading to ligament formation differs for nanofuel and EW droplets. For EW droplets, ligaments are ejected from craters. Contrastingly, for nanofuel droplets, hollow cavities due to bubble rupture are responsible for ligament formation. Therefore, r_{local} in nanofuels should be scaled with r_b (bubble radius before ejection) in Equations 3.17-3.20. Thus, for nanofuel droplets, equation (3.20) becomes

$$v_{lig}\big|_{th} \sim \sqrt{\frac{4\sigma r_b{}^2}{3\rho_l L_{lig} r_{lig}{}^2}} \tag{3.21}$$
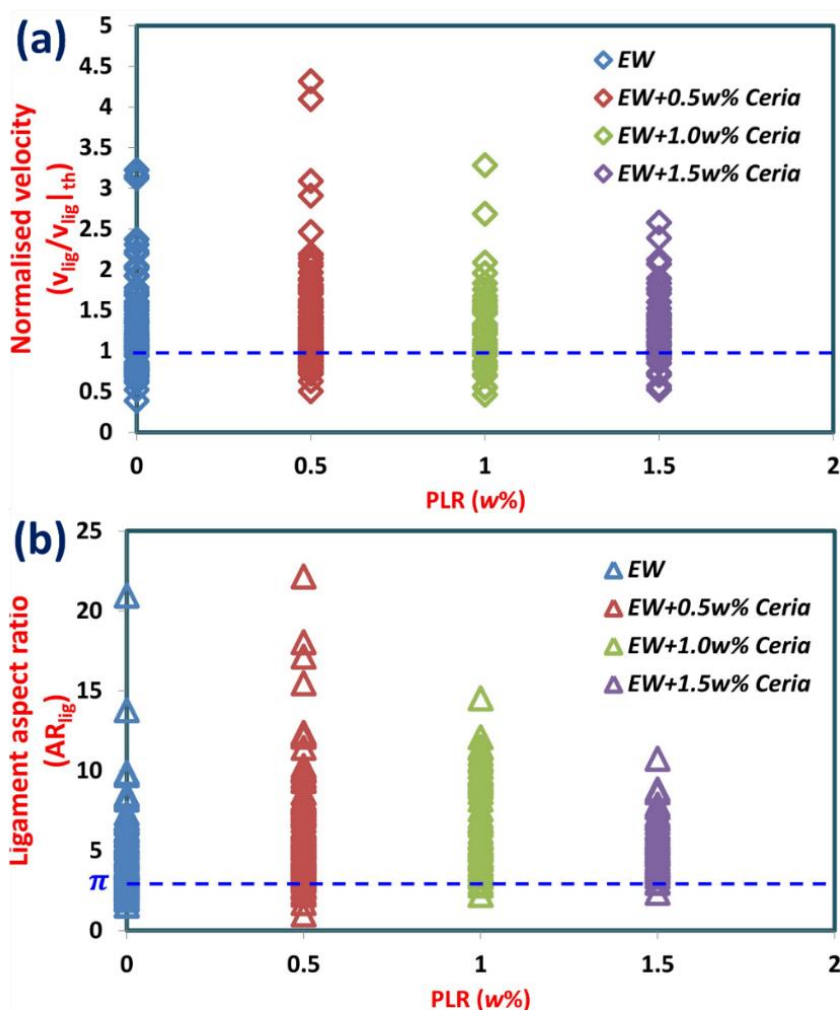
Figure 3.6. (a) Normalised velocity of ligaments for different particle loadings of ceria NPs. Experimental and theoretical value are of the same order. (b) Aspect ratios of ligaments for different PLRs. For most cases $AR_{lig} > \pi$, suggesting their Rayleigh-Plateau break-up.

Note that addition of ceria NPs and their subsequent agglomeration dynamics increases the nanofuel density. However, these variations are difficult to estimate. Hence, for first order analysis, these density variations are overlooked. Variation of normalised velocity with PLR is depicted in **Figure 3.6 (a)**. Theoretical and experimental velocities are of the same order for nanofuels like in pure EW droplets. Moreover, for most cases, $AR_{lig}\big|_{NPs}$ also turns out to be $> \pi$, implying Rayleigh-Plateau breakup (**Figure 3.6 (b)**).

3.5 Droplet shape and flame: A coupled system
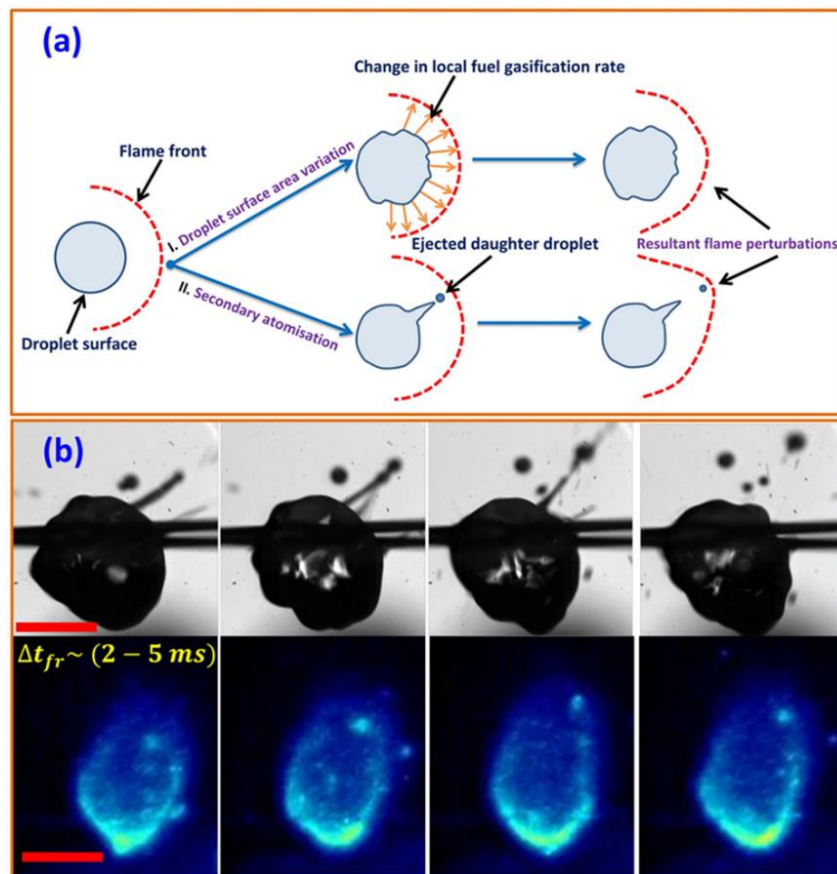
Figure 3.7. (a) Oscillations of droplet surface area and secondary atomisation alter the rate of fuel transport to the flame envelope. These surface events are felt as change in the flame standoff and fluctuations in spatial HR. (b) High speed (10,000 fps) images of EW droplet ejection events. A time lag (Δt_{fr}) exists between surface and flame events. Scales represent 0.5 mm and 5 mm respectively. (Video 3.4)

Section 3.3 discusses the droplet vaporisation mechanism and its variation with nanoceria inclusion. Furthermore, it has also been discussed that additional mass loss occurs with daughter droplet ejections (**Section 3.4**). Eventually, both are pertinent factors for the flame HR. **Figure 3.7(a)** depicts two different surface events that perturb the flame front; **I.** Variation of droplet surface area and (as discussed in **section 3.3** and **3.4**) **II.** Secondary atomisation (mechanisms are described in **section 3.4**). Undulations of fuel-air interface arising from internal boiling and Marangoni convection locally alters the surface area as well as the diffusive length that has to be overcome by fuel

vapor for reaching the flame front. In addition, ejected daughter droplets act as transporters of fuel parcels to the flame front. For both cases, perturbations in the amount of fuel reaching the flame is reflected through oscillations in flame area and temporal variation of spatial HR. Flame response is usually observed after a certain time scale (Δt_{fr}), as evident in **Figure 3.7(b)**. This discussion provides a heuristic understanding of droplet shape and flame coupling. Ejection events and their timings seem to be stochastic, but they cumulatively contribute to the flame fluctuations.

Previous studies [25], [83], [84] on droplet combustion with and without NPs have extensively reported temporal variation of $(d/d_0)^2$ and AR_d. However, burning of a multi-component/multiphase droplet is a composite problem of numerous spatio-temporal instabilities transpiring due to internal boiling, flame and droplet interactions and breakup to name a few. These physical phenomena manifest their presence at different length and time scales. Hence, exclusively considering the temporal history of either $(d/d_0)^2$ or (AR_d) reduces the system from multi-to-single degree of freedom. In the present study, $(d/d_0)^2$ and (AR_d) are inadequate to capture transient events such as instantaneous droplet rupture/ejections. Therefore, for meticulous investigation of instability evolution/decay due to NP addition, a multi-degree freedom model needs to be utilised. Proper Orthogonal Decomposition (POD) is a data reduction method which provides low dimensional approximations of high-dimensional processes [85]. It has been extensively utilised to study dynamic systems such as turbulent flows [86], interactions of air and liquid in swirl flows [87]**,** and combustion analysis using Particle Image Velocimetry (PIV) data [88]. It unveils the shape of dominant modes which is the reason for its applicability in fundamental investigations of droplet dynamics on vibrating substrate [89], jet flapping in cross-flow and deciphering intricate spray structures.

Currently, method of snapshots is utilised to evaluate the spatial modes. POD analysis serves two major purposes; a.) It enables us to detect the major coherent modes that constitute the droplet shape or the flame heat release as the case maybe; b.) POD ascertains the causality between droplet shape and flame heat release i.e. the degree of coupling. POD is performed on binary droplet images. Post-processed binary images are necessary to eliminate interference from the suspension wire. Zero-pixel value

represents the presence of droplet whereas unity valued pixels serve as background. POD approximates the data matrix $U \equiv u(i,j)$ (where i $(1,..,M)$ is the pixel number and j $(1,..,N)$ is the number snapshots) into summation of orthogonal spatial modes (φ_k) weighed by their temporal coefficients (a_k) (for $r \leq N$) given as

$$u(i,j) = \sum_{k=1}^{r} \varphi_k(i)a_k(j) \tag{3.23}$$

The spatial modes/basis vectors and the temporal coefficients are found by solving the eigen value problem, $CV = \lambda V$ as described in [89], where C is the temporal correlation matrix given as

$$C = \frac{1}{N}U^T U \tag{3.24}$$

Basis vectors of the decomposition in terms of kth eigenvalue (λ_k) and eigenvector (v_k) of C are given as

$$\varphi_k = \frac{1}{\sqrt{N\lambda_k}}Uv_k \tag{3.25}$$

and the respective temporal coefficients are given

$$a_k = \sqrt{N\lambda_k}v_k \tag{3.26}$$

Modal energy fraction related to r_{th} mode is represented as

$$x_e = \frac{\lambda_r}{\sum_1^r \lambda_r} \tag{3.27}$$

Energy fraction is utilised to estimate the essential number of modes required for droplet shape description.
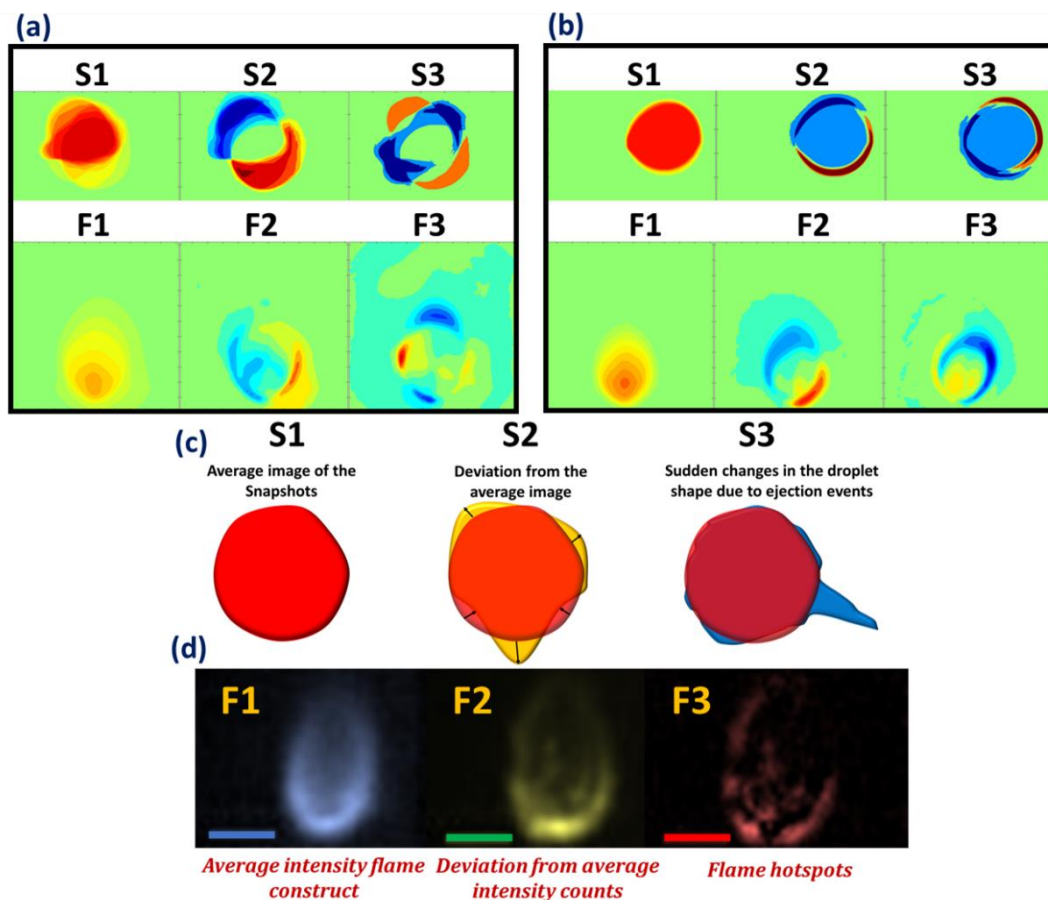
Figure 3.8 Coherent POD structures of droplet shape (S) and flame (F) for (a) EW droplets, and (b) PRL w = 1.5%, (c) First mode (S1) represents the average image of snapshots, S2 is the representation of volumetric stretching and S3 is the sudden change in droplet shape. Colour bar represents the intensity of spatial modes. (d) Physical representation of each mode. Scale bar represents 5mm. Colour bar represents the intensity of modes.

Figure 3.8(a) and (b) illustrates the principal modes of droplet shape (**S**) and flame (**F**) HR oscillations for both EW droplet and as well as for nanofuel with PLR $w = 1.5\%$. Three principle modes (for both droplet shape and flame) with cumulative energy fraction of ~99% are considered for the present study. Droplet shape modes (**Figure 3.8(c)**) contribute to different geometric attributes of the combusting droplet; Principle mode **S1** represents the average shape of the droplet across all the snapshots, **S2** represents the recurring deviations from the mean shape due to volumetric fluctuations which manifest as non-uniform stretching, and **S3** captures sudden changes in the droplet shape due to instantaneous ejection events at random locations. Furthermore, for the present experimental study, flame is a global construct of pixels

with differential intensity counts due to OH* chemiluminescence. The spatio-temporal variation of intensity counts enables instantaneous and average spatial HR calculations. Therefore, for computing POD modes of the droplet flame, tagged image file format (TIFF) of flame images are used and the rest of the POD algorithm remains the same (as described for the droplet shape shape). Principle flame mode **F1** provides the flame construct with mean pixel intensity, **F2** represents the deviation of snapshots from average image, and **F3** addresses the flame hotspot regions (**Figure 3.8(d)**).
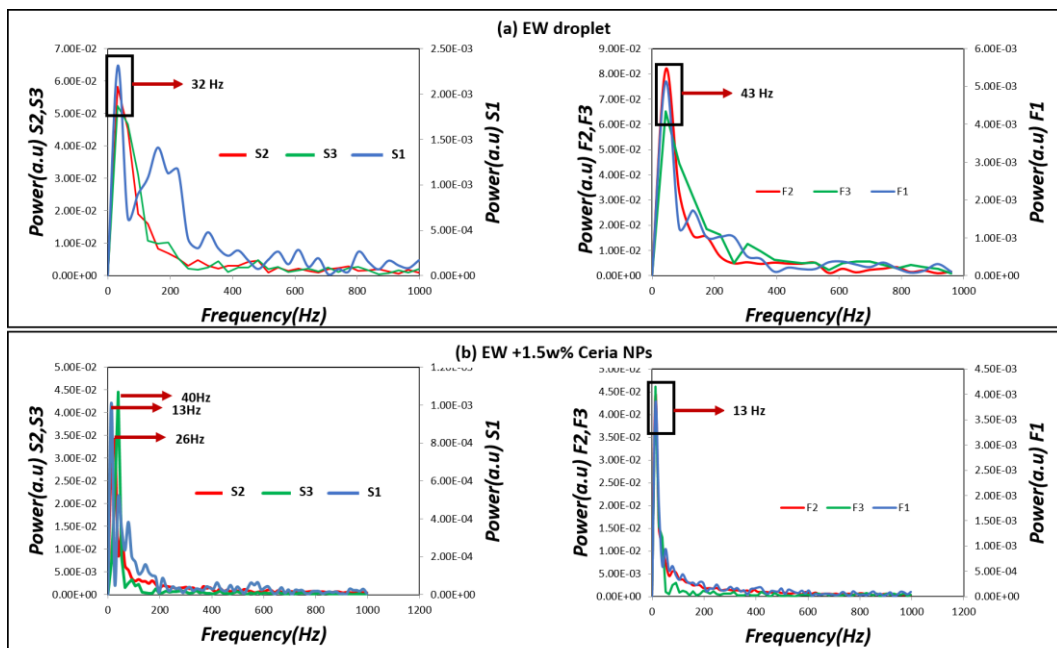
Figure 3.9. The frequency of oscillation of the principal modes of the droplet shape (S) and flame (F) for (a) Pure ethanol-water droplet, and (b) PLR $w = 1.5\%$. at $t = 0.2t_{total}$.

In the current scenario, NPs inhibit the fuel evaporation rate leading to increased burning time and reduced average HR. Undoubtedly, different droplet surface phenomenon affect the flame and spatial HR. The interplay between droplet shape and flame dynamics can be ascertained using POD temporal coefficients. Temporal coefficient (a_r) of r_{th} mode can provide insights into establishing a causality between shape and HR fluctuations. Variation of a_r for droplet shape and flame heat release is depicted in **Figure 3.10**. Temporal coefficient $a_1|_{shape}$ and $a_1|_{flame}$ are in-phase with same values ($\sim 0.05 \pm 0.02$) throughout the EW droplet lifecycle (**Figure 3.10(a)**). On the contrary, $a_2|_{shape}$ and $a_2|_{flame}$ are out of phase with each other. As a_2 is

associated with deviation of data from mean value, out of phase behaviour of shape and flame indicates a lag in flame response to droplet surface perturbation. To validate our conjecture, phase lag ($\Delta\theta$) is calculated by fitting a sinusoidal curve through temporal data corresponding to a_r. Values of $\Delta\theta$ varies~$(0.2 - 0.3)$ $radians$ (**Figure 3.10(a)**). Time scale (given as $\Delta\theta/2\pi f$, where f is the frequency of oscillation) corresponding to this lag $\sim O(10^{-3}) seconds$. The fuel parcels in the form of daughter droplets are ejected at a velocity of V_{dd} , therefore, time taken to traverse the flame stand-off distance (R_f) is give as R_f/V_{dd} which is found to be $\sim (2 - 5\ ms)$ and matches with the aforementioned phase-lag timescale . Furthermore, the principal modes of EW droplet shape and flame HR have similar frequency signatures, 32Hz and 43Hz, respectively (**Figure 3.9(a)**). Hence, the droplet shape and HR together emulates a synced system where shape oscillation is the driver and spatial HR is the driven entity. Note that the described combustion characteristics are consistent throughout the EW droplet lifecycle.
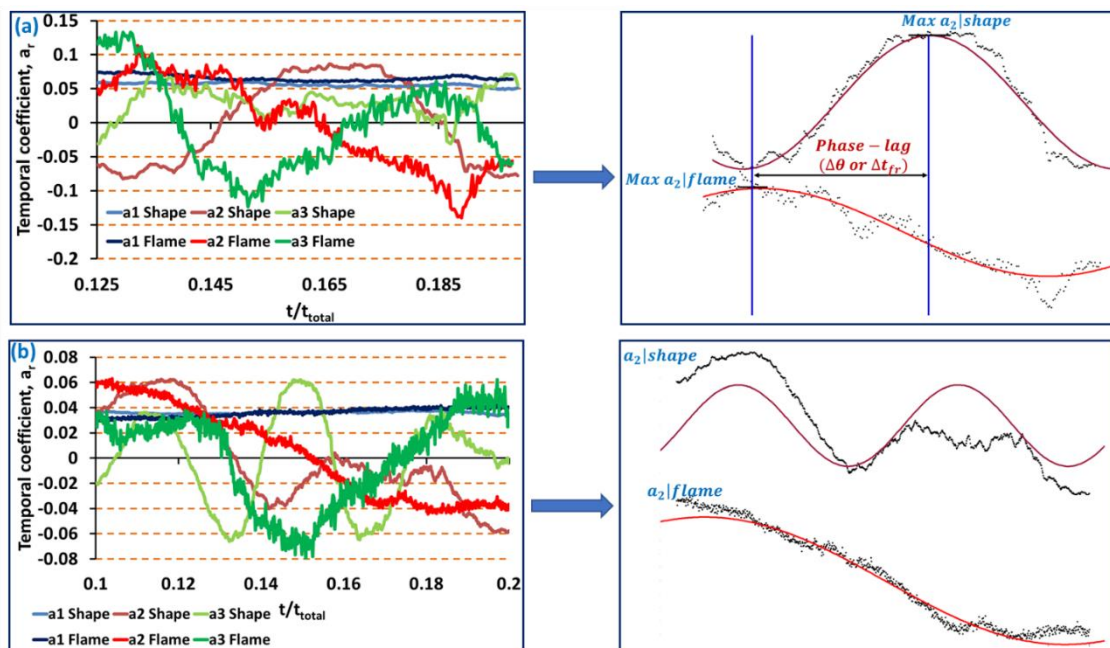
Figure 3.10. (a) Variation of POD temporal coefficients of EW droplet shape and flame at $t = 0.2t_{total}$ (b) Variation of POD temporal coefficients of droplet shape and flame for PLR $w = 1.5\%$ at $t = 0.2t_{total}$.

For nanofuels, across all PLRs, $a_1|_{shape}$ and $a_1|_{flame}$ have similar signature throughout droplet lifecycle (**Figure 3.10(b)**). However, the fluctuations of a_2 and a_3 corresponding to droplet shape are not reflected in their respective flame modes ($a_2|_{flame}$ and $a_3|_{flame}$). As shown in the **Figure 3.10(b)** for PLR $w = 1.5\%$, multiple troughs and crests are evident in $a_2|_{shape}$ which is not depicted in $a_2|_{flame}$. Additionally, the maximum amplitude of all the temporal modes, $a_r|_{shape}$ and $a_r|_{flame}$ shows a decrement ($\sim 50\%$). This signifies lower energy content of nanofuel as compared to EW. Further, it justifies our experimental observation of arrested surface undulations and suppressed ejection events for nanofuel droplets (**Video 3.5**). The incoherency is also depicted in the spectral response of the modes (**Figure 3.9(b)**). The first principal mode S1 and F1 oscillate at the same frequency of 13 Hz, suggesting a sync between the average droplet shape and flame HR. However, the flame responses (F2 and F3) to surface perturbances/ejection events (S2 and S3) do not exhibit similar frequencies (**Figure 3.9(b)**). Therefore, the flame remains insensitive to the droplet surface perturbations throughout the nanofuel combustion lifetime.

3.6 Conclusion
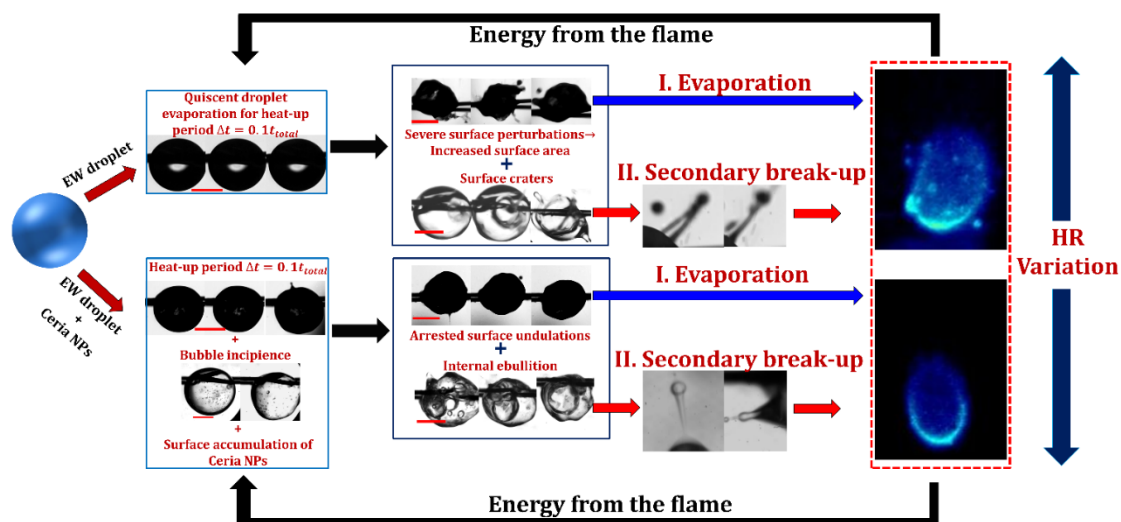
Figure 3.11. Schematic representation of droplet shape and flame interplay. The surface perturbations change the droplet surface area subjected to the flame whereas, daughter droplets are responsible to the additional mass loss. Cumulatively both are dominant parameters for defining the flame HR.

Change in combustion characteristics of ethanol-water blend with NP addition is elucidated in the present work encompassing three sections; **(i)** burning time scale, **(ii)** secondary atomisation pathways, and **(iii)** droplet shape and flame HR coupling. Increased burning time with PLRs i.e. $t_{total}|_{NPs} \sim (2 - 2.5)t_{total}|_{EW}$ is one of the key findings of the present work, which indicates change in evaporation dynamics of EW droplets with addition of ceria NPs. Hence, the mechanism of fuel evaporation through porous media for nanofuels is advocated. Evaluated $t^*|_{NPs}$ approximates experimental t_{total} within $\sim(2.0\%)$ error for all PLRs. Time scale calculations from a semi-analytical standpoint suggest that classical d^2- law solely cannot predict these variations. As such a combination of Darcy's law and pure fuel evaporation, each with proper weightage is necessary for droplet burning time approximation. EW droplets undergo severe fragmentation due to the action of vapor recoil forces. This mechanism of secondary atomisation has been elucidated using a modified Weber number. The action of vapor recoil forces creates surface craters, generating high-speed liquid ligaments. These ligaments ultimately undergo Rayleigh-Plateau break-up at the tip ($AR_{lig} > \pi$). However, for NP laden droplets, expulsion of vapor bubbles is responsible for the formation of surface cavities. Mechanism of ligament formation and break-up remains similar as EW droplets albeit with different length scales. The theoretical and experimental ligament velocities are found to be of the same order using scaling analysis. Further, to account for the multi-dimensional nature of droplet shape and flame HR fluctuations, POD technique is utilised. Addition of NPs results in low energy content of spatial modes. For EW droplets, the evolution of temporal coefficient of droplet shape and flame modes establishes a correlation between the same albeit with a phase lag (time scale, $\Delta t_{fr} \sim (2 - 5\ ms)$). Contrarily, low energy content of shape modes of NP laden droplets impedes their synced- response with flame modes.

To summarize, the current work encompasses the inextricably linked mechanisms of evaporation, particle aggregation, internal boiling, surface deformation/secondary atomisation and flame heat release of functional droplets. **Figure 3.11** represents a schematic representation of the interlinked system of droplet evaporation, atomisation and flame HR. Pathway **I** represents the droplet evaporation process, where droplet is heated by the flame and vaporised. Further, the fuel vapor is consumed at the flame front releasing combustion energy. On the other hand, Pathway **II** illustrates the

mechanism of internal heterogeneous boiling which aids in droplet secondary atomization. The ejected daughter droplets travel and eventually vaporise at the flame front leading to further heat release. Both pathways simultaneously affect the combustion energy release rate (flame heat release) which in turn affects the droplet gasification rate (**Figure 3.11**).

Chapter 4

How Boiling Happens in Nanofuel Droplets

The previous chapters (**Chapter 2** and **Chapter 3**) demonstrate the combustion and vaporisation dynamics of nanofuel droplets in pendant mode. Burning droplets of the order of millimetres suspended over cross-wires [6], [18], [83], [84], [90] and single filaments (either horizontal or vertical) have been thoroughly investigated in the literature. These studies have provided fundamental insights about droplet burning, shape oscillations [23] and coupling of droplet deformations and heat release [44]. However, the presence of wire effects on both the total heat transfer as well as the nucleation dynamics and breakup in such pendant droplets.

Thereby there is a need to pursue the same investigations in a contactless environment. The plethora of available literature suggests that pendant nanofuel droplets undergo severe shape oscillations and exhibit vigorous boiling due to internal ebullition. However, it is still not conclusive whether the boiling is solely due to the wire or NP aggregates acting as hot spots. Pathak et al. [30] reported the existence of a critical PLR and input heat flux for the vapour bubble formation. However, it did not provide a quantitative criterion or the mechanism of internal boiling in such nanofuel droplets. Furthermore, the cited work is also confined to a single type of base-fuel thereby neglecting the role of vapor pressure (high or low) in determining the atomization modes. Therefore, the current work of acoustically levitated pure and NP laden droplets is extended to two types of base-fuels (ethanol and n-dodacane) under external radiative heating. Ethanol and dodecane correspond to high and low vapor pressure fuels respectively. Base fuels are seeded with Ceria NPs at dilute particle loading rates (PLR) between $0 - 0.5$ % by weight. Dilute NP loading ensures better nanofuel suspension stability. Reported work focuses on exploring the basal differences arising in evaporation and atomisation characteristics of two different fuels with NP inclusion. The present work particularly emphasises on the mechanism of internal boiling and the corresponding time scales necessary for the same. In particular, it is shown that by incorporating the combined effects of NP aggregation, formation of nucleation kernels, bubble incipience and growth, one can propose a timescale that can uniquely predict the

propensity of a nanofuel droplet to undergo internal ebullition. Interestingly, such a timescale will also predict the minimum droplet size that is required for boiling for any given PLR and external heating rate. Furthermore, this chapter is aimed to provide a conclusive answer to the role of wire in determining the atomization mode of a heated nanofuel droplet [91].

The paper is structured in the following way. Evaporation and atomisation dynamics of pure and particle laden droplets is elaborated in **Section 4.2** (**Figure 4.2** and **Figure 4.3**). **Figure 4.4** depicts the differences in the evaporation and atomisation modes of functional droplets with ethanol and dodecane as base fuels. **Section 4.4.1** offers physical insights into droplet stability (for understanding the precursor stage of droplet break-up, **Figure 4.6**). Secondary atomisation of pure and particle laden fuel droplets is described in **Section 4.4.2**. Atomisation mode involving catastrophic break-up is elucidated through modified weber number (We) (**Figure 4.7**). Droplet fragmentations through internal boiling are presented in **Section 4.4.2** (**Figure 4.9-4.12**). In particular, different types of bubble ejection events either at droplet pole or equator leading to significant surface/volumetric perturbations are explained. These occurrences are explained in **Section 4.4.2 (b)** which were not presented before in [17]. **Section 4.4.3** presents the time scale analysis for bubble incipience criterion for NP laden ethanol and DD-droplets. Lastly a unique three-dimensional regime map is proposed which connects the droplet breakup modes with PLR, heating rates and drop size (**Figure 4.15**). II. Experimental Methodology

4.1 Experimental Methodology

(a) Nanofuel preparation

Two base fluids, ethanol (research grade with 99.9% purity) and n-dodecane (99.9% purity) with substantial difference in vapour pressure are considered. Nanoparticles (NPs) of cerium oxide (Ceria, Ce_2O_3) with average particle diameter (d_p) of 25 nm procured from Sigma-Aldrich are dispersed in chosen base fuels. Thermophysical properties of base fuels and ceria NPs are tabulated in Table1. NP PLR varying between $(0 - 0.5\%)$ by weight (volume percentage 0-0.095 vol%) are considered. Stable

nanofluids are obtained by dispersing ceria NPs in ethanol by ultrasonication for 30 minutes (15 s alternate ON/OFF cycles of Trans o sonic D120/P model). Ethanol being a polar fluid tend to provide a better nanofuel stability without steric or electrostatic stabilisation. On the contrary, NP dispersion in n-dodecane requires steric stabilisation. Hence, a non-ionic surfactant with HLB value 11; Tween 85 (procured from Sigma-Aldrich) is incorporated during the preparation of n-dodecane based nanofuels. Proper capping of NPs with long chain surfactant inhibits their aggregation. Therefore, firstly, Tween 85 is added to Ceria NPs in 2:1 weight ratio and stirred forming a viscous fluid. N-dodecane is then added and the resultant mixture is subjected to ultrasonication for 30 minutes. Obtained nanofuels have shown considerable stability well beyond the experimental time scale.

	Molecular weight (g/mol)	Vapour Pressure (@ 25^{0}C)	Density (kg/m3)	Surface tension (mN/m @ 25^{0}C)	Boiling Point (^{0}C)
Ethanol [92]	46.07	5.3 kPa	789	22.5	78.2
N-dodecane [44]	170.33	17.65 Pa	750	25	216.2
Cerium oxide	172.114	-	7130	-	3500

Table 4.1. Physical Properties of the base-fuels and ceria nanoparticles

(b) Experimental Set-up

Droplets of size range $d_0 \sim (300 - 500)\mu m$ are acoustically levitated (Tec5 levitator, 100 kHz frequency, 154 dB). Sample liquids are introduced at the pressure node of the levitator using a syringe needle of inner diameter $\sim 0.45 mm$. Droplets are stabilised at the pressure node by adjusting the separation distance between reflector and transducer plates. Continuous CO_2 laser (Synrad 48, beam diameter ~ 3.5 mm, wavelength

$\sim$10.1μm μm, max power $(P_{max})\sim30$ Watts) is utilised to radiatively heat the droplets at multiple rates varying between $\sim(50\% - 90\%)P_{max}$ $\sim(1.05 - 1.89)MW/m^2$. Droplet shape oscillations are captured by weak back-illumination of the droplets with white light (Schott LLS) and high speed shadowgraphy (Phantom Miro 110) at 10000 fps with pixel resolution of 512X320 (spatial resolution of 4 μm/pixel) (**Figure 4.1**). Concurrently the droplet surface temperature is monitored through an IR camera (FLIR SC5200) at 566 fps. Additionally, internal dynamics of droplets are visualised at 5000 to 10000 fps through volumetric illumination by placing a diffuser in front of the
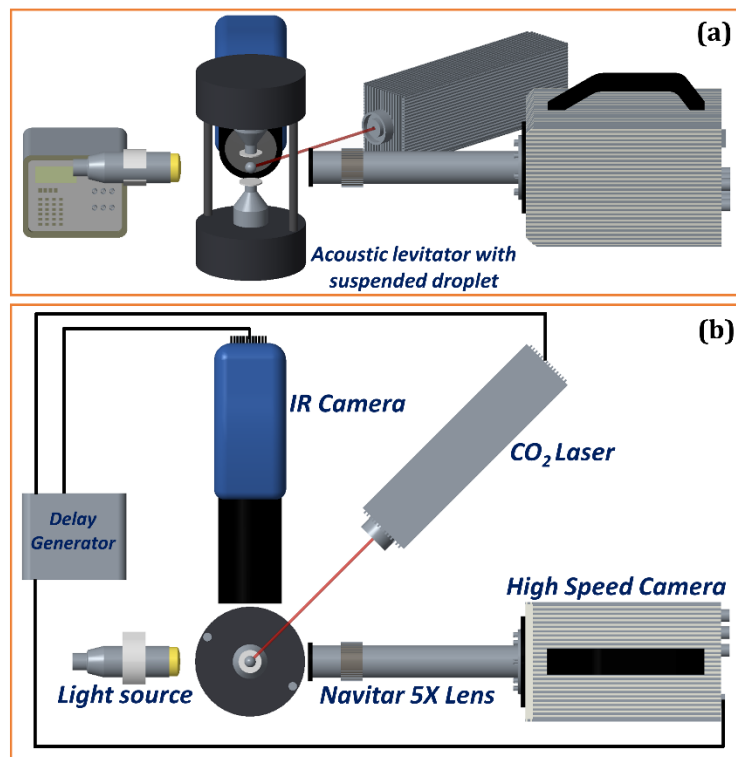
Figure 4.1. Schematics of the experimental set-up (a) Isometric view and (b) Top view. Simultaneous shadowgraphy (using high speed camera) and thermography (with IR camera) of the levitated droplet. All the equipments are synced using a delay generator.

light source (pixel and spatial resolution of 512X320 and 4 μm/pixel, respectively). Temporal history of volume-equivalent droplet diameter (d) regression is given as

$$\frac{\pi}{6}d^3 = \frac{4\pi}{3}a^2b \qquad (4.1)$$

Where a and b are semi-major and semi-minor axes of the droplet, extracted by converting the acquired gray scale images to binary format using Otsu thresholding technique [46].

4.2 Evaporation dynamics of pure and particle laden droplets
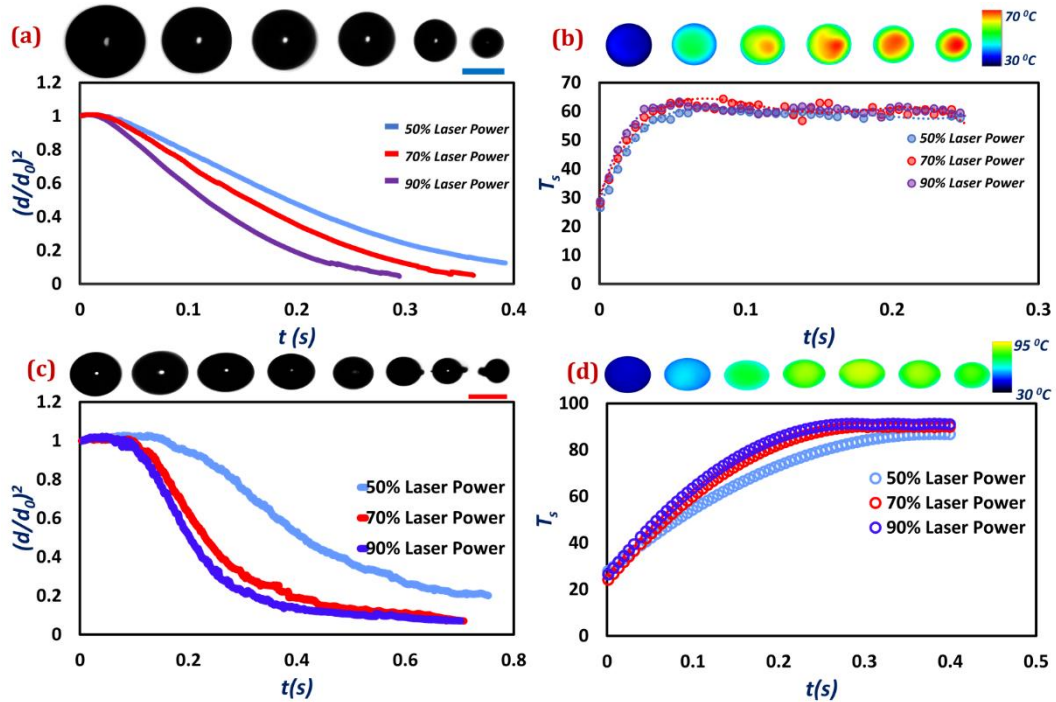
Figure 4.2. (a) Temporal variation of pure ethanol droplet diameter at different laser powers, (b) Temporal history of pure ethanol droplet temperature, (c) Temporal variation of pure dodecane normalised droplet diameter at different laser powers, and (d) Temporal history of pure dodecane droplet temperature. Scale bar represents 250 μm.

Figure 4.2(a) and **(b)** present the temporal history of pure ethanol droplet evaporation. Ethanol droplets with $d_0 \sim (300 - 500 \, \mu m \pm 10 \, \mu m)$ vaporise with two distinct, temporally resolved stages, Stage I; transient heat-up period $\Delta t \sim 0.1 \, \tau_{total}|_E$ ($\tau_{total}|_E$ is ethanol droplet lifetime) where entire absorbed irradiation goes into heating the droplet to the wet-bulb temperature ($T_s \sim 57 \pm 1 \, ^0C$) and Stage II; droplet evaporation proceeds at steady rate with constant surface temperature (T_s). Droplets of low vapour pressure fuel, n-dodecane, on the other hand vaporise at relatively placid rate $\sim O(10^{-8}) kg/s$ (**Figure 4.2(c)**). Evaporation characteristics for DD droplets are similar to pure ethanol for $d_0 < 450 \, \mu m$, Stage I; initial heating period of $\Delta t \sim 0.30 \, \tau_{total}|_{DD}$(

$\tau_{total}|_{DD}$ is evaporation time of pure dodecane droplets) and Stage II; at this stage dodecane (DD) droplets acquire a constant wet-bulb temperature ($T_s \sim 86 \pm 4$ ^{0}C) (**Figure 4.2(d)**). With increase in laser power, the total evaporation timescale (τ_{total}) of pure ethanol and DD droplets decreases (**Figure 4.2**). However, evaporation dynamics remain the same.   Droplets of pure ethanol vaporise at a faster rate $O(10^{-7})kg/s$ (nearly an order faster than pure DD droplets) due to the high vapour pressure of ethanol ($\sim$ 5.3 kPa @ 25^0c).
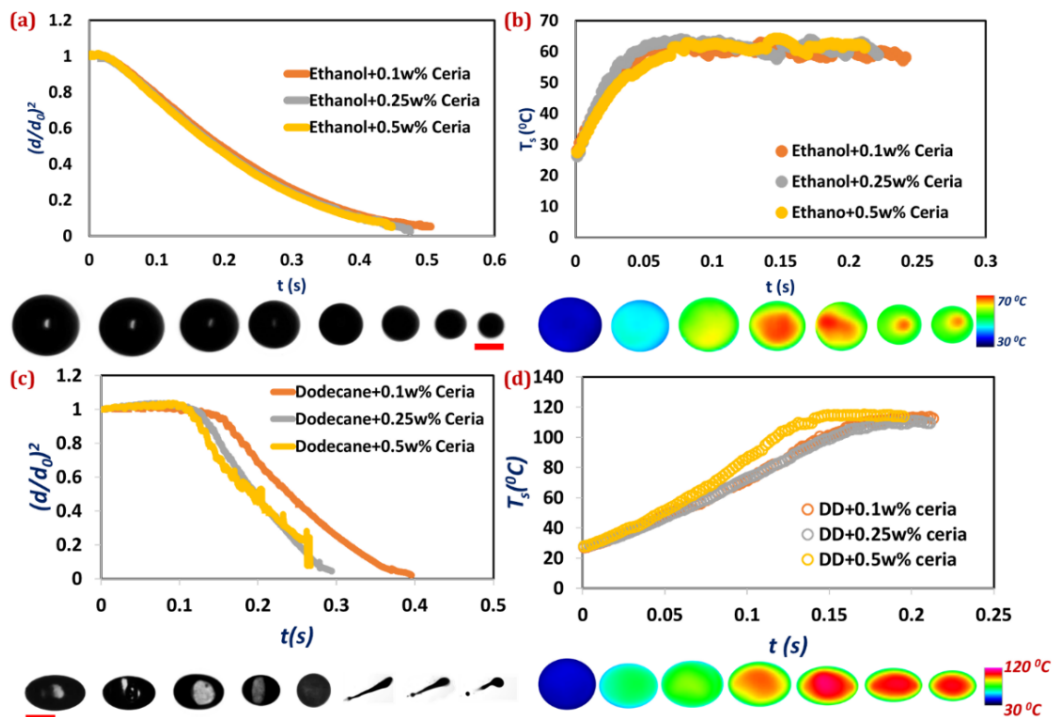
Figure 4.3. (a) Temporal variation of ethanol-based nanofuel droplet diameter for different PLRs at 1.05 MW/m2 laser power, (b) Temporal history of ethanol-based nanofuel droplet temperature, above trends are similar with increase in laser power. (c) Temporal variation of dodecane-based normalised droplet diameter (d_0<450μm) at 1.47 MW/m2 laser power for different PLRs, and (d) Variation of dodecane-based nanofuel droplet temperature. Scale bar represents 250 μm.

NP laden ethanol droplets exhibit strikingly similar evaporation characteristics to pure ethanol.   Total nanofuel droplet evaporation time remains nearly unaltered with NP addition i.e. $\tau_{total}|_{E+NPs} \sim \tau_{total}|_E$ with $\pm$ 10% variation.   Wet-bulb limit attained by nanofuel droplets also follows the same trend as pure ethanol. Effect of NP loading

(PLR) shows negligible influence on evaporation rate and surface temperature (**Figure 4.3(a)** and **(b)**).

However, DD droplets seeded with ceria NPs exhibit enhanced vaporisation rates. Observations reveal that increase in initial NP loading reduces total droplet lifetime to nearly half of pure dodecane i.e. $\tau_{total}|_{DD+NPs} \sim 0.5\, \tau_{total}|_{DD}$ (**Figure 4.3(c)**), at a given laser power. Nanofuel droplets attain an elevated wet-bulb temperature $\sim (112 \pm 3)^0 C$ at an enhanced rate of $dT/dt \sim (730 - 1150)^0 C/s$ (**Figure 4.3(d)**). Faster heat-up period followed by enhanced vaporisation stage suggests increase in heat absorption due to particle addition.

4.3   Atomisation dynamics of pure and nanofuel droplets

Atomization dynamics of ethanol and DD droplets are significantly different. Normally it is expected that atomization dynamics would be a function of PLR, initial droplet size (d_0), and laser power (I_{laser}) (heating rate). However, pure as well as particle laden ethanol droplets do not exhibit any secondary atomisation (**Figure 4.3(a)**) across all operating conditions. On the other hand, pure DD droplets exhibits continuous pinching of daughter droplets at the equator for all size ranges. In addition, DD droplets over a critical size $d_c \sim 450\,\mu m$, undergo a continuous cycle of catastrophic shattering (explained later) for all laser powers.

Droplets of DD-based nanofuel exhibit additional interesting observations. DD nanofuel droplets below a minimum diameter (d_{boil}) (which varies with PLR and laser heating rates), undergo pure evaporation (PE) coupled with continuous disintegration of mother droplet at equator (similar to their pure fuel counterpart). However, in the size range; $d_{boil} < d_0 < d_c$ (**Figure 4.3(c)**), secondary atomisation (SA) is ensued through internal boiling (IB) and subsequent bubble rupture. Increase in I_{laser} and consequent decrease in droplet lifetime controls this internal ebullition dynamics. Timescales required for NP aggregation, bubble nucleation and growth are not achieved when droplet lifetime is relatively shorter. Hence, d_{boil} shows an increase of $16 - 50\%$ with increase in I_{laser} for different PLRs $< 0.5 w\%$. Interestingly, beyond a critical size, $d_0 > d_c$ (where $d_c \sim 450\,\mu m$), DD based nanofuel droplets undergo acoustic flattening

and eventual catastrophic breakup (CB)) irrespective of PLR and laser heating rates (similar to pure DD).

A comparative analysis of the two sets of experiments (I. ethanol and II. dodecane as base fuels) exhibits numerous peculiarities in terms of droplet evaporation rate and secondary atomisation (comprehensively delineated in **Figure 4.4**). In the following sections, it is intended to provide physical insights into the atomization mechanisms and evaporation dynamics.

Evaporation & Atomisation Characteristics	BASE FUEL			
	Ethanol	Ethanol +NPs	Dodecane	Dodecane +NPs
PE	$d_0 < 500\ \mu m$ $0 \leq PLR \leq 0.5w\%$ $1.05MW/m^2 \leq I_0 \leq 1.89MW/m^2$	–	–
PE + SA (KH instability)	–	–	$d_0 < 450\ \mu m$ $0.1 \leq PLR \leq 0.5w\%$ $1.05MW/m^2 \leq I_0 \leq 1.89MW/m^2$	$d_0 < d_{boil}$ $0.1 \leq PLR \leq 0.5w\%$ $1.05MW/m^2 \leq I_0 \leq 1.89MW/m^2$
PE + SA (KH instability) + SA (IB)	–	–	–	$d_{boil} < d_0 < 450\ \mu m$ $0.1 \leq PLR \leq 0.5w\%$ $1.05MW/m^2 \leq I_0 \leq 1.89MW/m^2$
PE + SA (KH instability) + SA (CB)	–	–	$d_0 > 450\ \mu m$ $0 \leq PLR \leq 0.5w\%$ $1.05MW/m^2 \leq I_0 \leq 1.89MW/m^2$	

Figure 4.4. Evaporation and atomisation characteristics of pure and NP laden droplets.

4.4 Physical insights

4.4.1 Droplet shape and stability

Global observations of pure and NP laden droplets reveal that the droplet size and acquired shape are responsible for inception of instabilities. Therefore, the shape oscillations are looked into which are induced by the acoustic field and the laser flux which act as precursor events to the droplet breakup. Ethanol droplets (with and without ceria NPs) exhibit uniform shape with minimal change in aspect ratio (AR). Fast Fourier Transform (FFT) of AR shows low frequency oscillations $< 25Hz$ (**Figure 4.5**). Ethanol based nanofuel droplets also exhibit similar spectral characteristics in

terms of the dominant frequency. These findings for ethanol-based droplets are similar for all laser powers.
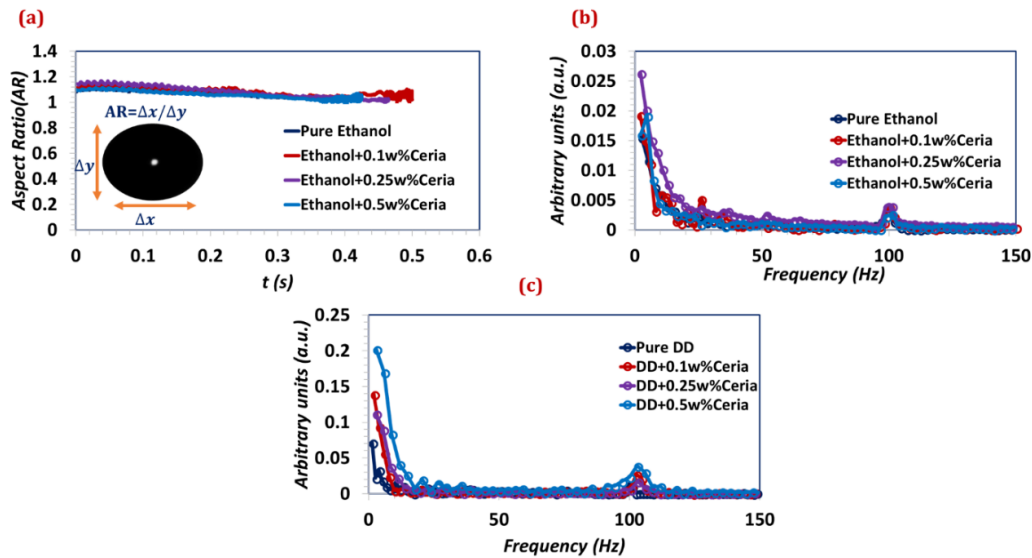
Figure 4.5. (a) Transient variation of ethanol-based droplet aspect ratio (AR) at 1.05 MW/m2 (b) Spectral response of ethanol droplet AR (pure and particle laden), (c) Spectral response of dodecane droplet AR (pure and particle laden).
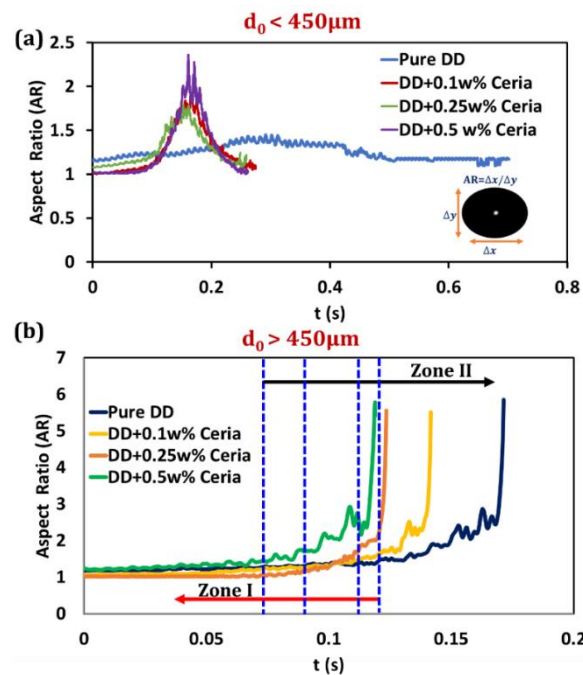
Figure 4.6. (a) Transient variation of dodecane-based droplet aspect ratio (AR) at 1.89 MW/m2 for $d_0<450\mu m$, (b) Time-history of droplet aspect ratio (AR) of pure and particle laden dodecane at 1.89 MW/m2 for $d_0>450\mu m$. Period of minimal variation in droplet AR is Zone I and Zone II represents the droplet lifetime where droplet AR increases rapidly.

DD droplets (pure and NP laden) acquire a slight ellipsoidal shape (AR > 1) during the evaporation. For $d_0 < 450\ \mu m$, AR of pure DD droplet remains greater than unity (**Figure 4.6(a)**) and exhibit low frequency oscillations ($< 25 Hz$) with aggravated amplitude compared to pure ethanol. Interestingly, for larger droplets ($d_0 > 450\ \mu m$), AR manifests monotonic increase till the point of CB. **Figure 4.6(b)** delineates two zones of droplet lifetime for $d_0 > 450\ \mu m$; I. droplet AR is nearly constant and II. droplet AR amplifies rapidly to a critical value (flattening) before breakup. The time scale associated with the sudden increase in droplet AR (Zone II) $\sim 50\ ms$ across all operating conditions. The trends are similar with increase in laser power. Not surprisingly, the AR values peak to the maximum in shorter time (zone I is shortened and not zone II) with increase in heating rate. It should be noted that due to the continuous increase in AR, FFT does not provide any significant insight on droplet oscillations. However, these findings do provide an idea about the precursor stage of CB for pure DD droplets.

For $PLRs$ $0.1\% - 0.5\%$, DD-based nanofuel droplets show ~15% to 50% increase (**Figure 4.6(a)**) in AR oscillations ($d_0 < 450\ \mu m$) suggesting severe deformations. These observations remain consistent with increase in laser power. For $d_0 > 450\ \mu m$, DD-based nanofuel droplets also undergo CB albeit at a faster rate (**Fig. 4.6b**; zone I timescale is shortened; zone II timescale remains the same). A detailed analysis of these break-up modes will be presented in subsequent section.

4.4.2 Secondary atomisation of pure and particle laden fuel droplets

(a) Secondary atomisation (SA) due to Kelvin-Helmholtz (KH) instability

Pure and nanofuel DD droplets are subjected to PE conjoined with secondary atomisation (SA) at equatorial region due to Kelvin-Helmholtz (KH) instability. Daughter droplets of size range $\sim 4 - 10 \mu m$ are incessantly pinched off from the droplet equator. Velocity field around the levitated droplet arising from the acoustic streaming is responsible for a relative motion between the droplet and its surrounding. This transpires as a shearing force on the droplet surface. Droplet equator (with the minimum radius of curvature) subjected to maximum shear stress is innately prone to

maximum atomisation [93]. This mode of SA is present for all laser heating rates and drop sizes of DD-based droplets (**Figure 4.4**).

(b) Secondary atomisation due to Catastrophic Break-up (CB)

Pure DD droplets with $d_0 > 450 \mu m$, experience extreme acoustic flattening and catastrophic break-up (CB). **Figure 4.7** presents the high-speed images of droplet under extreme acoustic flattening, rim formation, and subsequent break-up. Monotonic increase in droplet AR serves as precursor for CB. Secondary atomisation of pure DD droplets by CB mode occurs at $\tau_{CB} \sim 0.17 - 0.21 s$ (for laser power $1.89 MW/m^2 - 1.05 MW/m^2$) when the droplet surface tension decreases sharply due to radiative heating. Flattening of the droplet starts with an indent at the droplet pole due to acoustic loading. Eventually, the major portion of the liquid is transferred to the droplet periphery, leading to the formation of a thin central membrane. This central region undergoes further rupture due to the induced surface capillary waves. In addition, large daughter droplets ($d_d \sim 30 - 60 \mu m$) are formed after the disintegration of the rim; a high-pressure zone created by the liquid accumulation at droplet periphery.

Levitated droplets experience external excess pressure due to the non-homogeneity in surrounding acoustic field. Droplet stability is governed by the rivalry between external pressure forces i.e. the difference in Bernoulli pressure at droplet pole and equator ($\Delta p = P_{pole} - P_{eq}$) and the restoring surface tension forces (σR_c, where σ and R_c are fluid surface tension and droplet equatorial radius of curvature, respectively). Therefore, droplet stability can be quantified by the Modified Weber number (We), defined as the ratio of deforming and restoring forces, $We = \Delta p R_c / \sigma$ [93]. Pure ethanol droplets follow the criterion of $We < 1$ (**Figure 4.7**). The explanation for ethanol droplet exhibiting lower values of We reside in their response to the supplied heat. As explained in our previous works [93], [94], ethanol droplets attain wet-bulb limit at a faster rate ($dT_s/dt \sim 600 - 1200^0 C/s$). The major part of the supplied energy is consumed to vaporise the ethanol liquid, resulting in a faster evaporation rate and regression of droplet diameter, leading to a stable droplet. Contrastingly, due to the low vapour pressure of DD droplets, laser energy is utilised towards increasing the droplet temperature. Increase in T_s leads to $\sim 28\%$ reduction in surface tension ($0.025 N/m$ @298K to $0.018 N/m$ @363K) but a minimal change in droplet diameter. This

increases the Weber number leading to thermal instabilities. Smaller pure DD droplets i.e. $d_0 < 450 \mu m$ are less susceptible to these instabilities due to smaller R_c, ($We < 1$;**Figure 4.7**). For larger droplets ($d_0 > 450 \mu m$) , We shows a continuous increase up to a critical value. Following acoustic flattening, surface tension is unable to retain the droplet shape, thereby leading to significant deformation and atomisation.
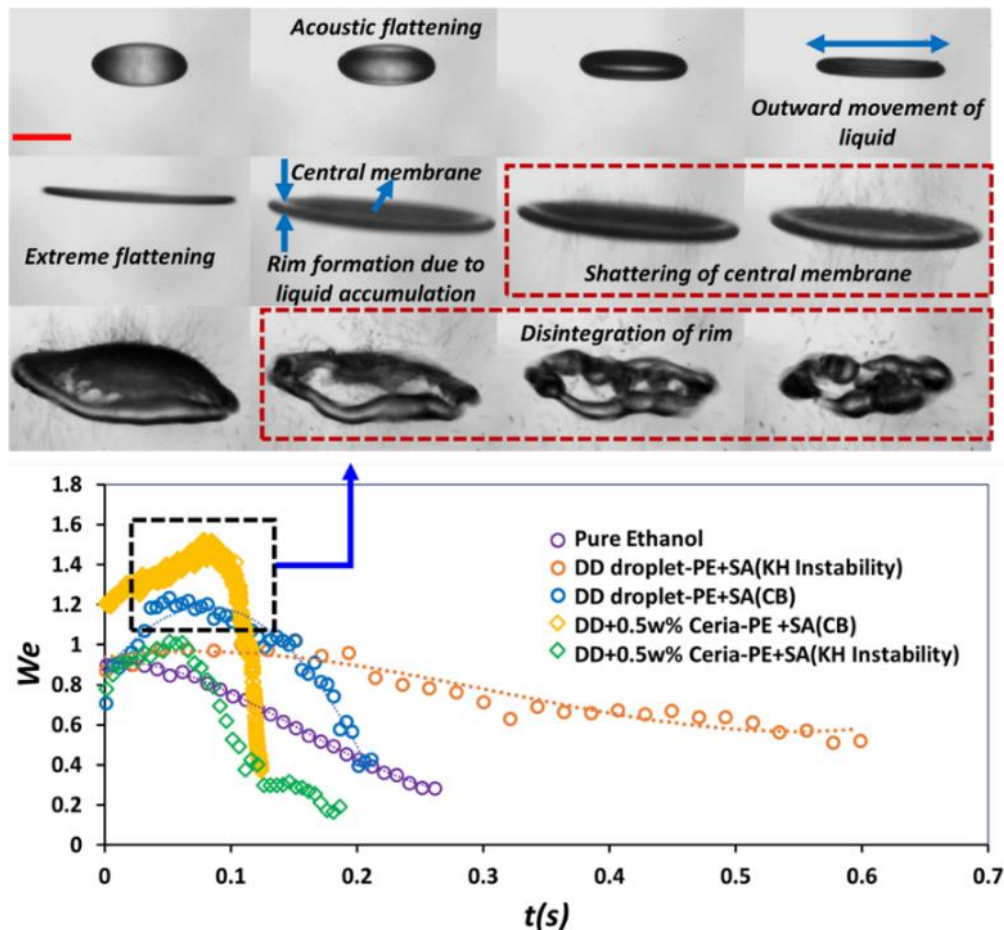
Figure 4.7. Variation of Weber number (We) for different functional droplets with time at 1.89 MW/m2 laser heating rate. Pure ethanol, pure and NP laden dodecane droplets (d_0<450μm) exhibit We <1. Whereas pure and NP laden dodecane droplets with d_0>450μm undergo severe fragmentation due to excess acoustic loading i.e. We>1. Scale bar represents 250 μm.

Catastrophic shattering of the parent droplet due to uncontrolled acoustic flattening is also exhibited by DD-based nanofuel droplets for $d_0 > 450$ μm for all laser heating rates (I_{laser}). This SA pathway is similar to the pure DD droplets as described above. Enhanced dT_s/dt and higher values of T_s lead to fast reduction in nanofuel surface

tension. Consequently, DD-based nanofuel droplets undergo more vigorous CB (**Figure 4.7**). A distinctive feature observed for DD-based nanofuel droplets is the internal boiling of the residual droplet left on the node after CB of the parent droplet (**Figure 4.8**). Note that this is a random observation which occurs only if a residual droplet stabilises on the node of the levitator. However, this finding suggests that adequate residence time is necessary to trigger internal ebullition in NP laden droplets which will be discussed next.
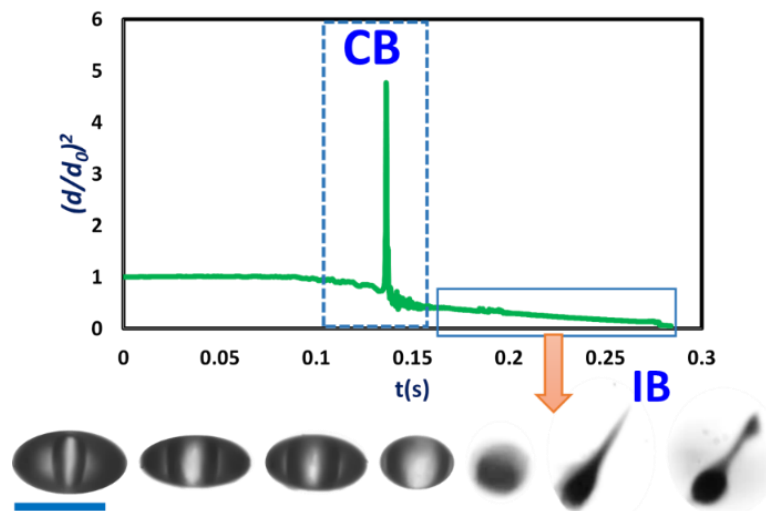
Figure 4.8. Normalised droplet diameter variation with time for PLR 0.5w% (dodecane-based nanofuel) with d0>450μm at 1.89MW/m2 laser power. Post catastrophic break-up (CB) of the parent droplet, if a residual stabilises at the pressure node, internal boiling (IB) is observed (isolated high-speed images). Scale bar represents 250 μm.

(c) Mechanism of secondary atomisation of nanofuel droplets due to internal boiling (IB)

SA of DD-based nanofuel droplets with $d_{boil} < d_0 < 450\mu m$ is effectively present due to the combination of KH instability and IB (**Figure 4.4**). In this section, the IB mode is explained along with its effects on droplet oscillations. It should be noted that IB is completely absent in pure DD droplets.

For DD-based nanofuel droplets exhibiting IB, bubbles are ejected through two different pathways; I. intermittent bubble ejections at the free surface of the droplet, and II. Continuous bubble expansion and final disintegration of the droplet (**Figure 4.9**). Distinct after-effects on droplet oscillations are prompted by these two pathways. During a bubble collapse, vicinal liquid rushes towards the low-pressure zone created by the formation of surface opening. Further, this in-flow generates a liquid ligament is formed which breaks up at the tip through Rayleigh-Plateau mechanism i.e. $L_{lig}/w_{lig} > \pi$ (where L_{lig} and w_{lig} are ligament length and width, respectively). Daughter droplets formed are ejected at velocity of $\sim O(10^{-1})m/s$. These observations are present for both ejection types. Henceforth, these atomisation modes are discussed in detail.
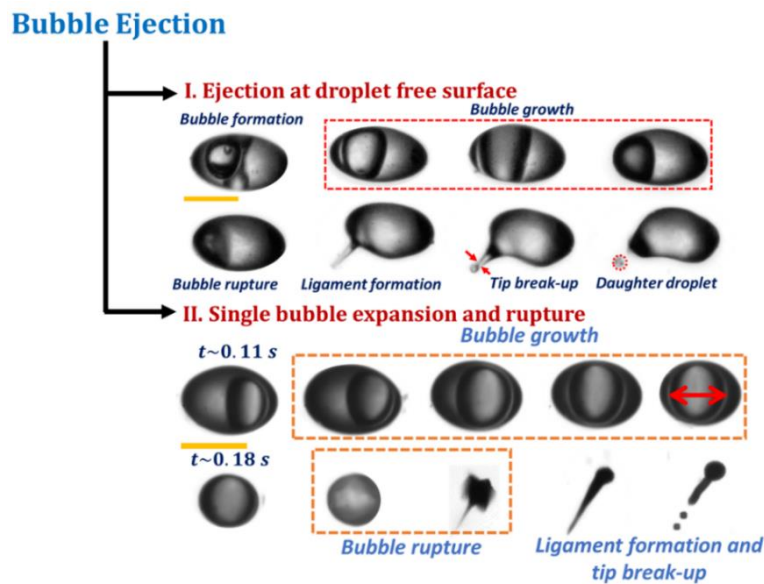
Figure 4.9. Two types of ejection events followed with ligament formation and tip break-up via Rayleigh-Plateau mechanism. Type I: A localised bubble ejection event at droplet free surface, and Type II: Rupture of a continuously growing bubble. Scale bar represents 350 μm.

For Type I ejection, bubble residence time, period between bubble incipience and ejection, $\tau_{res}|_{bubble}$ varies $\sim(2-11)\ ms$. Post ejection (Type I), a recoil force is imparted to the mother droplet due to the retraction of liquid ligament with excess energy $(K.E.|_{lig} \sim (\pi/8)\rho_l w_{lig}^2 L_{lig} v_{lig}^2$, where v_{lig} is the velocity of ligament) resulting in surface/volumetric oscillations. These oscillations take peculiar forms when bubble ejection happens either at droplet equator or droplet pole.

Pressure at the equator of levitated droplet is given as [93]

$$P_{eq} = P_{max}\sin(k_z z_{cg})J_0(k_r a) \tag{4.2}$$

and pressure at droplet pole is given as

$$P_{pole} = P_{max}\sin(k_z(z_{cg} - b)) \tag{4.3}$$

Where $P_{max} = P_0\gamma_0 Ma$, J_0 is the Bessel function of the zeroth order, Ma is the acoustic Mach number, k_z and k_r are the wavenumbers in the axial and radial directions, respectively and z_{cg} is the pressure node position. Variations in the characteristic length scales in horizontal direction (a) and vertical direction (b) lead to changes in pressures at droplet equator and pole

$$\delta P_{eq} = P_{max}k_r\sin(k_z z_{cg})J_1(k_r a)\delta a \tag{4.4}$$

$$\delta P_{pole} = P_{max}k_z\cos(k_z(z_{cg} - b))\delta b \tag{4.5}$$
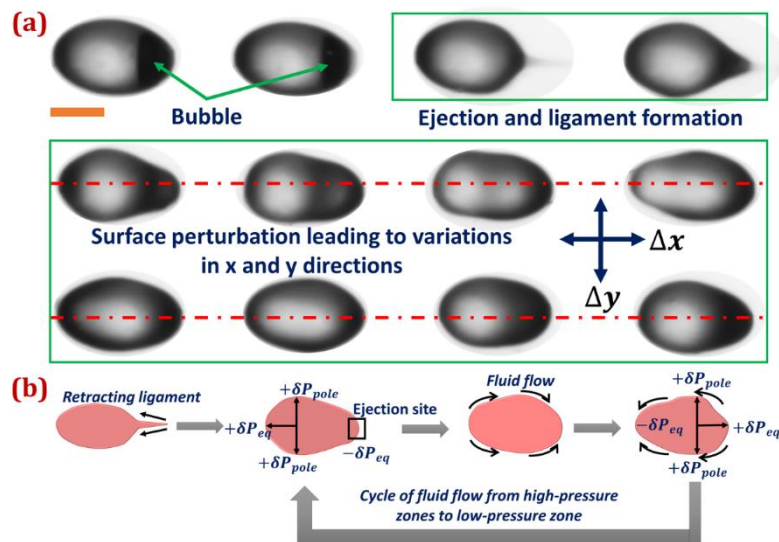
*Figure 4.10. (a) Type I ejection at the droplet equator. Scale bar represents 250 μm. (b) Pictorial representation of surface oscillation cycle arising due to the pressure differential created due to ejection at the droplet equator. (**Video 4.1**)*

The retraction of the liquid ligament leads to surface undulations of length scale $\sim O(10^{-2})mm$ in horizontal (δa) and vertical(δb) directions. These perturbations are symmetric about the droplet horizontal axis (**Figure 4.10 (a)**). These surface waves travel back and forth between the two horizontal extremities of the droplet. As these waves traverse on the droplet surface, liquid accumulation at droplet pole and the other side of the equator (opposite to the ejection spot) creates a local high-pressure zone. As a result, liquid flows from these corners to the low-pressure zone which is the original location of ejection. Again, a high-pressure zone is created on the ejection spot resulting in liquid transport back to other equatorial and polar regions of the droplet. This cycle continues until the droplet is stabilised (**Figure 4.10 (b)**).

On the other hand, oscillations arising from the ejection events at the droplet pole can also be explained in a similar fashion as equatorial ejection events. However, the after-effects in this case, are vigorous and not just constrained to surface undulations. Change in length scales especially in the vertical direction are of the order $\sim O(10^{-1})\ mm$ (marked by the blue arrows in **Figure 4.11**). Furthermore, timescale for droplet stabilisation is higher for pole ejection events ($\sim 8\ ms$) relative to the ejection events at the droplet equator ($\sim 1-4\ ms$).
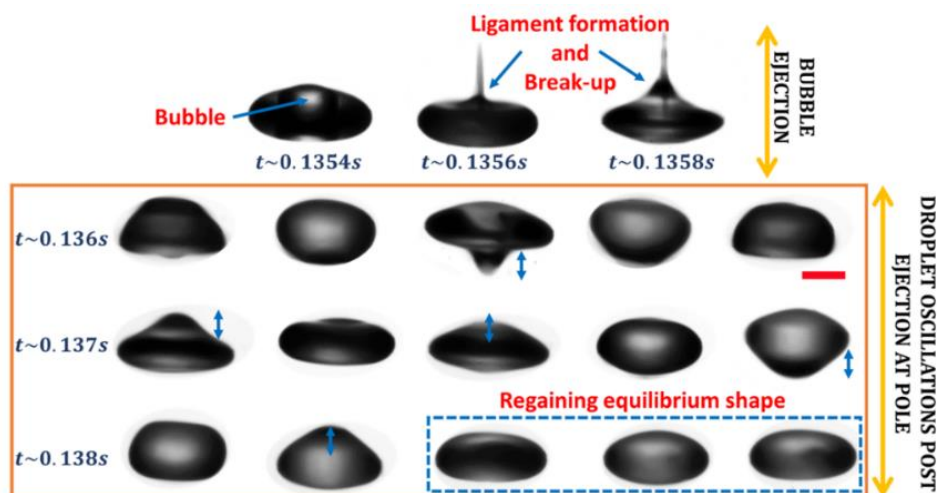
*Figure 4.11. Type I ejection at the droplet pole. Scale bar represents 250 μm. (**Video 4.2**)*

Type II ejection events are followed by continuous expansion of a vapor bubble with $\tau_{res}|_{bubble} \sim (75-120)\ ms$ around the time-scale $\tau_{nuc}|_{bubble} \sim 0.5\ \tau_{total}$. In due

course, droplet shape exhibits minimal variation with bubble expansion. The liquid layer between the bubble and droplet free surface grows thinner (**Figure 4.12**). During this period, bubble dimension is comparable to that of the droplet. Thinning of the liquid layer triggers multiple surface instabilities [95]. Eventually, the liquid film ruptures thereby atomising the parent droplet at a later stage $\sim 0.95\tau_{total}$. A liquid ligament resulting out of film rupture stretches and undergoes Rayleigh-Plateau tip break-up (similar to Type I ejection modes).
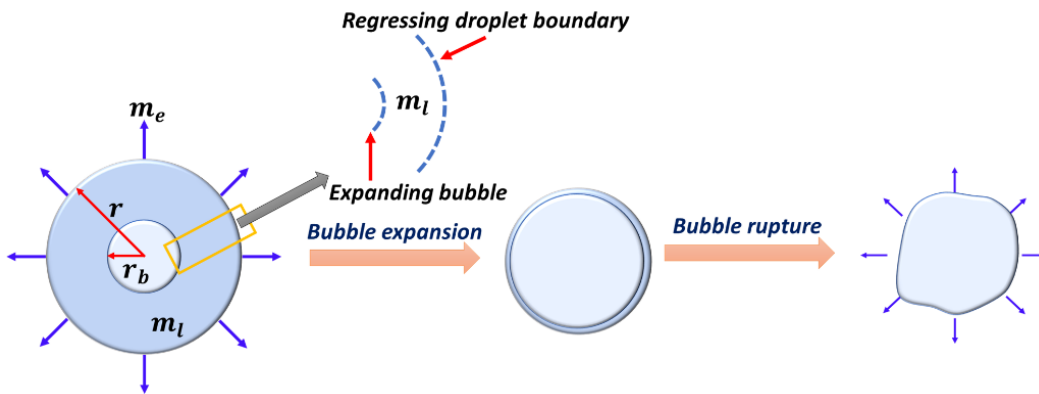
*Figure 4.12. Schematic representation of Type II ejection event. With increase in bubble size and decrease in droplet size, the entrapped liquid film undergoes thinning and rupture. (**Video 4.3**)*

4.4.3 Governing timescales for internal boiling in nanofuel droplets

In the previous section, different SA modes of DD-based nanofuel droplets have been explained. One of the key findings turns out to be the propensity of internal boiling for NP laden DD droplets. Intuitively, ethanol being a short carbon-chain alcohol with low boiling point should manifest boiling at low heating rate. Contrarily, for the same droplet size and heating rate, internal ebullition in dodecane (with higher boiling point) is relatively uncertain. Inclusion of NPs can probabilistically increase the ebullition due to the presence of additional nucleation sites. Interestingly, in the present case, addition of NPs triggers internal boiling in DD droplets but not in the ethanol counterpart. This observation is counterintuitive as well as intriguing. Another interesting observation is the existence of a minimum initial size (d_{boil}) of DD- based nanofuel droplets for

discernible vapour bubbles. This lower limit is strongly dependent on initial PLR and laser power. Furthermore, IB is also seen in the residual droplet (if present at the pressure node, as explained in **Section 4.4.2b**) after the CB of the parent droplet. Based on these observations, it can be suggested that sufficient residence time is required for IB. Henceforth, a detailed timescale analysis incorporating the coupled mechanism of NP aggregation and bubble incipience is presented. Further, the role of operating parameters on d_{boil} is elucidated.

Note that the data acquired in these experiments does not provide temperature variations inside the droplet. For the reported work, droplets are uniformly $(d_{laser} > d_0$, where d_{laser} is the laser beam diameter) irradiated by a continuous laser. Hence, local laser cavitation [96] can be omitted. Acoustic levitation provides a better option for probing the absolute possibility of NP triggered boiling by eliminating external contact (interference from the wire [19], [20]) as in the case of pendant droplets. In the present work, the peculiar bias of heterogenous nucleation towards DD nanofuel suggests the formation of NP aggregates leading to local hot-spots. Henceforth, to investigate our hypothesis, a time scale analysis is presented as follows.

NP diffusion time scale ($\tau_{diffusion}$) is given as

$$\tau_{diffusion} = \frac{r^2}{D_{diffusion}} \tag{4.6}$$

where $D_{diffusion}$ is particle diffusion coefficient calculated using Stokes-Einstein equation [97], is found $\sim O(10^3)s$ for both, ethanol and dodecane nanofuel droplets. Here, $\tau_{diffusion} \gg \tau_{\text{total}}$ implying that droplet internal homogenisation is not possible with particle diffusion. The heat and mass transfer effects arising from acoustic streaming are significant [91]. One of the significant effects is the droplet internal circulation, induced due to the presence of shear at liquid/gas interface. Velocity scale ($u_{internal}$) of this internal flow is given as [98]

$$u_{internal} = \sqrt{\frac{\mu_0 \rho_0}{\mu_l \rho_l}} u_{max} \tag{4.7}$$

The internal circulation time scale ($\tau_{internal}$) scales as

$$\tau_{internal} \sim \frac{r_0}{u_{internal}} \tag{4.8}$$

where u_{max} is the speed of sound in the gaseous phase given as Mau_0, u_0 is the sound velocity in the air, and Ma is the acoustic Mach number calculated fron the relation, $SPL = 197 + 20logMa$ [98]. The scale of internal circulation velocity, $u_{internal}$ is found $\sim O(10^{-1})m/s$ and $\tau_{internal}$ varies $\sim O(10^{-3})s$ for ethanol and DD droplets. Thus, $\tau_{internal} \ll \tau_{total}$ which suggests homogenisation of droplet interior due to internal circulation. This further implies that presence of internal velocity impedes preferential accumulation of NPs at the droplet surface. It is also shown further that the shear rate arising from internal circulation is crucial for NP aggregation kinetics.

Cerium oxide NPs, being benign will neither participate in a chemical reaction nor stimulate one. Thus, chemical changes with NP inclusion can be ruled out. This infers ceria nano-additives can be responsible for physical changes such as increased heat absorption, internal boiling, and droplet secondary atomisation. Such physical changes are seen and documented in multiple experimental studies [6], [26], [44]. Relative motion of NPs in the base liquid is a controlling factor for suspension stability. Shear rate and change in surface temperature leads to enhanced particle-particle collision and subsequent aggregation. Particle aggregation due to the action of shear forces is termed as orthokinetic aggregation. Particle aggregation time scale (τ_{agg}) for orthokinetic aggregation is given as [99]

$$\tau_{agg} = \frac{\pi D}{4\dot{\gamma}(3-D)}({\varphi_0}^{-1} - 1) \tag{4.9}$$

where φ_0 is initial particle concentration, D is the fractal dimensionality, and the shear rate inside the droplet is given by $\dot{\gamma}$. Shear rate ($\dot{\gamma}$) is given as $\sim u_{internal}/r_0$. Aggregation timescale for ethanol-based and DD-based nanofuels shows a continuous decrease with increase in NP PLR, suggesting enhanced propensity of the nanofuels towards aggregation. Propensity toward internal ebullition in the functional droplets is

explained using a non-dimensional timescale given as τ_{agg}/τ_{total} (**Figure 4.13**). As illustrated in **Figure 4.13**, for ethanol-based droplets, $\tau_{agg}/\tau_{total} \gg 1$. However for DD-based droplets, $\tau_{agg}/\tau_{total} < 1$. Therefore, NP aggregation through orthokinetic aggregation is dominant for DD-based nanofuel droplets. Average size of these agglomerates (d_{agg}) can be estimated using the following correlation [99]

$$d_{agg} = d_P \varphi_0^{1/(D-3)} \tag{4.10}$$

For PLRs $(0.1 - 0.5)\ w\%$, d_{agg} is found $\sim 3 - 15\ \mu m$. These large agglomerates serve as local hotspots and nucleation sites for bubble incipience in DD-based nanofuel droplets. Whereas $\tau_{agg}/\tau_{total} > 1$ for ethanol-based nanofuel droplets negates any significant NP aggregation during the droplet lifetime. Therefore, the absence of NP aggregates i.e. the necessary nucleation kernels, explains the lack of internal boiling in ethanol-based nanofuel droplets.
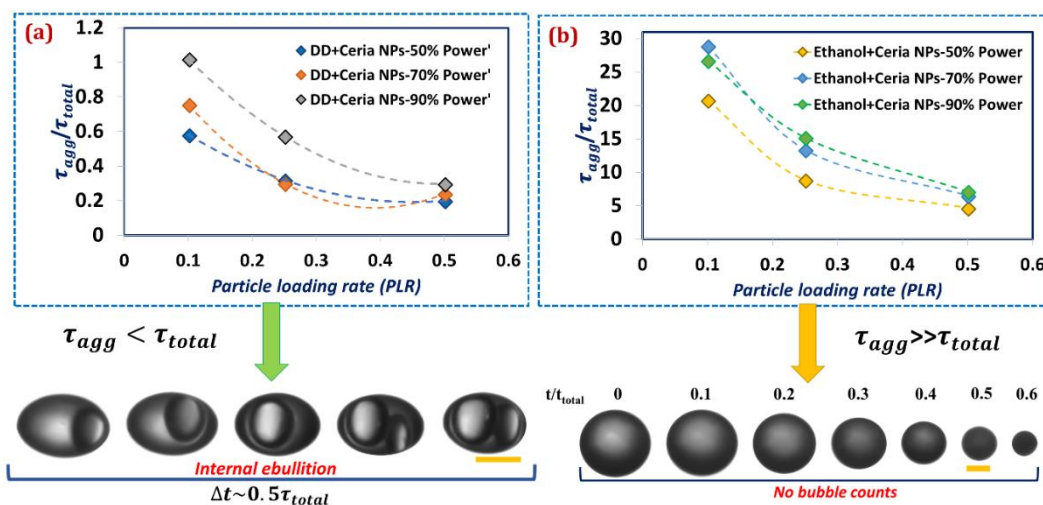
Figure 4.13. (a) Variation of τ_{agg}/τ_{total} for dodecane based nanofuels. DD-based droplet with $\tau_{agg}/\tau_{total} < 1$ exhibit internal boiling. (b) Variation of τ_{agg}/τ_{total} for ethanol based nanofuels. Inclusion of NPs in ethanol droplets does not trigger heterogeneous nucleation as $\tau_{agg}/\tau_{total} \gg 1$. Scale bar represents 250 μm.

Aforementioned discussion suggests the mechanism of formation of vapour bubbles for DD-based nanofuels due to NP agglomeration. However, for IB, a critical initial droplet size exists which varies with NP loading rate. Times scales of aggregate formation

(τ_{agg}) and bubble formation (τ_{bubble}), cumulatively affect the internal ebullition. In other words, inequality between droplet lifetime and the total sum of τ_{agg} and τ_{bubble} governs the formation of bubbles in DD-based droplet. Therefore, if $\tau_{agg} + \tau_{bubble} \leq \tau_{total}$, sufficient resident time is available for bubble incipience and growth; else droplet evaporates without any discernible internal boiling even though incipient kernels are present. For the present PLR levels, densities of DD-based nanofuels show $\sim 0.05\%$ to 0.5% variation. Thus, initial droplet mass for different PLRs can be considered almost constant. For the same laser irradiation rate, DD-based nanofuel droplets exhibit significant reduction in the evaporation time, $\tau_{total}|_{DD+NPs} \sim 0.5\,\tau_{total}|_{DD}$ for all PLRs. This disparity arises due to excess radiation absorption by the nanoparticles (~ 2 times than that of pure DD-droplets). A theoretical droplet evaporation time-scale considering the excess heat absorption for droplet diameter d_0 , can be given as

$$\tau_{th} = \frac{\frac{2}{3}\rho_l(c_{pl}\Delta T + h_{fg})}{2I_{laser}}d_0 \tag{4.11}$$

I_{laser} is the incident laser flux, c_{pl} is specific heat capacity of the liquid, $\Delta T = T_s - T_0$ represents the difference in droplet wet-bulb temperature and initial temperature, h_{fg} is latent heat of vaporisation of the liquid, and ρ_l is the liquid density.

Note that the consideration of radiation absorption by nanofuel droplets to be twice as that of pure DD-droplets is purely observational. Exact calculation of the absorbed heat by the NPs involves consideration of Mie theory and absorption coefficients of ceria NPs in the base fuel. These relevant values are not standard and vary from one base-fuel to another. These estimations require a separate set of studies and is beyond the scope of this paper. Therefore, the experimental observations can be useful for a first-order evaluation.

For different laser powers, variation of the bubble dimension can be given as

$$\frac{dm_{bubble}}{dt}h_{fg} = 2\dot{Q}_{laser} \tag{4.12}$$

Therefore, time scale for bubble growth to any radius R_{bubble} can be given as

$$\tau_{bubble} = \frac{\frac{4}{3}\pi\rho_l(R_{bubble}{}^3 - r_{agg}{}^3)h_{fg}}{2\dot{Q}_{laser}} \tag{4.13}$$

Here, $\dot{Q}_{laser}$ is the laser power absorbed by the droplet which is equivalent to $I_{laser}\pi r_0{}^2$ (I_{laser} is the incident laser flux, r_0 is initial droplet radius).

From **Figure 4.8** and **Figure 4.13**, it is evident that either before ejection or during droplet fragmentation, bubble dimension (R_{bubble}) is of the same order as the droplet. Hence, τ_{bubble} is found to be $\sim O(10^{-1} - 10^{-2})s$ for all laser powers (1.05 MW/$m^2 - 1.89$ MW/m^2). This calculation also matches with the order of the experimental data. **Figure 4.14** a, b and c represents the variation of a non-dimensional parameter (τ^*) defined as the ratio of $\tau_{agg} + \tau_{bubble}$ and τ_{th}, with droplet initial diameter. The plot suggests that when droplet lifetimes are smaller i.e. $\tau^* > 1$, droplet should not exhibit boiling. However, for droplet sizes above than a critical value (d_{boil}), boiling is discernible because $\tau^* < 1$. For a fixed laser power, the critical value of d_{boil} decreases with increase in PLR. However, with increase in laser energy, reduction in droplet evaporation time-scale inhibits bubble formation in droplets. Hence, the critical droplet size increases by $\sim 20\% - 40\%$ for $1.05 - 1.89$ MW/m^2 laser powers. To validate this hypothesis, another non-dimensional time-scale $\left(\tau^{**} = (\tau_{agg} + \tau_{bubble})/\tau_{total}\right)$ is postulated using the experimental droplet lifetime (**Figure 4.14** (d), (e) and (f)). Experimental findings show a similar trend when compared to the theoretical findings. For all laser powers, PLR= $0.5w\%$ shows the minimum critical d_0 whereas PLR= $0.1w\%$ exhibits the maximum threshold due to the large value of τ_{agg}.
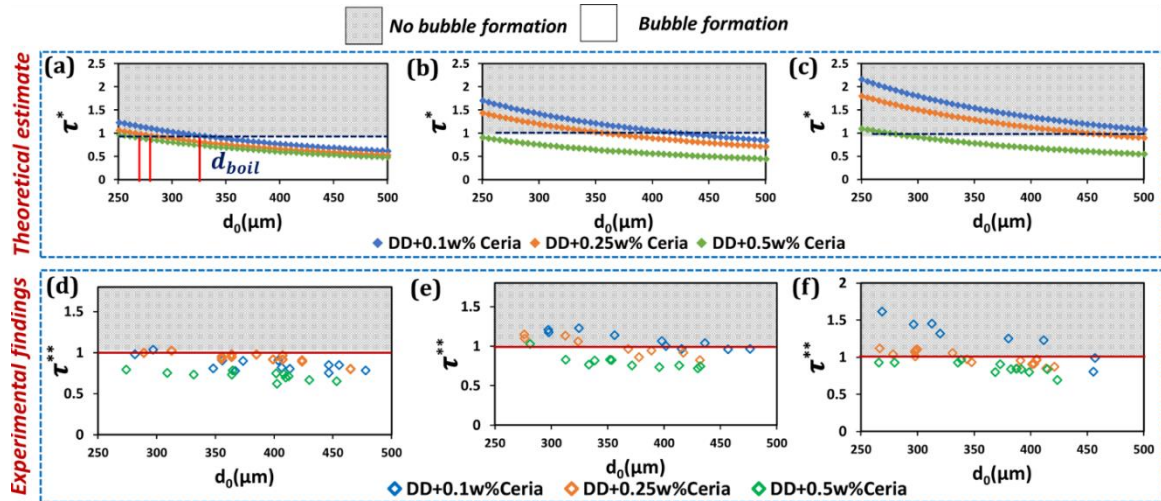
Figure 4.14.   Variation of non-dimensional parameter τ^* with initial droplet diameter for different PLRs (a) for laser power 1.05 MW/m2 (b) for laser power 1.47 MW/m2 (c) for laser power 1.89 MW/m2. Variation of experimental non-dimensional parameter τ^{**} with initial droplet diameter for different PLRs (d) at 1.05 MW/m2, (e) at 1.47 MW/m2, and (f) 1.89 MW/m2, respectively.

Plots in **Figure 4.15** clearly demarcate three regions of evaporation and atomisation characteristics for different PLR, d_0 ,and laser heating rates for DD-based nanofuel droplets. **Figure 4.15** (a), (b), and (c) are two dimensional plots for the variation of evaporation and atomisation characteristics with droplet size and PLR at a fixed laser heating rate. For all input heat flux a minimum droplet diameter (d_{boil}) exists with $\tau^{**} < 1$ suggesting internal boiling. **Figure 4.15** (d) presents the three-dimensional correlation among the operating variables ($d_0, PLR, \& I_{laser}$). For $PLRs < 0.5w\%$ with increase in laser power, d_{boil} increases. Although due to the faster NP aggregation in PLR $0.5w\%$, d_{boil} is similar for all heating rates. For all laser powers, secondary atomisation through CB mode is invariably present for $d_0 > d_c$ ($d_c{\sim}450\mu m$) .
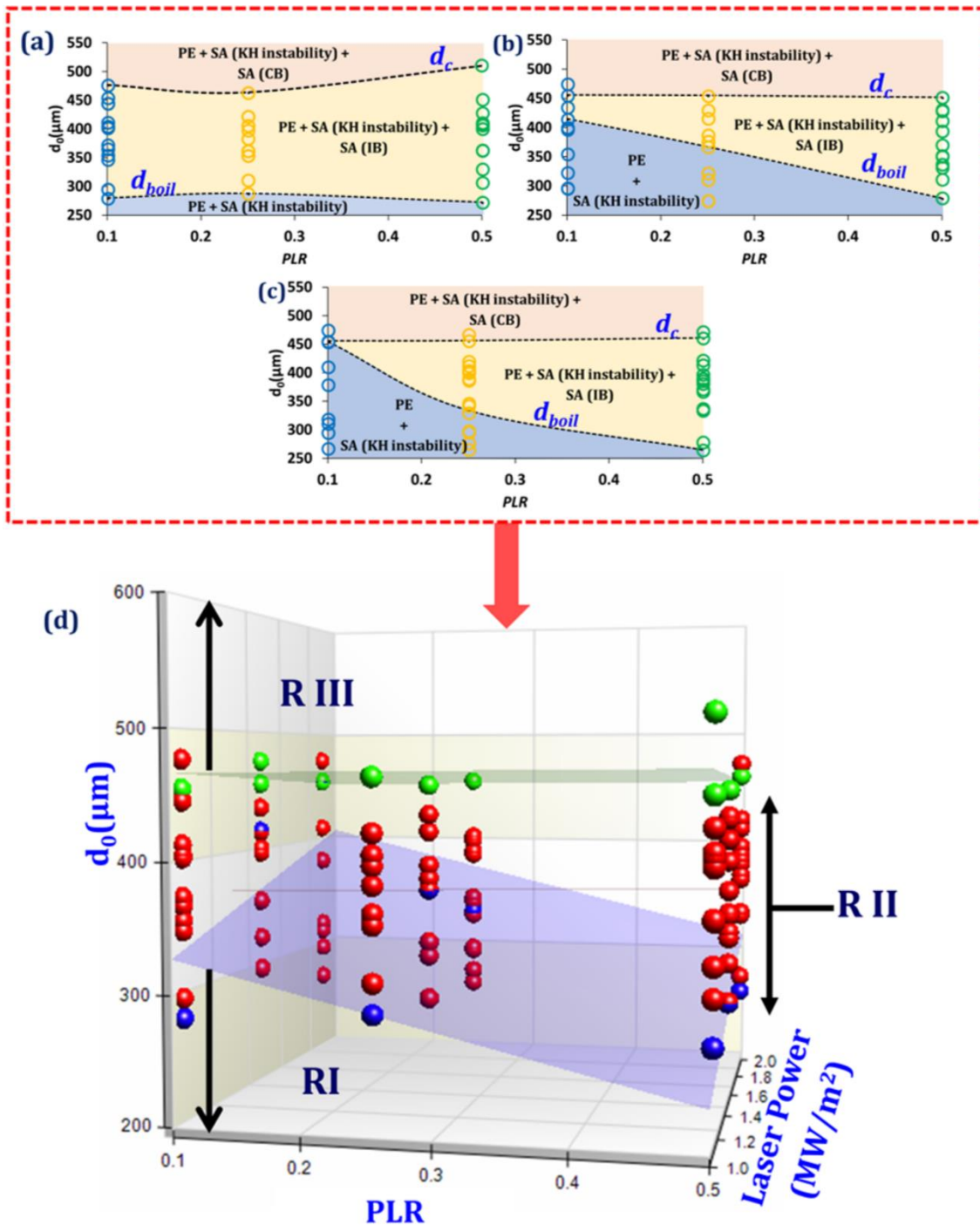
Figure 4.15. Two-dimensional map of evaporation and atomisation dynamics with particle loading rate and initial droplet diameter (a) at 1.05 MW/m2, (b) at 1.47 MW/m2, (c) at 1.89 MW/m2, (d) Three-dimensional plot of droplets undergoing different regimes of evaporation and atomisation modes with PLR and laser heating rate. All data points are droplet initial size. Regime R I signify PE+ SA (KH instability), Regime R II shows the unique mode of droplet atomisation through IB i.e. PE+ SA (IB)and Regime R III undergo CB; PE+ SA (CB).

4.5 Conclusion

The current work outlines the evaporation and atomisation dynamics of two different types of nanofuels; (i) ethanol -based (high vapour-pressure) nanofuel and (ii) dodecane-based (low vapour-pressure) nanofuel. Droplet lifetime of several functional droplets exhibit similar trend; Stage I: input energy is utilised in the sensible heating of the droplet and Stage II: the period after attaining the wet-bulb limit where input energy is solely responsible for vaporisation. Pure ethanol droplets undergo pure evaporation and do not exhibit secondary atomisation. On the other hand, low-vapour pressure fuel, n-dodecane vaporises at lower rate and exhibits two modes of secondary atomisation. For $d_0 < 450 \mu m$, DD droplets undergo pure evaporation and pinching off daughter droplets at the equator due to KH instability. With increase in droplet size $(d_0 > 450 \mu m)$, another mode of secondary atomisation is triggered as catastrophic break-up. This mode of atomisation is characterised by modified Weber number (We).

Addition of ceria NPs does not affect the evaporation timescales in ethanol droplets. Whereas for dodecane-based nanofuel, the droplet lifetime reduces to nearly half of the pure droplet, $\tau_{total}|_{DD+NPs} \sim 0.5\, \tau_{total}|_{DD}$. Further, NP addition to DD-droplet also triggers internal boiling unlike the ethanol-based nanofuel droplets. Aggregates of NPs are the incipient kernels for heterogenous boiling. A time scale analysis based on orthokinetic NP aggregation and droplet evaporation time $(\tau_{agg}/\tau_{total})$ suggests that lack of NP aggregates (d_{agg}) in ethanol-based nanofuels. DD-based nanofuels exhibit three regimes of evaporation and atomisation characteristics for all PLRs and laser heating rate based on the initial size. Below a minimum droplet size (d_{boil}), DD-based nanofuel droplets show similar trend as pure DD droplets i.e. combination of PE and SA due to KH instability albeit at a faster rate. For droplets above a critical radius (d_c), DD-based nanofuel droplets undergo CB (similar to the pure DD droplets). For droplets sizes, $d_{boil} < d_0 < d_c$, nanofuel droplets exhibit unique modes of SA through IB. Bubble ejection events result in the formation of a liquid ligament which undergoes Rayleigh-Plateau tip break-up generating daughter droplets. The lower limit (d_{boil}) shows a strong dependence on PLR and laser heating rates. A non-dimensional parameter τ^*, defined as the ratio of the sum of NP aggregation and bubble growth time scales and theoretical droplet lifetime $((\tau_{agg} + \tau_{bubble})/\tau_{th})$, is utilised to estimate the

theoretical values of d_{boil}. If $\tau^* > 1$, lack of enough residence time for NP aggregation and bubble growth results in lack of discernible bubbles. Whereas for $\tau^* < 1$, bubble formation is probabilistic (**Figure 4.14 a, b,** and **c**). Considering the experimental droplet evaporation timescale, a similar trend is observed for τ^{**} vs d_0 (**Figure 4.14 d, e,** and **f**). A three-dimensional map is presented in **Figure 4.15(d)** to provide the different regimes of evaporation and atomisation modes as functions of PLR, initial droplet size, and laser heating rate.

Chapter 5

Self-tuning and topological transitions in a free-falling nanofuel droplet flame

Numerous research investigations, as previously mentioned, report a plethora of experimental findings [6], [18], [23]–[26], [44], [100], [101] pertaining to the droplet (pure/multi-component) combustion in a pendant mode, encompassing the corresponding vaporization and atomization characteristics. Combustion dynamics of droplet in the pendant configuration inherently constitute the heat transfer effects to and from the flame. Conductive heat transfer to droplet through wire-support potentially increases the gasification rate. Furthermore, wire support can also act as a heat sink and subsequently, decrease the heat transfer to the droplet. On the other hand, for particle laden droplets, research investigations also claim that, particle with more affinity towards the suspension wire can lead to preferential agglomeration thereby changing the internal-flow dynamics. This further necessitates the study of evaporation/combustion dynamics of nanofuel droplets in a contactless environment. While **Chapter 2** and **3** are focused on pendant mode droplet combustion, **Chapter 4** presented a time scale analysis of vaporization by considering the cumulative effects of orthokinetic nanoparticle (NP) aggregation, droplet evaporation lifetime and bubble growth rate. Furthermore, a non-dimensional time scale is also coined in **Chapter 4** to estimate the minimum droplet diameter necessary to exhibit boiling, nevertheless without considering the presence of flame envelope and droplet motion which is encountered in my practical applications. In the current chapter, the combustion characteristics of free-falling droplets are investigated to provide lacunae of the previous chapters.

Tanvir et al. [29]studied the effects of added graphite nanoparticles on the burning rates of freely falling ethanol droplets. Using Monte Carlo simulations along with experiments, they proposed that radiation absorption (preferentially at droplet surface) by graphite nanoadditives reduces the droplet evaporation timescales. Further, in the same line of work Tanvir et al. [28] investigated the effect of seeded particle size (50 nm and 100nm) towards droplet combustion. They reported smaller NPs are responsible for higher degree of droplet burning rate enhancement. Guerieri et al. [31] reported

improved suspension stability and enhanced burning rates of droplets seeded with oxygen-containing particles, and nanoaluminum. Inclusion of energetic nanoparticle such as Al, increases the cumulative heat of combustion. Encompassing the practical facet, Basha et al. [102] studied the use of alumina and cerium oxide nanoparticles as additives to bio-diesel for combustion in CI engines. The findings indicate that the brake thermal efficiency of the power cycle increased along with a reduction in unwanted combustion products namely NOx, CO and unburnt hydrocarbons. Both these results were attributed to increased heat release. Similarly, Gumus et al. [103] added nanoparticles in diesel fuel. Their works indicated that in a CI engine, such solutions resulted in higher torque and brake thermal efficiency, with the beneficial effect of significant decrease in unwanted combustion products.

Aforementioned studies reporting droplet combustion dynamics (pure/particle laden) are mostly focused on droplet regression rate and the respective deviation from the classical $d^2 - law$. Nonetheless, till date research from the vantage of the droplet flame characteristics in a convective flow still remain sparse. In the presented work, the droplet (pure and nanoparticle laden) flame dynamics in a free-falling droplet (contactless) is isolated; (a) Envelope to wake flame transitions, (b) topographical self-tuning, and (c) Wake flame characteristics. Here, the envelope (diffusion tear-drop shape) to wake flame transition is described by incorporating the local flame strain variations when subjected to external flow-field. Acceleration under gravity modulate transient droplet velocity which in turn govern the droplet wake flame topography. Drawing a round-jet analogy, the self-tuning mechanism for flame construct and heat release is elucidated. Additionally, the variation of droplet burning rate for the functional nanofuel droplets and the respective controlling parameters for internal ebullition, is also explained.

5.1 Experimental Methodology

5.1.1 Nanofuel Preparation

The nanofuel solutions are prepared with n-dodecane as the base fuel and aluminium oxide (alumina, Al_2O_3) NPs as nano-additive (procured from Reinste Nano Ventures) of

an average size of 40 nm. To ensure steric stabilization, non-ionic surfactants; Tween 85 (Polyoxyethylene sorbitan trioleate) and Span 60 (both procured from Sigma-Aldrich) are first added to the alumina NPs in the 1:2 weight ratio to ensure homogeneous capping on the particles. The surfactants' percentage is kept low than that of the nanoparticles to avoid any effect on evaporation dynamics. Afterwards, liquid n-dodecane is added to the viscous mixture of particles and surfactant. Finally, the suspension is subjected to ultrasonication for 1 hour (15 s alternate ON/OFF cycles of Trans o sonic D120/P model). In the present experimental study, five cases of functional droplets with varying alumina concentration are considered; (i) 0 wt. %, (ii) 0.5 wt. % (0.095 vol%) of alumina, (iii) 1.0 wt. % (0.191 vol. %), alumina, (iv) 5.0 wt. % (0.955 vol. %), of alumina, and (v) 10 wt. % (1.91 vol. %), of alumina.

5.1.2 Experimental Set-up
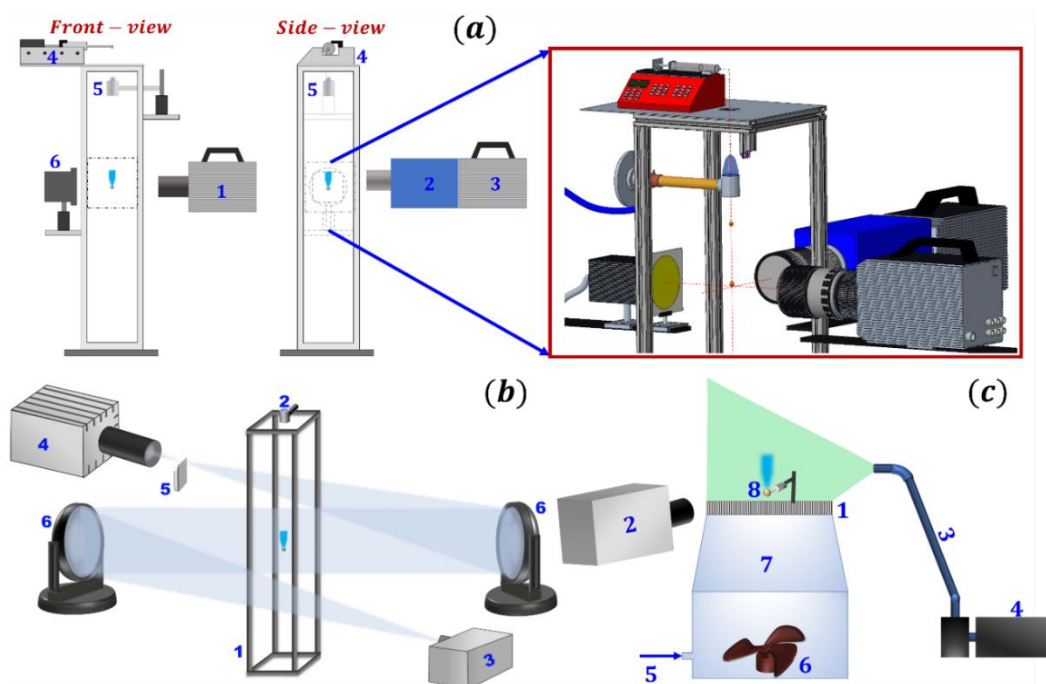
Figure 5.1. (a) Illustrates the drop-tower arrangement for functional droplet combustion. The total droplet flight time is ∼1.2 seconds. The tower is divided into 18 regions of interests (ROIs) and droplet shape and flame images are simultaneously recorded for each of them. Finally, the history of droplet diameter regression and heat release (HR) is found by temporally stitching these data points. 1-High-Speed Camera, 2- High-Speed IRO, 3- High-Speed Camera, 4-Syringe pump and needle, 5-Pilot flame, 6-Strobe light. (b) Experimental set-up for Schlieren imaging; 1- Drop-tower, 2-Pilot-flame, 3-Light source, 4-High-Speed Camera, 5-Knife edge, and 6-Parabolic mirrors (c) Experimental set-up for High-speed flow visualization; 1-Wind

Tunnel, 2- High-Speed Camera, 3-Laser controller, 4- Flexible Laser arm, 5-Seeder inlet, 6-Fan, 7-Honeycomb mesh, 8-Pendant droplet.

5.1.3 Droplet shadowgraphy and flame chemiluminescence

The drop-tower facility of 2.3 m height has been used to study the combustion of a moving fuel droplet. Droplets of size $2.1 \pm .01 mm$ are generated using a hypodermic needle of inner diameter of .45mm attached to a syringe pump with flow rate of 0.002 ml/min. The droplets are passed through a methane pilot flame for primary ignition. The drop-tower has been divided into 18 Region of interests (ROIs) which individually occupy 17 mm vertical space and are nearly 100mm apart from each other. For each ROI, simultaneous high-speed imaging of droplet shape and flame chemiluminescence is performed (**Figure 5.1(a)**) as in **Chapter 2** and **3** [44], [100]**.** Droplet shadowgraphy images are acquired at 7000 fps with spatial resolution of $\sim 0.017\ mm/pixel$ (temporal resolution $\sim.143\ ms$ and $1024X1024$ pixel resolution) using a High-speed Star SA5 Photron camera (with a stroboscopic backlighting, Veritas constellation 120E) coupled with a combination 100 mm Tokina macro lens and 58 mm extension tube. Flame heat release (HR) rate is monitored using High-speed Star SA5 Photron camera coupled to high speed intensified relay optics (HS-IRO) (LaVision; IV Generation) with a UV lens (Nikon Rayfact PF10445MF-UV lens) and OH* bandpass filter (308 ± 10 nm) with spatial resolution of $\sim.017\ mm/pixel$ (temporal resolution and pixel resolution of $\sim.143\ ms$ and $1024X1024$, respectively). Both acquisition systems are synced using a delay generator.

5.1.4 High-speed Schlieren Imaging

The droplet flame dynamics and density perturbations are visualized using a high-speed schlieren system. A 150 W halogen lamp and two parabolic mirrors of 20 cm diameter are employed. The respective images are acquired by a Photron FASTCAM SA5 high speed camera at 20, 000 fps (temporal resolution $\sim 0.05\ ms$) at a pixel resolution of 704×520 (**Figure 5.1 (b)**).

5.1.5 High-speed Particle Image Velocimetry (PIV)

To determine the velocity field around the freely falling combusting fuel droplet, High-speed Particle Image Velocimetry (PIV) is preferred. However, due to technical

shortcomings, PIV is practically difficult for a moving system like a droplet under free fall. Hence, similar conditions are established by mimicking the relative velocities as encountered in drop-tower around a stationary combusting droplet suspended over a quartz rod of $150\mu m$ diameter. The pendant experimental setup also ensures that we can probe into the flame shape at low Reynolds number which is inaccessible in the drop-tower setup. **Figure 5.1(c)** depicts the experimental set-up for high-speed flow visualization. A dual-pulsed Nd:YLF laser with a wavelength of 532 nm and a pulse energy of 30 mJ per pulse was used as an illumination source. The cylindrical output beam of the laser (5 mm in diameter) is converted to a thin sheet of 1 mm thickness using a sheet making optics. The seeding particles of diethyl hexa sebacate (DEHS) (size 1–3 μm, density $\rho = 912 \ kg/m^3$) oil droplets are introduced near the fan at the bottom of the wind-tunnel using *Lavision* seeder. The seeded air is then carried vertically upwards vertically upwards through the air-flow generated by the fan and is passed through a honeycomb section to reduce the inherent flow inhomogeneities. A Photron model SA5 (frame rate 2 KHz at 1024X1024 pixel resolution) camera coupled with 100 mm Tokina macro lens is used to capture the instantaneous images. Furthermore, a 532 nm band-pass filter is coupled to the camera lens. The optical axis of the camera was aligned orthogonally to the horizontal axis of the laser sheet. The camera and laser were synchronized via a programmable tuning unit (PTU) to operate in double-frame mode. The laser pulse-separation timescale ($dt{\sim}150\mu s$) is chosen such that spatial displacement of the seeder particles in the dual-frame remain $< (1/4)$ of the interrogation window size [87], [104], [105].

5.2   Image processing and data analysis

Droplet Shape: The acquired droplet gray scale images are converted to binary, using Otsu Thresholding. The binary format is utilized to extract the instantaneous droplet area and shape descriptors (aspect ratio and centroid). The droplet diameter (d) is evaluated by equating the instantaneous droplet area to that of a circle i.e. $A_d = \pi d^2$.

Flame Heat Release (HR): High-speed OH^* chemiluminescence flame imaging enables quantitative assessment of the flame location and flame heat release (HR). Intensity thresholding technique is employed for flame heat release (Q) evaluation.

Flame boundary isolated based on a cutoff intensity (I). Pixels (i, j) with intensity $\geq$ I are ascribed with binary value 1, and those with intensity $< I$ are allocated 0. The resultant binary area is used to calculate the instantaneous line-of-sight flame area (A_f). This area is then superimposed with the corresponding actual raw image to evaluate $\overline{I_f}$,the flame average intensity. Further, the instantaneous flame heat release is evaluated as $Q = \overline{I_f} A_f$.

Note that for the drop-tower experiments, the presented data is ensemble averaged over $10 - 15$ runs with experimental uncertainty between ± 5 to $\pm 8\%$.

Vector-field from Particle Image Velocimetry (PIV): The recorded double frame Mie scattering images are processed to obtain instantaneous vector fields. The processing is carried out using Lavision Davis 8.4 software by applying standard vector field algorithm. Velocity vectors are calculated by cross-correlation method, using multiple passes, with two passes for an initial interrogation window of 64 x 64 pixels with 50% overlap, followed by 3 passes for a final window size of 32 x 32 pixels, with 75% overlap. The uncertainty of the vector field thus evaluated is $\approx \pm 3.0\%$ [87], [104], [105].

5.3 Global Observations

Droplet acceleration under the gravity ensues temporally varying relative motion of the surrounding gas phase. Consequently, the temporal variation of droplet shape and flame dynamics can also be formulated in terms of Reynolds number (Re) variation. The droplet in drop-tower facility initially experiences small velocity increments ($0 < Re < 5$). It is expected that during this period of flight, the natural convection effect is still dominant, and the flame retains the full envelope (**Figure 5.2c**). The effect of forced convection arising from the relative motion as compared to buoyancy is characterized using the Richardson Number; $Ri = Gr/Re^2$, here $Re = V_d d_0 / \nu$ is the Reynolds number and $Gr = g\beta(T_f - T_0)d_0^3/\nu^2$ is the Grashoff Number. The value of Ri (~40)
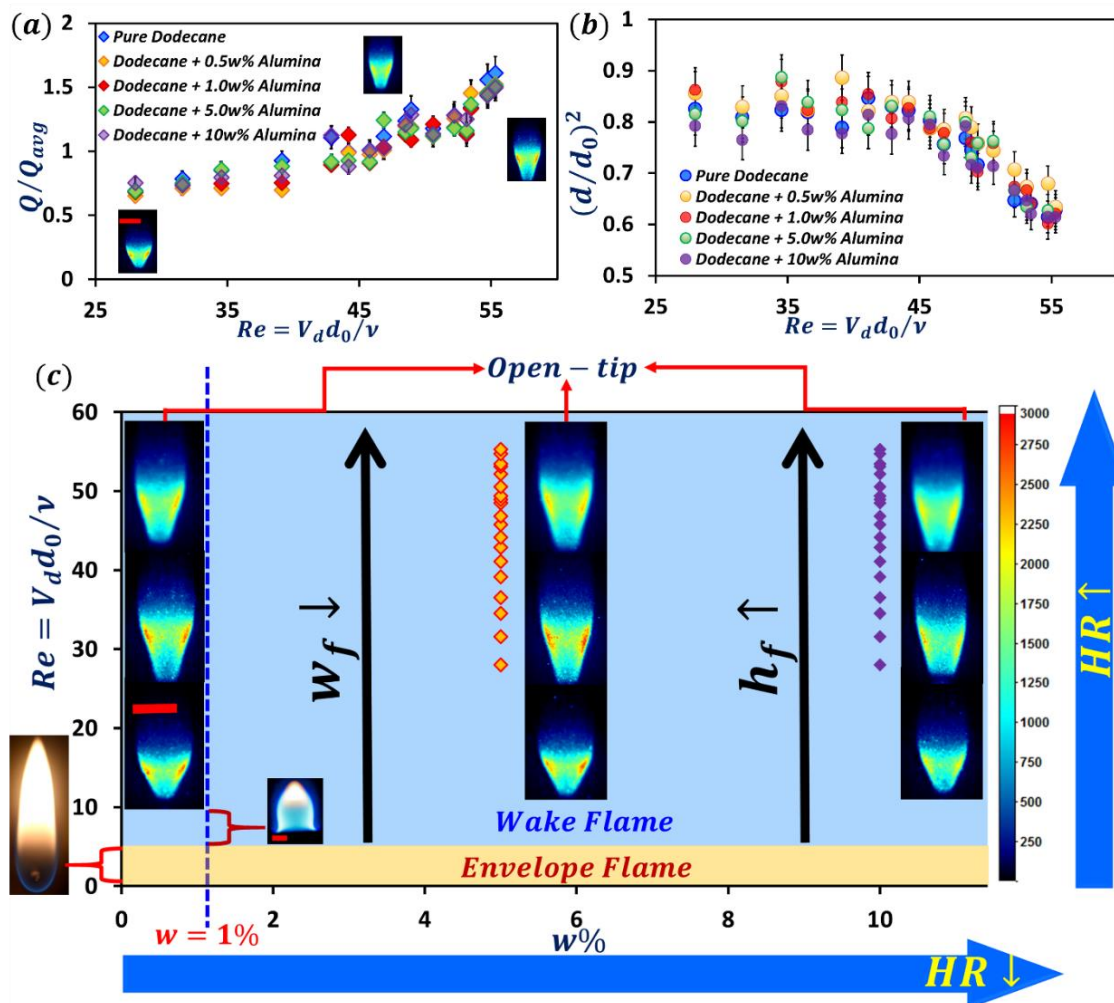
Figure 5.2. (a) Variation of flame heat release with dynamic variation of Reynolds number Re during droplet acceleration. (b) Normalized droplet regression throughout the droplet flight-time. (c) Regime-map representing flame characteristics for varying particle loading rates. Color map provides the intensity counts of the wake flame. All scale bars represent 2mm.

for low Re is rather large indicating conclusively dominance of buoyancy. It is also to be noted that the envelope flame is buoyant diffusion in nature (characteristic yellow color) with the characteristic tear drop shape. This part of the flame structure was quantified in the pendant droplet setup (Fig. 1c) due to technical limitations of imaging at a large height in the drop-tower facility (Fig. 1a).

However, with passage of time, the droplet velocity increases leading to enhanced Reynolds Number ($18 < Re < 60$). During this regime, Ri is found to vary between $\sim(0.1 - 0.5)$ suggesting increased dominance of forced convection over natural

convection. The flame first undergoes a transition ($Re > 5$) from a full envelope to a wake structure. The flame undergoes complete extinction at the forward stagnation point and subsequently changes its color to pale blue suggestive of intense premixing in the wake. The flame exhibits closed tip for 5<Re<10. The flame shape migrates to open brush beyond Re>10. **Figure 5.2(b)** illustrates the high-speed snapshots of the free-falling dodecane droplet flame which phenomenologically resembles a wake flame with open tip for Re>10. The droplet exhibits a blue wake-flame anchored at a height of $\sim 0.5mm$ from the rear stagnation point. In the wake flame regime, with further increase in Re (Re>18), flame topography exhibits increase in height h_f and reduction in width w_f during the fall suggesting a dynamic self-tuning mechanism (**Figure 5.2c**). Furthermore, flame HR exhibits continuous increase with Re (**Figure 5.2b**) which is explained in later sections.

On the other hand, droplet flames of nanofuel up to $1w\%$ PLR exhibits nominal changes in heat release (**Figure 5.2b**). However, for dense PLRs ($5w\%$ and $10w\%$), the flame HR experience $\sim 10 - 23\%$ reduction. Nonetheless, the individual flame dynamics remains phenomenologically similar to that of the pure dodecane droplet flame (**Figures 5.2a-c**).

Interestingly, for drop-tower experiments, droplet diameter showcases $\sim 20\%$ reduction during the total flight-time (**Fig. 5.2a**). Interestingly, the rate of diameter regression is found to be similar across all the functional droplets i.e. addition of alumina particles does not lead to variation in droplet evaporation rate. For this minor variation in droplet dimension, flame characteristic can be solely considered due to temporally evolving relative motion which inherently affects the hydrodynamic stability of the attached flame. Three pertinent facets of the droplet flame dynamics are outlined; **(i)** Flame extinction at forward stagnation point; envelope to wake flame transition, **(ii)** Anchored wake flame near droplet rear stagnation point, and **(iii)** Self-tuning of flame topography and HR signature, (**Figure 5.2(a)**).

As mentioned before, these flame features are inextricably interlinked with the relative motion of the droplet. Therefore, the effect of the surrounding relative flow-field on the droplet flame has been investigated by a separate set of flow-visualization experiments (as explained in **Figure 5.1(c)**) for droplets suspended in pendant mode. The velocities

are varied as $V_\infty \sim (0.4m/s - 3.5m/s)$ in order to mimic the relative flow conditions of drop-tower experiments particularly to quantify the envelope to wake flame transition regime. Note that in the following sections, the pendant mode data is provided to back the experimental observations pertaining to the free-falling burning dodecane droplets. Hereinafter, the governing parameters of the delineated droplet flame dynamics are discussed and elucidated. Further, the effects of nanoparticle loading on droplet evaporation and flame HR variations are also explained.

5.4 Droplet flame structure

5.4.1 Forward Flame Extinction

Local flame extinction involves the velocity-perturbations resulting in locally strained diffusion flame which have been thoroughly established by plethora of research studies pertaining to strain/opposed-flow diffusion flames [106]–[108]. Currently, flame extinction at the droplet forward stagnation point (**Figure 5.2(a)**) suggests existence of flame strain rate higher than a critical value ($\varepsilon_{critical}$).   In the absence of forced convection, local velocity-field produced due to buoyancy results in an inherent flame strain (ε_{fb}). In order to compute the flame strain, the tangential strain rate components in the flame using a cylindrical coordinate system (**Figure 5.3(a)**) is isolated. The tangential strain rate, $\varepsilon_{\theta\theta}$ consists of two components; $\varepsilon_{\theta\theta}^1$ and $\varepsilon_{\theta\theta}^2$,

$$\varepsilon_{\theta\theta} = \varepsilon_{\theta\theta}^1 + \varepsilon_{\theta\theta}^2 \tag{5.1}$$

where $\varepsilon_{\theta\theta}^1$ arises due to the variation in radial displacement, and the $\varepsilon_{\theta\theta}^2$ is the alteration due to the circumferential displacement, **Figure 5.3a**. Cumulatively, $\varepsilon_{\theta\theta}$ is given as,

$$\varepsilon_{\theta\theta} = \frac{u_r}{r} + \frac{\partial u_\theta}{r\partial\theta} \tag{5.2}$$

u_r is the radial velocity component and u_θ is the tangential velocity component. It is to be noted that, to evaluate $\varepsilon_{\theta\theta}$, both u_r and u_θ are required. Hence, the velocity values

are incorporated from the stream-function (ψ) of *Oseen's* solution of flow over a sphere of radius r_0 [106]–[109],

$$\psi \sim \frac{Vr_0^2}{4} sin^2\theta \left[2\left(\frac{r}{r_0}\right)^2 - 3\left(\frac{r}{r_0}\right) + \left(\frac{r_0}{r}\right) \right] \tag{5.3}$$

$$\therefore \qquad u_r = \frac{1}{r^2 sin\theta} \frac{\partial \psi}{\partial \theta}, u_\theta = \frac{1}{r sin\theta} \frac{\partial \psi}{\partial r} \tag{5.4}$$

Substituting the respective values of u_r and u_θ in equation (5.2),

$$\varepsilon_{\theta\theta} = \frac{Vcos\theta}{r} \left[-\frac{3}{4}\left(\frac{r_0}{r}\right)^3 + \frac{3}{4}\left(\frac{r_0}{r}\right) \right] \tag{5.5}$$

For the case of natural buoyant flame, the value of V can be scaled as the bulk velocity generated by balancing energy terms for the inertia and buoyant forces; $\rho V^2 \sim \rho g\beta\Delta T d_f$, thus $V \sim \sqrt{g\beta(T_{flame} - T_\infty)d_f}$, g is the acceleration due to gravity, β is the thermal expansion coefficient, T_{flame} and T_∞ is the flame and ambient temperature, respectively, and d_f is the flame standoff diameter. Furthermore, for flame extinction at the forward stagnation point ($\theta \sim 180°$), r can be scaled as the flame standoff distance (r_f) in equation (5.5). Incorporating all the numerical values for a naturally buoyant flame in equation (5.5), ε_{fb} is found $\sim 30s^{-1}$.

One can argue that the above analysis solely incorporates the aerodynamics of the system without considering the variations in the thermophysical properties of the system such as density. In that case, a porous burner of radius r_0 in a uniform flow of oxidiser (V_{ox}) also provides a suitable analogy as previously discussed by Seshadri et al. [110]. The strain rate at the stagnation surface on the fuel side (ε_{fuel}) is given as,

$$\varepsilon_{fuel} = \frac{V_{fuel}}{2r_f} \left(1 + \frac{V_{ox}\sqrt{\rho_{ox}}}{V_{fuel}\sqrt{\rho_{fuel}}} \right), \tag{5.6}$$

V_{fuel} is the fuel inlet velocity, ρ_{ox} and ρ_{fuel} are the oxidizer and fuel densities, respectively. V_{fuel} will scale as the diffusion velocity $\sim D_{DD/air}/r_f$ ($D_{DD/air}$ is the dodecane vapour diffusivity constant in the air) and for critical strain rate V_{ox} can be scaled as the natural convection velocity $\sim \sqrt{g\beta(T_{flame} - T_\infty)d_f}$. Equation (5.6) results $\varepsilon_{fuel} \sim 56\ s^{-1}$, similar value to that of equation (5.5). Experimentally, the transition from envelope to wake flame occurs for oxidizer velocity $\sim 0.5 m/s$. Substitution of this velocity in Equation 5.5 results in a strain rate value $\varepsilon \sim 67 s^{-1}$ (**Figure 5.3(b)**). It is therefore implied that the critical strain, $\varepsilon_{critical}$ at which forward extinction occurs lies somewhere in between $56\ s^{-1}$ to $67\ s^{-1}$. For falling droplet, the velocity regime, $V_d \sim 1.5 m/s - 4 m/s$ is always greater than the required value necessary to surpass $\varepsilon_{critical}$. Hence, the flame always resides in the droplet wake with forward extinction.
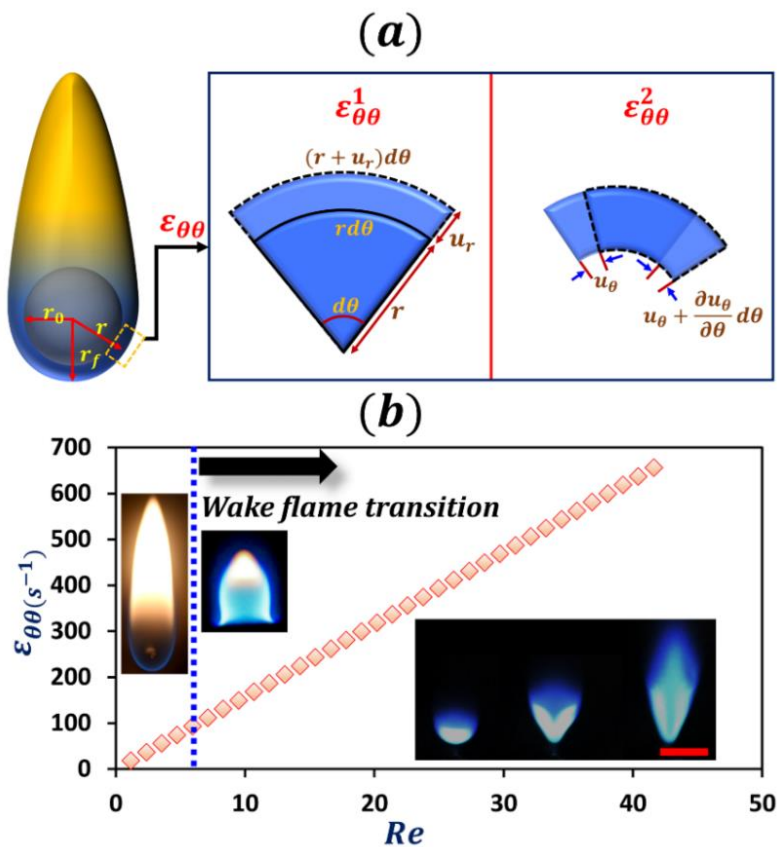
Figure 5.3.(a) Illustrative diagram of the fluid element under flow-train. (b) Region map of the flame depicting envelope to wake flame transition. Scale bar presents 5mm.

5.4.2 Dynamics of Wake Flame

(a) Cold-flow Case
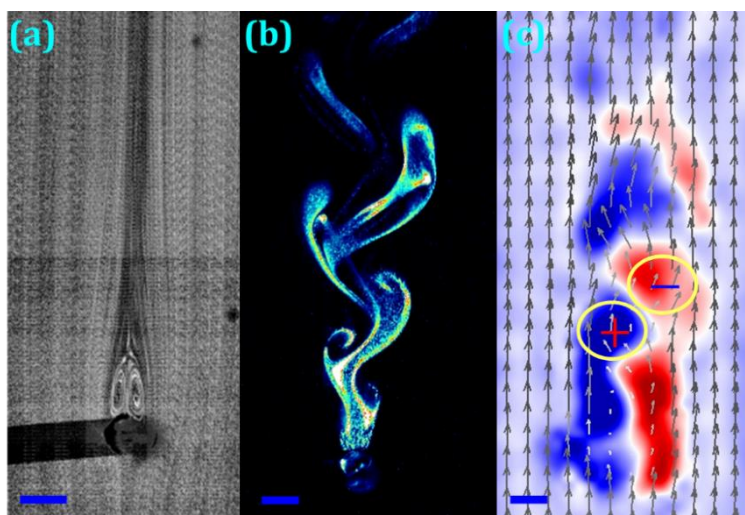
Figure 5.4. (a) Recirculation bubble at the rear droplet stagnation point for $Re_{f,cold}{\sim}37$. The average-field is generated over 500 Mie-scattering raw-images. (b) Instantaneous high-speed snapshot of the flow-flied Bernard Von-Karman (BVK) instability for $Re_{f,cold}{\sim}360$. PIV measurements depicting local vortex shedding for (c) $Re_{f,cold}{\sim}360$. All scale bars represent 2 mm.

The previous discussion imparted the physical understanding of the local flame extinction. Here, the mechanism of wake flame stabilization is explained. Numerous research [111], [112] have frequently mentioned that flame stabilization in a high velocity stream is a function of certain flow conditions. In the context of the current work, this discussion is necessary to highlight the simultaneous heat and mass transfer dynamics (droplet combustion) along with the influence of the flow field created via the droplet relative motion. Here, dodecane droplet acts both as a bluff-body as a well as a fuel source determining the flame HR and topology simultaneously.

Proceeding with the characterization of the cold-flow (non-combusting droplet) cases, the flow-field reveals a well-established recirculation bubble zone downstream of the droplet (**Figure 5.4(a)**). For the cold flow cases ($V_\infty{\sim}0.4m/s - 3.5m/s$), the Reynolds number ($Re_{f,cold} = V_\infty d_0/v_\infty$) varies as ${\sim}(37 - 360)$. At higher values of $Re_{f,cold} >$ 40, the wake region should exhibit *Bernard Von-Karman (BVK)* instability in the form of asymmetric vortex shedding as evident in previous literatures. *BVK* instability

predominantly appears for higher Reynolds number values ($Re_{f,cold} > 40$) where the eddies attached to bluff body are alternatively convected away in the form of opposite signed vorticities. For brevity, the BVK instability and its origin has not been discussed to the fullest and readers are advised to look into [113], [114]. Consequently, the experimental measurements corroborate the existence of *BVK* instability for the cold flow in the form of continuous vortex shedding (**Figure 5.4b-d**) at the characteristic frequency $f = St \frac{V_\infty}{d_0} \sim (180 - 400)\, Hz$, St is the Strouhal Number ~ 0.16 and is independent of the flow Reynolds number [115].

Thus, existence of Recirculation zone (RZ) in the cold flow cases supports the argument of flame stabilization regime in the flow-field. The recirculation zone behind a bluff body kinematically provides a low velocity region for flame holding. RZ acts as a premixing zone where evaporated fuel vapor (from the droplet) is fed from the droplet surface and instantaneously mixed with the recirculating air thereby providing a continuous supply of air-fuel mixture [38]. RZ is crucial for wake flame as it circulates heat from downstream hot product gases to droplet upstream making the air-fuel mixture flammable, thus maintaining a constant ignition source. Note that while the cold flow experiments have been conducted using a pendant droplet, the results translate directly to the free-falling case as well since the Reynolds numbers are well matched.

(b) Influence of flame heat release
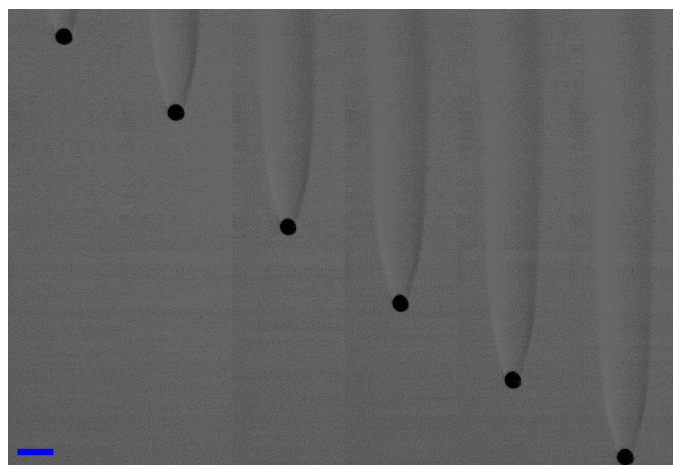
Figure 5.5. High-speed Schlieren Imaging for falling and combusting dodecane droplet. Scale bar represents 5mm.

In the previous section the cold flow-field has been characterized. Next, the influence of the flame exothermicity and the respective variations in the flow-field for the free-falling droplet in the drop tower facility is explained. Previous research investigations [111], [112] have highlighted the reduction in BVK instability and weakening of turbulence levels in combusting flows. Similarly, here, the instabilities previously seen in the cold flow is found to be diminished, as the flame exhibits a globally laminar and quiescent structure as mentioned before. However, in order reaffirm these chemiluminescence findings, Schlieren imaging of the combusting droplet is also conducted. The schlieren images (**Figure 5.5**) of the free-falling burning droplet depicts long laminar wake with no detectable coherent flow fluctuations. In other words, the wake instabilities are stabilized due to flame heat release. Moreover, this outcome can be explained from the generalized vorticity transport equation [112], given as

$$\frac{D\xi}{Dt} = (\xi \cdot \nabla)V - \xi(\nabla \cdot V) + \frac{\nabla\rho \times \nabla p}{\rho^2} + \nu\nabla^2\xi \qquad (5.7)$$

ξ is the vorticity, V is the flow velocity, ρ is the fluid density, p is the pressure, On the right-hand side of equation (7), first term (I) denotes the vortex stretching, second term (II) is the gas expansion term, third term (III) represents the baroclinic torque, viscous diffusion is represented by the lass term (IV). For axisymmetric, incompressible, and isobaric flow-fields, effective parameter for redistribution of vorticity is governed by the viscous diffusion term (IV). Substantial increase in the kinematic viscosity ($\sim O(10^1)$) of the gas at higher temperature i.e. in the presence of the flame, ensures rapid diffusion of vorticity thereby minimizing local flame-perturbations.

The downstream flow-field of a bluff-body comprises the wake region. However, expansion of hot gaseous products of flame alters the wake to a jet [111], [112]. RZ near the rear droplet stagnation point sustains continuous supply of fuel-vapour and air as well as sustains the continuous ignition of the same [27], [32]. The air-fuel mixture is convected downstream for complete combustion. Hence, the RZ can be considered as an inlet locale for dodecane vapour (**Figure 5.6**). The high-speed snapshots of the droplet flame also exhibit a close resemblance, phenomenologically, to a laminar jet-flame with an open-tip unlike the naturally buoyant diffusion flames (as mentioned

before). The flame as mentioned earlier is primarily premixed unlike the buoyant counterpart. The degree of premixedness varies along the flame length. Next, drawing an analogy with the round-jet flow expansion, insights into the dynamic flame characteristics are provided. The famous analytical work of Schlichting [40] assuming a point momentum source suggests that jet half-width is proportional to Re^{-1} [116], [117]. Furthermore, the corresponding spread of the jet (with downstream air-
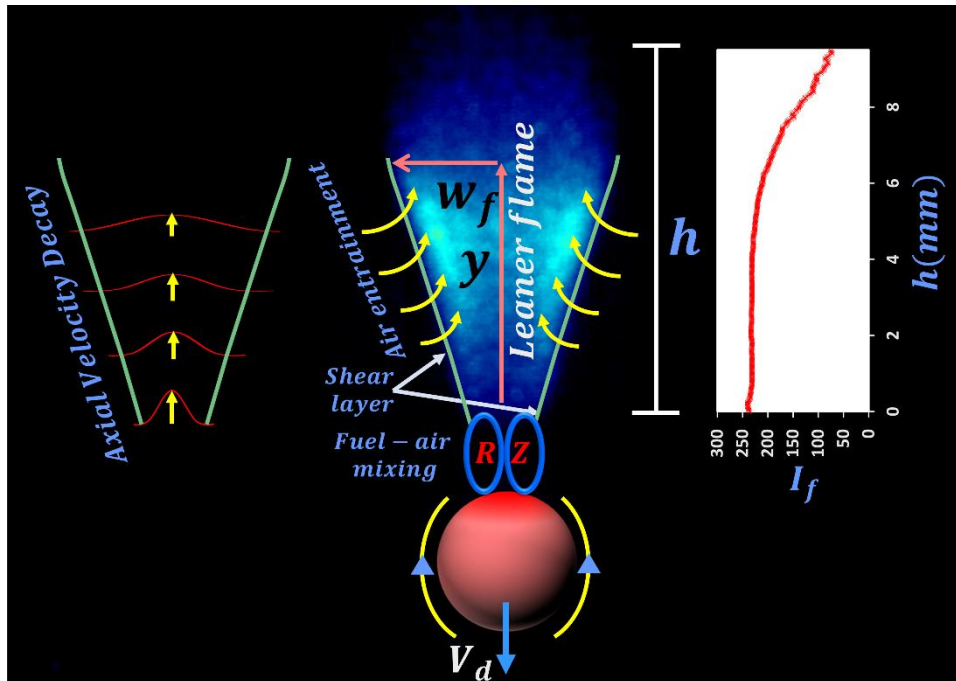
Figure 5.6. Pictorial representation of combustion of falling droplet with velocity V_d. RZ represents the recirculation zone at rear stagnation point. The droplet flame is analogous to a round jet with axial expansion and velocity decay. RZ provides the inlet for fuel-air charge. Along the axial direction (h), continuous entrainment of air results in leaner flame which is depicted in the spatial decrease of $OH*$ intensity (I_f).

entrainment) increases linearly along the axial location (y) for constant flow conditions; ; $w/w_{jet} = C(y - y_{vo})/Re$, where w_{jet} is the inlet jet radius and y_{vo} is the respective virtual origin . Interestingly, experimental results indicate similar features for dodecane droplet flame. Spatial variation of the flame width for a fixed Re follows approximately a linear trend (**Figure 7(b)**). Continuous downstream air-entrainment results in relatively leaner mixture along the flame length. This is corroborated from the OH^* chemiluminescence signature strength along the flame length, which shows a monotonic

decay (**Figure 5.6**) in HR. Furthermore, variation of flame width (evaluated from the PIV results at $y/d_0 \sim 5$) for increasing Re values is presented in **Figure 5.7(a)**, exhibits an inverse dependence as expected for a round jet.
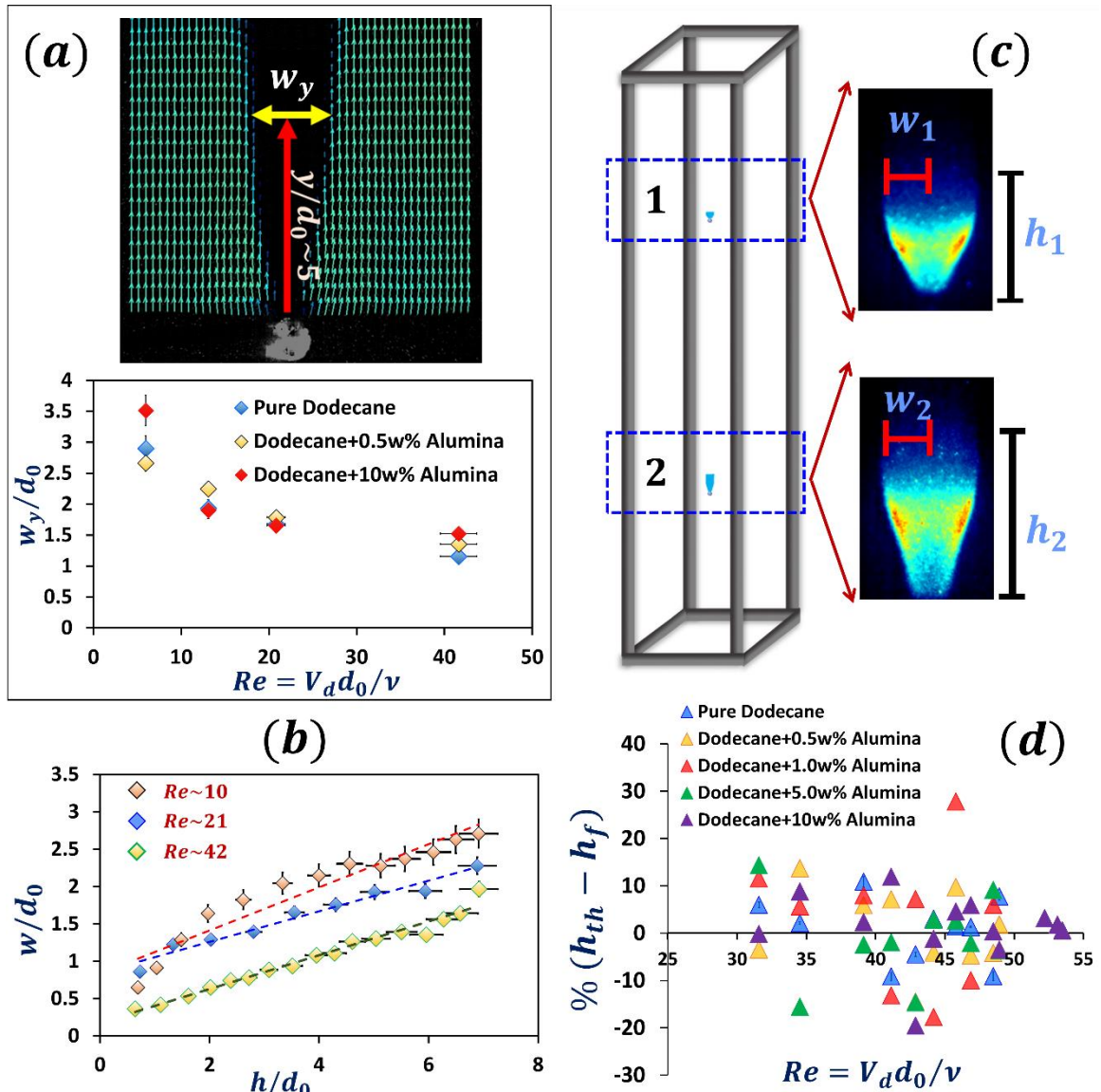
Figure 5.7. (a). Variation of flame width calculated a distance $h/d_0 \sim 5$ for different Re values. (b) Variation of flame width along the flame height. (c) Schematic illustration of flame evolution between Location 1 and Location 2. (d) Percentage variation of the experimental values of flame height from theoretical values evaluated from equation (5.12) for Re variation.

Spatio-temporal variation of flame topography with Re showcases increase in h_f and reduction of w_f. The topographical self-tuning of droplet flame suggests an inherent

hydrodynamic modulation similar to a jet-flow. Theoretically, using a round-jet analogy, half-width of flame with height h_1 for Re_1 (at location 1, **Figure 7(c)**) can be predicted as

$$\frac{w_{f1}}{r_{RZ}} \sim \frac{Ch_1}{Re_1} \tag{5.8}$$

The flame volume can be approximated to that of a cone

$$Vol_{f1} \sim \frac{1}{3}\pi w_{f1}^2 h_1 \tag{5.9}$$

The fuel-charge is fed through RZ of area A_{RZ} at a rate of $\sim \rho_{RZ}A_{RZ}V_{d1}$. Note that the A_{RZ} remains mostly constant for the range of Re in the current work. Hence, the timescale associated with fuel-charge residence in the reaction zone for combustion can be given as

$$t_{res1} = \frac{Vol_{f1}}{\rho_{RZ}A_{RZ}V_{d1}} = \frac{\frac{1}{3}\pi w_{f1}^2 h_1}{\rho_{RZ}A_{RZ}V_{d1}} \tag{5.10}$$

For Re_2 (at location 2, **Figure 5.7(c)**) can be predicted

$$t_{res2} = \frac{\frac{1}{3}\pi w_{f2}^2 h_2}{\rho_{RZ}A_{RZ}V_{d2}} \tag{5.11}$$

In the absence of enhanced flame-stretch effects, complete combustion of a fixed fuel is determined by its residence timescale in the combustion zone. Hence, for dodecane fuel-vapour, both residence times should be equal. Thus, equating both timescales and incorporating half-width expression from equation (5.8),

$$\frac{h_2}{h_1} = \frac{V_{d2}}{V_{d1}} \tag{5.12}$$

Equation 5.12 strikingly provides a linear relationship with the droplet velocity. **Figure 5.7(d)** presents the percentage variation of flame height (h_{th}) from theoretically predicted values of equation (5.12). The experimental values are found under $\pm 15\%$ deviation from the theoretical values. The error is primarily positive which indicates overestimation of the flame height (Equation 5.12). The positive source of errors usually crops from enhanced air entrainment with Re which should lower the burning length-scale h in the current problem.

Next, the continuous increase in the flame HR ($Q = \overline{I_f} A_f$) with dynamic variation of Re (**Figure 5.2a**) needs to be investigated. Flame HR as calculated in the current work, is dependent on two parameters; $\overline{I_f}$ and A_f. Instantaneous variation of these parameters is presented in **Figure 5.8(a)** and **(b)**, respectively. It is important to note that the A_f values exhibit continuous increase (due to increase in h_f as discussed previously), however, average intensity signatures remain nearly constant ($\pm 5\% - 10\%$) throughout the Re regime for a particular type of fuel (pure or functional) droplet. Therefore, this outcome further proves that increase in flame HR is predominantly a hydrodynamic effect which has been established using round-jet analogy.

5.5 Droplet Burning rate

The droplet regression rate exhibits minimal variation throughout the droplet fight-time and across nanoparticle loading. This observation, as mentioned before is intriguing and counter-intuitive at the same time. Addition of NPs is a highly sought research field in the combustion community due to their role in heat release enhancement and secondary atomization (via internal ebullition) [30], [44], [100], [118]. However, in the current scenario, it is evident that the addition of NPs does not initiate internal boiling. However, addition of NPs does modulate the gasification rate for higher values of PLR.

Accordingly, first the droplet regression rate is discussed. Droplet total vaporization rate ($\dot{m}$) is inextricably linked with the droplet surface area ($4\pi r_d^2$) exposed to the flame. Contrarily, the droplet real stagnation point resides closer to the wake flame, thereby, vaporization flux in this area is the highest (also previously mentioned [27]). This suggests that in the absence of the full droplet coverage by an envelope flame, the heat

input to the liquid-system decreases. Experimentally, the rear stagnation region of the droplet is found to be $\sim 10\%$ of the droplet diameter for pure DD droplets i.e. $\Delta l_{DD}/r \sim \Delta l_{NPs}/r \sim 0.25$ (**Figure 5.8(c)** and (**d**)). Hence, this region contributes in the most in the evaporation rate. However, due to the smaller area of this local region, the respective global temporal evolution of droplet diameter does not reflect the similar change.
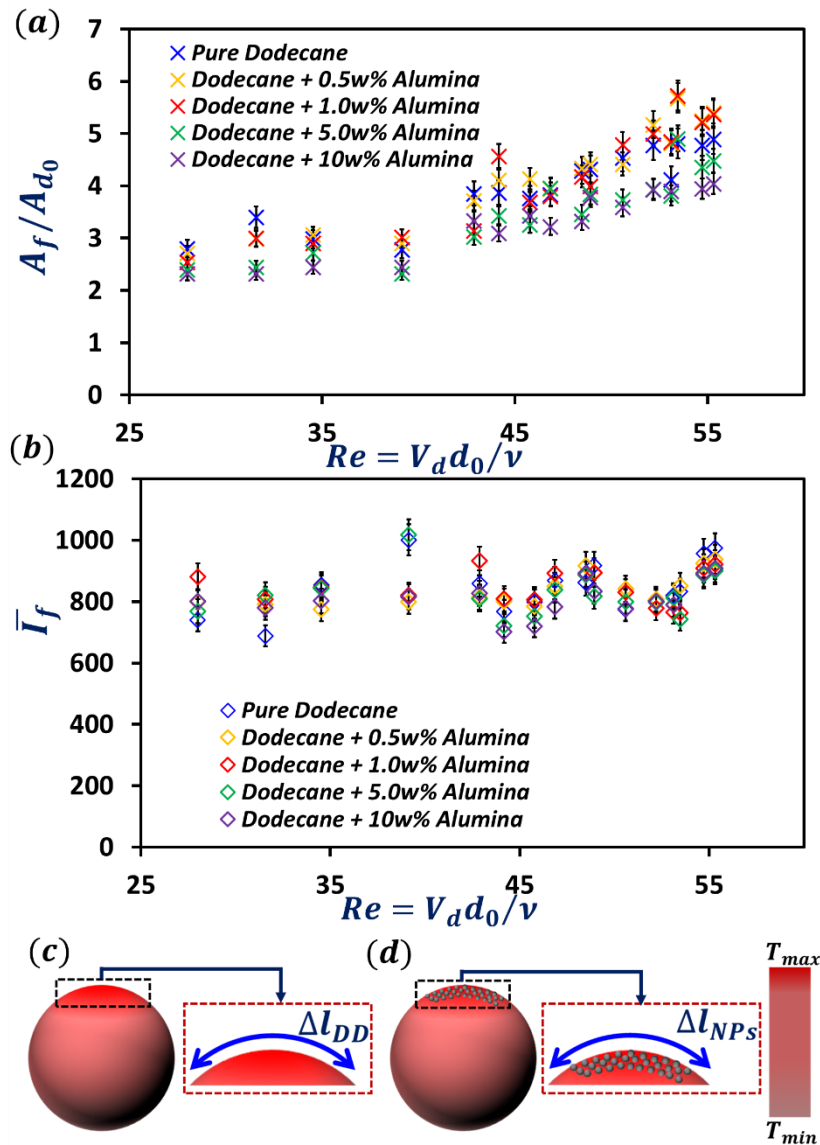
Figure 5.8. (a) Evolution of flame area with Re. (b) Average flame intensity variation with Re. Spatial variation of temperature of falling droplets undergoing combustion (c) Pure dodecane droplet. (d) Particle laden droplet.

5.6 Variation of flame heat release with particle addition

Preferential heating at the droplet surface as described previously does not show global effect on the regression rate. However, the flame heat release exhibits reduction for $5w\%$ and $10w\%$ PLRs. Reduction in the flame HR is the manifestation of the reduced fuel vaporization rate with NP loading. Droplet burning rate for pure dodecane considering classical $d^2 - law$ [66], is given as

$$\dot{m} = \frac{2\pi k_g r_0\, Nu}{c_{pg}} \ln\left(1 + B\right) \tag{5.13}$$

where c_{pg} and k_g are the fuel vapour specific heat capacity and the thermal conductivity of the air-fuel gaseous mixture, respectively, calculated at an average value of flame and droplet surface temperatures, $\bar{T} = (T_s + T_f)/2$ [66]. In the presence of external flow-field, Nusselt number is given as $Nu = 2\left[1 + \frac{0.276\, Re^{1/2} Pr^{1/3}}{\left(1 + 1.232/(RePr^{4/3})\right)^{1/2}}\right]$ [17], [66] which increases from 4.5 to 5.6 for Re range $\sim(25 - 55)$. B is the Spalding heat transfer number, given as $\frac{(\Delta h_c/v) + c_{pg}(T_\infty - T_s)}{h_{fg}}$. As previously discussed, droplet mass depletion is predominantly in a smaller region at rear droplet stagnation point (**Figure 5.8(c)**). Therefore, evaporation rate for this region (A_{DD}) can be given as

$$\dot{m}|_{DD} = \dot{m} \frac{A_{DD}}{4\pi r_0^2} \tag{5.14}$$

From spherical-cap geometry, $A_{DD} = 2\pi r_0^2 (1 - \cos\theta)$, where $\theta \sim 14°$ is the half-angle made by sector at the center. Note that $A_{DD}/4\pi r_0^2$ is ~ 0.02. This local depletion rate is found $\sim O(10^{-8}) kg/s$. $\dot{m}|_{DD}$ will increase by 24% for Re increase from 18 to 55. This also will result in some variation in $\bar{I}_f$ as seen in **Figure 5.8b.**

For the nanofuel droplets, accumulation of alumina NPs at the liquid-gas interface provides a physical barrier for the fuel evaporation. As a result, the evaporation mechanism is analogous to evaporation through a porous media, a previously mentioned by Pandey et al. [100]. Nanofuel local evaporation rate ($\dot{m}|_{NPs}$) through the skeletal network of NP aggregates is given as [100],

$$\dot{m}|_{NPs} = -2\pi r^2 (1 - \cos\theta)\frac{k\Delta P_{capillary}}{\mu\tau_{crust}} \tag{5.15}$$

$\Delta P_{capillary} = -2\sigma/a_p \sim -2MPa$, μ is effective fuel viscosity, k is the permeability constant from Carmen-Kozeny relation $k = \left(\frac{1}{180}\right)\frac{(1-\varphi)^3}{\varphi^2}a_P{}^2$ (φ is the particle packing fraction at the droplet surface ~ 0.52 [57]), and τ_{crust} is the scale of the particle accumulation thickness. Assuming the similar internal velocity-field, Pathak et al. [50] estimated the aggregate sizes of 50-fold form quickly for a nanosuspension droplet. Number density of 50-fold aggregates are higher for $5w\%$ and $10w\%$ is $\sim O(10^1)$ larger than that of the $w \leq 1\%$. As a result, droplets with dense PLRs will be susceptible to the surface precipitation of NP leading to skeletal porous structure. Droplets with lower PLR does not form skeletal network within the experimental timescale. Thus, for $5w\%$ and $10w\%$, accumulation thickness τ_{crust} can be taken as $\sim 50a_p \sim 1\mu m$. The calculated $\dot{m}|_{NPs}$ for $5w\% - 10w\%$ are found to be $\sim 0.5\dot{m}|_{DD}$. The lower rate of gasification does lead to lower flame surface area. Consequently, the flame HR decreases in nanofuel droplets compared to the pure counterpart.

Once again note that, the mass vaporization occurs only over 2% of the total droplet surface area ($A_{NP}/4\pi r_0^2$) i.e. only in a small region near the rear stagnation point. Thus, this change in $\dot{m}|_{NPs}$ is too small to be reflected in the global diameter regression rate (**Figure 5.2a**). In other words, the diameter regression is not sensitive to such variations in vaporization rate unlike a full envelope flame where the total droplet surface area participates in gasification.

5.7 Suppression of internal ebullition

Continuing with the other important observation of internal boiling suppression; the two plausible factors that may entail are either (i) lack of critical vapour phase nuclei or (ii) lack of critical energy flux to form the critical bubble nuclei. Timescale, t_{agg}, associated to the formation of NP aggregates can evaluated using either orthokinetic or perikinetic aggregation mechanism [119]. Droplet motion under the effect of gravity

ensures a relative motion at its surface which results in surface shear and eventually an internal velocity field ($u_{internal} = \sqrt{\frac{\mu_0 \rho_0}{\mu_l \rho_l}} V_\infty$ (V_∞ is the outside air-velocity) [119]).
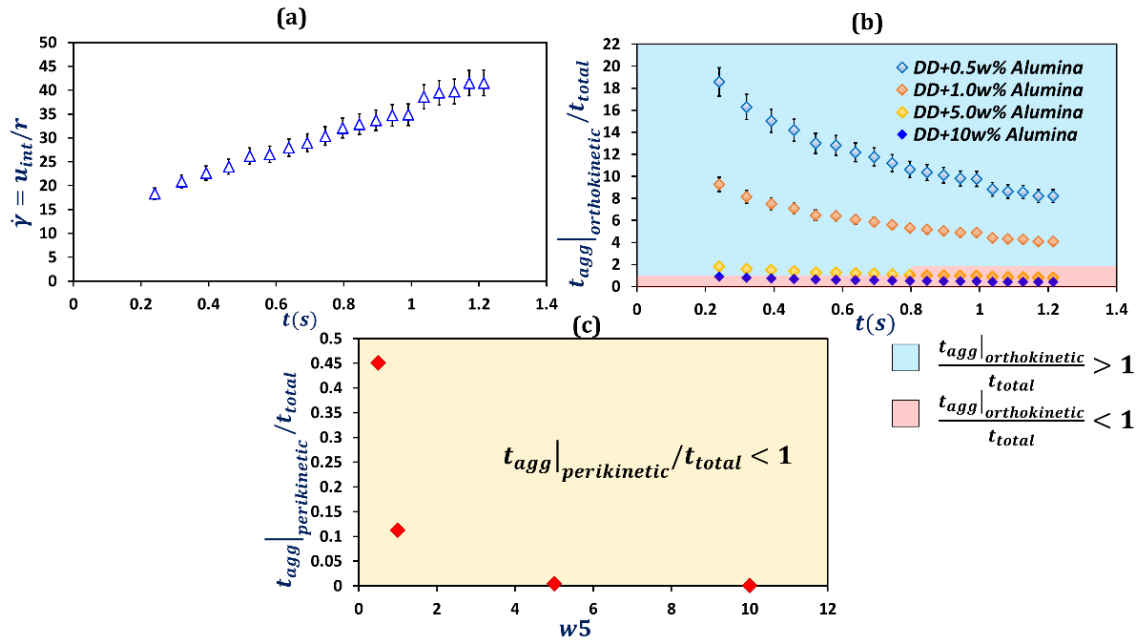
Figure 5.9. (a) Temporal varying internal shear rate ($\dot{\gamma}$) for falling droplet. (b) Timescale associated with orthokinetic particle aggregation during droplet flight. (c) falling droplet. (b) Timescale associated with perikinetic particle aggregation.

Alumina NPs are subjected shear forces ($\dot{\gamma}$, shear rate inside the droplet is given as $\sim u_{internal}/r_0$,) due to the internal velocity field resulting in enhanced particle collisions and agglomeration. The temporal variation of the internal shear rate ($\dot{\gamma}$) as shown in **Figure 5.9(a),** arises due to droplet acceleration due to the free-fall. The timescale necessary for orthokinetic aggregation is given as [99]

$$t_{agg}\big|_{orthokinetic} = \frac{\pi D}{4\dot{\gamma}(3-D)}(\varphi_0^{-1} - 1) \qquad (5.16)$$

where D is the fractal dimensionality [99]. The orthokinetic timescale is also time-dependent scale as $\dot{\gamma}$ is varying with time. For the nanofuel droplets, $t_{agg}\big|_{orthokinetic}/t_{total}$ for the droplet lifetime is given in **Figure 5.9(b)**. These results are rather interesting and suggest that particle aggregation will not occur ($t_{agg}\big|_{orthokinetic}/$

$t_{total} > 1$, Blue region, **Figure 5.9(b)**) for $w = 0.5\% - 1\%$. However, for $w = 5\%$ orthokinetic aggregation will be dominant post $\Delta t \sim 0.5 t_{total}$. Contrarily, for $w = 10\%$ orthokinetic aggregation will remain dominant throughout the droplet lifetime $(t_{agg}|_{orthokinetic}/t_{total} < 1$, Pink region, **Figure 5.9(b)**).

Next the timescale related to the perikinetic aggregation mechanism, given as

$$t_{agg}|_{perikinetic} = \frac{\pi \mu a_p^3}{k_b T_s} \varphi_0^{3/(D-3)} \tag{5.17}$$

k_b is the Boltzman constant. This evaluation suggests that the particle aggregation with this mechanism will occur for all PLRs ($t_{agg}|_{orthokinetic}/t_{total} < 1$, **Figure 5.9(c)**). Therefore, either way aggregate formation is probabilistic in the nanofuel droplets.

Above is the first order estimation for the existence of heterogeneous nucleation sites in the present case. Thus, the second argument of insufficient energy flux should be looked into. Attenuation of the droplet burning rate due to wake flame (non-envelope flame) presumably indicates substantial heat input reduction to the nucleation sites (NPs aggregates). Theoretically, the bubble growth time-scale can be formulated as,

$$\frac{dm_{bubble}}{dt} h_{fg} = f \dot{Q}_{abs} \tag{5.18}$$

Therefore, time scale for bubble growth to any radius r_{bubble} can be given as

$$t_{bubble} = \frac{\frac{4}{3} \pi \rho_l (r_{bubble}^3 - a_{agg}^3) h_{fg}}{f \dot{Q}_{abs}} \tag{5.19}$$

$\dot{Q}_{abs}$ is the absorbed energy by the aggregates from the surrounding flame, and f is the absorption efficiency which is a particle property. From equation (5.18), t_{bubble} is inversely proportional to the energy input from the flame. Due to area reduction $\dot{Q}_{abs}|_{wake}$ can be scaled as $\sim (A_{NPs}/A_d)\dot{Q}_{abs}|_{envelope}$. Subsequently, bubble growth timescale by increases by $\sim O(10^2) second$. This thereby answers the question that

formation of bubble within the droplet burning lifetime is impossible for the free-falling drop for the range of relative velocities encountered.

5.8   Conclusion

The present study investigates the dynamics self-tuning of free-falling droplet flame and the mechanisms thereof using a drop tower facility. A fuel droplet in the initial stages of its free fall exhibits very low Reynolds number ($Re < 5$), thereby assuring a full envelope buoyant diffusion flame which is sooty yellow in color. However, with passage of time, the droplet velocity increases leading to enhanced Reynolds Number ($5 < Re < 60$). During this regime, Ri is found to vary between $\sim(0.1 - 0.5)$ suggesting increased dominance of forced convection over natural convection. The flame first undergoes a transition ($Re > 5$) from a full envelope to a wake structure. The flame undergoes complete extinction at the forward stagnation point and subsequently changes its color to pale blue suggestive of intense premixing in the wake. The flame exhibits closed tip for $5 < Re < 10$. The flame shape migrates to open brush beyond $Re > 10$. Droplet flame exhibit dynamic topological self-tuning during the free-fall; increase in height h_f and reduction in width w_f. The flame dynamics of all particle loading cases remains phenomenologically same as compared to the pure dodecane droplet flame. Current work constituent three pertinent feature pertaining the droplet flame dynamics; (i)Flame transition from envelope-to-wake, (ii) Flame stabilization at droplet rear stagnation point, and (iii) Dynamic Self-tuning of flame topography and HR, (**Figure 5.2(a)**). The topological self-tuning of the droplet flame is found to be primarily hydrodynamic by implementing a round-jet analogy.

In the current work, wake-flame reduces the global energy input (due to reduction in droplet exposed area to the flame) thereby reducing the droplet burning rate (compared to full-envelope flame). Furthermore, diameter reduction if found same irrespective of the particle loading. As the droplet rear stagnation point is closest to the wake-flame, evaporation rate at this local region (2% of total droplet surface area) is maximum which does not get reflected in $(d/d_0)^2$ variation (**Figure 5.2b**). Inclusion of particle at low particle loading $\leq 1w\%$ exhibit minimal changes in flame HR. Contrarily, the flame HR experience $\sim 10 - 23\%$ reduction for dense loading ($5w\%$ and $10w\%$). Theoretical evaluation of the local evaporation rate suggests that dominant surface

precipitation of NPs for $5w\%$ and $10w\%$ can enable the formation of porous particle layer on the droplet. This further induces fuel vaporization through a porous media thereby reducing the evaporation rate and subsequently the flame HR. Internal ebullition is found to suppress for the particle laden droplets even though the aggregation timescales are less than the droplet flight-time. Using energy balance, it is shown that in the absence of sufficient energy (due to wake flame), the timescale associated with bubble formation increases by two orders surpassing the droplet flight time.

Chapter 6

Dynamic self-tuning, flickering and shedding in buoyant droplet diffusion flames under acoustic excitation

Flicker and flare of buoyant diffusion flames has been one of the fascinating problem statements associated with combustion research since 1900s. The low frequency band of flickering varying between $10 - 20\,Hz$ is found to be independent of the nozzle diameter and fuel type [34]. This prevalent and unique nature of diffusion flame oscillations stems from gravitational buoyancy. Research studies [34], [38], [120] have reported the presence of two types of vortices; smaller vortices inside the flame zone and large vortices outside the luminous zone. Continuous roll-ups of these local instabilities; toroidal vortices, impart the global flame oscillations [34], [35], [37]–[39]. Research studies also provided the theoretical estimate of the previously stated low frequency instabilities in such flames. For pool fires and jet flames, studies [35], [37], [39] have shown that the shedding frequencies for these vortex roll-ups are proportional to $\sqrt{g/l_0}$, where g is the acceleration due to gravity, and l_0 is the characteristic length scale. However, this scaling does not account for instances where this characteristic length is dynamic; like in droplet combustion. Research studies pertaining to the instabilities of droplet diffusion flames till date remain sparse. Furthermore, the augmentation/attenuation of these instabilities due to external excitations are not fully understood. Miglani et al. [24], showed that coupling of external acoustic perturbations and flame heat release control the internal ebullition propensity of nanofuel droplets. Recently, Bennewitz et al. [106] have reported the combustion behavior of a continuously fed fuel droplet flame in a standing pressure wave. They measured phase-locked OH* chemiluminescence intensity variation and flame deflection under different excitation frequencies at different locations relative to a pressure node. However, none of the reported studies have explained the mechanism responsible for the coupling between the external field and the flame.

In the current work, it is demonstrated that the transient availability of flickering frequencies in droplet diffusion flame determine the dynamic self-tuning in modes of oscillation throughout its lifetime. It is also shown that the flame response is a combination of multiple frequencies which are uniquely correlated to multiple convective length-scales. Further, the preferential coupling of flame with the external acoustic field has been discussed by comparing their individual spectral responses and energies. Acoustic disturbances advance at the speed of sound. However, existence of the flame boundary or local inhomogeneities result in local vortical disturbances which travel with the mean flow [111]. Hence, in order to elucidate the mechanism of acoustic-flame interaction, the concept of critical circulation build-up is introduced and the mechanism by which the acoustics adds to velocity disturbances and corresponding circulation leading to flame roll up is delineated.

6.1   Experimental Methodology

The current study investigates the combustion behavior of liquid n-dodecane droplets ($d \sim 1.5 \pm .05mm$) in a longitudinal acoustic force field. The droplets are suspended in pendant mode over a crosswire configuration (304 stainless steel) with dimension $\sim 0.2mm$. A Beyma CP800/Ti loudspeaker with working range of $\sim(0Hz - 20kHz)$ coupled with a stereo amplifier (Ahuja SSA – 100M) and function generator is used to generate acoustic excitation between ($5Hz - 3kHz$) and is placed upstream of the droplet at a distance of $6.5\ cm$. A PCB microphone (7 kHz sampling rate, SN ratio Table 6.1) is mounted near the speaker exit plane to record the amplitude level of the acoustic field.

Table 6.1. The signal to noise ratio

$f_{excitation}\ (Hz)$	Signal-to-noise (SN) Ratio
50	153.20
100	151.52
500	1553.32
1000	5012.19
1500	4597.56
2000	5306.40
2500	5689.02
3000	5489.02
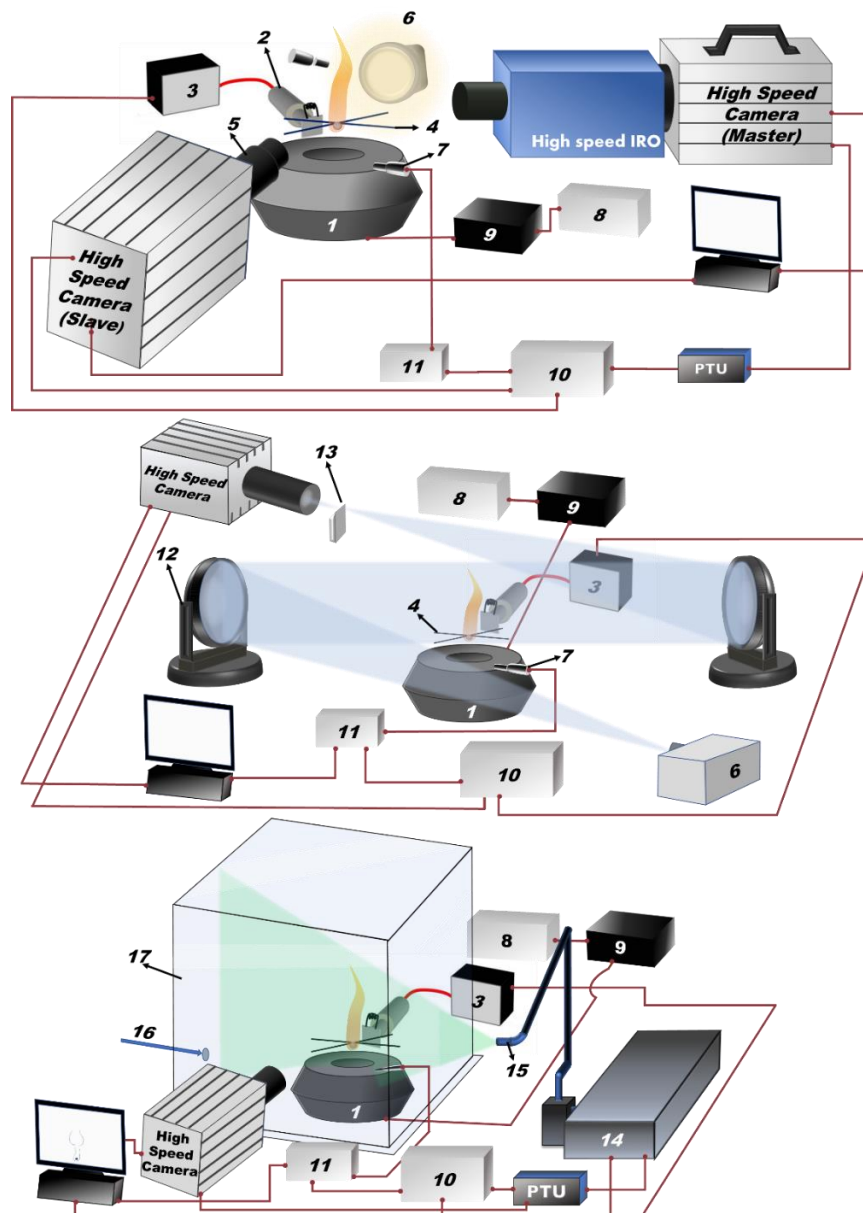
Figure 6.1. Simultaneous acquisition of droplet shape and OH^* Chemiluminescence. The High-speed cameras, heater/solenoid actuator, and microphone are synchronized using a delay generator (b) High-speed schlieren system (c) High-speed flow visualization using Particle Image Velocimetry (PIV). 1. Speaker (Beyma CP800/Ti Loudspeaker range $0 - 20\ kHz$), 2. Coil Heater attached to Linear Solenoid Actuator, 3. Heater control unit, 4. Crosswire, 5. Navitar 1X lens, 6. Light Source, 7. PCB Microphone, 8. Function generator (BK Precision), 9. Amplifier (Ahuja SSA-100M Stereo Amplifier), 10. Delay Generator (BNC), 11. Microphone Data acquisition system, 12. Parabolic mirrors, 13. Knife edge, 14. Laser controller, 15. Laser arm, 16. Seeder inlet, 17. Closed acrylic chamber.

Ignition of the droplets is achieved at atmospheric pressure using a coil-heater controlled by a linear solenoid actuator. The temporal history of the droplets is captured at 7000 fps using a Photron Fastcam SA5 high-speed camera coupled with a Navitar 1X lens with back illumination. High-speed flame OH^*-Chemiluminescence is acquired using a coupled system of Intense Relay optics (IRO) and SA5 high-speed camera mounted with a UV lens and OH^* band-pass filter. Both cameras, heater/solenoid actuator, and microphone are synchronized using a delay generator (for more details please refer to **Figure 6.1(a)**). Schlieren imagining is also performed for droplet flame (**Figure 6.1(b)**). The velocity field in the vertical direction ($U'_a = \sqrt{(1/t) \sum_1^t (U(x,y) - U_{mean}(x,y))^2}$, $U(x,y)$ is the instantaneous velocity and U_{mean} is the temporal mean velocity at spatial position (x,y), respectively) excited by the acoustics is measured using high speed particle image velocimetry (PIV).

Flame Heat Release (HR): Intensity thresholding technique is employed for flame heat release (Q) evaluation. Flame boundary isolated based on a cutoff intensity (I). Pixels (i,j) with intensity $\geq I$ are ascribed with binary value 1, and those with intensity $< I$ are allocated 0. The resultant binary area is used to calculate the instantaneous line-of-sight flame area (A_f). This area is then superimposed with the corresponding actual raw image to evaluate $\overline{I_f}$, the flame average intensity. Further, the instantaneous flame heat release is evaluated as $Q = \overline{I_f} A_f$.

6.1.1 High-speed Schlieren Imaging

The droplet flame dynamics and density perturbations are visualized using a high-speed schlieren system. Two parabolic mirrors of 20cm diameter and a LED light source (Veritas 120 E) are employed. The respective images are acquired by a Photron FASTCAM SA5 high speed camera at 7000 fps (pixel resolution of 1024×1024 (**Figure 6.1(b)**).

6.1.2 High-speed Particle Image Velocimetry (PIV)

Figure 6.1(c) depicts the experimental set-up for high-speed flow visualization using Particle Image Velocimetry (PIV). A dual-pulsed Nd:YLF laser with a wavelength of 532 nm and a pulse energy of 30 mJ per pulse was used as an illumination source. The

cylindrical output beam of the laser (5 mm in diameter) is converted to a thin sheet of 1 mm thickness using a sheet making optics. The acoustic-system, droplet, and the ignition system are placed in an optically accessible acrylic cuboid box (70 $cmX52cmX70cm$). The seeding particles seeded of diethyl hexa sebacate (DEHS) (size 1–3 μm, density $\rho = 912 \ kg/m^3$) oil droplets are introduced from the bottom of the box using *Lavision* seeder. In order to ensure homogeneity, seeder is switched off, and the acoustic-excitation and image acquisition are initiated after 10-20 seconds. In this study, a Photron model SA5 (frame rate 7 KHz at 1024X1024 pixel resolution) camera couple with 100 mm Tokino macro lens is used to capture the instantaneous images. The optical axis of the camera was aligned orthogonally to the horizontal axis of the laser sheet. The camera and laser were synchronized via a programmable tuning unit (PTU) to operate in single-frame mode. Note that the single-frame mode provides pulse separation time ($\Delta t = 1/7000$, inverse of the acquisition frame rate) between two frames. Furthermore, a 532 nm band-pass filter is coupled to the camera lens. The recorded Mie-scattering images for the cold acoustic excitation are postprocessed using Lavision Davis 8.4 software by applying standard vector field algorithm [104], [121]. For combusting droplet, the acquired raw images are utilized to quantify the shedding height (**Figure 6.3** and **Figure 6.11**). However, they have not been used to reconstruct the velocity field.

6.1.3 Band Pass Filtering
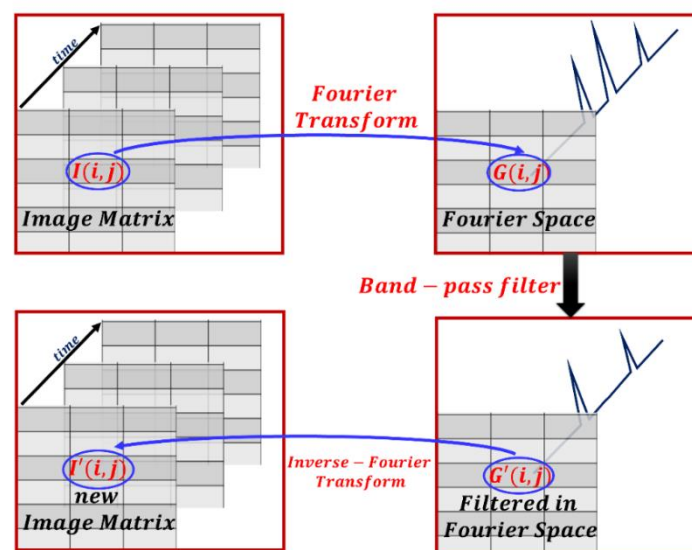
Figure 6.2. Band-Pass Filtering

From the time series of the OH* chemiluminescence images, temporal evolution of the intensity for each pixel $I_{ij}(t)$ has been converted into the frequency domain $G_{ij}(s)$ using Fourier transform (**Figure 6.2**). A band-pass filter of required frequency window has been applied on the $G_{ij}(s)$ time series and an inverse Fourier transform is applied further to convert it back into the temporal domain $I_{ij}{}'(t)$. Thus, the newly acquired time series data pertaining to each pixel at different time instances $I_{ij}{}'(t)$ are used to reconstruct a new time series of images.

6.2 Global Observations for acoustically excited droplet flames
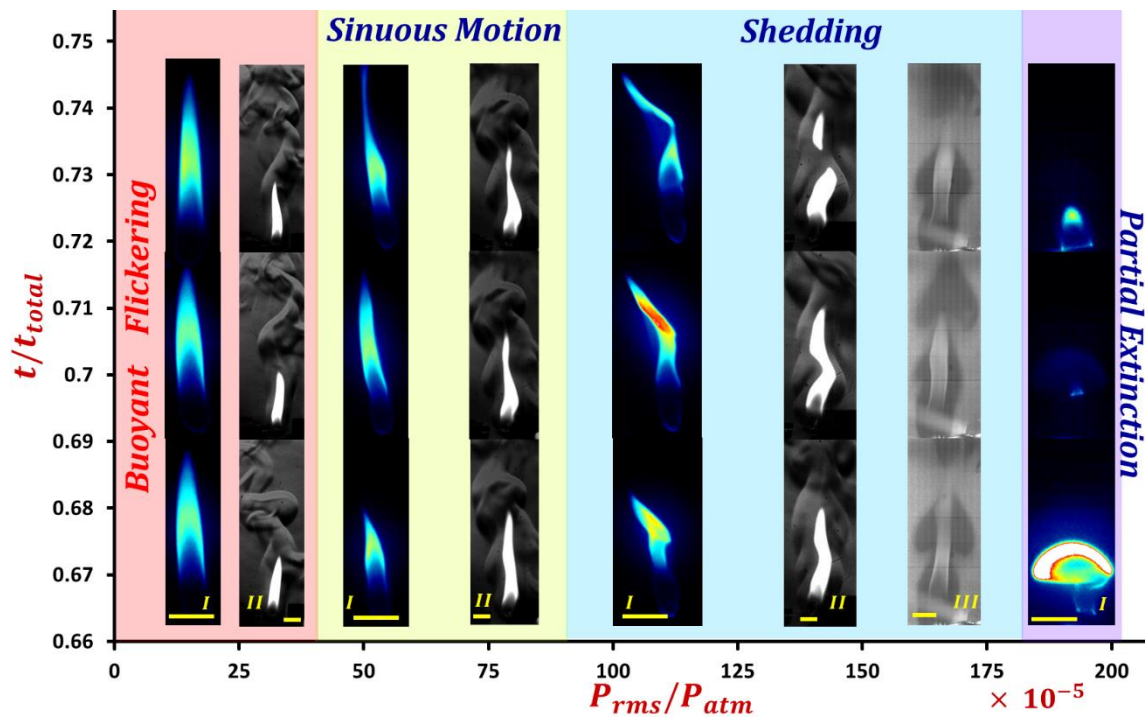
Figure 6.3. Regime map for global flame response under acoustic excitation (t_{total} is the total droplet lifetime and P_{atm} is the atmospheric pressure). Here, one of the sample instability cycles is represented for brevity. The coloured images (I) are OH Chemiluminescence flame signature, the shadowgraphs (II) are the flame schlieren images, the Mie scattering images (III) provide the circulation build-up and shedding height. All scale bars for chemiluminescence, schlieren and Mie scattering images represent 10mm.*

The global flame characteristics (construct and features) with variation in pressure amplitude (P'_{rms}) for forced flames are illustrated in **Figure 6.3**. It is shown later that the

speaker generates excitations at high frequency tones as well as a low frequency band $(0 - 100\ Hz)$ simultaneously. For such bands of frequency of excitation ($f_{excitation}$), velocity amplitude (U'_a) exhibits an increasing trend with increase in P'_{rms} (**Figure 6.4**). Global flame response for lower pressure amplitudes ($P'_{rms}/P_{atm} < 41 \times 10^{-5}$) resembles naturally buoyant flame, irrespective of $f_{excitation}$ values. The flame manifests aggravated sinuous motions for $41 \times 10^{-5} < P'_{rms}/P_{atm} < 90 \times 10^{-5}$. Subsequently, between $90 \times 10^{-5} < P'_{rms}/P_{atm} < 185 \times 10^{-5}$ ($0.10 < U'_a < 0.21 m/s$), heightened flame flickering instabilities (straining and shedding) in the form of sinuous and varicose modes are present. Further increase in pressure amplitude, $P'_{rms}/P_{atm} > 185 \times 10^{-5}$ ($U'_a > 0.21\ m/s$) results in partial extinction and reignition of the flame envelope in cycles.
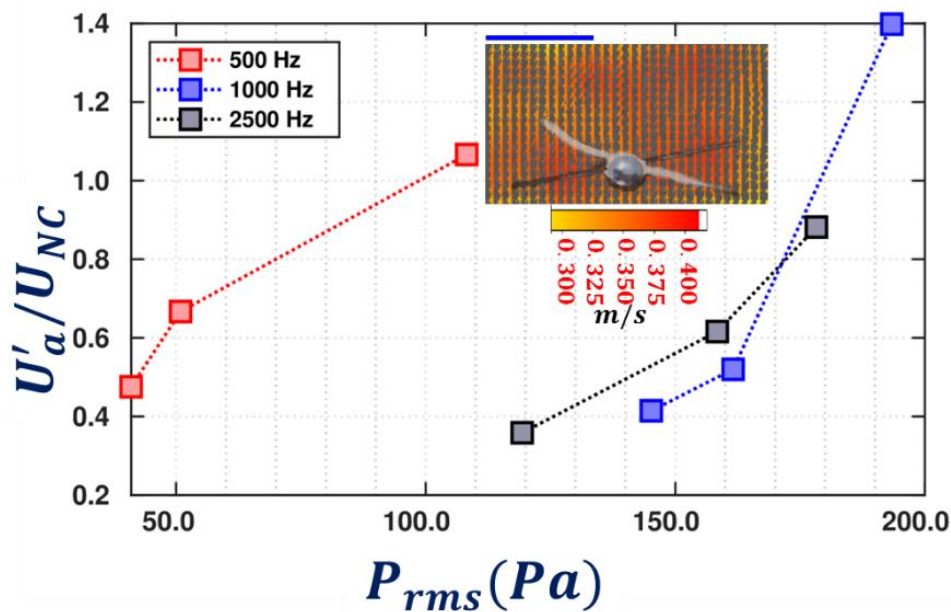
Figure 6.4. Variation of the root mean square (r.m.s) velocity amplitude (U'_a) with r.m.s. Pressure amplitude (P_{rms}), scale bar represents 5mm.

The effects of acoustic field are further delineated in **Figure 6.5**. The flame regions are demarcated based on local flame responses. Region RI comprises of the flame location below the droplet equatorial plane i.e. the radial flame standoff. This region exhibits a bulk oscillatory translation with a mean stand-off (δ_{mean}, **Figure 6.5**), identified as the "wind effect" (**Video 6.1**). This phenomenon arises due to sweeping-off of the fuel-air

mixture from the flame standoff during the acoustic push-cycle and relaxation during pull (readjustment of stoichiometric plane). It is to be noted that this oscillation does not manifest as perturbations of flame topography or heat release.

Figure 6.5. Pictorial representation of the regional flame response under acoustic excitation. Scale bar represents 3 mm.

The second region, RII denotes the instability growth region where continuous growth of the local vortex-sheet due to buoyancy-induced vorticity results in a critical circulation ($\Gamma_{critical}$) build-up [34], [35], [37]–[39]. Subsequently, periodic detachment of these toroidal vortices ensues flame flicker. However, the governing parameters and inherent assumptions will be discussed in detail in the later sections. RII displays significant fluctuations when exposed to the external acoustic field especially in terms of characteristic shedding height, H. Experimentally, shedding height for the acoustic (ac) cases is found to be shortened as compared to the naturally buoyant flame (NC) i.e. $H_{ac} < H_{NC}$. It is to be noted that the degree of reduction, $|H_{ac} - H_{NC}|$, depends on the

magnitude of U'_a. The spatial region beyond H, with combined effects of shedding and heightened velocity, is denoted by Region RIII.
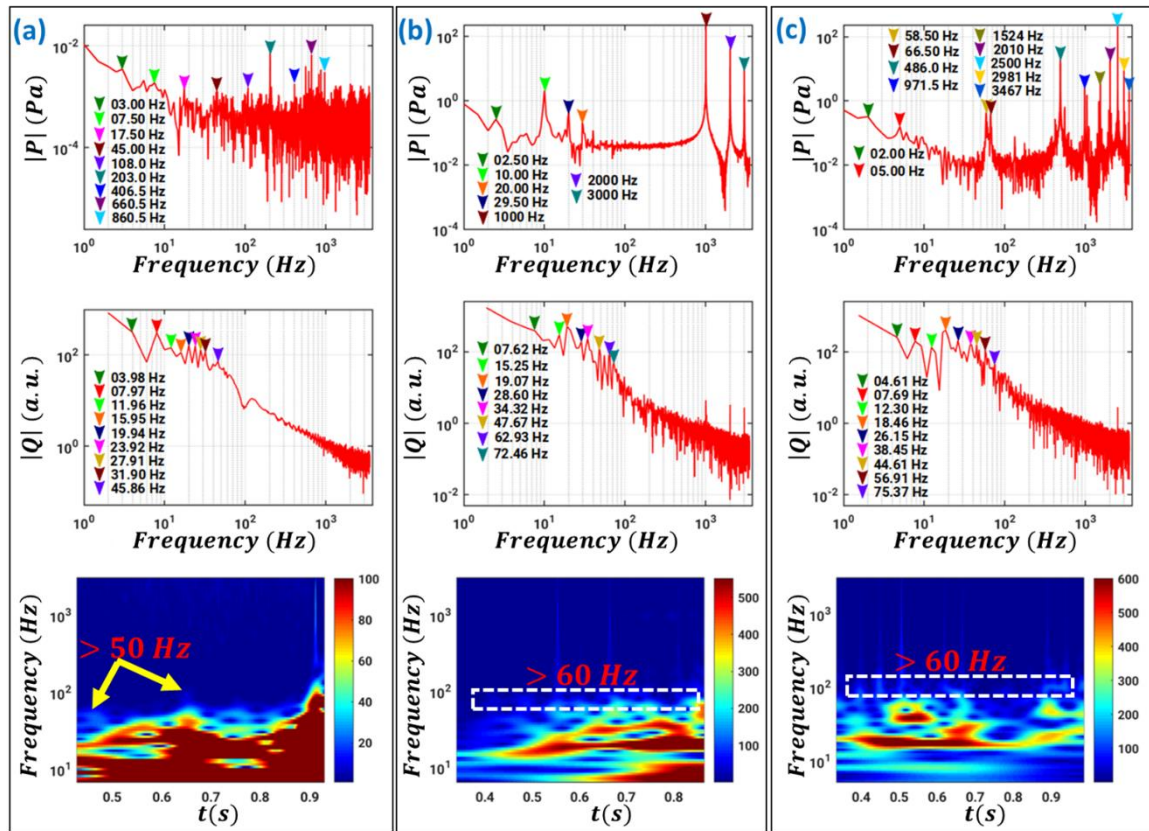
Figure 6.6. Spectral signature of the acoustic field pressure (top), Spectral signature of flame HR (middle), and Continuous Wavelet Transform of flame HR (bottom), for (a) Naturally buoyant flame $f_{excitation} \sim 0Hz$, (b) $f_{excitation} \sim 1000Hz$ (c) $f_{excitation} \sim 2500Hz$.

The pressure signature of the excitation field for isolated frequencies ($f_{excitation} \sim 0Hz, 1kHz,$ and $2.5kHz$) is provided in **Figure 6.6** (a-c, top row). The corresponding flame heat release (HR) spectral response (FFT and Continuous wavelet transform (CWT)) are presented in **Figure 6.6** (a-c, last two rows). The flame HR is quantified as $Q = \overline{I_f} A_f$ ($\overline{I_f}$ is the flame average intensity and A_f is the line-of-sight flame area) [9]. The speaker pressure signature is not a single-tone, rather it generates multi-tone longitudinal waves. It can be seen that even when the speaker is excited at 1 kHz, significant pressure amplitude is seen in the low frequency bands (0-100 Hz). The Fast Fourier spectrum (FFT) of the flame HR for dodecane droplets exhibits multiple peaks of comparable energies. However, the frequency signatures (for both unforced and forced conditions) of heat release are predominantly in the lower-frequency band $\sim(6 - 22Hz)$ with no high frequency modes. The spectral energy ratio

$[|Q_{acoustics}|/|Q_{NC}|$ (where $|Q_{acoustics}|$ and $|Q_{NC}|$ is the spectral energy of low-frequency-band for acoustic and natural convection cases, respectively, **Figure 6.7**)] reveal augmentation in heat release at specific low frequencies. Furthermore, an interesting fact is construed through the flame CWT, which shows temporal evolution of certain higher auxiliary flame frequencies ($> 50\ Hz$) as annotated in **Figure 6.6** (a-c, last two rows), for all conditions (forced or unforced). These frequencies commence at a later time in the burning time cycle. Additionally, the spectral response of flame HR and area, A_f, are similar (**Figure 6.8**). Hence, once again, the flame -acoustic interactions are not present at higher frequencies. The characteristic timescale of the acoustic field at any given frequency is written as $t_{ac} \sim 1/f_{excitation}$; the characteristic diffusion timescale is given as $t_{diff} \sim \left(\delta_{flame}^2 / \mathcal{D}_{DD/air} \right)$, where $\mathcal{D}_{DD/air}$ is the binary diffusion coefficient of dodecane-vapour in air and δ_{flame} is the flame stand-off distance. For the higher frequency range, $f_{excitation} \sim (150\ Hz - 3kHz)$, it is found that $t_{ac} \ll t_{diff}$, hence, interaction between flame and acoustic forcing is not feasible even though the velocity field shows strong response to the higher frequency acoustics.
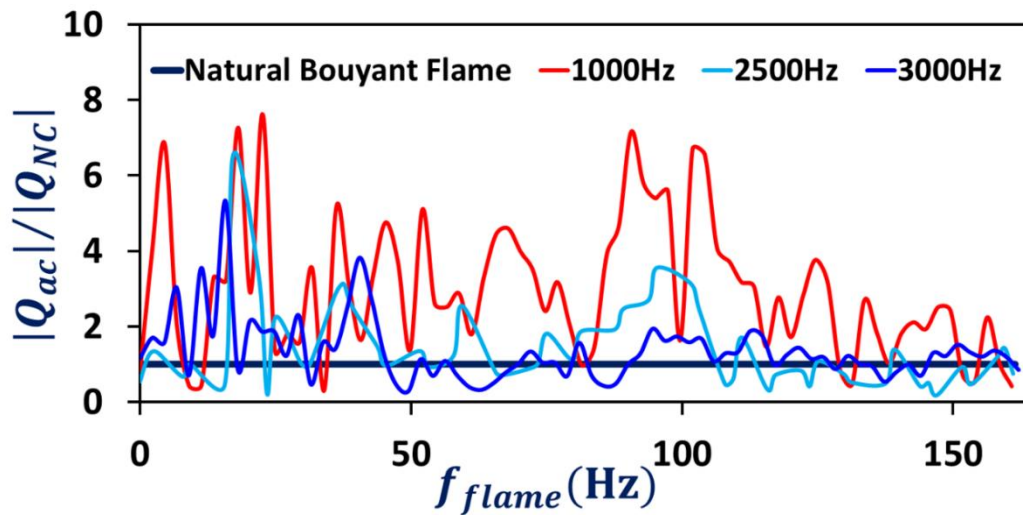
Figure 6.7. Variation of low-band frequency amplitudes under acoustic excitation as compared to unforced droplet flame.

Above experimental observations instigate multiple set-of questions. Firstly, the appearance of auxiliary flame response frequencies with progression in droplet lifetime,

which resembles a self-tuning mechanism. Finally, what is the mechanism of circulation build-up under acoustic excitation leading to shedding i.e. variation of H_{ac}.
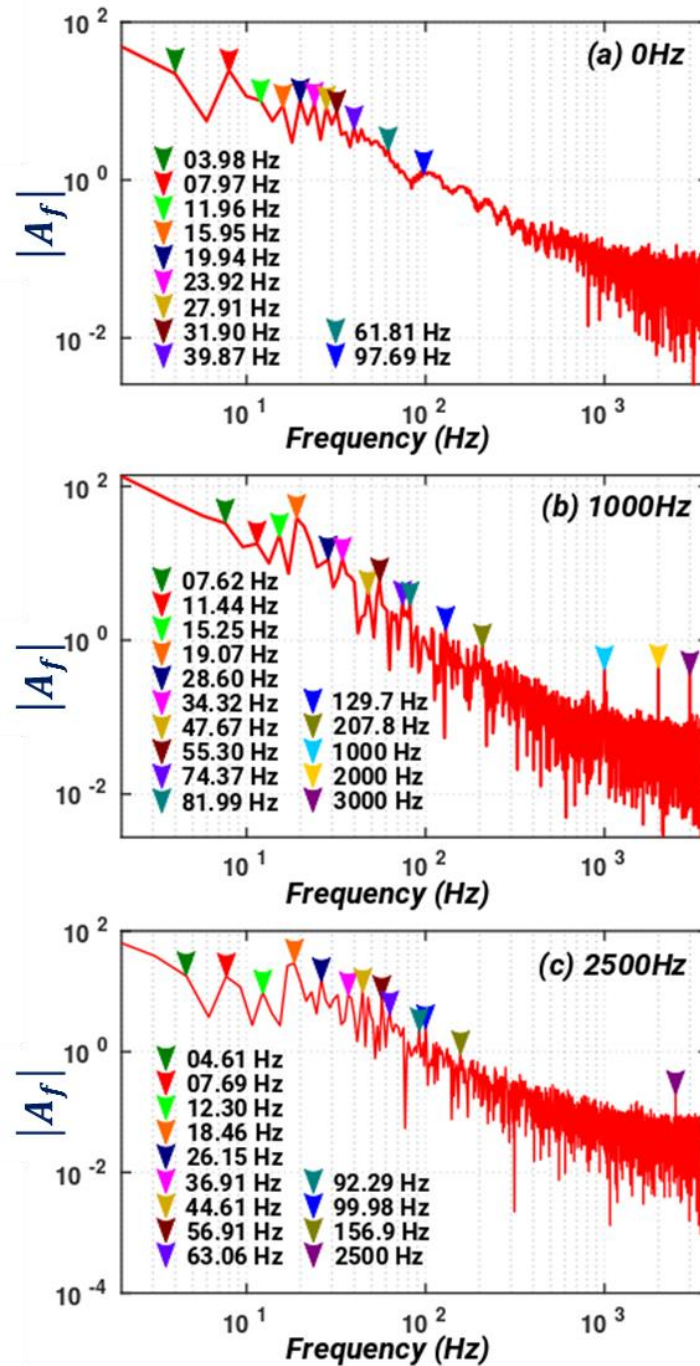
Figure 6.8. Fast Fourier Transform of instantaneous line-of-sight flame area (A_f) for (a) Naturally buoyant flame $f_{excitation} \sim 0Hz$ (b) $f_{excitation} \sim 1000Hz$ ($P_{rms} \sim 161.58\,Pa$) (c) $f_{excitation} \sim 2500Hz$ ($P_{rms} \sim 178.26\,Pa$).

6.3   Self-tuning of droplet diffusion flame

Kinematic formulation of Cetegen et al. [37] quantified the puffing/shedding frequency ($f_{shedding}$) of pool/fires and plumes as function of convective terms using Richardson (Ri) number, given as,

$$f_{shedding} = K\sqrt{\frac{g}{D}}\left[\left(1 + \frac{1}{Ri}\right)^{1/2} - \frac{1}{\sqrt{Ri}}\right]^{-1} \tag{6.1}$$

where constant K depends on the flame and ambient densities, and D is the nozzle diameter. For naturally buoyant flames ($Ri \rightarrow \infty$), equation (6.1) presents $g^{1/2}D^{-1/2}$ dependence.

It is therefore expected that following a similar thought process, the respective frequency for droplet diffusion flame should scale as $f_{flame} \sim \sqrt{g/d_0}$ (d_0 is the initial droplet diameter). First and foremost, unlike pool fires/jet-flames where the dimensions of fuel nozzles are always constant, droplet regression corresponds to a shrinking fuel source. Consequently, the mentioned scaling fails to account for the transient behaviour of the system.
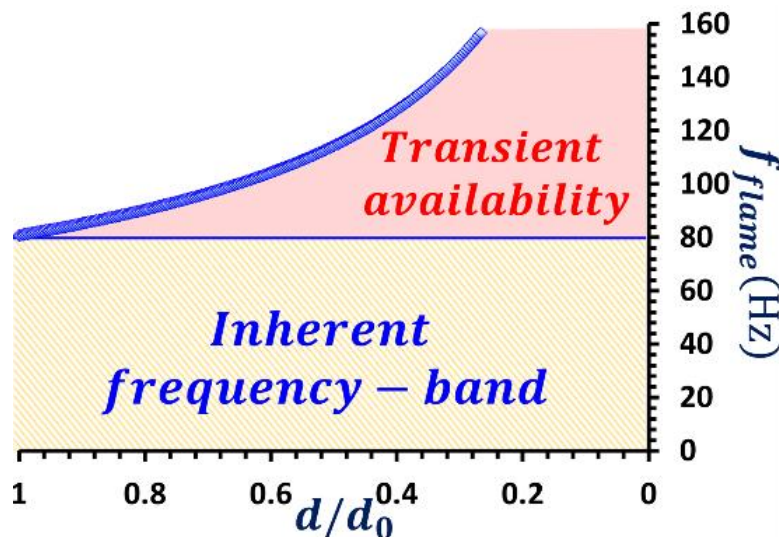
Figure 6.9. Schematic illustration of the available frequencies (f_{flame}) for flame oscillations with droplet regression.

Here, it is hypothesized that a single droplet flame is inextricably linked with the transient droplet dimension and will manifest temporally varying spectral signature throughout the droplet lifetime. As mentioned in plethora of droplet combustion/evaporation literature [23]–[26], [44], [100], [118]; droplet lifetime can be segmented into two temporal stages; (i) Stage I- Heat-up period ($t \sim 0.1 t_{total}$) with constant diameter, and (ii) Stage II ($t > 0.1 t_{total}$)- continuous diameter regression. During Stage I, the input energy is utilized in the bulk-heating of the droplet whereas during Stage II, input energy from the flame envelope is solely responsible for the latent heat of vaporization. Therefore, the flame frequency response (f_{flame}) will be given as

$$f_{flame} \leq \begin{cases} \sqrt{g/d_0}, & t < 0.1 t_{total} \\ \sqrt{g/d}, & t \geq 0.1 t_{total} \end{cases} \quad (6.2)$$
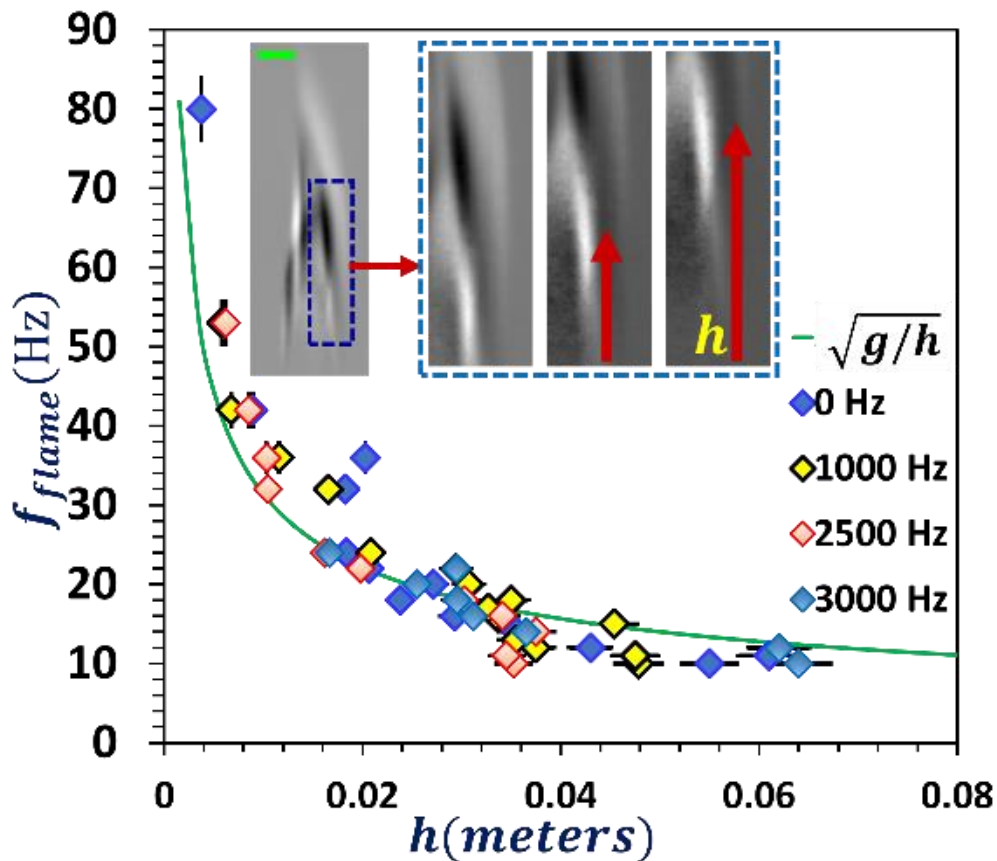
Figure 6.10. Flame oscillation frequencies; Theoretical vs Experimental. The sample subset represents the 10 Hz band-pass filtered flame images for unforced flame. Scale bar represents 5 mm.

Note that equation (6.2) presents an inequality which is explained hereinafter. In general Equation 6.2 dictates that the flame may exhibit any frequency as long as it is lower than $\sqrt{g/d}$. The regression of the droplet with time lowers the value of "d", thereby allowing the flame to exhibit higher order frequencies in accordance to Equation (6.2). For instance, for $10\ \mu m$ and 1 mm droplets, maximum allowable frequencies are $990\ Hz$ and $99\ Hz$, respectively. In order words, a droplet flame undergoes self-tuning exhibiting newer and higher frequency bands during the course of its diameter regression (**Figs. 6.6** and **6.9**). In summary, along with the inherent frequency-band (given by the initial droplet size), temporal evolution of higher frequencies is imminent as seen in the current study (**Figs. 6.6 a**-c (last row) and **Figure 6.9**).

The multiple frequencies associated with flame HR suggest existence of multiple convective length-scales along the flame (R-II zone) which arise due to local perturbations of the velocity field (U_a') induced by low frequency acoustics. These length-scales may not necessarily be represented by a single shedding height which represents the maximum perturbation limit. In order to quantify these inherent dimensions, band-pass filters (**Figure 6.2**) centred around discrete frequency values are applied on the raw chemiluminescence images, for example; a band-pass FFT filter for 10 ± 0.5 Hz is applied to evaluate the vertical length-scales corresponding to $10\ Hz$. Post-filtering, multiple instantaneous vertical length scales are identified in the form of local bright spots (**Figure 6.10**). Maximum spatial displacement (h) of these bright spots is temporally isolated using particle-tracking Mosaic suite (**Video 6.2**) in Fiji Software [79]. It is seen that these displacement scales when normalized as $\sim\sqrt{g/h}$ (green line in **Figure 6.10**), matches exactly with the experimentally observed frequencies (**Figure 6.10**). In other words, individual convective length-scales are uniquely correlated with corresponding flame response frequencies. There also exists very low frequency $< 10Hz$ subharmonics in the flame spectrum which originates from vortex coupling mechanism. In summary, the acoustic energy (**Figure 6.6** (a) top row) at low frequencies feed to the inherent unstable vortical modes of the droplet flame.

6.4   Periodic roll-up of toroidal vortices in droplet diffusion flames for unforced and forced conditions

Experimental and theoretical studies [34], [35], [37]–[39] have reiterated that continuous feeding of circulation from the locally perturbed region (near the fuel entry) generates a critical circulation which eventually leads to downstream shedding/puffing of the flame. In the context of diffusion flames ($Ri \rightarrow \infty$), gravitational term is pivotal for vorticity generation. Hence the vorticity transport equation can be given,

$$\frac{D\xi}{Dt} = \frac{\rho_{air}}{\rho^2}(\nabla\rho \times g) + \nu\nabla^2\xi \tag{6.3}$$

ω is the vorticity, ρ is the local fluid density, ρ_{air} is the air density, and ν is the fluid viscosity. The last term in the R.H.S. of equation (6.3) represents the vorticity-diffusion which can be neglected as compared to the first term [35], [39]. Proceeding with similar approach as provided by Xia et al. [39], the temporal variation of circulation is given as the summation of the gravity generated vorticity and the initial circulation strength fed by the virtue of initial velocity,

$$\frac{d\Gamma}{dt} = \rho_{air}g\left(\frac{1}{\rho_{air}} - \frac{1}{\rho_{flame}}\right)\Delta h_{NC} + \frac{d\Gamma_{initial}}{dt} \tag{6.4}$$
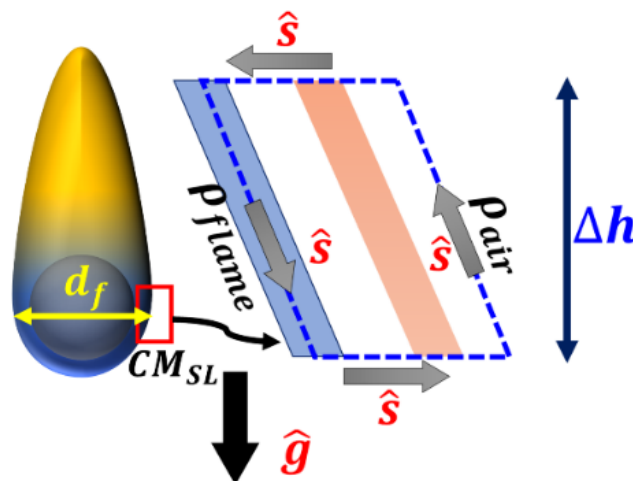
Figure 6.11. Shear layer (CM_{SL}) surrounding the droplet flame envelope. The dashed box ($\hat{s}$) is the material contour surrounding the vortex sheet segment.

Δh_{NC} represents the vortex sheet length (vertically) for the control-mass CM_{SL} (**Figure 6.11**). For the droplet flame, the locally perturbed area is the flame stand-off. Here the local perturbations are convected downstream with continual addition of circulation. Hence, the velocity induced at the flame stand-off (d_f) due to natural convection (U_{NC}) is responsible for the initial vortex-sheet and can be scaled as $\sqrt{g\beta(T_f - T_{air})d_f}$, T_f and T_{air} is the flame and ambient temperature, respectively [106]. Thus,

$$d\Gamma_{initial} = -U_{NC}dh \tag{6.5}$$

Substituting $dh = U_{NC}dt$

$$\frac{d\Gamma_{initial}}{dt} = -U_{NC}^2 \tag{6.6}$$

Further, equation (6.4) can be given as

$$\frac{d\Gamma}{dt} = \rho_{air}g\left(\frac{1}{\rho_{air}} - \frac{1}{\rho_{flame}}\right)\Delta h_{NC} - U_{NC}^2 \tag{6.7}$$

Integration of equation (6.7) over the time period of flicker ($t_{flicker}$) provides the critical circulation for naturally buoyant flame ($\Gamma_{citical}|_{NC}$). Thus,

$$\Gamma_{citical}|_{NC} = \int_0^{t_{flicker}} \frac{d\Gamma}{dt} \tag{6.8}$$

The time period of flicker can be given as $t_{flicker} = k_1\sqrt{H_{NC}/g}$ (as $f_{flame} \sim \sqrt{g/h}$,) where k_1 is the proportionality constant and H_{NC} is the vertical height where the vortex-sheet rolls-up into a toroidal vortex i.e. pinching-off of the flame.

Finally, the critical circulation strength is given as,

$$\Gamma_{citical}|_{NC} = \rho_{air}k_1g^{1/2}H_{NC}^{3/2}\left(\frac{1}{\rho_{air}} - \frac{1}{\rho_{flame}}\right) - U_{NC}^2 k_1 g^{-\frac{1}{2}}H_{NC}^{\frac{1}{2}} \tag{6.9}$$

Next, presence of an acoustic field introduces instantaneous density fluctuations. Thus, ambient density and flame density can be given as the summation of mean and fluctuation component, $\rho_{air} + \rho'_{air}\sin(\omega t - Ky)$ and $\rho_{flame} + \rho'_{flame}\sin(\omega t - Ky)$, ω is the angulation frequency of oscillations and K is the wavenumber.

$$\left.\frac{d\Gamma}{dt}\right|_{ac} = (\rho_{air} + \rho'_{air}\ sin(\omega t$$

$$- Ky))g\left(\frac{1}{(\rho_{air} + \rho'_{air}\ sin(\omega t - Ky))}\right.$$

$$\left. - \frac{1}{(\rho_{flame} + \rho'_{flame}\ sin(\omega t - Ky))}\right)\Delta h_{ac}$$

$$+ \frac{d\Gamma_{initial}}{dt}$$

(6.10)

Moreover, acoustics also augments the initial (at flame stand-off, d_f) rate of circulation addition ($d\Gamma_{initial}/dt$). A generalized velocity form is proposed, $U'_a\ sin(\omega t - Kd_f) = \sum_{i=1}^{N} U'_{ai}\ sin(\omega_i t - Kd_f)$ and similarly for the flame, $U'_f\ sin(\omega t - Kd_f) = \sum_{i=1}^{N} U'_{fi}\ sin(\omega_i t - Kd_f)$, U'_a and U'_f represent the *r.m.s.* amplitude of the velocity for air and the flame, respectively, N is the total number of frequencies, and ω_i represents the individual angular frequencies. Disturbances pertaining to the acoustic excitation travel with a characteristic velocity equal to the speed of sound. Contrarily, the respective vorticity disturbances (due to the presence of flame boundary and flow inhomogeneity) created *en route* propagate through the system with bulk convective motion [111]. In the current case, the convective flow is determined by the natural buoyancy (U_{NC}) of the flame. Therefore, external acoustic field couple with the inherent unstable vortical modes of droplet flame leading to enhanced U'_a. Hence, along the shear layer of droplet diffusion flame (**Figure 6.11**),

$$\frac{d\Gamma_{initial}}{dt} = (U'_a sin\ (\omega t - Kd_f))^2$$

$$- (U_{NC} + U'_f sin(\omega t - Kd_f))^2$$

(6.11)

Further,

$$\left.\frac{d\Gamma}{dt}\right|_{ac} = (\rho_{air} + \rho'_{air}\ sin(\omega t - Ky))g\left(\frac{1}{(\rho_{air} + \rho'_{air}\ sin(\omega t - Ky))}\right.$$

$$\left. - \frac{1}{(\rho_{flame} + \rho'_{flame}\ sin(\omega t - Ky))}\right)\Delta h_{NC}$$

$$+ (U'_a\ sin(\omega t - Kd_f))^2 - (U_{NC} + U'_f sin(\omega t - Kd_f))^2$$

(6.12)

The periodic terms post integration of equation (6.11) over the time period $t_{flicker} = k_1\sqrt{H_{ac}/g}$ (H_{ac} is the vertical height where flame pinches-off in the acoustically perturbed system) are eliminated,

$$\Gamma_{citical}|_{ac} = \rho_{air}k_1g^{1/2}H_{ac}^{3/2}\left(\frac{1}{\rho_{air}} - \frac{1}{\rho_{flame}}\right) - U_{NC}^2k_1g^{-\frac{1}{2}}H_{ac}^{\frac{1}{2}} \tag{6.13}$$

$$+ \frac{U_a'^2 - U_f'^2}{2}k_1g^{-1/2}H_{ac}^{1/2}$$

Interestingly, equation (6.13) is a unique relation which is independent of $f_{excitation}$. This further infers that irrespective of $f_{excitation}$, critical circulation is a function of U_a'. In order to exhibit flickering, critical circulation of naturally buoyant flame ($\Gamma_{citical}|_{NC}$) should be the limiting condition for acoustically excited diffusion flame should i.e. $\Gamma_{citical}|_{NC} = \Gamma_{citical}|_{ac}$. Equating (6.9) and (6.13),

$$1 = \left(\frac{H_{ac}}{H_{NC}}\right)^{\frac{3}{2}} + U_{NC}^2g^{-1}\frac{\left(H_{ac}^{1/2} - H_{NC}^{1/2}\right)}{H_{NC}^{3/2}(\rho^* - 1)} + U_a'^2\frac{(\rho^* + 1)}{2}g^{-1}\frac{H_{ac}^{1/2}}{H_{NC}^{3/2}} \tag{6.14}$$

U_f' is scaled as $(\rho_{air}/\rho_{mean})\,U_a'$ and $\rho^* = \rho_{air}/\rho_{mean}$

Equation 6.14 is illuminating. It shows that the acoustic frequency has no dependence on shedding height H_{ac}. In other words, only the perturbation magnitude $U_a'^2$ determines the shedding lengthscale. Equation 6.14 also suggests that compared to a buoyant diffusion flame with no external perturbations, H_{ac} will exhibit shorter length-scales ($\sim(5\% - 25\%)$ reduction).

Figure 6.12 presents the variation of the ratio of experimentally observed shedding height and corresponding theoretical values (Equation 6.14) as a function of U_a' for several frequencies of excitation. It is evident that the theoretical predictions and experimental results agree with each other within the maximum uncertainty of $\pm20\%$ for $U_a' < 0.21m/s$. Beyond this velocity threshold, there is a huge deviation ($\sim60\%$) [$U_a' > U_{NC}$, where $U_{NC}\sim0.2m$]. Such disparity arises due to flame extinction at the droplet forward stagnation point. The extinction of the flame envelope can be interpreted as an outcome of excessive flame strain beyond a certain U_a'.
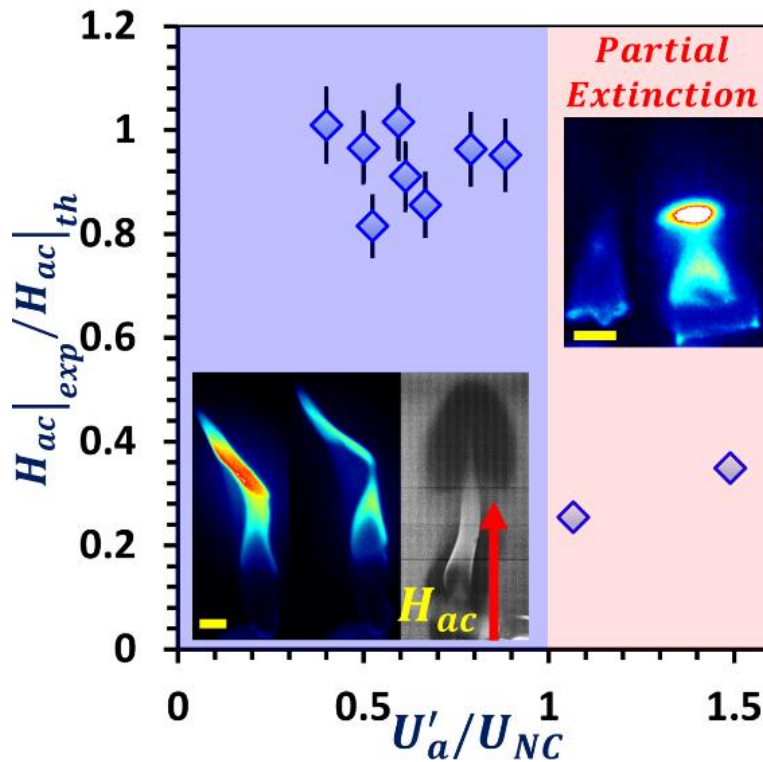
Figure 6.12. Variation of acoustic shedding height with the velocity amplitude. $H_{ac}|_{exp}$ is the experimental shedding height and $H_{ac}|_{th}$ is the theoretical shedding height from equation (6.14). Scale bar represents 5mm.

6.5 Conclusion

In summary, the presented research investigation elucidates the dynamics of droplet diffusion flame oscillations with and without external acoustic excitation. Here, the conventional purview of diffusion flame flickering is merged with the innate transiency of droplet combustion. The current study encompasses three pertinent facets of droplet diffusion flames;

(a) Spectral signature of a single droplet flame cannot be solely scaled using initial diameter rather it is transient in nature. The availability of the highest possible frequency is a function of instantaneous droplet diameter.

(b) The flame response is always associated with the low-frequency band $\sim(6 - 22)$ Hz. Moreover, using bandpass filtering, the existence of multiple vertical length scales in the flame RII regime is isolated. The flame response frequencies are well

correlated with kinematic scaling $\sqrt{g/h}$, simultaneously across multiple convective length-scales.

(c) The flame shedding height is found to be dependent on the velocity amplitude induced by the acoustic field, while being independent of the excitation frequency.

Chapter 7

Conclusions and Future Scope

7.1 Summary of the work

The pressing need for high-performance fuels in combustion applications has motivated a search for fuels containing as much energy as possible per unit mass. Addition of micron and sub-micron scale metal and metalloid particles to conventional fuels, like Jet-A, works as a "energy enhancer" i.e. less liquid with more energy, providing increased energy from smaller amounts of liquid fuels. Research endeavors pertaining to the heterogeneous fuel systems date back to 1940s. Heinz Muller's group of Bavarian Motor Works (BMW) investigated the effects of addition of aluminium and magnesium particles to diesel fuel. However, the engines showed poor performances due to incomplete combustion of the additives [122]. Recent advent into nanotechnology has reoriented the prime focus from the micron-sized particles as "liquid fuel-extender" to the nanoparticles (1-100 nm). The higher surface area to volume ratio result in enhanced thermo-physical properties of nanoparticles as compared to their bulk medium. One of the main advantages provided by addition of metallic nanoparticles (aluminum, iron, boron, and others) is the increased attainable specific energy due to reduced temperatures of metal combustion. Furthermore, nanoparticles of metallic oxides, like cerium oxide, help reduce soot emissions and pollutants like carbon monoxide and nitrous oxides because of their ability to oxidize soot particles in their precursor stage. Nanofuels have also been shown to reduce ignition delay and increase ignition probability. In all practical combustors or engines, liquid fuel is sprayed in the form of droplets which subsequently vaporize and burn. Study of single droplet combustion/evaporation has proven to be a fundamental building block in the context of full-fledged spray combustion investigations. Droplet vaporization time scale controls the overall mixing and homogeneity of fuel spray in real combustors. Hence, understanding of single droplet dynamics holds the key towards translating the fundamental insights to application domains. The presented work identifies the complex interplay of NP addition and droplet burning/internal boiling characteristics. Along with

droplet surface and internal dynamics, the study also provides first of a kind understanding of topology and transitions for a droplet flame under free-fall. Furthermore, using classical concept of vortex-sheet roll up mechanism, flame flickering is understood for droplet diffusion flames with and without external acoustic perturbations.

1) To recapitulate, the current work offers insights into the combustion dynamics and modes of secondary atomization of both low-vapor-pressure and high-vapor-pressure fuels nanofuel droplets using time-resolved optical diagnostic techniques such as, high-speed shadowgraphy, high-speed OH*chemiluminescence imaging. It is evident that heterogeneous nucleation due to NP addition leads to severe droplet shape/volumetric oscillations and opens the pathway for secondary atomization for low vapor pressure droplets. Further, the enhanced fuel vaporization and transfer of daughter droplets to the flame front control the heat release rate. For Ethanol-Water blend as the base liquid, NP addition incites heterogeneous internal boiling. However, formation of a gel structure due to NP accumulation at the droplet surface alters the fuel evaporation rate. Employing a combination of Darcy's law and pure fuel evaporation rate, each with proper weightage, droplet burning time is approximated. Further, POD technique is utilised to report the coupling between the dominant modes of droplet shape and HR. This analysis showcases that addition of NPs and their subsequent superficial accumulation imparts low energy content of shape modes of NP laden droplets which impedes their synced- response with flame modes.

2) The experimental work on acoustically levitated nanofuel droplets under external radiative heating identifies the parameters governing internal ebullition. This work isolates the sole effects of NPs on boiling propensity in the absence of any wire/fiber effects. Using a theoretical non-dimensional time scale, a three-dimensional regime map is proposed which depicts the critical values of droplet size, particle loading, and external heating rate that is necessary to initiate internal ebullition.

3) Flame dynamics in free-falling droplet combustion unearths the transient topological self-tuning; transient envelope to wake transitions, flame width and height evolution, which is found to be primarily hydrodynamic in nature. Reduction in droplet burning

rate is accounted with reduced global energy input due to reduction in droplet exposed area to the wake flame. Consequently, addition of particle does not manifest discernible effects on droplet burning rate and internal ebullition propensity although for sense loading $5w\%$ and $10w\%$, flame HR exhibits $\sim 10 - 23\%$ reduction. Furthermore, it also shown that reduced flame energy input increases the characteristics timescale of bubble formation which exceeds the droplet flight time. Subsequently, internal boiling remains absent. This study put forwards several pertinent aspects that can be studied in the future, such as, effect of droplet size and surrounding conditions where complete droplet combustion can be achieved.

4) The evolution of vortical structures around the buoyant diffusion flames and their interplay with flame structure is important for fire research studies where flame spread, shedding, and air-entrainment are important parameters. A canonical study is performed which can provide insights into the effects of external perturbations to such systems. The instabilities of naturally buoyant droplet diffusion flames, both with and without an external pressure (acoustic) field is investigated. This work employs the classical vortex-shedding mechanism to elucidate flickering of droplet diffusion flames which has never been reported before. The mathematical formulation of the droplet flame-acoustic interaction suggests that only fluctuating component of the external perturbation alters the rate of vortex-sheet roll-up. Thus, if the external forced field has multiple frequencies and fluctuating component, they can be superimposed to provide a global unsteady flow field. This can be useful for mimicking droplet combustion in turbulent flows which is universal to all practical combustors.

7.2 Future scope and research directions

- **Effects of NP size and morphology:** For future studies, effects of NP size and morphology variation can provide fundamental insights into to nanofuel combustion. It can be anticipated that variation of heat absorption rate (further controlling droplet evaporation rate) and perikinetic aggregation rate (controlling aggregation and bubble incipience from the aggregates) will lead to different atomization and combustion behaviour for different NP sizes.

- **Applications in micronisation and encapsulation:** The non-dimensional timescale parameter coined for externally heated nanosuspension droplets in Chapter 4 can also be utilized to suppress internal ebullition in particle laden droplets for the purposes of *micronisation* and *encapsulation*. Micronisation and drying of particle-laden droplets ensure controlled removal of the base solvent and optimized residue architecture. Consequently, processes like encapsulation and composite particle self-assembly can be achieved. Self-assembly of particles constitutes the pertinent facet of pharmaceutical, biotechnological, and food industries. Encapsulation is characterized by an active liquid core and a shell surrounding it, which is a separate entity and varies (chemically and physically) depending on the liquid core composition. It is a widely accepted method for drug delivery, material handling and food processing [123]. For instance, during vaccine vitrification an active biologic is encapsulated within an amorphous solid excipient [124]. Encapsulation is also helpful in protecting food/beverages from moisture and polluting contents of the surroundings. One technique to achieve encapsulation of an active core is through solvent extraction and evaporation. This method primarily employs an aqueous polymer/particle suspension with volatile liquid components, such as acetone. During the drying process, acetone, being volatile, evaporates, which instigates polymer/particle precipitation at the droplet-air interface. Complete evaporation of the volatile component and surface precipitation of dispersed particles encapsulates the aqueous phase leading to microcapsules.

- **Optical diagnostics for transient particle density with droplet regression:** Particle aggregation dynamics in nanofuel droplet combustion still remains elusive due to transient dynamics of the system. Quantification of particle aggregation and accumulation can provide the information regarding the; absolute gelation timescales, packing fraction, wetting of particles, to name a few. Therefore, simultaneous information of droplet regression along with particle dynamics through new optical diagnostic techniques such as time-shift method [125] is necessary.

- **Nanofuel spray combustion:** In Chapters 4 and 5, the effect of thermal interference/nucleation process due to suspension wire is eliminated. However,

in order to address the applicability of nanofuels in industrial/commercial applications, full-fledged spray combustion needs to be considered. Such investigations will precisely demarcate two pertinent facets; optimization of working conditions; pressure and temperature, and development of novel nanofuel injector designs. Research studies have previously attempted to study the sub-grid of spray systems; combustion of single and clusters of droplets. Spray combustion is a multi-phase and multi-scale system where each of these aspects are coupled and occur simultaneously via the physical and chemical phenomena of liquid atomization, gasification, and combustion. While nanofuel spray combustion studies remain sparse, efforts in this direction are likely to bridge the gap between the fundamental and commercial applications thereby bringing the nanofuel from laboratory to several social platforms. With the pressing need to meet ever-increasing energy demand, the combustion systems utilizing fossil fuels have been the major contributors to the carbon footprint. As the combustion of conventional energy resources continue to produce significant Green House gas (GHG) emissions, there is a strong emphasis to either upgrade or find an energy-efficient eco-friendly alternative to the traditional hydrocarbon fuels. The ability to manufacture materials with custom-tailored properties at the nanoscale has led to the discovery of a new class of fuels containing nanoparticles (NPs). These fuels may reduce emissions, improve ignition, and overall offer a cleaner sustainable energy source. Since there is an increase in combustion efficiency due to nanoadditives, it can lead to huge savings which is good for the economy as India imports 70% petroleum fuels. From an experimental point-of-view, the initial success indicator of such studies lies with the efficiency of the high-pressure test rig and applicability of state-of-the-art optical diagnostic techniques. Further, the next step will be with the completion of extensive experiments for multiple fuel-nanoparticle combinations and generating a possible regime-map as a function of flow conditions and particle quantity and properties. Additionally, these data sets can be cross-checked with the fundamental correlations provided in the literature. In the long run, the success indicator is the quantitative estimation of nanoadditives on fuel emission signature. This is paramount for tackling NO_x (nitrogen oxide) and CO_2 emissions. Furthermore, based on the nanofuel controlling parameters emission discharge from big power plants can be revisited.

- **Flame transitions for free-falling droplet; effect of droplet size and co-flow:**
  In chapter 5, the flame transitions are established based on the fact that droplet

regression is minimal. Furthermore, here the relative velocity between droplet and the surrounding is solely given by droplet motion due to free-fall. Therefore, next set of investigations can be studied for burning droplets injected in a co-flow by varying droplet size and surrounding flow velocity. Further, this configuration can also be utilized for the synthesis of a wide variety of single- and multi-component metal oxide nanoparticles via the single droplet-to-particle route of the Flame spray pyrolysis (FSP) technique [126-128]. Nanoparticle synthesis in a spray flame offer several challenges such as steep temperature gradients, turbulence and reduced timescales of the droplets. It has been reported in several recent experimental investigations [129-131] that single droplet combustion can be useful in order to overcome these shortcomings with the added advantage of exploring low-volatility and low-cost precursors. Hence, the droplet evaporation and flame HR signatures reported in Chapter 5 will be useful to design the nanoparticle synthesis experiments and draw conclusions in terms of non-dimensional working parameters such as Reynold number.

- **Laser Incandescence (LI) for effects of NP addition on soot reduction:** As previously stated, addition of certain NPs (Cerium oxide, CeO_2) to conventional fuel system results in soot reduction. Hence, soot measurements in NP laden droplet flames using optical diagnostics such as LI, can be marked as the next step which can further translated to full spray studies as previously mentioned.

- **Determining the effects of acoustic characteristics for droplet-flame-acoustic interactions for nanofuels:** The droplet flame-acoustic interaction study presented in **Chapter 6** concluded that the flame shedding height is dependent on the velocity amplitude. This conclusion can be further taken to determine the impact of the acoustic characteristics (r.m.s. pressure and external frequency) on the velocity amplitude. This would make this analysis fully dependent on the experimental boundary conditions, as opposed to dealing with the uncertainty of determining how the acoustics ultimately affects the velocity field. The coupling of oscillatory pressure and unsteady combustion heat-release instigates thermo-acoustic instabilities inside a gas-turbine combustion chamber. It has been recently proposed that apart from the perform enhancing properties of nanoadditives, they can also assist in damping of previously mentioned

thermo-acoustic instabilities in liquid rocket engines (LRE's). Pfeil et al. [132] studied the effects of soluble additive ammonia borane (AB), NH_3BH into ethanol for the LRE model combustor. For a loading of 6 % by weight, they reported an axial bimodal heat release distribution throughout the combustor as compared to pure ethanol. Thus, based on such alterations in the acoustic-flame interactions, theoretical analysis presented in Chapter 6 can be further employed for insights into nanofuel droplet flame-acoustic interactions.

- **Droplet flame-vortex interaction:** Following the results from **Chapter 6,** droplet flame oscillations under the action of external vortical structures/eddies can be a whole new direction to unearth. It will be interesting to formulate the flame transitions and oscillation frequency, as function of vortex dimension and momentum.

Bibliography

[1] S. U. Choi and J. A. Eastman, "Enhancing thermal conductivity of fluids with nanoparticles," Argonne National Lab., IL (United States), 1995.

[2] J.-H. Lee *et al.*, "Effective viscosities and thermal conductivities of aqueous nanofluids containing low volume concentrations of Al2O3 nanoparticles," *International Journal of Heat and Mass Transfer*, vol. 51, no. 11–12, pp. 2651–2656, 2008.

[3] R. Mahtab, J. P. Rogers, and C. J. Murphy, "Protein-sized quantum dot luminescence can distinguish between" straight"," bent", and" kinked" oligonucleotides," *Journal of the American Chemical Society*, vol. 117, no. 35, pp. 9099–9100, 1995.

[4] R. Shukla, V. Bansal, M. Chaudhary, A. Basu, R. R. Bhonde, and M. Sastry, "Biocompatibility of gold nanoparticles and their endocytotic fate inside the cellular compartment: a microscopic overview," *Langmuir*, vol. 21, no. 23, pp. 10644–10654, 2005.

[5] S. Jain, D. G. Hirst, and J. M. O'sullivan, "Gold nanoparticles as novel agents for cancer therapy," *The British journal of radiology*, vol. 85, no. 1010, pp. 101–113, 2012.

[6] Y. Gan, Y. S. Lim, and L. Qiao, "Combustion of nanofluid fuels with the addition of boron and iron particles at dilute and dense concentrations," *Combustion and Flame*, vol. 159, no. 4, pp. 1732–1740, 2012.

[7] H. Tyagi *et al.*, "Increased hot-plate ignition probability for nanoparticle-laden diesel fuel," *Nano letters*, vol. 8, no. 5, pp. 1410–1416, 2008.

[8] J. L. Sabourin *et al.*, "Effect of nano-aluminum and fumed silica particles on deflagration and detonation of nitromethane," *Propellants, Explosives, Pyrotechnics: An International Journal Dealing with Scientific and Technological Aspects of Energetic Materials*, vol. 34, no. 5, pp. 385–393, 2009.

[9] D. Jackson, D. Davidson, and R. Hanson, "Application of an aerosol shock tube for the kinetic studies of n-dodecane/nano-aluminum slurries," in *44th AIAA/ASME/SAE/ASEE joint propulsion conference & exhibit*, 2008, p. 4767.

[10]   C. Allen, G. Mittal, C.-J. Sung, E. Toulson, and T. Lee, "An aerosol rapid compression machine for studying energetic-nanoparticle-enhanced combustion of liquid fuels," *Proceedings of the Combustion Institute*, vol. 33, no. 2, pp. 3367–3374, 2011.

[11]   B. Rotavera, A. Kumar, S. Seal, and E. L. Petersen, "Effect of ceria nanoparticles on soot inception and growth in toluene–oxygen–argon mixtures," *Proceedings of the Combustion Institute*, vol. 32, no. 1, pp. 811–819, 2009.

[12]   M. A. Lenin, M. R. Swaminathan, and G. Kumaresan, "Performance and emission characteristics of a DI diesel engine with a nanofuel additive," *Fuel*, vol. 109, pp. 362–365, 2013.

[13]   T. Shaafi, K. Sairam, A. Gopinath, G. Kumaresan, and R. Velraj, "Effect of dispersion of various nanoadditives on the performance and emission characteristics of a CI engine fuelled with diesel, biodiesel and blends—a review," *Renewable and Sustainable Energy Reviews*, vol. 49, pp. 563–573, 2015.

[14]   V. Sajith, C. B. Sobhan, and G. P. Peterson, "Experimental investigations on the effects of cerium oxide nanoparticle fuel additives on biodiesel," *Advances in Mechanical Engineering*, vol. 2, p. 581407, 2010.

[15]   R. N. Mehta, M. Chakraborty, and P. A. Parikh, "Nanofuels: Combustion, engine performance and emissions," *Fuel*, vol. 120, pp. 91–97, 2014.

[16]   V. A. M. Selvan, R. B. Anand, and M. Udayakumar, "Effect of Cerium Oxide Nanoparticles and Carbon Nanotubes as fuel-borne additives in Diesterol blends on the performance, combustion and emission characteristics of a variable compression ratio engine," *Fuel*, vol. 130, pp. 160–167, 2014.

[17]   C. K. Law, *Combustion physics*. Cambridge university press, 2010.

[18]   Y. Gan and L. Qiao, "Combustion characteristics of fuel droplets with addition of nano and micron-sized aluminum particles," *Combustion and Flame*, vol. 158, no. 2, pp. 354–368, 2011.

[19]   I. Javed, S. W. Baek, and K. Waheed, "Evaporation characteristics of heptane droplets with the addition of aluminum nanoparticles at elevated temperatures," *Combustion and Flame*, vol. 160, no. 1, pp. 170–183, 2013.

[20] I. Javed, S. W. Baek, and K. Waheed, "Autoignition and combustion characteristics of heptane droplets with the addition of aluminium nanoparticles at elevated temperatures," *Combustion and Flame*, vol. 162, no. 1, pp. 191–206, 2015.

[21] I. Javed, S. W. Baek, and K. Waheed, "Effects of dense concentrations of aluminum nanoparticles on the evaporation behavior of kerosene droplet at elevated temperatures: The phenomenon of microexplosion," *Experimental thermal and fluid science*, vol. 56, pp. 33–44, 2014.

[22] M. N. Bello *et al.*, "Reaction dynamics of rocket propellant with magnesium oxide nanoparticles," *Energy & Fuels*, vol. 29, no. 9, pp. 6111–6117, 2015.

[23] A. Miglani, S. Basu, and R. Kumar, "Insight into instabilities in burning droplets," *Physics of Fluids*, vol. 26, no. 3, p. 032101, 2014.

[24] A. Miglani, S. Basu, and R. Kumar, "Suppression of instabilities in burning droplets using preferential acoustic perturbations," *Combustion and Flame*, vol. 161, no. 12, pp. 3181–3190, 2014.

[25] A. Miglani and S. Basu, "Coupled mechanisms of precipitation and atomization in burning nanofluid fuel droplets," *Scientific reports*, vol. 5, p. 15008, 2015.

[26] A. Miglani and S. Basu, "Effect of particle concentration on shape deformation and secondary atomization characteristics of a burning nanotitania dispersion droplet," *Journal of Heat Transfer*, vol. 137, no. 10, p. 102001, 2015.

[27] L.-W. Huang and C.-H. Chen, "Flame stabilization and blowoff over a single droplet," *Numerical Heat Transfer, Part A: Applications*, vol. 27, no. 1, pp. 53–71, 1995.

[28] S. Tanvir and L. Qiao, "Effect of addition of energetic nanoparticles on droplet-burning rate of liquid fuels," *Journal of Propulsion and Power*, vol. 31, no. 1, pp. 408–415, 2014.

[29] S. Tanvir and L. Qiao, "Droplet burning rate enhancement of ethanol with the addition of graphite nanoparticles: Influence of radiation absorption," *Combustion and Flame*, vol. 166, pp. 34–44, 2016.

[30] B. Pathak and S. Basu, "Phenomenology of break-up modes in contact free externally heated nanoparticle laden fuel droplets," *Physics of Fluids*, vol. 28, no. 12, p. 123302, 2016.

[31] P. M. Guerieri, R. J. Jacob, H. Wang, D. J. Kline, and M. R. Zachariah, "Droplet combustion of kerosene augmented by stabilized nanoaluminum/oxidizer composite mesoparticles," *Combustion and Flame*, vol. 211, pp. 1–7, 2020.

[32] C.-H. CHEN and F.-B. WENG, "Flame stabilization and blowoff over a porous cylinder," *Combustion science and technology*, vol. 73, no. 1–3, pp. 427–446, 1990.

[33] S. Parag and V. Raghavan, "Experimental investigation of burning rates of pure ethanol and ethanol blended fuels," *Combustion and Flame*, vol. 156, no. 5, pp. 997–1005, 2009.

[34] L.-D. Chen, J. P. Seaba, W. M. Roquemore, and L. P. Goss, "Buoyant diffusion flames," in *Symposium (International) on Combustion*, 1989, vol. 22, pp. 677–684.

[35] D. Moreno-Boza, W. Coenen, A. Sevilla, J. Carpio, A. L. Sánchez, and A. Liñán, "Diffusion-flame flickering as a hydrodynamic global mode," *Journal of Fluid Mechanics*, vol. 798, pp. 997–1014, 2016.

[36] B. M. Cetegen and Y. Dong, "Experiments on the instability modes of buoyant diffusion flames and effects of ambient atmosphere on the instabilities," *Experiments in Fluids*, vol. 28, no. 6, pp. 546–558, 2000.

[37] B. M. Cetegen and T. A. Ahmed, "Experiments on the periodic instability of buoyant plumes and pool fires," *Combustion and flame*, vol. 93, no. 1–2, pp. 157–184, 1993.

[38] J. Buckmaster and N. Peters, "The infinite candle and its stability—a paradigm for flickering diffusion flames," in *Symposium (International) on Combustion*, 1988, vol. 21, pp. 1829–1836.

[39] X. Xia and P. Zhang, "A vortex-dynamical scaling theory for flickering buoyant diffusion flames," *Journal of Fluid Mechanics*, vol. 855, pp. 1156–1169, 2018, doi: 10.1017/jfm.2018.707.

[40] T. Edwards *et al.*, "Development of an experimental database and kinetic models for surrogate jet fuels," in *45th AIAA Aerospace Sciences Meeting and Exhibit*, 2007, p. 770.

[41] S. S. Vasu, D. F. Davidson, Z. Hong, V. Vasudevan, and R. K. Hanson, "n-Dodecane oxidation at high-pressures: Measurements of ignition delay times and OH concentration time-histories," *Proceedings of the Combustion Institute*, vol. 32, no. 1, pp. 173–180, 2009.

[42] S. S. Vasu, D. F. Davidson, and R. K. Hanson, "Jet fuel ignition delay times: Shock tube experiments over wide conditions and surrogate model predictions," *Combustion and flame*, vol. 152, no. 1–2, pp. 125–143, 2008.

[43] P. J. Linstrom and W. G. Mallard, "The NIST Chemistry WebBook: A chemical data resource on the internet," *Journal of Chemical & Engineering Data*, vol. 46, no. 5, pp. 1059–1063, 2001.

[44] K. Pandey, K. Chattopadhyay, and S. Basu, "Combustion dynamics of low vapour pressure nanofuel droplets," *Physics of Fluids*, vol. 29, no. 7, p. 074102, 2017.

[45] K. S. Suslick and G. J. Price, "Applications of ultrasound to materials chemistry," *Annual Review of Materials Science*, vol. 29, no. 1, pp. 295–326, 1999.

[46] N. Otsu, "A threshold selection method from gray-level histograms," *IEEE transactions on systems, man, and cybernetics*, vol. 9, no. 1, pp. 62–66, 1979.

[47] K. Kannaiyan and R. Sadr, "The effects of alumina nanoparticles as fuel additives on the spray characteristics of gas-to-liquid jet fuels," *Experimental Thermal and Fluid Science*, vol. 87, pp. 93–103, 2017.

[48] A. Faghri and Y. Zhang, *Transport phenomena in multiphase systems*. Elsevier, 2006.

[49] M. Elimelech, J. Gregory, and X. Jia, *Particle deposition and aggregation: measurement, modelling and simulation*. Butterworth-Heinemann, 2013.

[50] B. Pathak, P. Deepu, S. Basu, and R. Kumar, "Modeling of agglomeration inside a droplet with nanosuspensions in an acoustic field," *International Journal of Heat and Mass Transfer*, vol. 59, pp. 161–166, 2013.

[51] N. M. Aybers and A. K. Dagsöz, "The mechanism of drop formation from gas or vapour bubbles," *Wärme-und Stoffübertragung*, vol. 1, no. 2, pp. 80–86, 1968.

[52] D. M. Newitt, "Liquid entrainment 1. The mechanism of drop formation from gas vapour bubbles," *Trans. Instn. Chem. Engrs*, vol. 32, pp. 244–261, 1954.

[53] J. M. Boulton-Stone and J. R. Blake, "Gas bubbles bursting at a free surface," *Journal of Fluid Mechanics*, vol. 254, pp. 437–466, 1993.

[54] A. Pearson, E. Cox, J. R. Blake, and S. R. Otto, "Bubble interactions near a free surface," *Engineering analysis with boundary elements*, vol. 28, no. 4, pp. 295–313, 2004.

[55]   J. R. Blake and D. C. Gibson, "Growth and collapse of a vapour cavity near a free surface," *Journal of Fluid Mechanics*, vol. 111, pp. 123–140, 1981.

[56]   F. M. White, "Fluid mechanics, 1999," *Me Graw-Hill*, 1979.

[57]   W. A. Sirignano, *Fluid dynamics and transport of droplets and sprays*. Cambridge university press, 2010.

[58]   M. N. Rahaman, *Ceramic processing and sintering*. CRC press, 2017.

[59]   J. Oh, P. Heo, and Y. Yoon, "Acoustic excitation effect on NOx reduction and flame stability in a lifted non-premixed turbulent hydrogen jet with coaxial air," *International journal of hydrogen energy*, vol. 34, no. 18, pp. 7851–7861, 2009.

[60]   M. Lauer, M. Zellhuber, T. Sattelmayer, and C. J. Aul, "Determination of the heat release distribution in turbulent flames by a model based correction of OH* chemiluminescence," *Journal of Engineering for Gas Turbines and Power*, vol. 133, no. 12, 2011.

[61]   B. O. Ayoola, R. Balachandran, J. H. Frank, E. Mastorakos, and C. F. Kaminski, "Spatially resolved heat release rate measurements in turbulent premixed flames," *Combustion and flame*, vol. 144, no. 1–2, pp. 1–16, 2006.

[62]   R. Santhosh and S. Basu, "Transitions and blowoff of unconfined non-premixed swirling flame," *Combustion and Flame*, vol. 164, pp. 35–52, 2016.

[63]   V. Nori and J. Seitzman, "Chemiluminescence measurements and modeling in syngas, methane and jet-A fueled combustors," in *45th AIAA aerospace sciences meeting and exhibit*, 2007, p. 466.

[64]   I. Kimura, "Stability of laminar-jet flames," in *Symposium (International) on Combustion*, 1965, vol. 10, pp. 1295–1300.

[65]   T.-Y. Toong, "Mechanisms of combustion instability," in *Symposium (International) on Combustion*, 1965, vol. 10, pp. 1301–1313.

[66]   S. R. Turns, *An introduction to combustion*, vol. 499. McGraw-hill New York, 1996.

[67]   C. H. Wang and C. K. Law, "Microexplosion of fuel droplets under high pressure," *Combustion and Flame*, vol. 59, no. 1, pp. 53–62, 1985.

[68]   S. C. Wong and S. R. Turns, "Disruptive burning of Aluminum/Arbon slurry droplets," *Combustion science and technology*, vol. 66, no. 1–3, pp. 75–92, 1989.

[69]   D. Levi-Hevroni, A. Levy, and I. Borde, "Mathematical modeling of drying of liquid/solid slurries in steady state one-dimensional flow," *Drying technology*, vol. 13, no. 5–7, pp. 1187–1201, 1995.

[70]   C. H. Wang, X. Q. Liu, and C. K. Law, "Combustion and microexplosion of freely falling multicomponent droplets," *Combustion and flame*, vol. 56, no. 2, pp. 175–197, 1984.

[71]   R. Bhatia and W. Sirignano, "Vaporization and combustion of metal slurry droplets," in *29th Aerospace Sciences Meeting*, 1993, p. 282.

[72]   N. Tsapis *et al.*, "Onset of buckling in drying droplets of colloidal suspensions," *Physical review letters*, vol. 94, no. 1, p. 018302, 2005.

[73]   V. Y. Rudyak, A. A. Belkin, and V. V. Egorov, "On the effective viscosity of nanosuspensions," *Technical Physics*, vol. 54, no. 8, pp. 1102–1109, 2009.

[74]   T. Niioka and J. Sato, "Combustion and microexplosion behavior of miscible fuel droplets under high pressure," in *Symposium (International) on Combustion*, 1988, vol. 21, pp. 625–631.

[75]   V. S. Nikolayev, D. Chatain, Y. Garrabos, and D. Beysens, "Experimental evidence of the vapor recoil mechanism in the boiling crisis," *Physical review letters*, vol. 97, no. 18, p. 184503, 2006.

[76]   M. M. Avulapati, L. C. Ganippa, J. Xia, and A. Megaritis, "Puffing and micro-explosion of diesel–biodiesel–ethanol blends," *Fuel*, vol. 166, pp. 59–66, 2016.

[77]   A. Mansour and N. Chigier, "Disintegration of liquid sheets," *Physics of Fluids A: Fluid Dynamics*, vol. 2, no. 5, pp. 706–719, 1990.

[78]   L. De Luca and M. Costa, "Instability of a spatially developing liquid sheet," *Journal of Fluid Mechanics*, vol. 331, pp. 127–144, 1997.

[79]   I. F. Sbalzarini and P. Koumoutsakos, "Feature point tracking and trajectory analysis for video imaging in cell biology," *Journal of structural biology*, vol. 151, no. 2, pp. 182–195, 2005.

[80]   P. Deepu, S. Basu, and R. Kumar, "Dynamics and fracture of ligaments from a droplet on a vibrating surface," *Physics of Fluids*, vol. 25, no. 8, p. 082106, 2013.

[81]   L. Duchemin, S. Popinet, C. Josserand, and S. Zaleski, "Jet formation in bubbles bursting at a free surface," *Physics of fluids*, vol. 14, no. 9, pp. 3000–3008, 2002.

[82]   B. Pathak and S. Basu, "Deformation pathways and breakup modes in acoustically levitated bicomponent droplets under external heating," *Physical Review E*, vol. 93, no. 3, p. 033103, 2016.

[83]   M. Ghamari and A. Ratner, "Combustion characteristics of diesel and Jet-A droplets blended with polymeric additive," *Fuel*, vol. 178, pp. 63–70, 2016.

[84]   M. Ghamari and A. Ratner, "Combustion characteristics of colloidal droplets of jet fuel and carbon based nanoparticles," *Fuel*, vol. 188, pp. 182–189, 2017.

[85]   A. Chatterjee, "An introduction to the proper orthogonal decomposition," *Current science*, pp. 808–817, 2000.

[86]   G. Berkooz, P. Holmes, and J. L. Lumley, "The proper orthogonal decomposition in the analysis of turbulent flows," *Annual review of fluid mechanics*, vol. 25, no. 1, pp. 539–575, 1993.

[87]   K. Rajamanickam and S. Basu, "Insights into the dynamics of spray–swirl interactions," *Journal of Fluid Mechanics*, vol. 810, pp. 82–126, 2017.

[88]   S. H. R. Müller, B. Böhm, M. Gleißner, R. Grzeszik, S. Arndt, and A. Dreizler, "Flow field measurements in an optically accessible, direct-injection spray-guided internal combustion engine using high-speed PIV," *Experiments in fluids*, vol. 48, no. 2, pp. 281–290, 2010.

[89]   P. Deepu, S. Chowdhuri, and S. Basu, "Oscillation dynamics of sessile droplets subjected to substrate vibration," *Chemical Engineering Science*, vol. 118, pp. 9–19, 2014.

[90]   P. M. Guerieri, R. J. Jacob, J. B. DeLisio, M. C. Rehwoldt, and M. R. Zachariah, "Stabilized microparticle aggregates of oxygen-containing nanoparticles in kerosene for enhanced droplet combustion," *Combustion and Flame*, vol. 187, pp. 77–86, 2018.

[91]   A. L. Yarin, G. Brenn, O. Kastner, D. Rensink, and C. Tropea, "Evaporation of acoustically levitated droplets," *Journal of Fluid Mechanics*, vol. 399, pp. 151–204, 1999.

[92]   S. Basu, A. Saha, and R. Kumar, "Thermally induced secondary atomization of droplet in an acoustic field," *Applied Physics Letters*, vol. 100, no. 5, p. 054101, 2012.

[93]   S. Basu, A. Saha, and R. Kumar, "Criteria for thermally induced atomization and catastrophic breakup of acoustically levitated droplet," *International Journal of Heat and Mass Transfer*, vol. 59, pp. 316–327, 2013.

[94]   A. Sanyal, S. Basu, and R. Kumar, "Experimental analysis of shape deformation of evaporating droplet using Legendre polynomials," *Physics Letters A*, vol. 378, no. 5–6, pp. 539–548, 2014.

[95]   D. C. K. Rao, S. Karmakar, and S. Basu, "Atomization characteristics and instabilities in the combustion of multi-component fuel droplets with high volatility differential," *Scientific reports*, vol. 7, no. 1, pp. 1–15, 2017.

[96]   S. R. G. Avila and C.-D. Ohl, "Fragmentation of acoustically levitating droplets by laser-induced cavitation bubbles," *Journal of Fluid Mechanics*, vol. 805, pp. 551–576, 2016.

[97]   C. R. Wilke and P. Chang, "Correlation of diffusion coefficients in dilute solutions," *AIChE Journal*, vol. 1, no. 2, pp. 264–270, 1955.

[98]   S. Basu, E. Tijerino, and R. Kumar, "Insight into morphology changes of nanoparticle laden droplets in acoustic field," *Applied Physics Letters*, vol. 102, no. 14, p. 141602, 2013.

[99]   L. G. Bremer, P. Walstra, and T. van Vliet, "Estimations of the aggregation time of various colloidal systems," *Colloids and Surfaces A: Physicochemical and Engineering Aspects*, vol. 99, no. 2–3, pp. 121–127, 1995.

[100] K. Pandey and S. Basu, "High vapour pressure nanofuel droplet combustion and heat transfer: Insights into droplet burning time scale, secondary atomisation and coupling of droplet deformations and heat release," *Combustion and Flame*, vol. 209, pp. 167–179, 2019.

[101] Y. Gan and L. Qiao, "Radiation-enhanced evaporation of ethanol fuel containing suspended metal nanoparticles," *International Journal of Heat and Mass Transfer*, vol. 55, no. 21–22, pp. 5777–5782, 2012.

[102] J. S. Basha and R. B. Anand, "An experimental study in a CI engine using nanoadditive blended water–diesel emulsion fuel," *International journal of green energy*, vol. 8, no. 3, pp. 332–348, 2011.

[103] S. Gumus, H. Ozcan, M. Ozbey, and B. Topaloglu, "Aluminum oxide and copper oxide nanodiesel fuel properties and usage in a compression ignition engine," *Fuel*, vol. 163, pp. 80–87, 2016.

[104] K. Rajamanickam and S. Basu, "Insights into the dynamics of conical breakdown modes in coaxial swirling flow field," *Journal of Fluid Mechanics*, vol. 853, pp. 72–110, 2018.

[105] K. Rajamanickam and S. Basu, "On the dynamics of vortex–droplet interactions, dispersion and breakup in a coaxial swirling flow," *Journal of Fluid Mechanics*, vol. 827, pp. 572–613, 2017.

[106] J. W. Bennewitz *et al.*, "Periodic partial extinction in acoustically coupled fuel droplet combustion," *Combustion and Flame*, vol. 189, pp. 46–61, 2018.

[107] C. I. Sevilla-Esparza, J. L. Wegener, S. Teshome, J. I. Rodriguez, O. I. Smith, and A. R. Karagozian, "Droplet combustion in the presence of acoustic excitation," *Combustion and Flame*, vol. 161, no. 6, pp. 1604–1619, 2014.

[108] H. S. Sim, M. A. Plascencia, A. Vargas, and A. R. Karagozian, "Acoustically Forced Droplet Combustion of Liquid Fuel with Reactive Aluminum Nanoparticulates," *Combustion Science and Technology*, pp. 1–25, 2019.

[109] R. L. Panton, *Incompressible flow*. John Wiley & Sons, 2013.

[110] K. Seshadri and F. A. Williams, "Laminar flow between parallel plates with injection of a reactant at high Reynolds number," *International Journal of Heat and Mass Transfer*, vol. 21, no. 2, pp. 251–253, 1978.

[111] T. C. Lieuwen, *Unsteady combustor physics*. Cambridge University Press, 2012.

[112] S. J. Shanbhogue, S. Husain, and T. Lieuwen, "Lean blowoff of bluff body stabilized flames: Scaling and dynamics," *Progress in Energy and Combustion Science*, vol. 35, no. 1, pp. 98–120, 2009.

[113] H. Bénard, "Formation de centres de giration a l'arrière d'un obstacle en movement," *Comptes Rendus Academie des Sciences*, vol. 147, pp. 839–842, 1908.

[114] M. Provansal, C. Mathis, and L. Boyer, "Bénard-von Kármán instability: transient and forced regimes," *Journal of Fluid Mechanics*, vol. 182, pp. 1–22, 1987.

[115] A. Roshko, "On the drag and shedding frequency of two-dimensional bluff bodies," 1954.

[116] V. H. Schlichting, "Laminare strahlausbreitung," *ZAMM-Journal of Applied Mathematics and Mechanics/Zeitschrift für Angewandte Mathematik und Mechanik*, vol. 13, no. 4, pp. 260–263, 1933.

[117] D. T. Landfried, A. Jana, and M. Kimber, "Characterization of the behavior of confined laminar round jets," *Journal of Fluids Engineering*, vol. 137, no. 3, p. 034501, 2015.

[118] K. Pandey and S. Basu, "How boiling happens in nanofuel droplets," *Physics of Fluids*, vol. 30, no. 10, p. 107103, 2018.

[119] R. Kumar, E. Tijerino, A. Saha, and S. Basu, "Structural morphology of acoustically levitated and heated nanosilica droplet," *Applied Physics Letters*, vol. 97, no. 12, p. 123106, 2010.

[120] L.-W. Chen, "Application of PIV measurement techniques to study the characteristics of flame–acoustic wave interactions," *Flow Measurement and Instrumentation*, vol. 45, pp. 308–317, 2015.

[121] K. Rajamanickam, A. Potnis, K. S. Kumar, D. Sivakumar, and S. Basu, "On the influence of geometrical parameters on the spray characteristics of high shear injectors," *Experimental Thermal and Fluid Science*, vol. 109, p. 109872, 2019.

[122] J. D. Clark, "Ignition!: An informal history of liquid rocket propellants," *Rutgers University Press*, 1972.

[123] V. Nedovic, A. Kalusevic, V. Manojlovic, S. Levic, and B. Bugarski, B, "An overview of encapsulation technologies for food applications", *Procedia Food Science*, vol. 1, pp.1806-1815, 2011.

[124] B. A. Morgan, Z. Xing, E. D. Cranston, and M. R. Thompson, "Acoustic levitation as a screening method for excipient selection in the development of dry powder vaccines", *International journal of pharmaceutics,* vol. 563, pp. 71-78, 2019.

[125] S. Rosenkranz, W. Schäfer, C. Tropea, and A. M. Zoubir, "Modeling photon transport in turbid media for measuring colloidal concentration in drops using the time-shift technique", *Applied optics*, vol. 55, no. 34, pp.9703-9711, 2016.

[126] W.Y. Teoh, R. Amal, L. Mädler, Flame spray pyrolysis: an enabling technology for nanoparticles design and fabrication, *Nanoscale*, vol. 2, pp. 1324–1347, 2010.

[127] G.L. Messing, S.C. Zhang, G.V. Jayanthi, Ceramic powder synthesis by spray pyrolysis, *Journal of the American Ceramic Society,* vol. 76, no. 11, pp. 2707–2726, 1993.

[128] I.W. Lenggoro, Y. Itoh, N. Iida, K. Okuyama, Control of size and morphology in NiO particles prepared by a low-pressure spray pyrolysis, *Materials Research Bulletin*, vol. 38, pp. 1819–1827, 2003.

[129] C.D. Rosebrock, T. Wriedt, L. Mädler, K. Wegner, The role of microexplosions in flame spray synthesis for homogeneous nanopowders from low-cost metal precursors, *AIChE Journal*, vol. 62, pp. 381–391, 2016.

[130] F. Meierhofer, H. Li, M. Gockeln, R. Kun, T. Grieb, A. Rosenauer, U. Fritsching, J. Kiefer, J. Birkenstock, L. Mädler, S. Pokhrel, Screening precursor–solvent combinations for Li4Ti5O12 energy storage material using flame spray pyrolysis, *ACS Applied Materials & Interfaces*, vol. 9, pp. 37760–37777, 2017.

[131] C.D. Rosebrock, N. Riefler, T. Wriedt, L. Mädler, D.T. Stephen, Disruptive burning of precursor/solvent droplets in flame-spray synthesis of nanoparticles, *AIChE Journal*, vol. 59 , pp. 4553–4566, 2013.

[132] M. A. Pfeil, S. F. Son, and W. E. Anderson, "Influence of ammonia borane on the stability of a liquid rocket combustor", *Journal of Propulsion and Power*, vol. 30, no. 2, pp.290-298, 2014.